VACUUM MAGNETIC FLUX SURFACE MEASUREMENTS MADE ON THE

COMPACT TOROIDAL HYBRID

Except where reference is made to the work of others, the work described in this dissertation is my own or was done in collaboration with my advisory committee. This dissertation does not include proprietary or classified information.

_____

Joshua T. Peterson

Certificate of Approval:

_____	_____
Gregory J. Hartwell Associate Research Professor Physics	Stephen F. Knowlton, Chair Professor Physics
_____	_____
James D. Hanson Professor Physics	Edward Thomas, Jr. Professor Physics

_____

Joe F. Pittman
Interim Dean
Graduate School

VACUUM MAGNETIC FLUX SURFACE MEASUREMENTS MADE ON THE COMPACT TOROIDAL HYBRID

Joshua T. Peterson

A Dissertation

Submitted to

the Graduate Faculty of

Auburn University

in Partial Fulfillment of the

Requirements for the

Degree of

Doctor of Philosophy

Auburn, Alabama
August 09, 2008

VACUUM MAGNETIC FLUX SURFACE MEASUREMENTS MADE ON THE

COMPACT TOROIDAL HYBRID

_____
Signature of Author

August 09, 2008
Date of Graduation

DISSERTATION ABSTRACT

VACUUM MAGNETIC FLUX SURFACE MEASUREMENTS MADE ON THE COMPACT TOROIDAL HYBRID

Joshua T. Peterson

Doctor of Philosophy, August 09, 2008
(B.S., University of Wisconsin, Stevens Point, 2000)

203 Typed Pages

Directed by Stephen F. Knowlton

Understanding the behavior of plasmas in magnetic confinement fusion devices typically requires accurate knowledge of the magnetic field structure. In stellarator-type confinement devices, the helical magnetic field is produced by currents in external coils. The field lines may be traced experimentally in the absence of plasma. Vacuum magnetic field mapping experiments were performed on the recently-constructed Compact Toroidal Hybrid (CTH) with a movable electron gun and phosphor-coated screen. These experiments verify the range of accessible magnetic configurations, compare the actual

magnetic configuration with the design configuration, and identify vacuum field errors that lead to perturbations of the vacuum magnetic flux surfaces. The experimental field mapping results are compared to computer simulations based on accurate models of the magnet coils that produce the field. Modifications are made to the coil models to achieve better agreement between the simulations and the experimental results. This process resulted in a model of the CTH magnetic coils of that accurately describes the experimental field mapping results and can be used as the basis of a better model of the vacuum magnetic field of CTH in preparation for plasma studies.

ACKNOWLEDGEMENTS

The author would like to thank Dr. Gregory Hartwell for assistance and advice given during the course of the field mapping experiments and data analysis. Thanks are also due to Dr. James Hanson and Jorge Munoz for the simulation computer codes used within this dissertation. Lastly, many thanks to Dr. Stephen Knowlton for his persistence and patience in guiding me through this process.

Style manual or journal used AIP Style Manual

Computer software used Microsoft Word

TABLE OF CONTENTS

LIST OF FIGURES

LIST OF TABLES

CHAPTER 1: INTRODUCTION

1.1 FUSION AND PLASMAS

Nuclear fusion occurs when two or more nuclei combine to form one larger nucleus, such as two hydrogen nuclear isotopes fusing together to form one helium nucleus. During the fusion reaction of small nuclei, e.g., hydrogen, enormous amounts of energy are released. The fusion reaction of a tritium nucleus, consisting of one proton and two neutrons, combining with a deuterium nucleus, consisting of one proton and one neutron is shown in Fig. 1.1. The products of the reaction are a ^{4}He nucleus (α particle) with a kinetic energy of 3.5 MeV and a neutron with a kinetic energy of 14.1 MeV. The total amount of energy released is 17.6 MeV. By comparison, the binding energy of an H_2 molecule, representative of a typical chemical reaction, is significantly smaller at 4.5 eV.

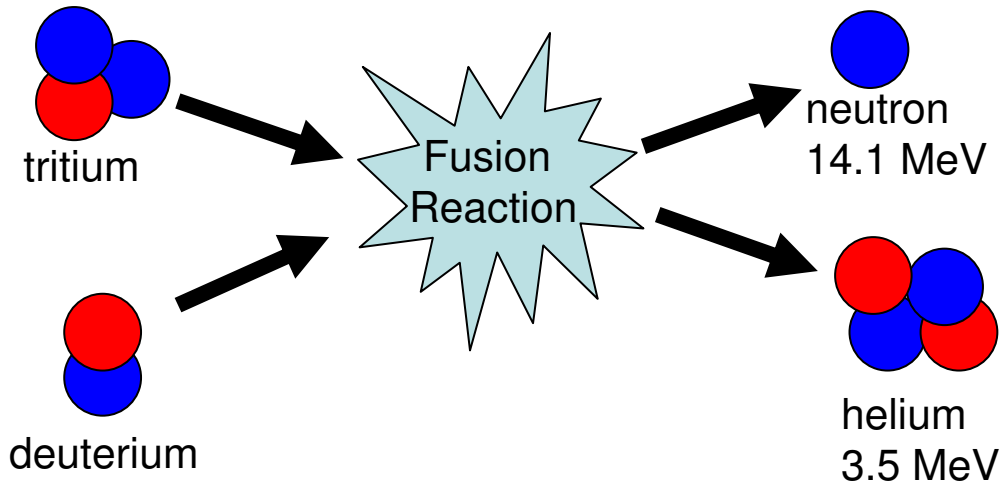

Fig. 1.1 Tritium-Deuterium fusion reaction

If the fusion reaction could be contained and the released energy captured, fusion power plants could be used to produce significant levels of electrical energy, without the release of greenhouse gases associated with the burning of fossil fuels. It is this promise of fusion-powered electric energy that has driven much of fusion research over the past fifty years.

By contrast, nuclear fission takes place when one large nucleus is split into two smaller ones, such as uranium splitting into its radioactive daughter elements. For elements heavier than iron, this process also releases energy and is used in the nuclear power plants currently in operation. The energy released by a typical uranium fission reaction is 207MeV per reaction.

While nuclear fission also avoids producing greenhouse gases, it does have several major drawbacks as a power source. These include safe storage and containment of the long-lived radioactive waste produced by the fission process, the possibility of a meltdown occurring in the power plant releasing radioactive material to the environment, and the scarcity of fissionable uranium on the planet. In many people's minds, these drawbacks reduce the usefulness of fission as a clean long-term energy source.

Fusion, on the other hand is not limited by these problems. Fusion does not produce nearly the amounts of long-lived radioactive waste that fission does and therefore long term storage of waste is not required. A major accident occurring in a fusion power plant involving a runaway reaction is considered unlikely, because there is only several seconds worth of fuel in the fusion chamber at any instant. Lastly, the primary fuel sources are the heavy isotopes of hydrogen, deuterium and tritium. Deuterium is highly abundant consisting in 0.015% of the hydrogen found in water. The

radioactive tritium isotope required for the deuterium-tritium reaction is not found naturally on earth but can be bred from atoms such as lithium. Fusion power thus offers the possibility of a near limitless source of clean safe energy. The major problem with fusion power is achieving the necessary conditions required for significant levels of fusion reactions to occur, conditions which are comparable to that of the core of a star.

A successful fusion reaction of two positively charged nuclei occurs when they are brought close enough together so that the attractive strong force overcomes the repulsive Coulomb force. In order to do this, the reactants must initially have a great deal of kinetic energy. The Coulomb potential barrier between two protons as a function of their separation distance is shown in Fig. 1.2. As the two nuclei approach each other the potential energy of the system increases up to an energy U_b~ 1 MeV, at a separation distance of r_n~10^{15} m. At this point the contribution of the short-range strong force decreases the potential energy of the system to a potential energy of $-U_0$.

Classically, particles would need energies of at least 1 MeV to pass over the Coulomb barrier. Therefore the approaching nucleus with energy $\varepsilon < U_b$ in Fig. 1.2, should only reach a separation distance of r_{tp} before the repulsive electric force repels the nuclei. However, due to quantum mechanical uncertainties, particles with lower energy may tunnel through the barrier, thus allowing fusion reactions to occur which are classically forbidden. Also, given a thermal Maxwellian distribution of particles, a significant population of the particles in the high energy tail have energies in excess of U_b, even though the energy on average is lower than the potential barrier. Therefore fusion can take place in a hydrogenic plasma with average temperatures far lower than the Coulomb potential barrier height.

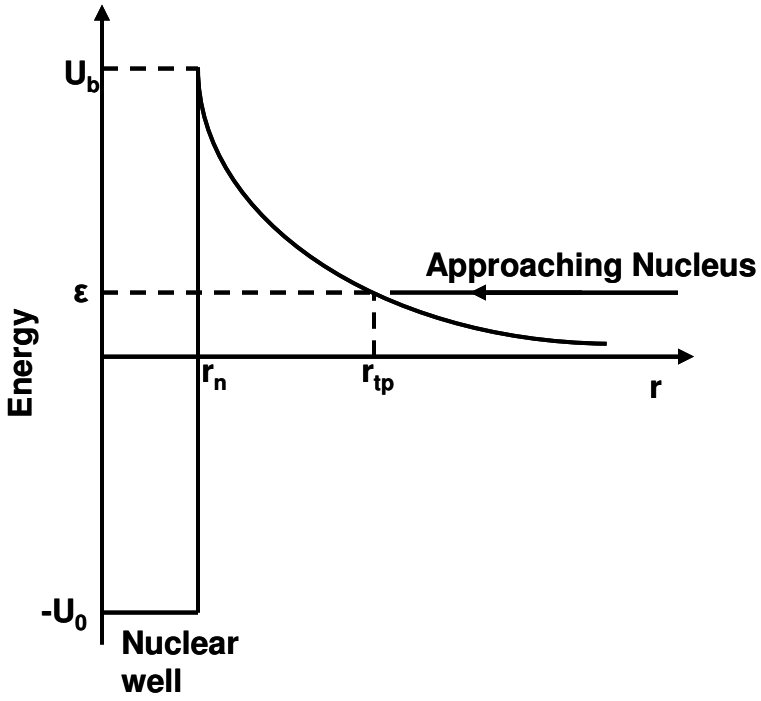

Fig. 1.2 Potential energy of two protons [1]

Plasmas capable of fusion reactions consisting of deuterium and tritium nuclei must have characteristic temperatures on the order of 10 keV. This energy corresponds to temperatures on the order of 100,000,000 K. It is common in plasma physics to express temperatures in energy units of electron volts, eV as given in Eq. 1.1,

$$\varepsilon = \frac{1}{2} mv^2 = kT \rightarrow 1eV = 11{,}600K \tag{1.1}$$

where ε is the kinetic energy of the particle, k is Boltzmann's constant, and T is the absolute temperature in Kelvin.

Another important factor in describing nuclear interactions is the effective cross-sectional area of two-particle collisions. The cross-section is proportional to the probability for the nuclear interaction between two particles to occur, and is a measure of the effective area of the nuclear target which in plasma physics is dependent on the

energies of the particles. Fig. 1.3 shows the cross-section vs. particle energies for several possible fusion reactions.

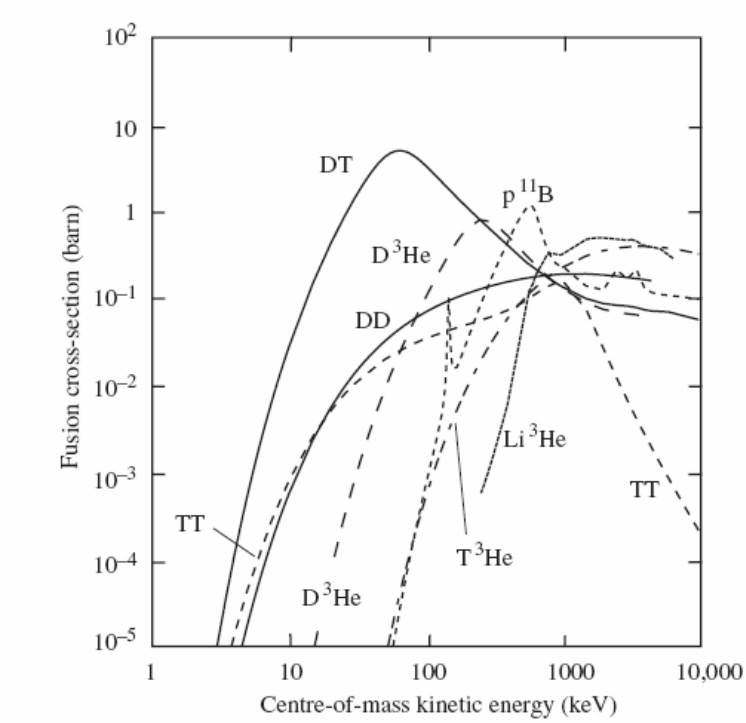

Fig. 1.3 Fusion cross-section vs. energy[2]

With knowledge of the cross-sections for fusion reactions, one can define the average reactivity or the probability of reaction per unit time per unit density of target nuclei, as given in Eq. 1.2[3],

$$< \sigma \cdot v >= \int_0^\infty \sigma(v) \cdot v \cdot f(v) \cdot dv \qquad (1.2)$$

where σ is the cross-section between the two particles, v is their relative velocity, and f(v) is the distribution function of the relative velocities. The distribution function is normalized such that the value of the integral is 1 when integrated over all velocities.

Of the reactions depicted in Fig. 1.3, the tritium-deuterium reaction has the largest cross-section and also the largest average reactivity at the lowest energies, and therefore is considered to be the most likely candidate for fusion power.

1.2 Confining Fusion Plasmas

At the high temperatures required for fusion to occur, the light atoms become fully ionized, such that the electrons are no longer bound to the nucleus. This ionized gas is known as a plasma, and exhibits special properties because all the constituents are charged particles and highly mobile. Plasmas are considered to be the fourth state of matter in that they behave differently from the gaseous, liquid and solid states. A good understanding of plasma physics is crucial to the development of fusion energy.

The extremely high temperature plasmas necessary for fusion, make containing the plasma one of the largest challenges in fusion research. The plasma cannot be simply heated and maintained in a conventional solid container but must be contained using more unconventional methods, of which there are several possibilities.

In nature, fusion takes place in the core of a star where the high temperature dense plasma is confined to the stellar core by the gravitational pressure of the star's outer layers. Gravitational confinement is impossible on earth, because of the enormous mass required to exert the necessary pressure for containment.

Fusion also successfully takes place in the hydrogen bomb which produces the conditions necessary for fusion by placing deuterium and tritium inside a conventional fission bomb. The explosion of the surrounding bomb implodes the fusion fuel, raising the temperature and density momentarily to levels necessary for fusion. The hydrogen

bomb's explosive nature and radioactive waste of the uranium by-products make this an unusable source of energy.

For controlled fusion reactions on earth, there are two main areas of research being conducted. The first is inertial confinement, which is conceptually similar to the hydrogen bomb. In this type of confinement, a hydrogen fuel pellet is struck with powerful lasers or energetic ion beams, compressing the pellet and momentarily raising the temperature and density to the conditions necessary for fusion to occur. Controlled inertial confinement fusion research is expected to achieve the energy break-even point within the next decade.

The second approach to controlled fusion research is magnetic confinement. Magnetic confinement uses the plasma's charged nature to contain the plasma inside a magnetic "bottle" according to the following principle.

The Lorentz force law, Eq. 1.3,

$$\vec{F} = q\,(\vec{E} + \vec{v} \times \vec{B}) \tag{1.3}$$

describes the force on a particle with charge q in the presence of electrical and magnetic fields $\vec{E}$ and $\vec{B}$. Here $\vec{v}$ is the velocity of the particle. In a uniform magnetic field, charged particles will gyrate in small circles around a given magnetic field line. The center of the gyral motion is referred to as the guiding center. As shown in Fig. 1.4, the guiding center of the charged particle orbit travels freely along the magnetic field line with velocity $V_{\|}$, but its motion perpendicular to the field lines is restricted. This restriction, effectively traps the charged particles on magnetic field lines.

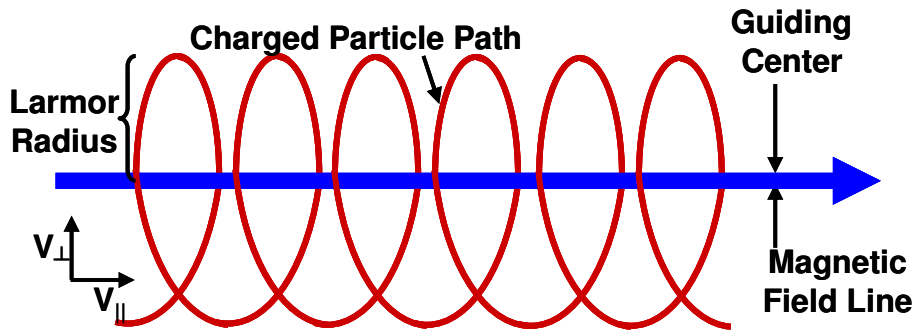

Fig. 1.4 Guiding center motion

The radius of the particle path, known as the Larmor radius r_L, is given by Eq. 1.4.[4]

$$r_L = \frac{m\, v_\perp}{|q|\, B} \tag{1.4}$$

Here m is the particle mass, $v_\perp$ is the particle velocity perpendicular to the magnetic field, and B is the magnitude of the magnetic field.

The objective of magnetic confinement is to minimize the flow of plasma into the chamber walls. Therefore in order to have good plasma confinement, charged particles following magnetic field lines need to do one of two things; either reverse direction before they reach the chamber wall, or follow field lines which do not intersect the chamber wall.

Many of the first magnetic confinement experiments were performed on linear machines which tried to employ the first approach. In linear plasma devices such as OGRA, DCX, and ASTRON[5], the confining magnetic field was oriented largely parallel to the walls of the chamber. Extensive, unsuccessful efforts were made to plug the ends of the device with magnetic mirrors, reducing the flux of plasma from the ends of the

cylinder. The escaping plasma lost from the ends of the machine resulted in poor particle confinement and low plasma densities.

To address the problem of particle loss from the ends of the linear machine, magnetic configurations in the shape of a torus (a doughnut shape) were proposed and tested. In a toroidal geometry, magnetic field lines can be designed to remain within the toroidal volume of the chamber. Particles traveling along such field lines cannot readily leave the plasma without undergoing collisional diffusion or transport due to plasma turbulence. Today, the torus is the most common shape of magnetic confinement experiments. The geometry of the torus is shown in Fig. 1.5.

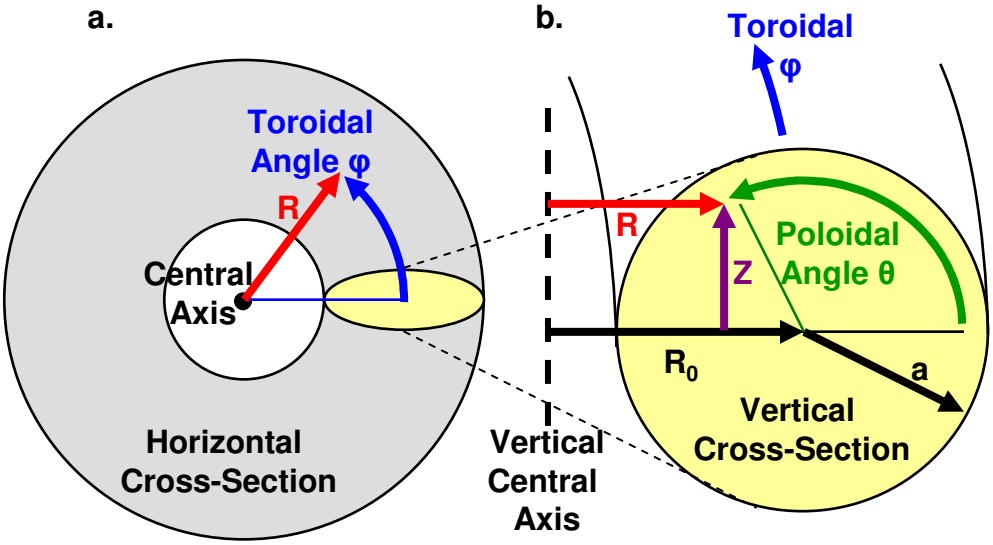

Fig. 1.5 Toroidal coordinate system
a) Top view of torus
b) Cross-sectional side view of torus

The toroidal angle φ, describes the angular location around the large circumference of the torus (the "long" way around the torus). The poloidal angle θ, describes the angular location in the torus within a vertical plane (the "short" way around the torus). Within this dissertation, the toroidal angle φ is measured counterclockwise

from the east side of the torus (as viewed from above). The poloidal angle θ, is measured counterclockwise from the outer midplane of the torus (while looking in the toroidal direction). In standard cylindrical coordinates (R, φ, Z), the vertical position of a point Z, is the distance above or below the horizontal midplane of the torus. The radial position of a point R, is distance from the central axis of the machine. The major radius of the torus R_0, is the radial distance from the central axis to the center of the toroidal volume. The minor radius a, is the distance from the circular axis of the torus to the torus wall.

There are currently two main types of magnetic confinement devices which have a toroidal geometry, the tokamak[6] and the stellarator[7,8]. In both of these, magnetic field lines define a closed volume inside the toroidal chamber having magnetic field components in both the toroidal and poloidal directions. In the tokamak, the toroidal field is produced by a set of planar external coils distributed at equally-spaced toroidal angles around the machine, while the poloidal field necessary for plasma confinement is produced by an inductively-driven current within the plasma. The dependence of plasma confinement on internal plasma currents, make the tokamak susceptible to current-driven instabilities and disruptions, where the plasma can become hydrodynamically unstable and rapidly decay, at which point confinement is lost. A major disruption in a fusion reactor could severely damage the reactor wall, vacuum vessel, and surrounding structures. The mitigation of disruptions in tokamaks is a major area of research.[9] Despite the potential drawback of disruptions, tokamaks have achieved the highest temperatures and densities of any magnetically confined plasma.

In contrast, stellarators produce the toroidal and poloidal fields required for confinement by means of currents in external coils, without the dependence on a toroidal

plasma current. In comparison to the planar coils of the tokamak, the coils of stellarators are three-dimensional, often having a helical shape. The plasmas produced by stellarators are inherently more macroscopically stable than those produced by tokamaks, because of the lack of current flowing within the plasma which could lead to disruptions.

The Compact Toroidal Hybrid (CTH) is a stellarator with the capability of generating internal toroidal plasma currents. As such, it represents a hybrid device between a tokamak and a currentless helical device. The major radius of CTH is R_0 =0.75 m. The minor radius is a_{vv} = 0.29 m. The magnetic field of CTH has a value |B| • 0.7 T. Because one of the major topics of this dissertation is obtaining a physical description of the magnetic coil structure, more details about the CTH device will be given throughout the text.

1.3 Magnetic Field Configurations of Stellarators

For effective magnetic confinement in the toroidal magnetic field geometry of tokamaks and stellarators, the magnetic field lines must define nearly circular paths within the vacuum vessel. To lowest order, the radius of curvature of the individual field lines is the radial coordinate R_c, as pictured in Fig. 1.6. Because of the toroidal curvature of the magnetic field lines, the charged particles of the plasma undergo a net drift perpendicular to the magnetic field. This curvature drift, $\overrightarrow{v_R}$, is given by Eq. 1.5.[10]

$$\overrightarrow{v_R} = \frac{m v_{\|}^2}{q} \frac{\overrightarrow{R_c} \times \vec{B}}{R_c^2 B^2} \tag{1.5}$$

Here $v_{\|}$ is the particle velocity parallel to the magnetic field.

Also, in the toroidal geometry, the strength of the field typically decreases with increasing radius.[11] Therefore the gradient of the magnetic field is inward, as shown in Fig. 1.6. This gradient in the strength of the magnetic field produces a second particle drift known as the grad-B drift, $\overrightarrow{v_{\nabla B}}$ given by Eq. 1.6.

$$\overrightarrow{v_{\nabla B}} = \pm \frac{1}{2} v_{\perp} r_L \frac{\vec{B} \times \overrightarrow{\nabla B}}{B^2} \tag{1.6}$$

Adding Eq.(1.5 and 1.6) gives the net drift expressed in Eq. 1.7.

$$\overrightarrow{v_R} + \overrightarrow{v_{\nabla B}} = \frac{m}{q}\left(v_{\parallel}^2 + \frac{1}{2} v_{\perp}^2\right) \frac{\overrightarrow{R_c} \times \vec{B}}{R_c^2 B^2} \tag{1.7}$$

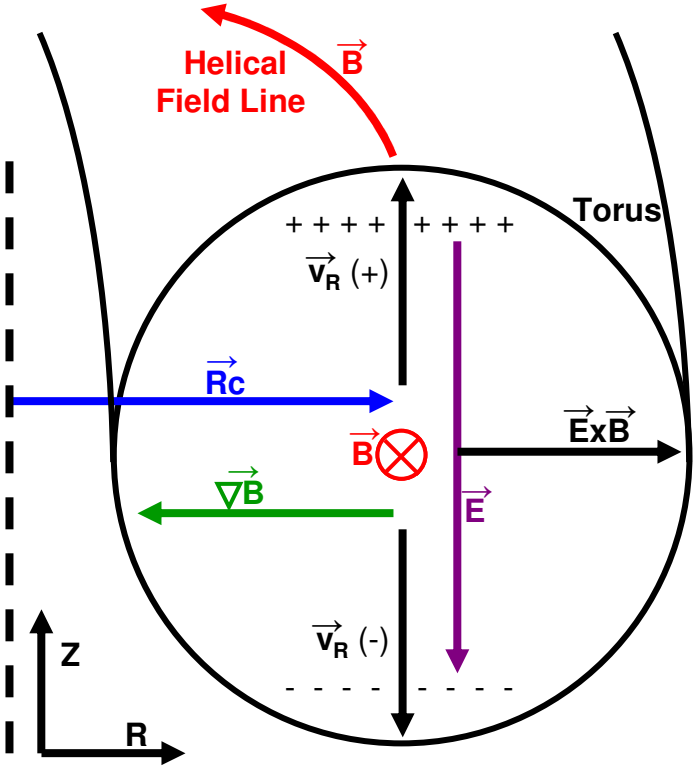

Fig. 1.6 Toroidal field geometry and particle drifts

The dependence of the drift on the sign of the charge in Eq. 1.7, has the effect of separating the positive and negative charges perpendicular to both $\overrightarrow{R_c}$ and $\vec{B}$. In Fig.

1.6, the positive charges are seen to experience an upward drift, $\overrightarrow{v_R}$ (+), and the negative charges experience a downward drift, $\overrightarrow{v_R}$ (-). The separation of charges creates an electric field downward. The presence of the electric field leads to an $\vec{E}\times\vec{B}$ drift, given by Eq. 1.8.

$$\overrightarrow{v_E} = \frac{\vec{E}\times\vec{B}}{B^2} \tag{1.8}$$

This drift velocity is outward for the fields depicted in Fig. 1.6. Therefore the confinement of charged particles is impossible with pure toroidal fields due to the particle drifts that are created by the toroidal geometry.

To overcome this effect, field lines in toroidal machines must have a helical configuration, in which the magnetic field has a poloidal component in addition to a toroidal component. The effect of the additional poloidal field on the positive charges is shown in Fig. 1.7. As described earlier, the positive particles drift upward (1) due to the curvature and grad-B drifts of the magnetic field. But because the particles are now following the helical field lines, the upward drifting positive charges are carried toward the bottom of the vessel (2) as they travel toroidally due to the poloidal component of the magnetic field. Once in the lower half, the curvature and grad-B drift continues to be in the upward direction (3) but is now toward the center of the chamber. Therefore we see that the net vertical drift upward is cancelled by the presence of the poloidal field. Similar behavior exists for the negative charges, in that the particles drift downward, but are carried poloidally to the top. As a result, charge separation does not occur within the

plasma. Without charge separation, no electrostatic field is present, leading to no radial $\vec{E}\times\vec{B}$ drift, resulting in much better confinement of the plasma.

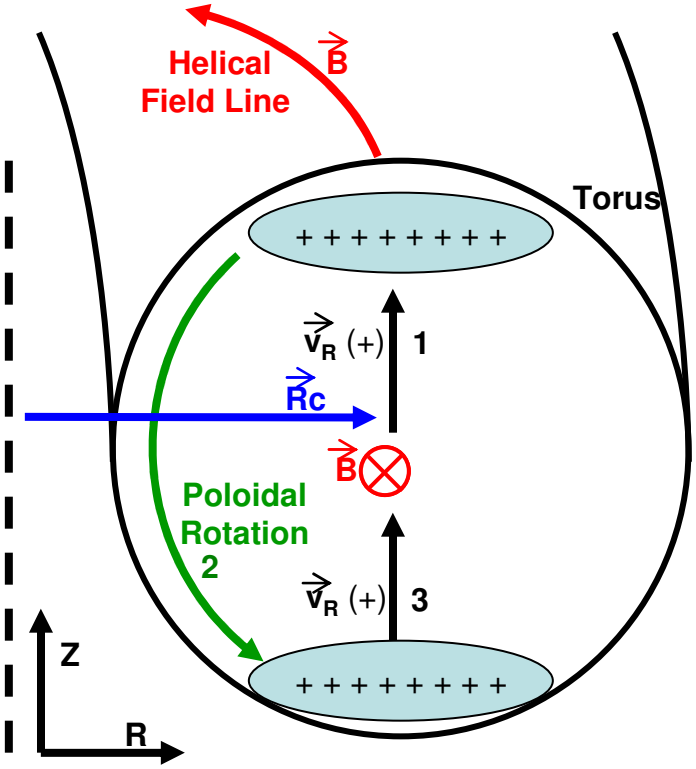

Fig. 1.7 Drifts cancelled by helical field

If a magnetic field line in a toroidal plasma device effectively defines a closed surface after making a large number of toroidal transits, that surface is said to be a magnetic flux surface. In CTH and other toroidal plasma devices, the coils are designed to produce magnetic field lines that define a set of concentric magnetic flux surfaces.[12] Such a surface contains a constant amount of toroidal magnetic flux Ψ, given by Eq. 1.9,

$$\psi = \int_{\text{Area}} \vec{B}\cdot ds\,\hat{\varphi} = \text{Const} \qquad (1.9)$$

where the integral is taken over the cross-sectional area of the torus. Because a field line, by definition, must lie in on flux surface, one requires [13]

$$\nabla\psi \cdot \vec{B} = 0 \,. \qquad (1.10)$$

Eq.1.10 indicates that magnetic field lines are not allowed to cross the flux surfaces. Therefore particles that are trapped following field lines also remain trapped on a given magnetic flux surface.

Magnetic flux surfaces representing different helical field lines are nested inside one another forming concentric surfaces[14], as shown in Fig. 1.8. Each flux surface encloses a different amount of magnetic flux, which can be used to characterize or label that flux surface. The innermost flux surface is ideally defined by a line, and is referred to as the magnetic axis.

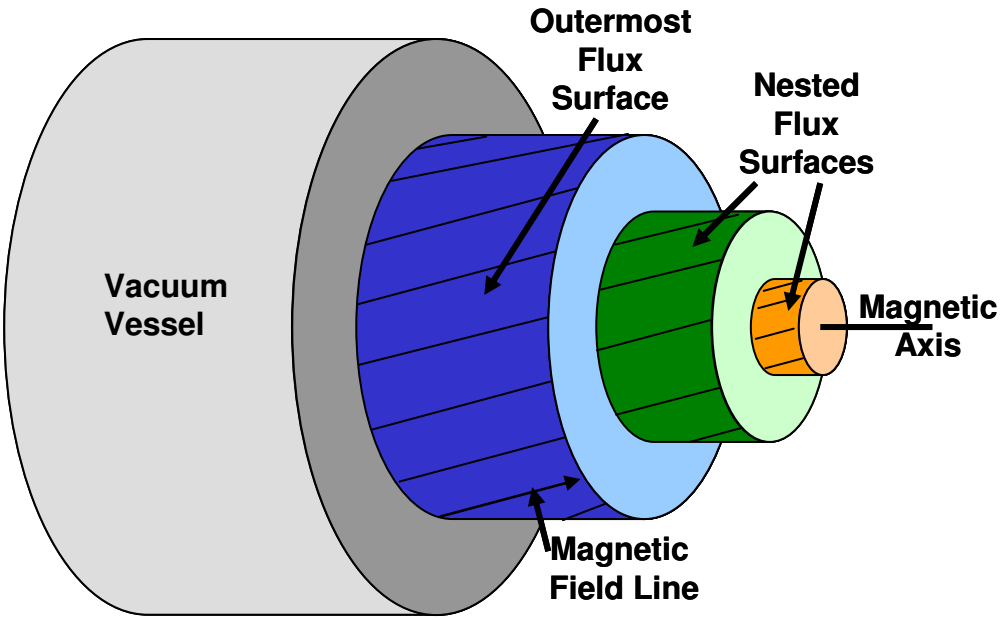

Fig. 1.8 Nested flux surfaces within vacuum vessel

By computing the paths of a number of different field lines, one can make a puncture plot of the field lines as they intersect one toroidal cross-sectional plane, and thus visualize the flux surfaces. A computed surface of section (SOS) puncture plot with several nested flux surfaces is shown in Fig. 1.9 for the CTH device.

The simulation of Fig. 1.9 was performed with the integreble field torsatron (IFT)[1516] field-line following code. IFT uses the Biot-Savart law to calculate the magnetic fields within the vacuum vessel produced by currents in specified magnetic coils. The puncture plot of Fig. 1.9 was produced by following field lines starting at different radial locations and following them through 100 toroidal transits.

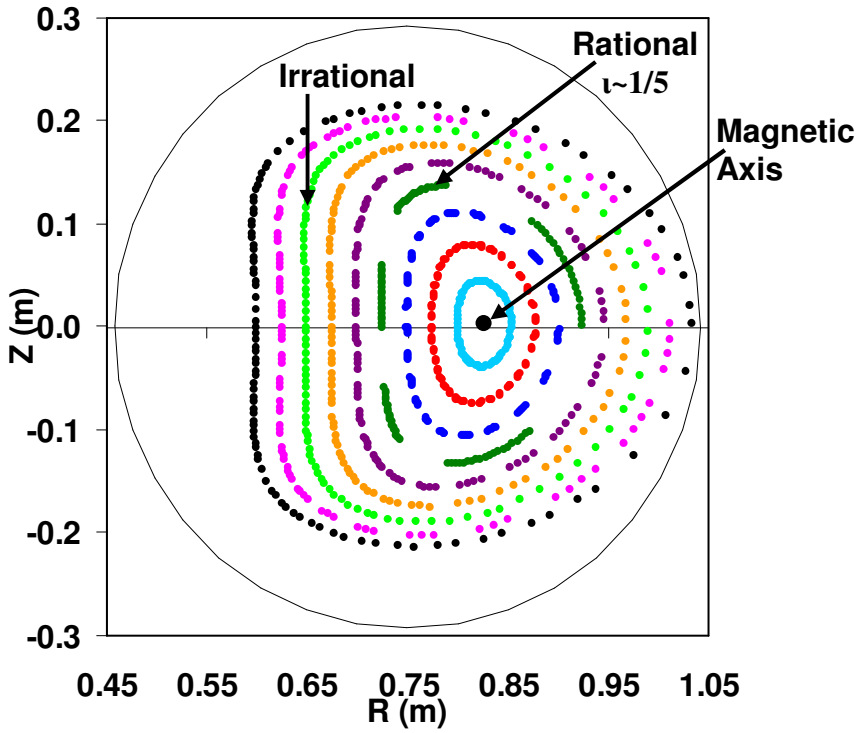

Fig. 1.9 Computed puncture plot of several magnetic field lines
The shape and rotational transform of ten different magnetic flux surfaces are revealed in the puncture plot. Among the surfaces visible are the magnetic axis in the center and several nearly rational and irrational surfaces.

The helical twist of a field line as it undergoes its toroidal and poloidal transits around the torus is characterized by a parameter known as the rotational transform, denoted as ɩ. In the limit of and infinite number of toroidal (or poloidal) transits, the rotational transform can be defined as the ratio of the number of poloidal circuits to the number of toroidal circuits made by a field line (Eq. 1.11).

$$\iota = \lim_{n\to\infty} \frac{n}{m} \tag{1.11}$$

Here n is the number of poloidal circuits of the field line (toroidal mode number) and m being the number of toroidal circuits of the field line (poloidal mode number).

If the field line on a given flux surface undergoes an integer number of poloidal rotations in a finite integer number of toroidal rotations, the flux surface is said to be a rational surface. Rational surfaces with values of m and n which are small (for example $n< 3$, $m < 20$) are considered to be low-order rational surfaces. Rational surfaces can be identified both experimentally and through simulation and will be a large focus of this dissertation. An example of a nearly rational surface can be seen in Fig. 1.9. The surface represented by the dark green points has a rotational transform close to, $\iota = 1/5$ as can be seen by the 5 clusters of points. If this were the exact $\iota = 1/5$ surface, only 5 points would appear in the plot instead of the 5 clusters.

If on the other hand, the field line returns to its original poloidal location only after an infinite number of toroidal rotations, ι has an irrational value and the flux surface is said to be an irrational surface. To distinguish high-order rational surfaces (rational surfaces with large m values), from irrational surfaces a sufficient number of toroidal transits must be observed experimentally or performed in the simulation. The light green points in Fig. 1.9 represent a surface which is considered irrational. To determine if this surface is truly irrational, one would have to follow the field line for an infinite number of toroidal transits. If the field line returns to its starting location in a non-infinite number of toroidal transits, it is a merely rational surface with a large m value.

The innermost of all these closed nested magnetic flux surfaces is the magnetic axis shown in both Fig. 1.8 and Fig. 1.9. The magnetic axis is a singular magnetic surface defined by the unique field line that returns upon itself after each toroidal transit.[17] The volume contained within the magnetic axis is zero. However, the magnetic axis still represents a flux surface and therefore has a rotational transform associated with it. Also because of its singular dimensions, the magnetic axis can be easily found both experimentally and through simulations. Therefore it will be used extensively throughout this dissertation to diagnose the magnetic configuration of CTH. Lastly, the singular nature of the magnetic axis puts it in a class of surfaces known as fixed points.[18] Other fixed points include the O and X points of magnetic islands discussed in Ch. 7.

1.4 Goals of Dissertation

The purpose of this research is to extensively measure the so-called "vacuum" magnetic field properties created by only the magnetic field coils on the CTH device. In doing so, the existence of closed nested magnetic flux surfaces produced by the newly-constructed CTH machine is shown. Experimental measurements of the magnetic axis position and rotational transform created by the vacuum fields are discussed. A quantitative comparison is made between the experimental results and those predicted through simulation using a design model of the CTH coils. To better match the measurements of the magnetic configuration to the modeling results, modifications are made to the coil simulation model with a newly developed coil optimization routine. The thrust of this work is that field-mapping measurements can provide a sensitive and useful technique to assess the accuracy of relatively complex coil geometries. In addition, it is

found that the ambient or background field can play an important role in the interpretation of experimental results. Lastly, the measurement and manipulation of flux surfaces containing magnetic islands will be performed through the use of 15 error correction coils.

Motivation for this research comes from the goals of the CTH project as a whole. The CTH machine was built to investigate the MHD stability of ohmic currents in a compact stellarator plasma over a wide range of magnetic field configurations. Also, plasma measurements made on the CTH machine are going to be used to test a new 3-dimensional plasma equilibrium reconstruction code. Plasma simulations and reconstruction codes such as this rely heavily on knowledge of the plasma and magnetic field structure revealed in MHD equilibrium codes such as VMEC.[19] Codes such as VMEC require accurate knowledge of the vacuum magnetic fields produced by currents in the coils of the machine to accurately model the plasma. Therefore, verification of the coil parameters responsible for the vacuum fields is fundamental in the ability to understand the plasma equilibrium parameters and stability.

The magnetic flux surfaces in the absence of a plasma are measured with a technique called electron-beam vacuum field-mapping[20,21]. Vacuum field mapping exploits the fact that closed flux surfaces can be produced in stellarators without a plasma, and has been used previously in numerous stellarator experiments.[22,23]

The outline of the dissertation is as follows.

Chapter 2 gives a physical description of the various coil sets located on CTH.

Chapter 3 discusses the fields produced by each coil set and the effect that these fields have on the various magnetic flux surfaces.

Chapter 4 describes the field mapping experimental setup and data analysis procedures.

Chapter 5 presents a new coil optimization routine that is used to improve the agreement between the simulation and experimental field mapping results. In addition Ch. 5 presents experimental evidence showing the apparent effect magnetization of nearby ferromagnetic material is having on the field mapping results. Following this, the complications due to magnetization, in relation to using the optimization routine, are addressed.

Chapter 6 presents the experimental results of the field mapping studies. A quantitative comparison is made between the field mapping and simulation results. The procedure and application of modifying the coil model to best fit the experimental data is discussed.

Chapter 7 discusses the identification of magnetic islands in certain CTH vacuum configurations. The experimental procedure for controlling, and reducing, the size of the magnetic island using error correction coils is described and demonstrated.

CHAPTER 2: CTH DESIGN

2.1 CHAPTER INTRODUCTION

The magnetic field configuration of the Compact Toroidal Hybrid (CTH) is produced by six independent electro-magnetic coil sets positioned around the toroidal vacuum vessel containing the plasma. The main components of the CTH device are illustrated in Fig. 2.1. These components include; the vacuum vessel, the helical field coil (HF), the vertical field coils (OVF, TVF, RF, SVF), the toroidal field coils (TF), and the ohmic heating coils (OH-1,2,3).

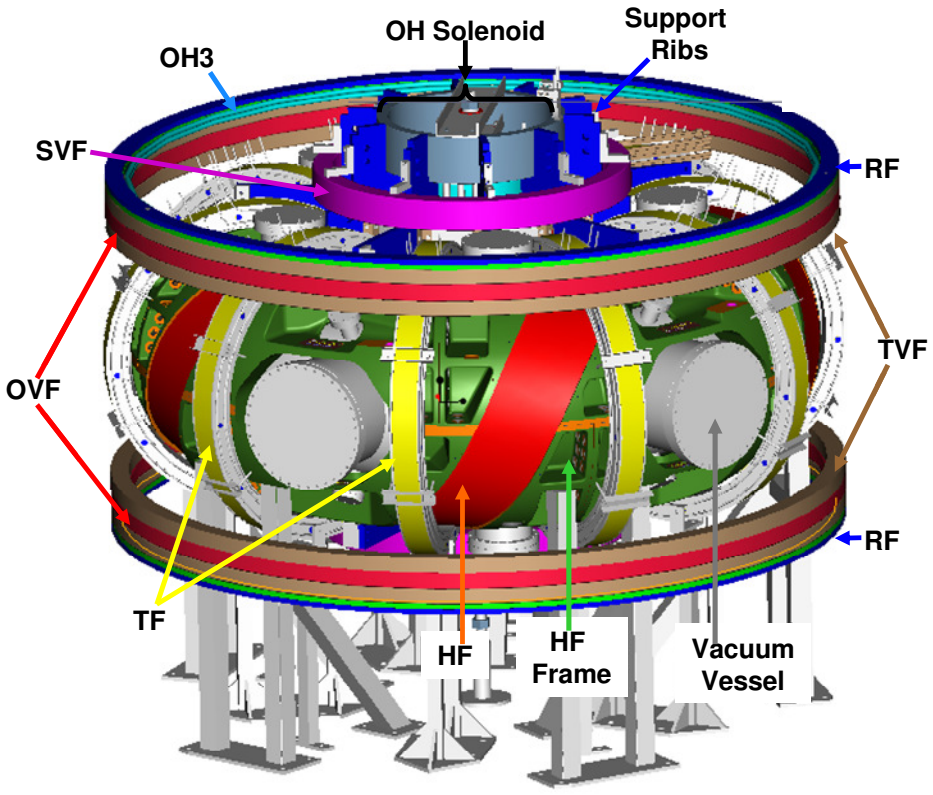

Fig. 2.1 CTH device

Each of the various coil systems is designed to be both field period, and up-down symmetric. In this way the magnetic configuration of CTH exhibits a vertical symmetry at two toroidal locations per field period in which the flux surfaces are up-down symmetric about the midplane. Between these symmetry planes, the flux surfaces have an odd symmetry about the midplane with respect to the toroidal angle.

This chapter will provide a physical description of the CTH device. Also included are aspects of the construction process which relate to maintaining the symmetry of the machine, along with techniques used to determine the accuracy with which the coils were wound compared to their designed geometry.

2.2 VACUUM VESSEL

The vacuum vessel of CTH, shown in Fig. 2.2, is a large stainless steel torus. The vacuum vessel is circular in both the poloidal and toroidal directions. The vacuum vessel has a major radius of $R_0 = 0.75$ m and minor radius of $a_{vv} = 0.29$ m, with a low aspect ratio of $A_p = R_0/a_{vv} = 2.6$. The vessel wall has an average thickness of 5 mm, and is made of Inconel 625, a stainless steel alloy. This alloy was selected for its high electrical resistivity and low magnetic permeability.

The interior of the vacuum vessel is accessed through a total of 25 circular ports as shown in Fig. 2.2. All ports are sealable with standard Varian-type copper gasket flanges. The 5 large side ports are located 72° apart at toroidal locations of φ= 36, 108, 180, 252, and 324°. The side ports are centered on the outer midplane. Above and below each side port are smaller angle ports located at poloidal angles $\theta = \pm 60°$.

Five pairs of top-bottom ports are located halfway between the side ports at the toroidal angles, φ = 0, 72, 144, 216, and 288°. The vertical axis of each of the top and bottom ports is centered at a radial distance of R=0.711 m, radially inward of the vacuum vessel major radius R_0 to accommodate the location of the HF coil.

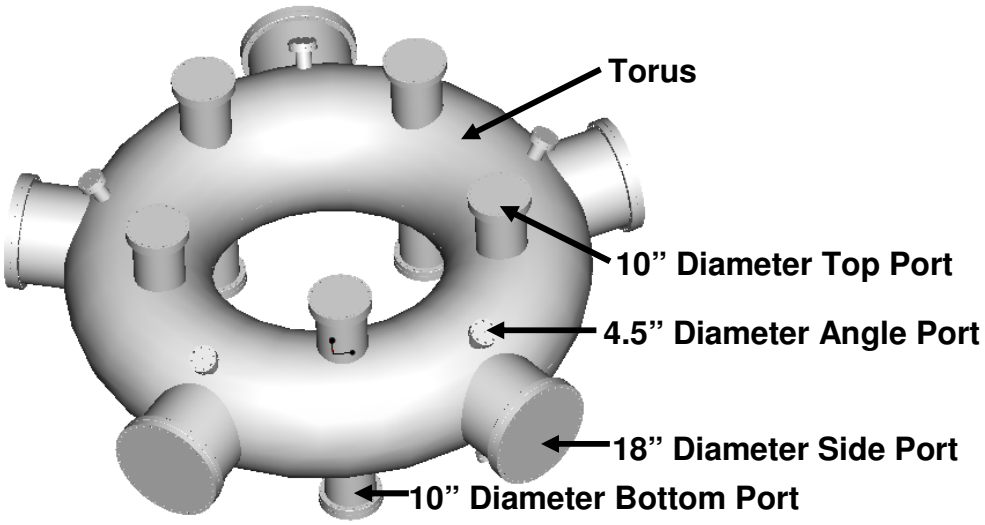

Fig. 2.2 The CTH vacuum vessel

2.3 THE HELICAL FIELD COIL

The helical field coil is a single coil composed of multiple filaments wound to make 2 toroidal circuits (ℓ=2) and 5 poloidal circuits (m=5). In doing so, the HF coil defines the five-fold toroidal periodicity of CTH. Because the current in the HF coil is unidirectional, the magnetic configuration of CTH is in the class of stellarators called a torsatron.

The helical path followed by the center of the HF coil pack is defined by a HF coil winding law. The winding law is defined by parameterizations of the coil pack minor radius and the toroidal angular locations as functions of the poloidal angle θ. The general

series expressions for the radial (minor radius) and toroidal winding laws are given in Eq. 2.1 and Eq. 2.2.

$$r_c(\theta) = a_{r0} + a_{r1}\,\mathrm{Cos}(\theta) + a_{r2}\,\mathrm{Cos}(2\theta) + \ldots + b_{r1}\,\mathrm{Sin}(\theta) + b_{r2}\,\mathrm{Sin}(2\theta) + \ldots \qquad (2.1)$$

$$\varphi(\theta) = 2/5\,\theta + a_{f0} + a_{f1}\,\mathrm{Cos}(\theta) + a_{f2}\,\mathrm{Cos}(2\theta) + \ldots + b_{f1}\,\mathrm{Sin}(\theta) + b_{f2}\,\mathrm{Sin}(2\theta) + \ldots \qquad (2.2)$$

The coefficients (a_{r0}, a_{r1}, a_{r2}, b_{r1}, b_{r2},…) are in units of meters and the coefficients (a_{f0}, a_{f1}, a_{f2}, b_{f1}, b_{f2},…) are in radians.

The specific coefficients of the design winding law were chosen by an optimization process in which several factors were considered. [24] The winding law was optimized to produce closed magnetic flux surfaces that remain within the low aspect ratio vacuum vessel volume, while simultaneously minimizing the stochasticity of the magnetic field lines (deviations from magnetic surfaces) particularly on the outermost flux surfaces. In addition, for ease of construction, and to generate large closed flux surfaces that could be inscribed within the circular CTH vacuum vessel, the winding law was chosen to have a constant minor radius about the toroidal axis of the vessel. The coefficients of the design radial and toroidal winding laws that adequately meet these requirements are given by Eq. 2.3 and Eq. 2.4. A three dimensional plot of the winding law defined by Eq. 2.3 and Eq. 2.4 is shown in Fig. 2.3, indicating the helical path of the center of the HF coil around the toroidal vacuum vessel.

$$r_c(\theta) = 0.385\ \mathrm{m} \qquad (2.3)$$

$$\varphi(\theta) = 2/5\,\theta - .252\,\mathrm{Sin}(\theta) + .052\,\mathrm{Sin}(2\theta) - .024\,\mathrm{Sin}(3\theta) \qquad (2.4)$$

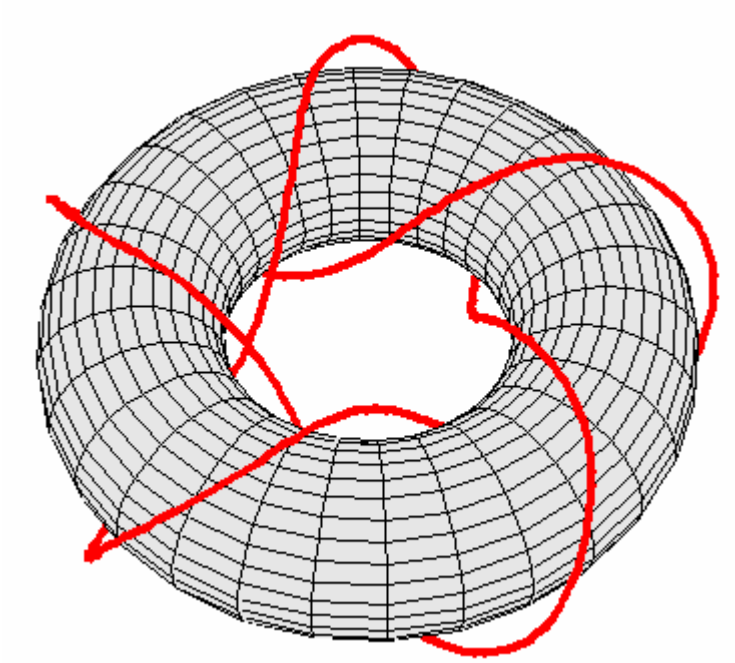

Fig. 2.3 HF coil winding law

The lack of sine dependent terms in the radial winding law of Eq. 2.3 and cosine dependent terms in the toroidal winding law of Eq. 2.4, results in a HF coil that exhibits symmetry about the midplane. In Ch.6, we will see that the vertical position of the magnetic flux surfaces is highly sensitive to the vertical symmetry of the HF coil.

The cross-section of the multi-filament HF coil pack is rectangular with the geometrical center of the HF coil pack defined by the winding law shown in Fig. 2.3. The edges of the rectangular pack define curves parallel to the local winding law. The coil is composed of 96 conductor filaments arranged to be 6 turns deep (0.133 m in depth) by 16 turns wide (0.265 m), as illustrated in Fig. 2.4.

The HF coil is constructed with rectangular flexible copper rope[25]. The dimensions of the rope without electrical insulation are 0.0144 by 0.0197 m. In the center of the copper rope is a nylon water cooling tube. Because the HF coil is crucial to

magnetic field of CTH, an electrical short circuit in the HF coil would be catastrophic to the CTH experiment. Therefore, two layers of fiberglass and one layer of insulating Kapton tape were applied as precautionary electrical insulation layers to prevent a short circuit from occurring within the coil.

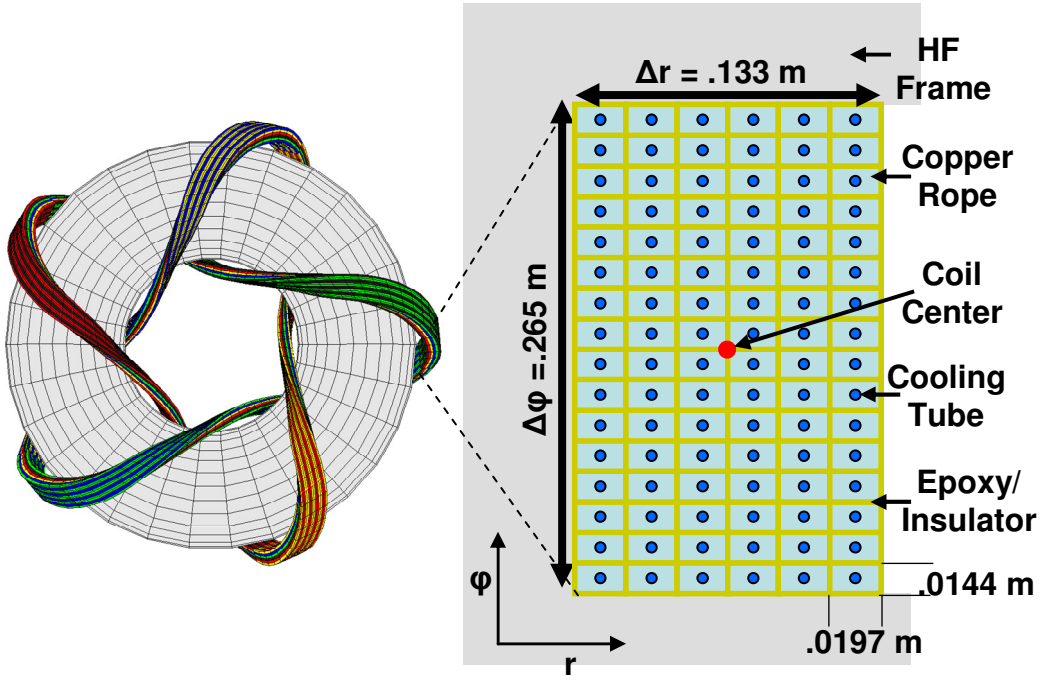

Fig. 2.4 HF coil pack (cross-section)
The HF coil shown on the left is shown without the support structure of its winding frame. The expanded view of the cross-section of the coil pack shows the rectangular arrangement of the 96 filaments

The HF coil is wound into the trough of an aluminum frame that surrounds the vacuum vessel, as shown in Fig. 2.5. The frame was designed in collaboration with the Princeton Plasma Physics engineering staff[26] and built by JP Pattern[27] The frame is composed of 10 identical sections, and when assembled, forms a continuous trough in which the HF coil lies. The rectangular trough within the aluminum frame was machined to dimensions of 0.265 m wide by 0.140 m deep (±.0005 m). With the use of a rigid winding form machined to the correct winding law, it was expected that the HF coil

would follow the designed winding law to much better tolerances than were achieved in the previous torsatron built at the Auburn Fusion Laboratory, the Compact Auburn Torsatron (CAT)[28]. The frame also provides mechanical support for the HF coil against gravitational and magnetic forces. The frame pieces are electrically insulated from each other to ensure that no toroidal current flows through them.

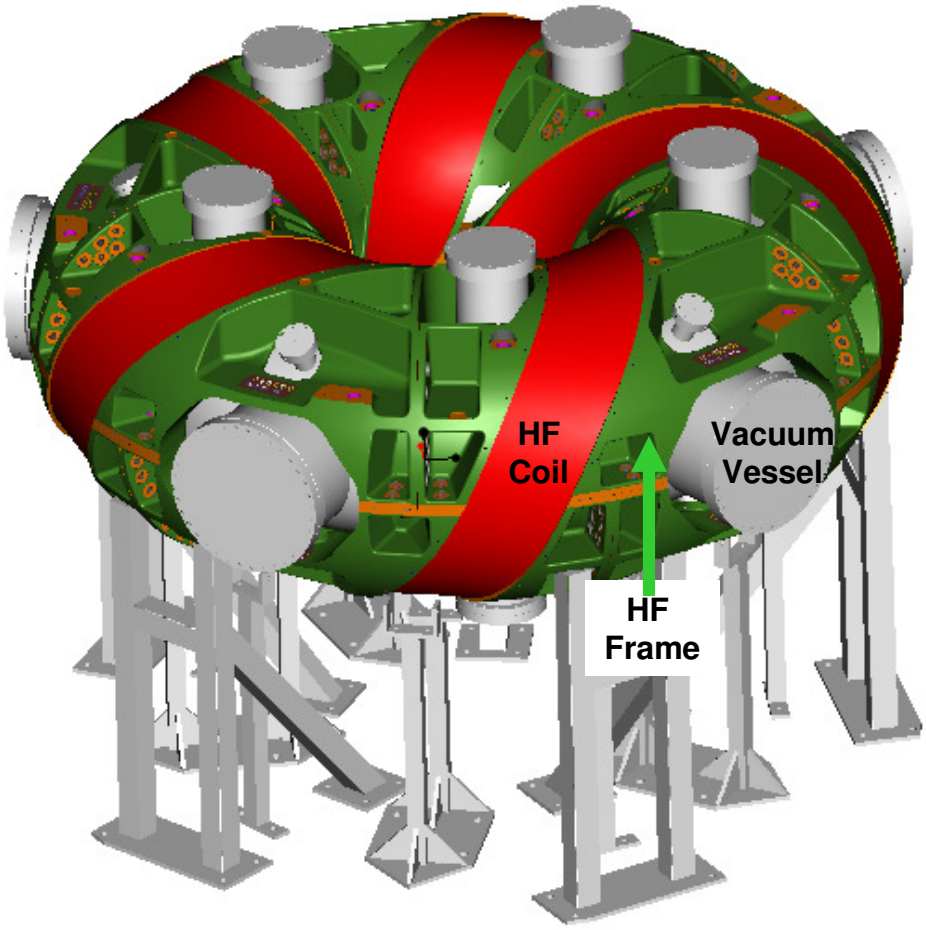

Fig. 2.5 HF coil in the HF frame

Because the outside of the HF coil is not restricted by the frame pieces, during the construction process there was the tendency for the conductor to sag downward in the lower half due to gravity. To prevent this from occurring and ensure that the top and

bottom of the coil were wound to the same position within the frame, measurements of the coil radius were made during the construction process. Prior to winding the HF coil, the minor radial distance d_0, of the trough depth was measured from a measurement brace placed across the trough to the bottom of the HF coil trough as shown in Fig. 2.6. These depth measurements of the minor radius were made on each field period at 7 poloidal locations (θ=45, 90, 135, 180, 225, 270, 315°) at 8 locations across the coil.

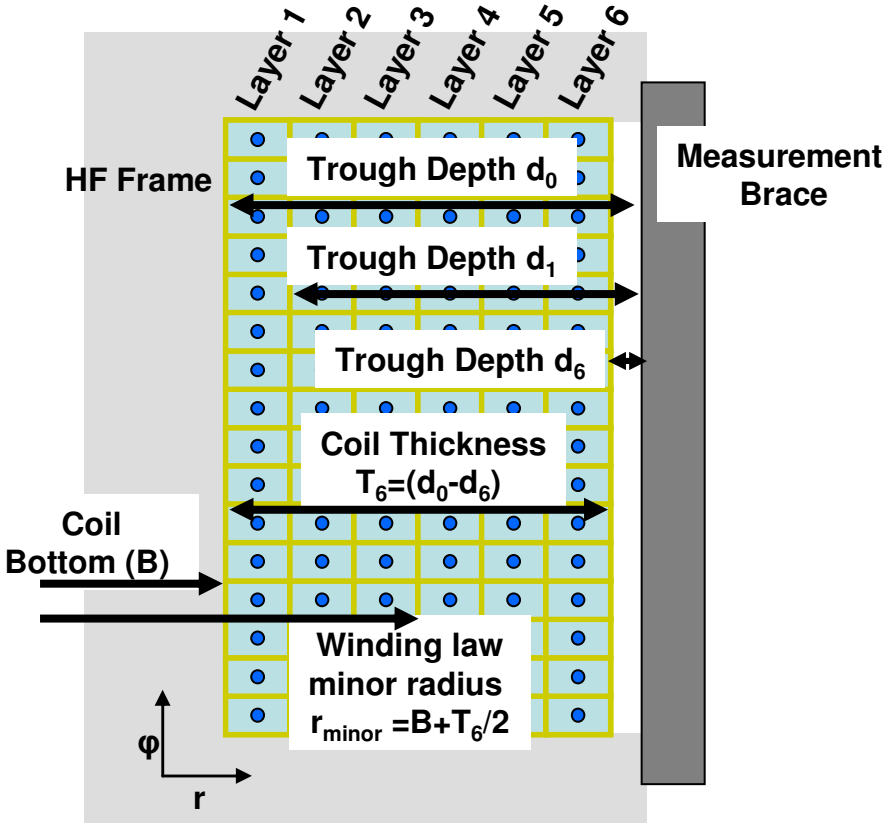

Fig. 2.6 HF coil depth measurement technique

Upon the completion of each layer of the HF coil during the construction process, similar measurements of the coil depth were made, shown by d_1 through d_6 in Fig. 2.6. From the initial measurements of the trough and the successive depth measurements of each layer, the coil thickness of each layer T_i, can be calculated as $T_i=d_0-d_i$ where "i" is

the index for each coil layer. Through these measurements any variations in the coil minor radius with poloidal angle could be determined and fixed as the coil was being built.

In addition, the HF coil minor radius r_{minor}, of the completed coil can be calculated as r_{minor} = B+1/2 T_6 where B is the minor radius distance to the bottom of the coil trough. The various measurements of the coil minor radius for the completed coil as a function of poloidal angle for each section of HF coil is shown in Fig. 2.7. The different colors represent measurements made at different field periods, while the multiple points at each location represent multiple measurements made across the width of the coil. Nearly all the radial measurements show the as-built coil to have a smaller radius than the design winding law, of r = .385 m.

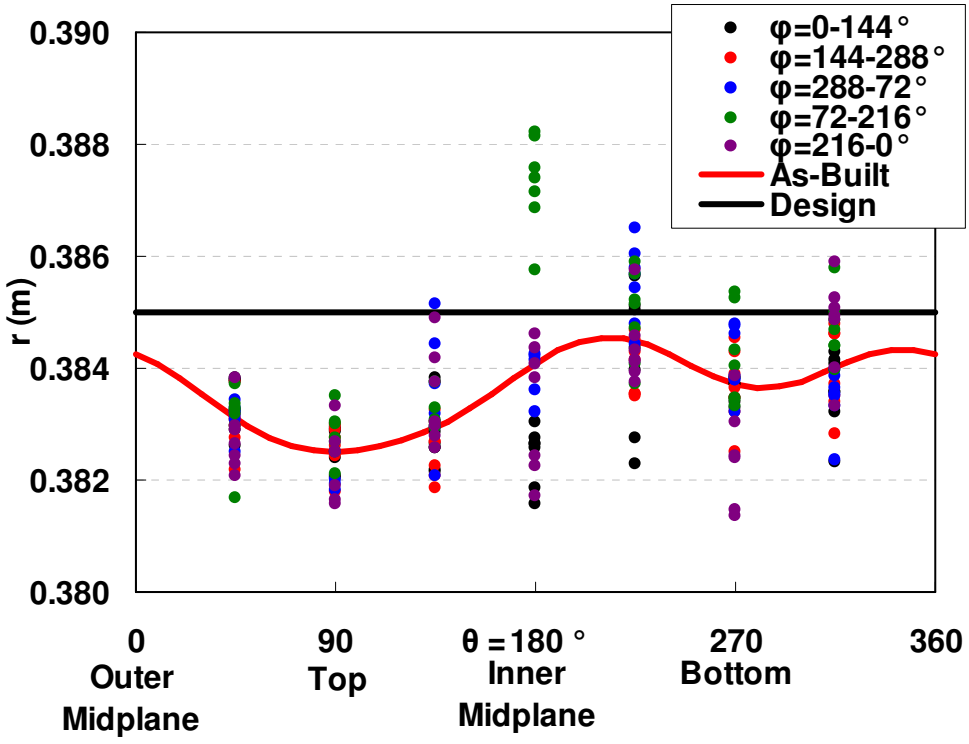

Fig. 2.7 Measured HF minor radius vs. poloidal angle

In Fig. 2.7, notice that the spread in the data is 2- 6 mm depending on the poloidal angle. There is little spread (±1 mm) in the data where the coil passes over the top of the torus ($\theta \approx 90°$) because at this location the coil winding and the depth measurements were relatively easy to perform. At the inner midplane of the coil ($\theta \approx 180°$) where both coil construction and coil depth measurements were more difficult to perform there is a larger spread in the measured coil depth of up to ± 3 mm. Lastly, on the bottom of the coil ($\theta \approx 270°$) where the coil tended to sag due to gravity the spread in the data is ±2 mm. Due to the overall inaccuracy of the measurement method, all data points should include a ±2 mm error bar. In hindsight, performing the measurements with a coordinate measuring machine (CMM) would have greatly improved the accuracy of the measurements. Such a device was not available to us at the time, but one was used later when aligning the poloidal field coils.

In order to develop an improved HF coil winding law that more accurately describes the actual, as-built HF coil, the depth measurements were used as a basis for adjusting the model of the coil minor radius as a function of poloidal angle θ. The radial coefficients (a_{r0}, a_{r1}, a_{r2}, a_{r3}, b_{r1}, b_{r2}, b_{r3}) in the design winding law were varied to fit the minor radius measurements resulting in an "as-built" winding law given by Eq. 2.5.

$$\begin{aligned} r_c(\theta) = .3836 + 0\,\mathrm{Cos}(\theta) + .0005\,\mathrm{Cos}(2\theta) + .0001\,\mathrm{Cos}(3\theta) \\ - .0007\,\mathrm{Sin}(\theta) + .0002\,\mathrm{Sin}(2\theta) - .0001\,\mathrm{Sin}(3\theta) \end{aligned} \tag{2.5}$$

During this fitting procedure, the HF coil was assumed to be field-period symmetric. The as-built winding law is shown in Fig. 2.7 as the solid red curve with the design winding law shown as the solid black line. The existence of sine terms in the new winding law break the assumed up-down symmetry of the coil. A detailed discussion of

the effect of the new winding law on the predicted magnetic flux surfaces is given in Ch.6.

2.4 CIRCULAR COIL SETS

In addition to the HF coil, several sets of circular coils are installed on the CTH device. These consist of poloidal field coils, toroidal field coils, ohmic heating coils, and ohmic heating decoupling coils as shown in Fig. 2.1. The measured values of the circular coils are listed in Table 2.1. These values differ by less than 1 mm from the design specifications.

Coil	Radius (m)	Vertical Position (m)	Turns	Width (m)	Height (m)
OVF	1.266	±0.523	16	0.064	0.064
TVF (outer)	1.268	±0.583	54	0.064	0.055
TVF (inner)	1.268	±0.464	54	0.064	0.055
RF	1.268	±0.629	36	0.064	0.037
SVF	0.524	±0.609	120	0.071	0.110
TF	0.515	NA	48	NA	NA
OH1	0.190	±0.302	44	0.041	0.604
OH2	0.315	±0.748	12	0.041	0.169
OH3	1.227	±0.54	1	0.019	0.038
TVFD	0.251	±0.431	124	0.031	0.289
SVFD	0.151	±0.240	200	0.031	0.460

Table 2.1 Measured values of circular coils
The radial and vertical distances define the distance to the center of the coil pack. The ± sign of the vertical position indicates the location above and below the midplane of the upper and lower coils. The number of turns listed is for each individual coil not the coil set. The width and height define the rectangular cross-section size of each coil set in the radial and vertical directions, respectively.

The main poloidal field coil pack consists of an outer vertical field (OVF) coil, trim vertical field (TVF) coils, and a radial field (RF) coil, all epoxied together. The shaping vertical field (SVF) coils are also poloidal field coils with a smaller radius. Each poloidal coil set consists of a pair of horizontal coils, centered along the central axis of

CTH located equidistance above and below the machine midplane. A cross-section of the upper OVF/TVF/RF coil pack is shown in Fig. 2.8. Notice that the TVF coil is comprised of an upper and lower coil within each pack that sandwiches the OVF coil. The copper conductor in each of the poloidal field coils is hollow, allowing each coil to be internally water-cooled. The TVF and RF coils are made from the same copper conductor, therefore the RF coil is identical to 4 layers of the TVF coil. Currently 2 axial layers (18 turns) are electrically removed from each TVF coil set (both the upper and lower) for improved plasma performance. The removed layers of the upper coil pack are illustrated in Fig. 2.8.

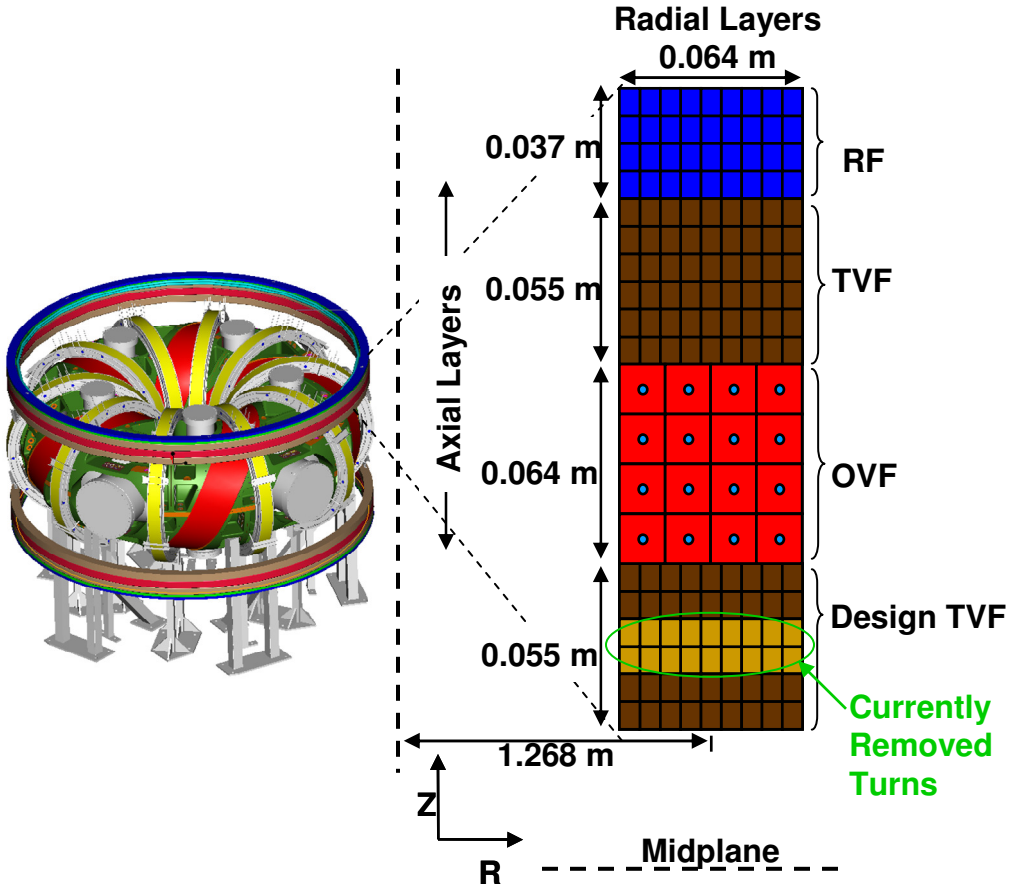

Fig. 2.8 Cross-section of the upper vertical field coil pack

CTH is equipped with 10 circular toroidal field (TF) coils, as shown in Fig. 2.9. The TF coils are evenly spaced around the machine toroidally at $\Delta\varphi = 36°$ intervals, starting at $\varphi = 18°$. Each TF coil is centered on the midplane and encircles the vacuum vessel poloidally. The TF coil conductor is wound into aluminum troughs made of two identical semi circular frame pieces which encircle the vacuum vessel. The TF conductor is flexible copper rope with a rectangular cross-section similar to the HF coil conductor, but with smaller dimensions and without an internal cooling tube. Each TF coil was wound in place around the completed HF coil, and the use of flexible copper rope made this task easier than if solid copper conductor was used. The TF coils are cooled by water circulating through tubes welded to the exterior of the TF frame pieces.

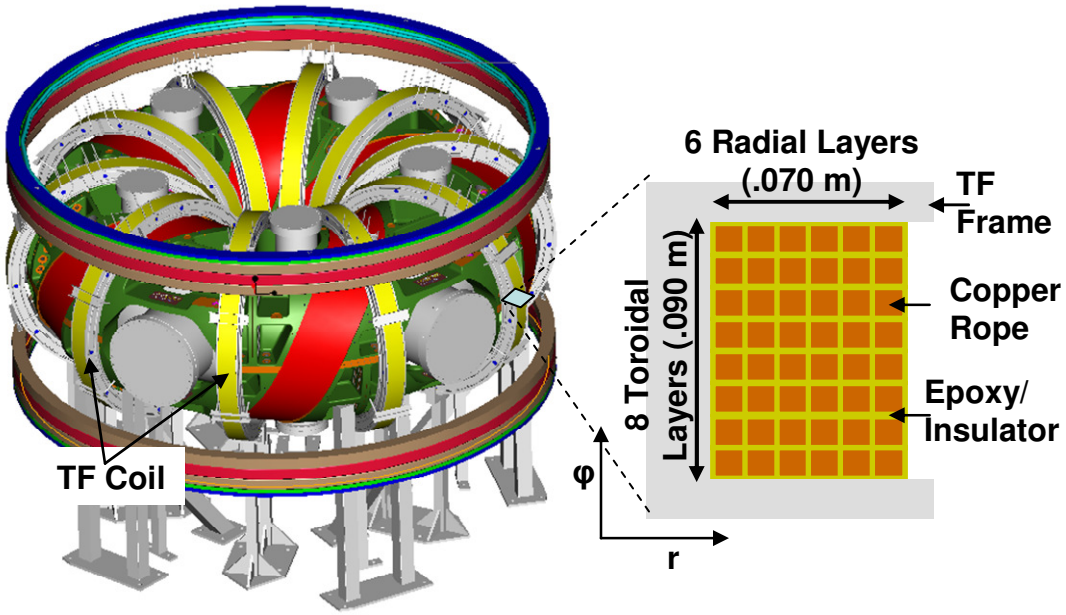

Fig. 2.9 Cross-section of the TF coil

The ohmic heating (OH) coils consist of 3 poloidal coil sets, OH1, OH2, and OH3, all connected in series. They comprise the primary side of a transformer, with the

plasma ring effectively being the single-turn secondary winding of the transformer. A monotonically-changing flux through the conducting plasma ring induces a unidirectional current to flow in the plasma. Because the changing field of the OH coils would affect the steady vacuum fields required for confinement, the OH coil set is designed to produce minimal magnetic flux within the volume of the vacuum vessel. As with the poloidal field coils, each of the OH coil sets consists of a pair of coils, centered horizontally on the central axis of CTH, and distributed symmetrically above and below the midplane of the vessel. The OH1 and OH2 coils are part of the central stack of coils shown in Fig. 2.10 located in the center of the machine. The OH3 coil is visible in Fig. 2.1 just inside the OVF coil pack. The OH1 and OH2 coils are built from the same copper stock with a hole for water cooling in the center. The OH3 coils each consist of 1 turn, made from two 3/0 gauge insulated cables electrically connected in parallel.

The changing OH flux induces a voltage on not only the plasma loop, but also on all the other poloidal coils. To decouple the OH flux from the TVF coils, two TVF decoupler (TVFD) coils are connected in anti-series with the TVF coil. The size and number of turns in TVFD coils were selected to nearly cancel the mutual inductance between the OH and TVF coil sets. Similarly, the SVF coils have their own corresponding decoupler coils, the SVFD. The TVFD and SVFD coils are part of the central stack of coils located in the center of the vessel along the central axis, as shown in Fig. 2.10. The mutual inductance of the TVFD coil was designed to nearly cancel the induced OH voltage on the 108-turn TVF coil, and therefore is overcorrecting for the 90-turn TVF coil currently in use.

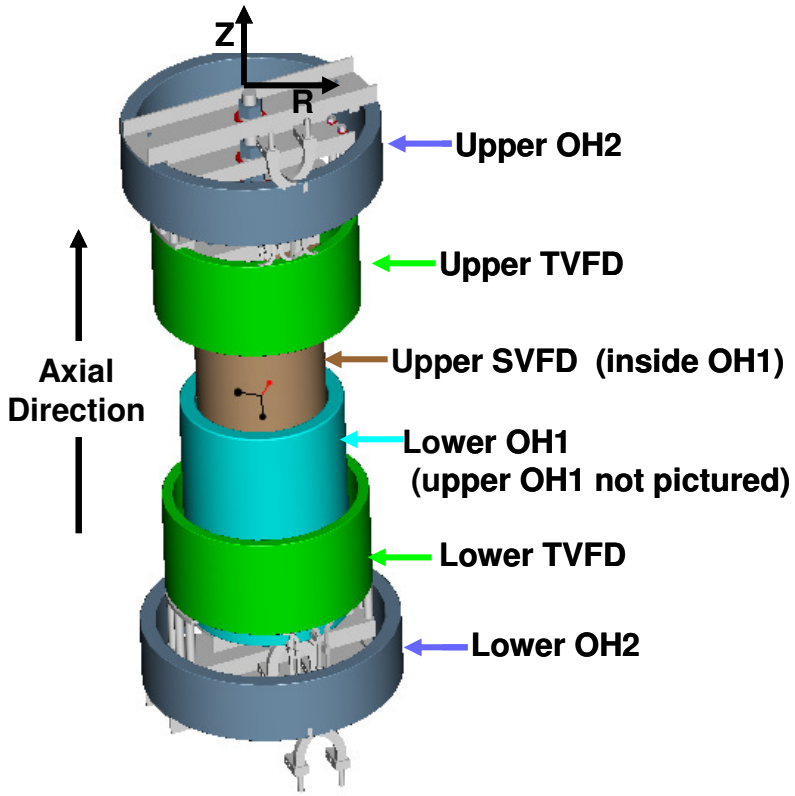

Fig. 2.10 Central stack solenoid

2.5 Minimizing Symmetry Breaking Errors

While the CTH coil sets are designed to produce magnetic field geometries that are identical from one field period to the next, small errors in the coil winding or the superposition of background fields (earth's field, nearby magnetized objects) can produce symmetry-breaking errors that affect the flux surfaces. This is discussed in Ch.7 where we will see the consequences of error fields in the production of magnetic islands.

During the design process of CTH, efforts were made to minimize symmetry-breaking errors from occurring within any of the coil sets. The electrical feeds for the various coil sets were designed to minimize the magnetic dipoles they create. For the HF and TF coils, the junctions from the coil feeds to the rope were fabricated from copper

bar stock of the same width as the rope so that the connector fits snugly into the coil pack, minimizing the introduction of stray magnetic dipole moments. In addition, the electrical feeds of the HF coil were staggered about the midplane, with four of the five HF field periods have identical electrical connections. The fifth field period is slightly different due to the electrical input lines. The electrical feeds on the TF coils were staggered above and below the midplane, resulting in an up-down symmetry within a field period. The electrical feeds of the poloidal field coils were made symmetrical about the midplane. Lastly, the electrical input lines connecting the coils to the power supplies were constructed in quadrupole formation to further reduce the effects created by these fields. Modeling made prior to the coil construction showed that the error fields created by the electrical feeds while in this formation have little effect on the flux surfaces found within the vacuum vessel.

CHAPTER 3: MAGNETIC FIELDS PRODUCED BY CTH

The goal of this chapter is to: a) show the field structure produced by the various CTH coils sets; and b) explain how the field structure of the coil sets influences the magnetic flux surfaces.

3.1 HF/OVF/TVF FIELDS

To produce closed toroidal magnetic flux surfaces that are contained within the vacuum vessel, the field produced by the HF coil must be supplemented with a vertical field. On CTH the net vertical field is typically produced by a combination of the OVF and TVF coils. The OVF coil is connected in series with the HF coil and the vertical field produced is sufficient to produce closed toroidal magnetic flux surfaces that are contained within the vacuum vessel, albeit the surfaces are located near the radial outboard wall of the vacuum vessel. To shift the flux surfaces inward and increase the volume they enclose, an additional vertical field is supplied by the independently controlled TVF coils. Before we consider the TVF vertical field and the effects it has, let's first observe the magnetic field produced by the HF/OVF coils alone.

The magnetic field produced by the HF/OVF coils is shown in a horizontal cross-section of the midplane, in Fig. 3.1(a). The red rectangles show where the HF coil intersects the z=0 plane. The HF current comes out of the page on the outside of the vacuum vessel and goes into the page on the inside of the vacuum vessel. The OVF

current is in the negative φ direction. The magnetic field direction in the cross-section plane is indicated by the direction of the arrows, while the magnitude of the field is proportional to the length of the arrows. The field inside the vessel is in the negative φ direction and is non-uniform with respect to the toroidal angle.

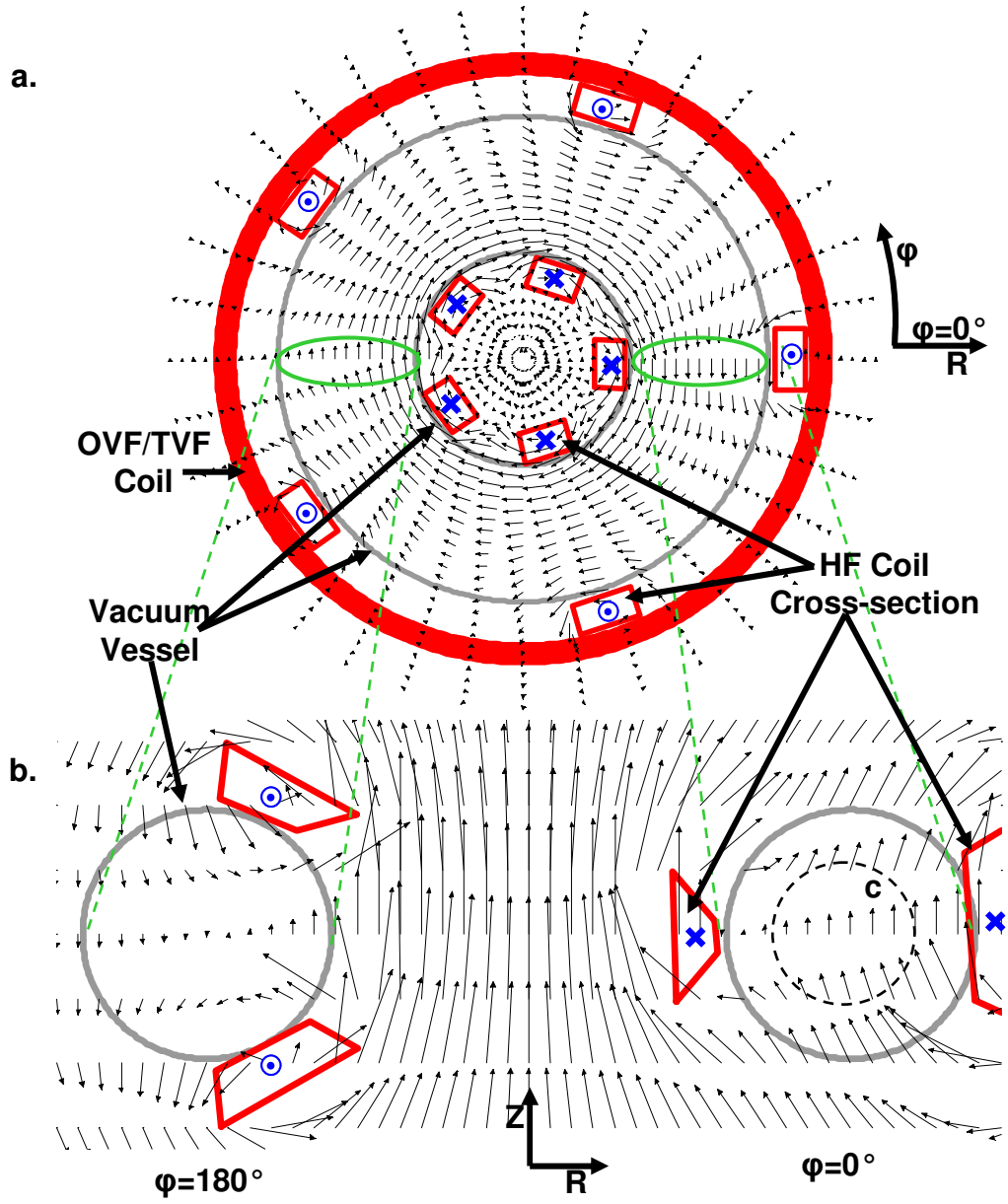

Fig. 3.1 HF/OVF field vectors.
a) Top view of torus on the z=0 plane
b) Side view torus on the φ=0/180° plane

The magnetic field produced by the HF/OVF coils in a vertical cross-section is shown in Fig. 3.1(b) with the φ=180° plane on the left and the φ=0° plane on the right. The red trapezoids represent the location of the HF coil as it intersects the φ=0/180° plane. The HF current is in the positive φ direction, into the page at φ=0° and out of the page at φ=180°. The poloidal fields at the two toroidal angles shown are significantly different with no clear structure visible.

The magnitude of the field strength |B|, in the φ=0/180° vertical plane produced by 300 A in the HF/OVF coil system is shown in Fig. 3.2. This expanded view of the field structure in space shows the vacuum vessel cross-section as the two circles near the center of the figure. The field strength in this region is on the order of $|B|=10^{-2}$ T.

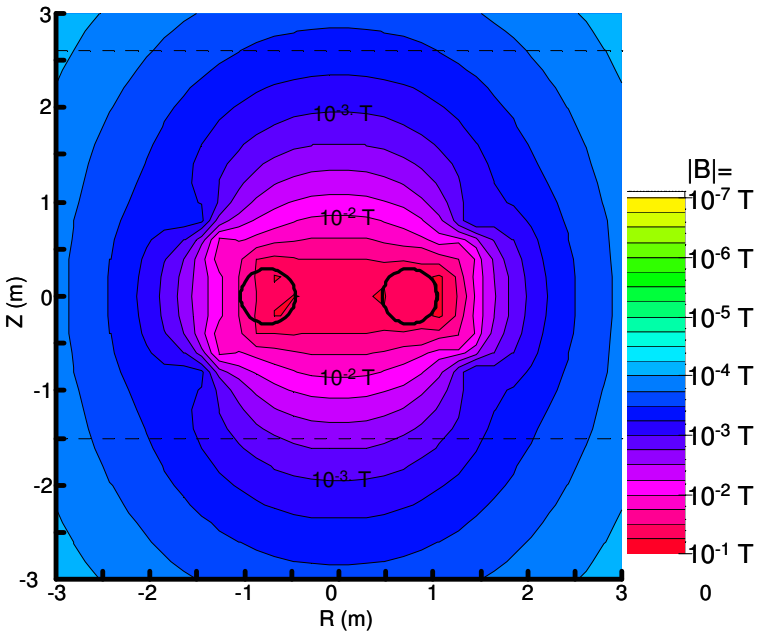

Fig. 3.2 HF/OVF field strength
I_{HF}=300 A

In Fig. 3.2, the dashed lines above and below the midplane represent the vertical locations of the floor and ceiling. As discussed later in Ch. 5 and 6, magnetization of

nearby ferromagnetic material by the CTH magnet coils will be invoked as a possible explanation of unexpected effects seen during field-mapping experiments. This will require knowledge of the field structure in extended reaches of space including the floor and ceiling.

Now lets consider how the complicated field structure shown in Fig. 3.1 produces closed nested flux surfaces that have a nonzero rotational transform, given the following problem. Consider a situation without current flowing inside the vacuum vessel region like that shown in Fig. 3.1. Then by Ampere's law, Eq. 3.1, the line integral of the magnetic field along any closed contour inside the plasma must be zero.

$$\oint_c \vec{B} \cdot \vec{dl} = \mu_0 I = 0 \tag{3.1}$$

This is contrary to what our intuition tells us how a field line with a nonzero rotational transform should be, since it would seem that a field line with a non-zero rotational transform would require a net non-zero poloidal field according to Eq. 1.11. Instead the existence of flux surfaces with a rotational transform in currentless stellarator plasmas is due to oscillations of the toroidal and poloidal components of the field as the field line undergoes its toroidal progression.[29] This is demonstrated in the following example.

Consider the toroidal and vertical fields on the midplane at four toroidal locations, φ=0,10,20,30°. The negative of the toroidal field $-B_\varphi$, and vertical field B_z, are plotted vs. the radial position for the different toroidal angles in Fig. 3.3. At the midplane, the vertical and poloidal directions are either parallel or antiparallel such that one could think of the vertical fields shown in Fig. 3.3 as representing poloidal field components.

Consider the field components on the midplane at a radial location of R=.9 over the range of toroidal angles. At φ=0°, the vertical component of the field is upward and

the toroidal component of the field is strong, while at φ=30°, the vertical component of the field is downward and the toroidal component of the field is weak. The stronger toroidal field at φ=0° allows a field line to experience the upward portion of vertical field for a shortened "period". While the weaker toroidal field at φ=30° allows a field line to experience the downward portion of vertical field for an extended "period". The extended period spent in the downward portion exceeds the shortened period spent in the upward portion. Thus, after one field period the field line has undergone a net downward vertical shift. Obviously this is a highly simplified very specific example and is not intended to prove the existence of the rotational transform but merely to illustrate how oscillations in the toroidal and poloidal fields could make it possible for a field line to have a nonzero poloidal rotational.

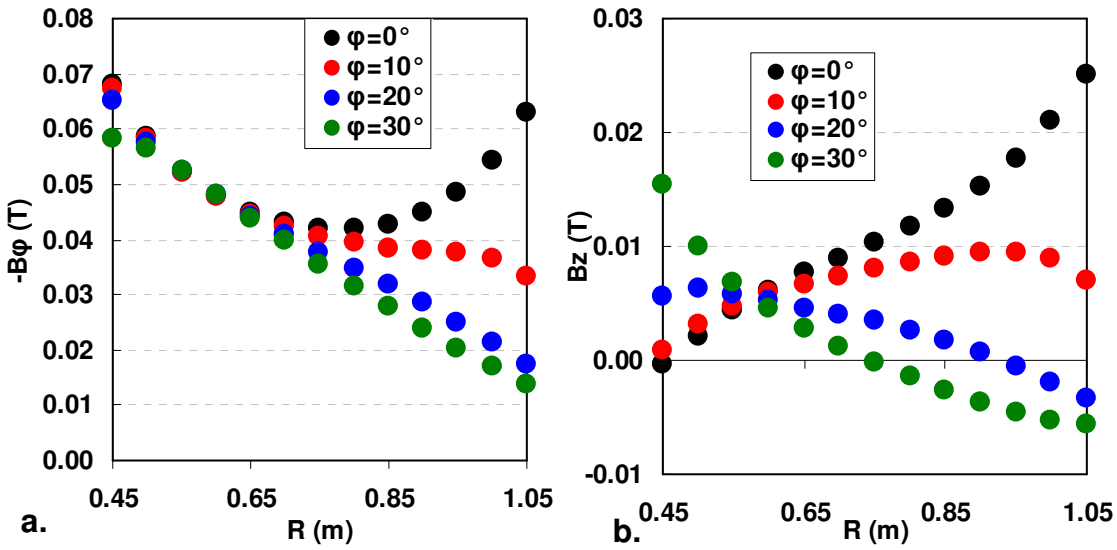

Fig. 3.3 Toroidal and vertical field strengths of the HF/OVF coils
Field strengths computed at $I_{HF/OVF}$ =300 A

It is the oscillatory interaction of the toroidal and poloidal field components that cause the field lines of a flux surface to undergo a net poloidal rotation commonly

thought of as the rotational transform. To demonstrate this, we follow a field line located on a magnetic surface with a rotational transform of $\iota = 1/3$ as it proceeds toroidally around the vacuum vessel. Shown in Fig. 3.4(a) is a 3-D view of the field line trajectory as it undergoes 3 toroidal circuits and 1 poloidal circuit. Shown in Fig. 3.4(b) are the radial and vertical positions of the same field line projected onto the R, Z plane over all toroidal angles. The field line is seen to undergo radial and poloidal gyrations as we would expect but overall after 3 toroidal circuits the field line returns to its original location, revealing that it has a rotational transform of $\iota = 1/3$.

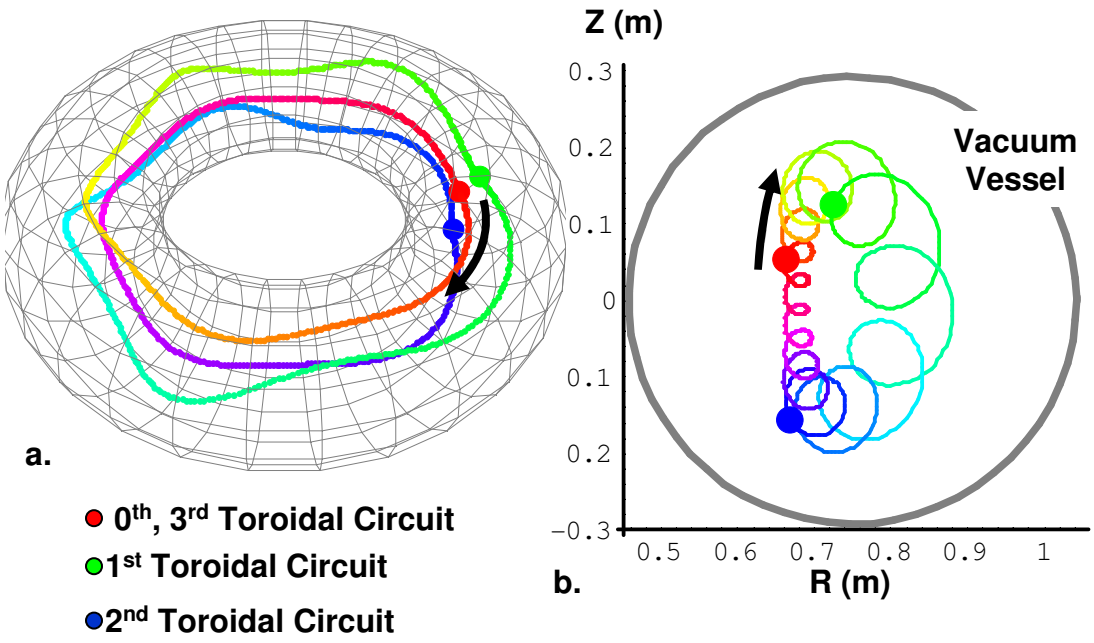

Fig. 3.4 field line trajectories ($\iota = 1/3$)
a) 3-D field line trajectories.
b) Projection of the field line onto a poloidal cross-section

Shown in Fig. 3.5 is the number of poloidal rotations vs. the number of toroidal rotations for 3 flux surfaces with different rotational transforms. The field line followed in Fig. 3.4 is shown as the black curve undergoing 1 poloidal rotation for every 3 toroidal rotations. The red line represents a field line with a larger rotation transform, located

outside the ι=1/3 surface. The blue line represents a field line located inside the ι =1/3 surface with a smaller rotation transform. The average slope of these curves would give the rotational transform of the corresponding flux surface. The gyrations that we saw in the field line in Fig. 3.4(b) give the curves in Fig. 3.5 their wavy nature. Also the 5 fold periodicity of the CTH device is visible, in that for every toroidal rotation, the field line makes 5 poloidal oscillations. From Fig. 3.5 we see that field lines contained inside the vacuum vessel experience a net poloidal progression, despite the fact that the line integral of the magnetic field along any poloidal contour must be zero according to Eq. 3.1.

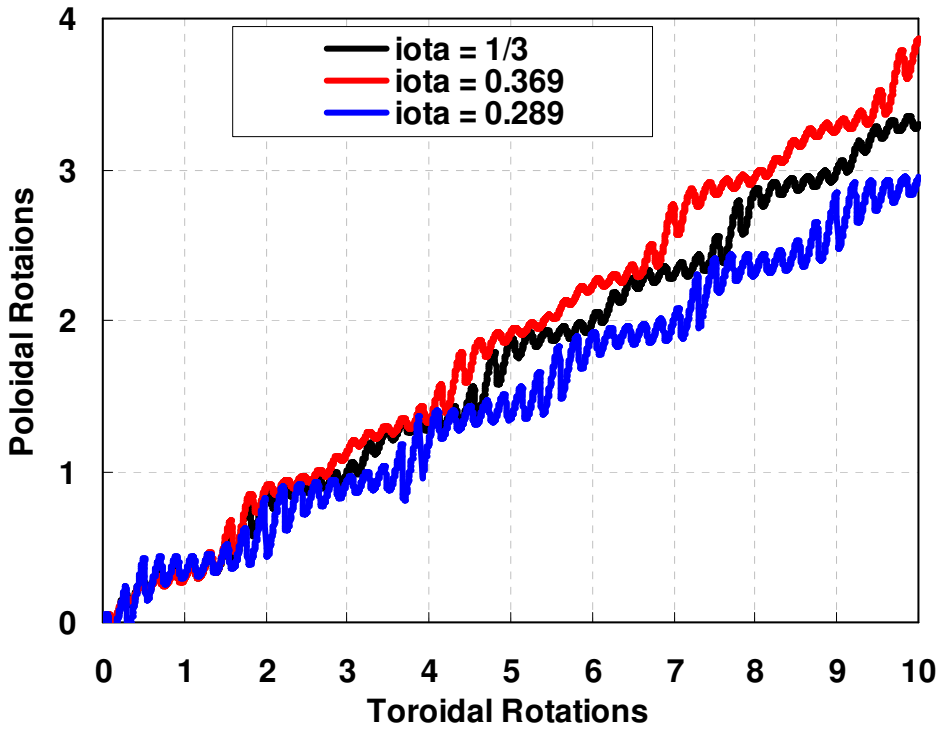

Fig. 3.5 Net poloidal and toroidal rotation of field lines

To illustrate how field lines with a net poloidal rotation produce closed nested flux surfaces contained within the vacuum vessel, we look at a surface of section (SOS) puncture plot shown in Fig. 3.6(a). A SOS plot such as this is produced with the IFT field

line-following code by following field lines toroidally and recording the location of the field line each time it intersects a poloidal plane, φ=36° in this case. After many toroidal circuits of a field line the shape and rotational transform of a flux surface are apparent. The different colored flux surfaces in Fig. 3.6 are obtained by starting the field line integration at different radial positions. The magnetic axis is shown in the center of nested surfaces and the last closed flux surface approaches the vacuum vessel wall. The rotational transform vs. the area of the various flux surfaces found in Fig. 3.6(a) are shown in Fig. 3.6(b).

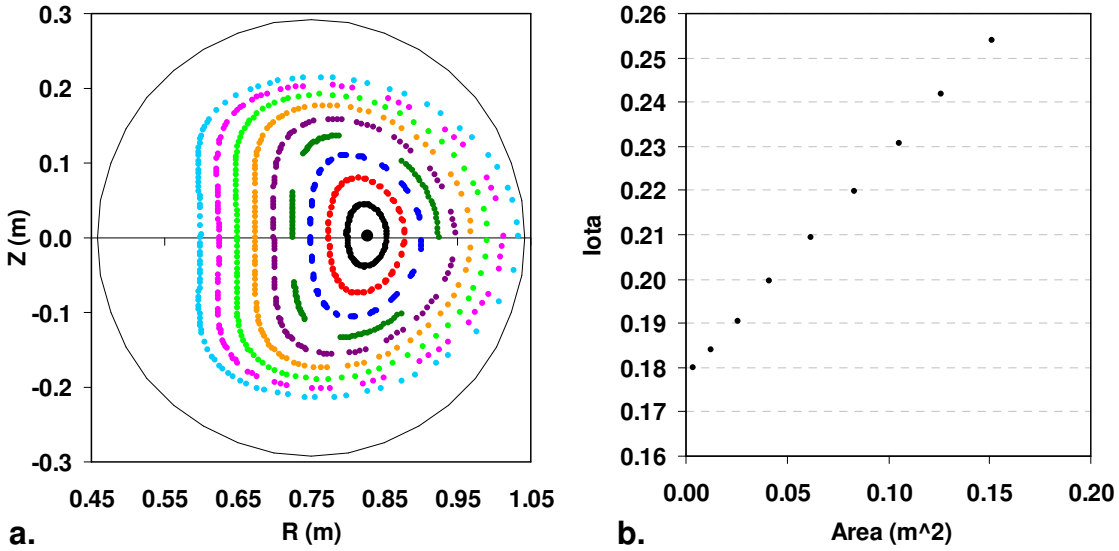

Fig. 3.6 SOS plot and rotational transform vs. area
I_{HF}=300 A, I_{TVF}=40.7 A

In the examples of the closed flux surfaces shown already, the field of the TVF coil was used to shift the radial position of the flux surfaces within the vacuum chamber. We are now in a position to consider how the additional field of the TVF coils was affecting the field lines. The magnetic field vectors produced by the TVF coil alone are shown in a cross-section of the machine through the φ=0/180° plane in Fig. 3.7(a). The

TVF current is in the negative φ direction, out of the page on the right and into the page on the left, and the current in the TVFD coils is in the positive φ direction. We see that inside the vacuum vessel, the field is nearly uniform and downward.

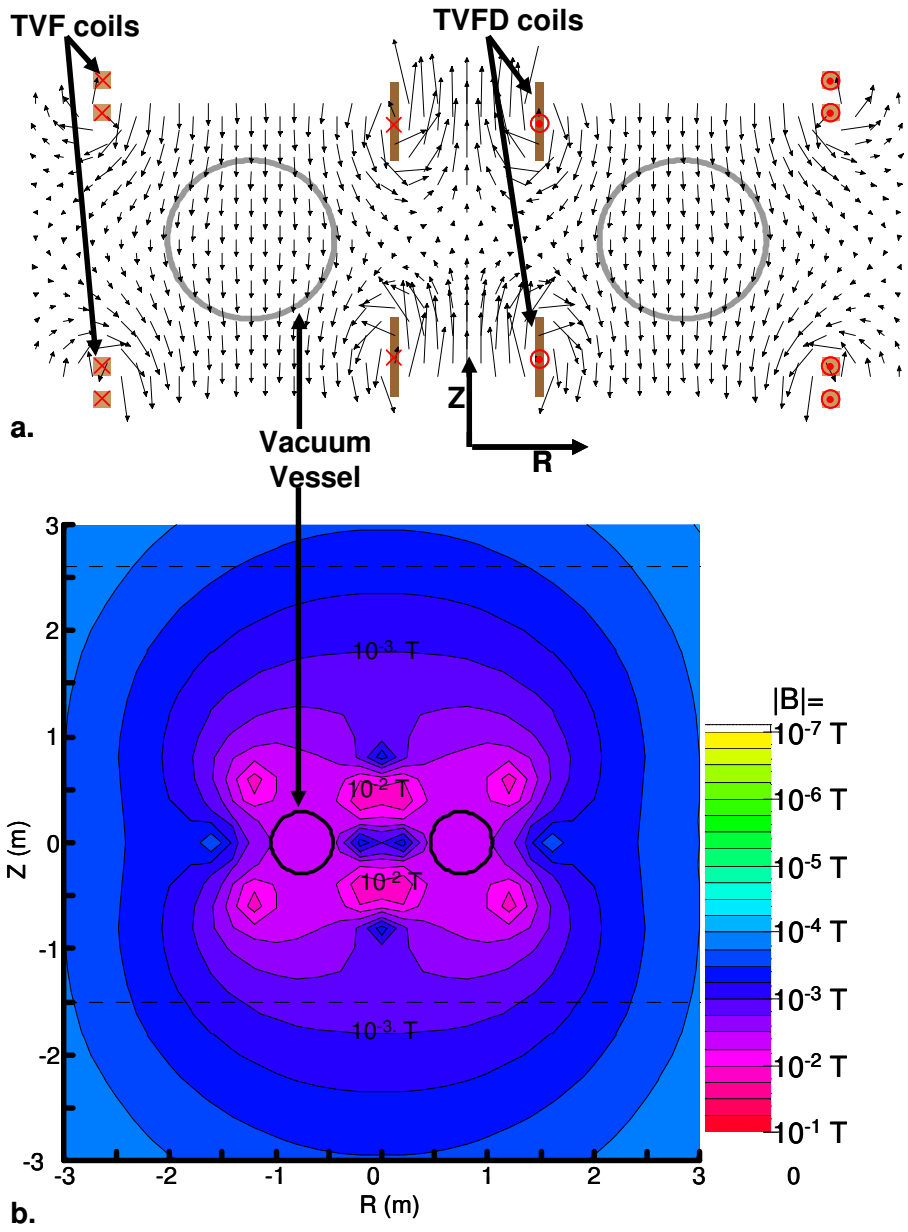

Fig. 3.7 TVF field vectors and strengths
I_{TVF} = 54 A

The field strength produced by 54 A in the TVF coils is shown in Fig. 3.7(b). During field mapping experiments with an HF current of I_{HF} =300 A the TVF current is varied from I_{TVF} =30 to 54 A. Inside the vacuum vessel the field strength is in the 10^{-3} T range. The fields produced by the OVF and TVF coils have similar structure and magnitudes, due to the similarities in the coils' size, location, and number of turns.

The effect the additional TVF vertical field has on the magnetic flux surfaces is qualitatively shown in the context of a simplified HF/OVF field model, similar to that shown in Fig. 3.4(b). The simplified model neglects the gyrations of the field line trajectories and represents the flux surfaces to be circular, as pictured by the red arrows in Fig. 3.8(a). Field vectors on the outboard side of the magnetic axis have downward components and field vectors on the inboard side have upward components. The poloidal field decreases with minor radius as indicated by the smaller arrows, and must be zero at the magnetic axis.

The application of a uniform downward vertical field is shown in Fig. 3.8(b) with the green arrows. Adding the components of the two fields in the different regions we find the following behavior in different regions:

Region A the field line is pushed to a smaller minor radius

Region C the field line is pushed to a larger minor radius

Region B the field lines add together and are stronger

Region D the field lines subtract from each other and become weaker

At a location inward of the original magnetic axis in region D, the fields must cancel. This is the new magnetic axis position where the total net poloidal field is zero. Completing the nested surfaces by connecting the arrows of the new poloidal field, we

see there is an overall shift of the closed nested flux surfaces radially inward shown in Fig. 3.8(c) in black. Thus the addition of a downward field shifts the magnetic axis and rest of the surfaces radially inward.

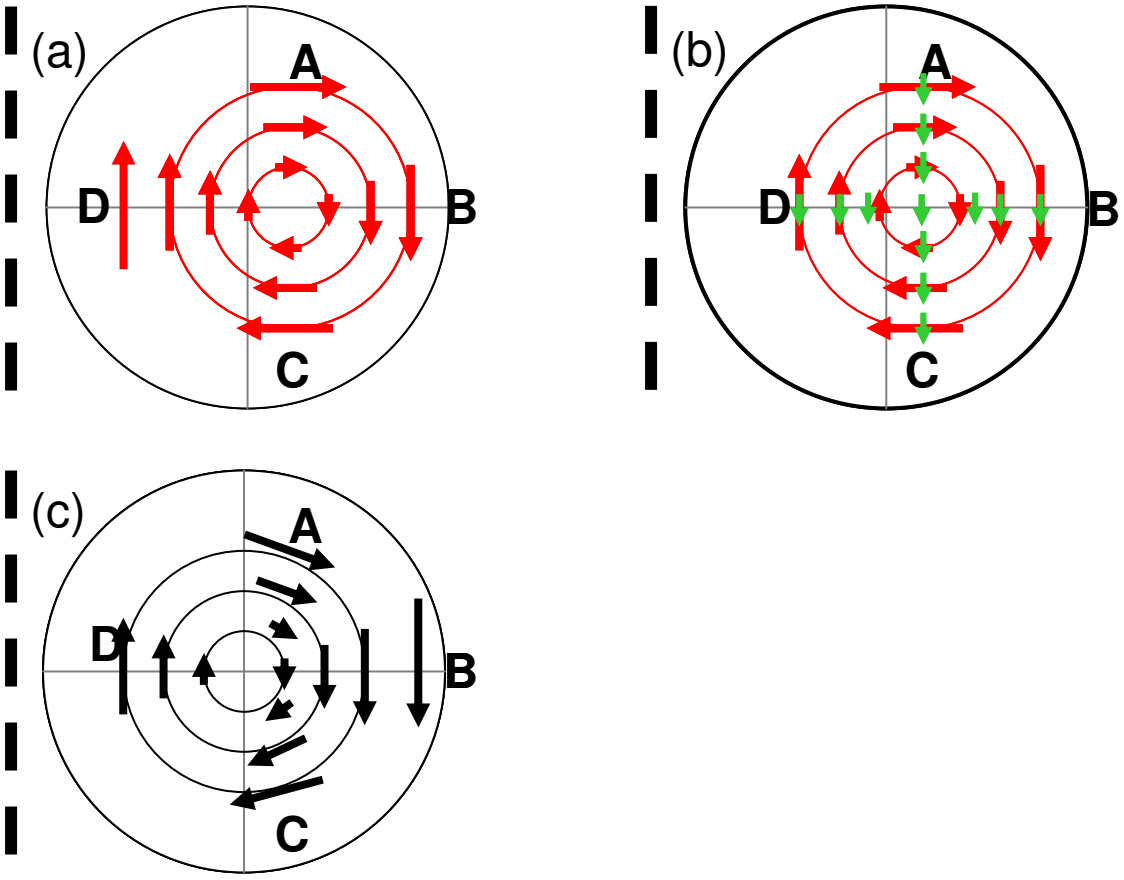

Fig. 3.8 Schematic of the HF/OVF/TVF fields
a) Schematic of the average poloidal field of the HF/OVF coils.
b) Addition of TVF downward vertical field
c) Resultant flux surfaces are shifted inward

This simplified model is numerically confirmed in the actual stellarator geometries of CTH. The magnetic axis locations are computed with IFT using different TVF currents. The results are shown in a top down view of the vacuum vessel in Fig. 3.9(a). Without any TVF current, the axis remains inside the vacuum vessel due to the downward field supplied by the OVF coil. The additional downward fields of the TVF

coils, shifts the magnetic axis radially inward. Shown in Fig. 3.9(b) are the radial locations of the magnetic axis at two toroidal port locations over a range of TVF currents. Lastly, the rotational transform of the magnetic axis vs. the TVF current is shown in Fig. 3.9(c). As the TVF current is increased, the rotational transform of the magnetic axis decreases.

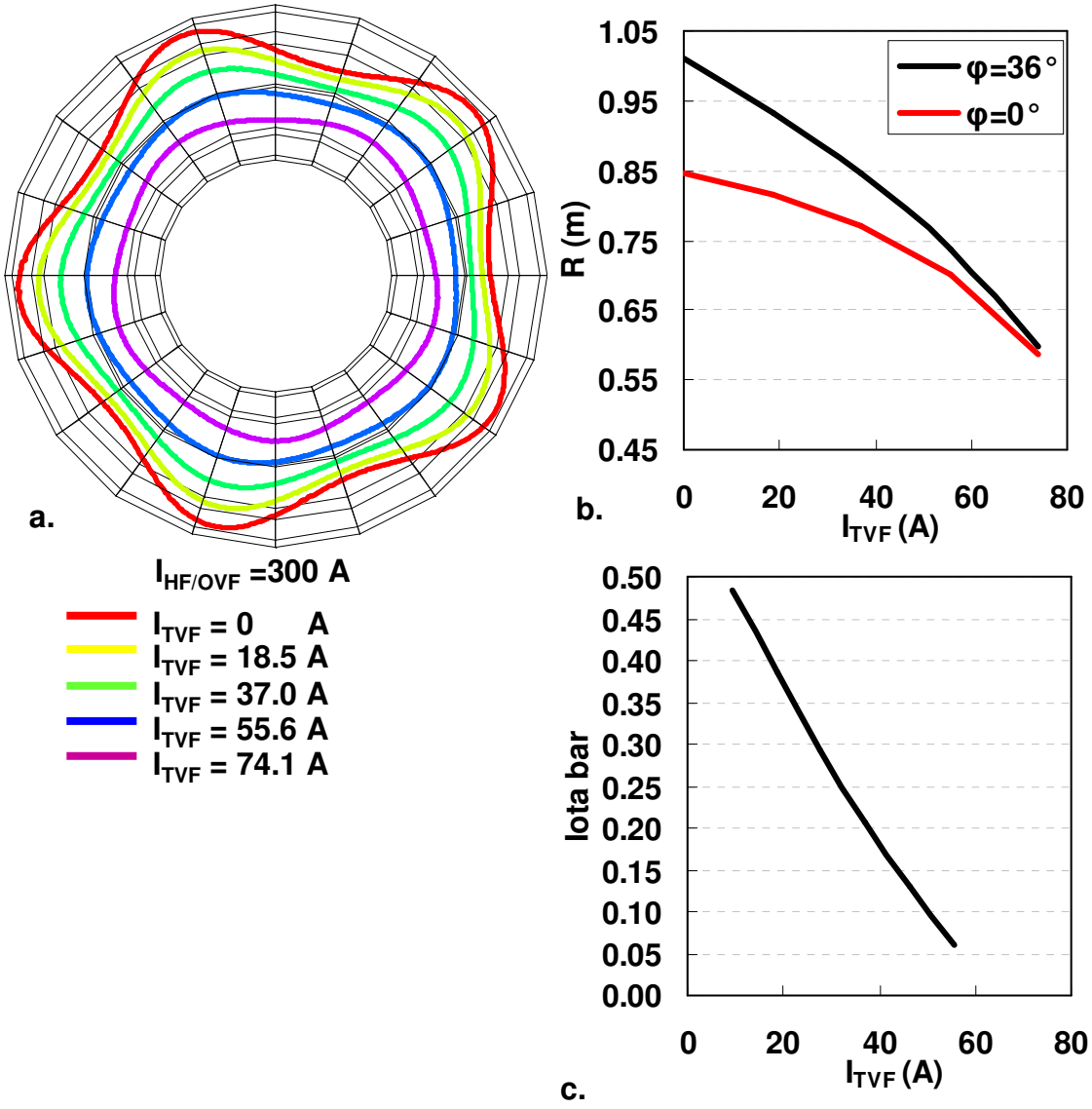

Fig. 3.9 Magnetic axis position and rotational transform vs. I_{TVF}.

3.2 RF FIELDS

The purpose of the RF coils is to produce a radial field inside the vacuum vessel to shift the flux surfaces up or down depending on the polarity of the RF coil current. To produce the radial field, the current in the upper and lower RF coils are in opposite directions.

The fields produced by the RF coils in φ=0/180° vertical plane are shown in Fig. 3.10. Inside the vacuum vessel region the net RF field is inward. The magnetic field vectors in the immediate vicinity of the RF coils are omitted in the figure to highlight the smaller radial fields within the vacuum vessel. The field strength produced inside the vacuum vessel by 35 A in the RF coils is $|B| \sim 10^{-3}$ T.

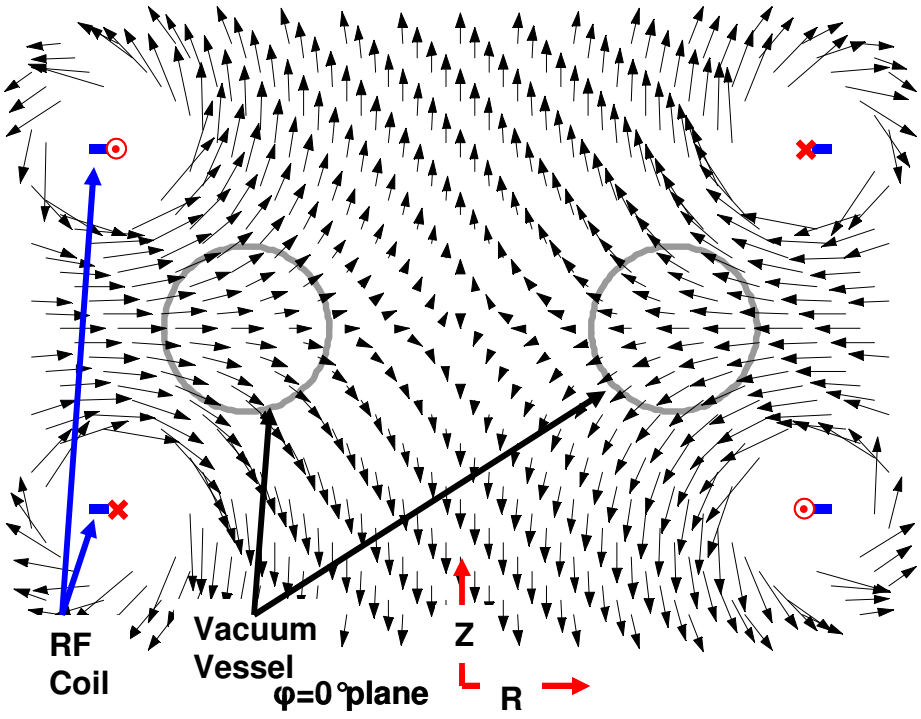

Fig. 3.10 RF field vectors and strengths

The effect the radial field has on the flux surfaces is qualitatively shown in Fig. 3.11. The net poloidal field of the HF/OVF/TVF coils is shown in red. The uniform

inward RF field is shown in blue. Adding the components of the two fields in the various regions results in the following. In region C, the inward RF field adds to the inward HF/OVF/TVF field. In region A, the inward RF field subtracts from the outward HF/OVF/TVF field. At a location above of the original magnetic axis in region A, the fields must cancel. This is the new magnetic axis position where the total net poloidal field is zero. The combined fields of the HF/OVF/TVF, and RF coils are shifted upward shown in Fig. 3.11(b). In this way, the RF coils shift the vertical position of the plasma.

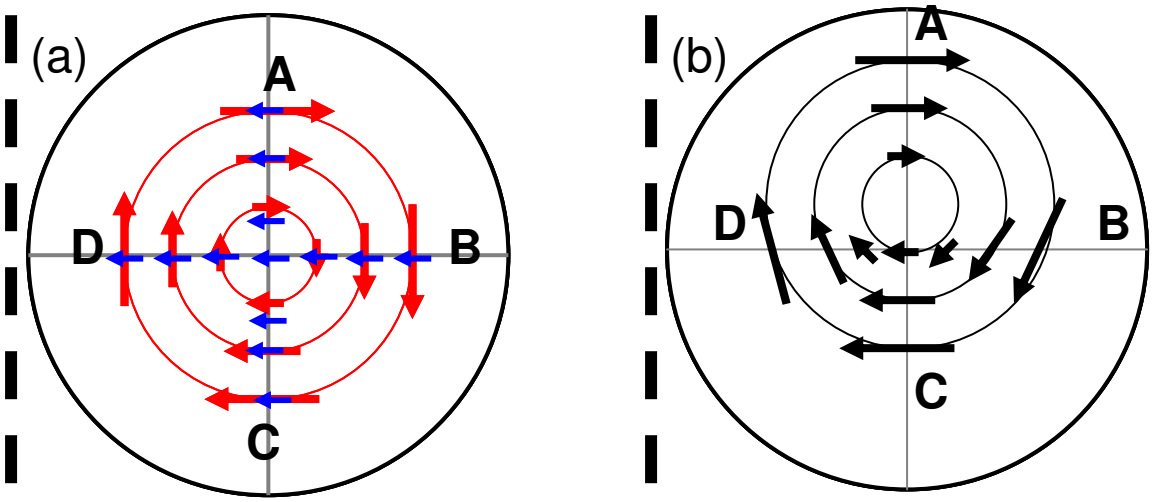

Fig. 3.11 Schematic of the RF fields effect on the flux surfaces

The vertical location of the magnetic axis vs. the RF current as computed with IFT is shown in Fig. 3.12. A positive RF current (inward field) moves the magnetic axis upward demonstrated in Fig. 3.11, whereas a negative RF current (outward field) moves the magnetic axis downward. The RF field does not significantly alter the radial location of the flux surfaces.

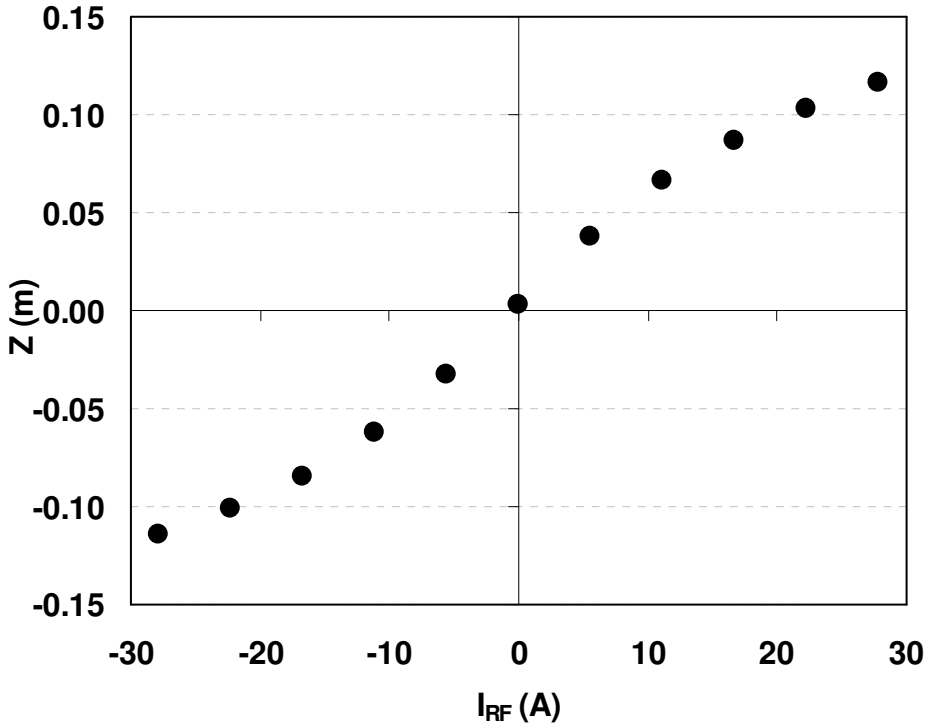

Fig. 3.12 Vertical position of the magnetic axis vs. RF current
I_{HF}=300 A, I_{TVF}=40.7 A

The RF coils were added to the design of CTH as a precautionary measure to counter possible up-down asymmetries that might be produced by errors in coil placement, coil construction, or residual fields from local ferromagnetic materials. It should be noted that while ferromagnetism will be shown to have a noticeable effect on the measured flux surfaces, the resultant errors are not so large as to require the routine use of the RF coils to vertically center the plasma.

3.3 SVF FIELDS

The size and location of the SVF coils produce a non-uniform vertical field inside the vacuum vessel which influences the average vertical elongation and the rotational transform shear or radial variation of the rotational transform of the flux surfaces.

Shown in Fig. 3.13(a) are the magnetic field vectors in the φ=0° poloidal plane, with the φ=180° plane having been omitted to view the quadrupole field created by the SVF coils inside the vacuum vessel. The field is upward, strongest on the inside and weakest near the outside. Near the top of the vessel the field has an inward components and outward components near the bottom of the vessel. The field strength inside the vessel produced by 35 A in the SVF coils varies in magnitude from $|B|\sim 3\times10^{-3}$ T on the inboard side to $|B|\sim 2\times10^{-4}$ T on the outboard side.

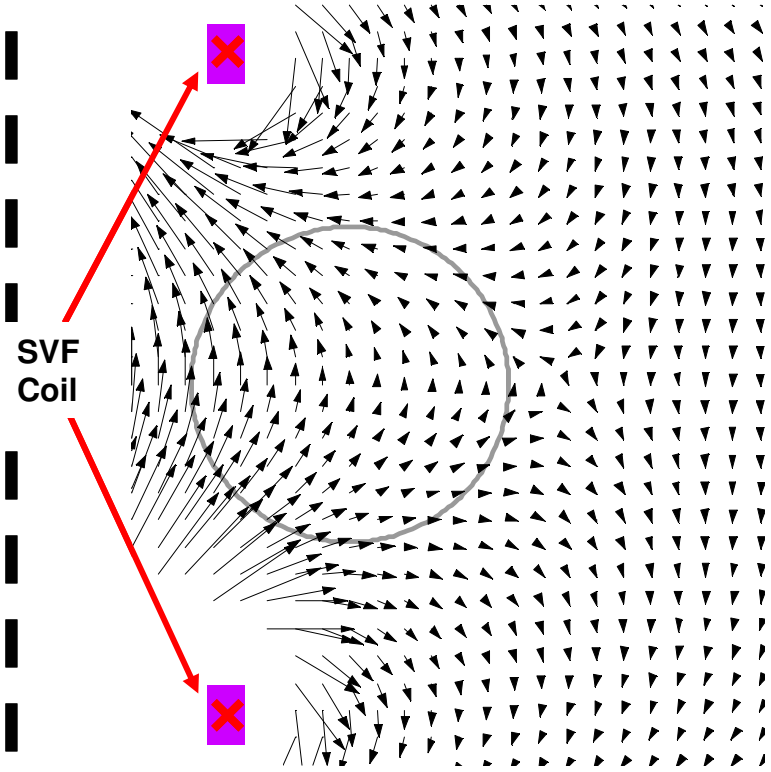

Fig. 3.13 SVF field vectors and strengths
I_{SVF} = 35 A

The qualitative model of the SVF field interacting with the HF/OVF/TVF field is depicted in Fig. 3.14. The red arrows in Fig. 3.14(a) represent the simplified poloidal field produced by the HF/OVF/TVF coils. The purple arrows represent the non-uniform quadrupole field produced by the SVF coils. Adding the two sets of field components in

the different regions, results in a stronger upward field in region D, while in region B the downward field is slightly smaller. The surfaces of the combined fields shown in Fig. 3.14(b) are shifted outward and vertically elongated. If the SVF current polarity is reversed, the resulting flux surfaces are vertically compressed and shifted radially inward.

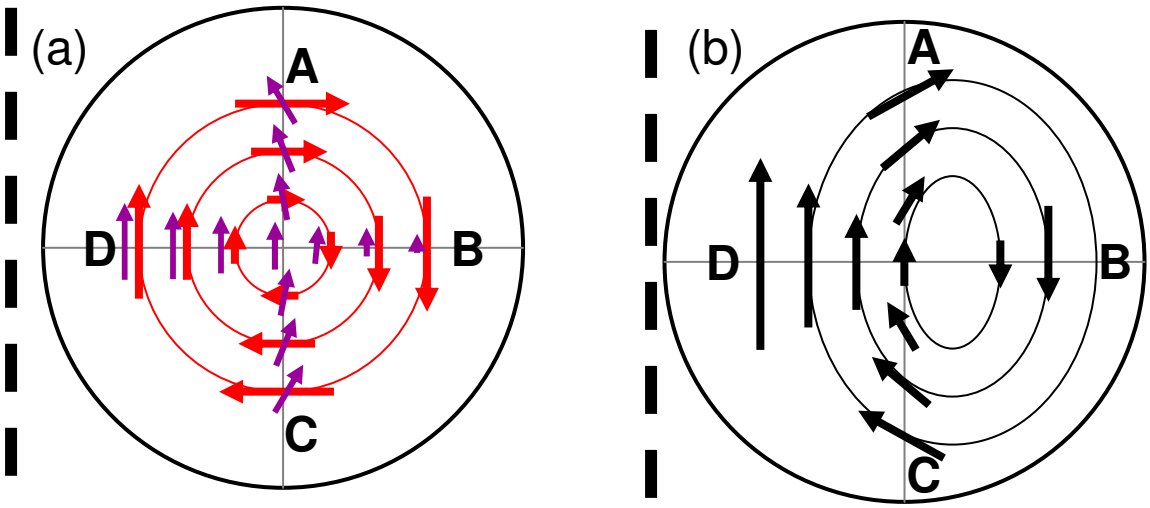

Fig. 3.14 Schematic of the SVF fields effect on the flux surfaces

Simulation SOS plots demonstrate these effects in Fig. 3.15. When the SVF current is positive (an upward field), the surfaces are elongated in the vertical direction and shifted radially outward as shown in Fig. 3.15(a). When the SVF current is negative (a downward field), the surfaces are compressed in the vertical direction and shifted radially inward as shown in Fig. 3.15(b).

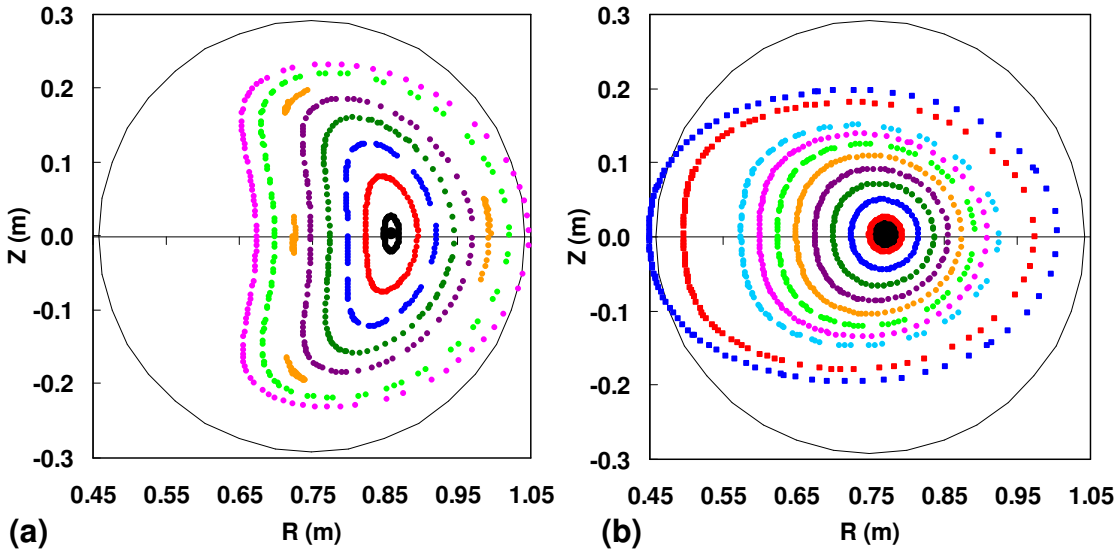

Fig. 3.15 SOS plots with different SVF currents
I_{HF} =300 A, I_{TVF} =-40.7 A, φ=36°
a) I_{SVF} = +40 A
b) I_{SVF} = -40 A

The non-uniform vertical fields of the SVF coils not only alter the vertical elongation of the flux surfaces, but also affect the radial derivative of the rotational transform otherwise known as the shear. In a cylindrical approximation[30] the shear S, is given as

$$S = \frac{r^2}{2\pi R}\frac{d\iota}{dr}. \tag{3.2}$$

Here r is the minor radius of the flux surface and R is the major radius of the magnetic axis. Experimentally it is difficult to compute $\frac{d\iota}{dr}$ because the minor radius r of the surface varies depending on poloidal angle. On the other hand, the area A, enclosed by the surface in a poloidal plane is much easier to calculate. Assuming a circular cross-section of the flux surfaces, the shear equation can be written as

$$S = \frac{(A/\pi)^{3/2}}{R}\frac{d\iota}{dA} \tag{3.3}$$

where now the shear is expressed in terms of the change in ι vs. the change in area, a quantity much easier to experimentally determine.

The rotational transform vs. the flux surface area is shown in Fig. 3.16(a) for a range of simulation SVF currents. The average shear increases with SVF current. In Fig. 3.16(b) the average slope of each rotational transform profile, is plotted vs. the current in the SVF coils. The average shear of the rotational transform is computed to be negative in extreme cases of negative SVF current.

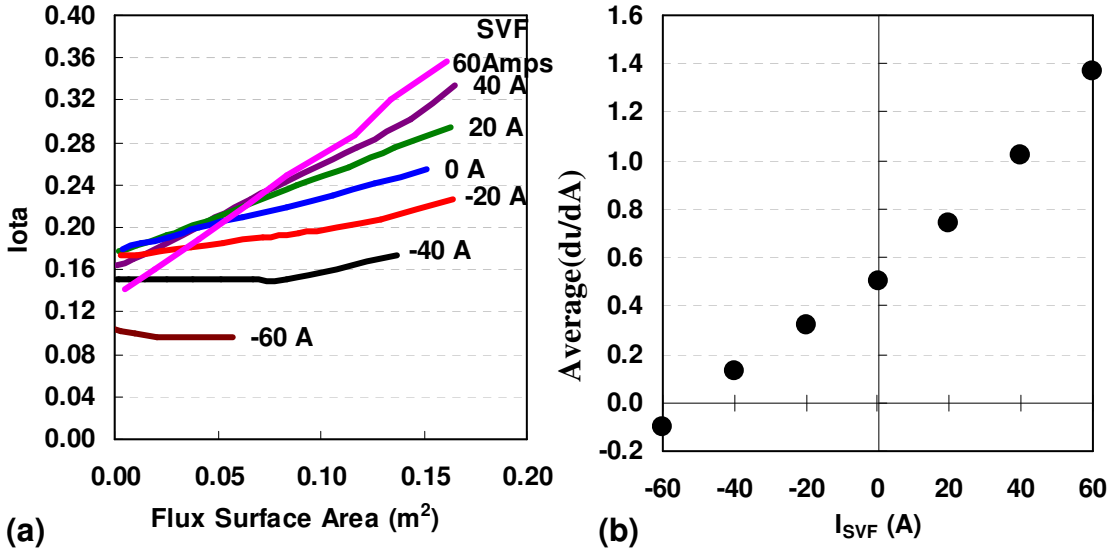

Fig. 3.16 Rotational transform dependence on SVF current
I_{HF} =300 A, I_{TVF} =-40.7 A

3.4 TF FIELDS

The purpose of the TF coils is to raise or lower the net rotational transform of the plasma depending on the polarity of the TF coil current. To raise the rotational transform, the toroidal field of the TF coils is in the opposite direction to the toroidal field produced by the HF coil. This decreases the net toroidal field, B_φ, which has the effect of raising the rotational transform across the entire radius of the plasma. To lower the rotational transform the TF field is the same direction as the HF field, increasing the overall toroidal field.

The field vectors produced by the TF coils computed on the midplane are shown in Fig. 3.17(a). The field is in the positive φ direction, opposite that of the HF's toroidal field shown in Fig. 3.1. The field strength produced by 125 A in the TF coils is shown in Fig. 3.17(b). Inside the vessel the field strength decreases as 1/R from ~.03 T on the inboard side to ~.01 T on the outboard side. It should be mentioned here that the field produced by the TF coils is primarily contained to region of space within and immediately surrounding the vacuum vessel, with negligible field present in the ceiling and floor. This will be significant in Ch. 5 and 6 when the effects of magnetization on ferromagnetic material will play an important role in determining the magnetic axis position.

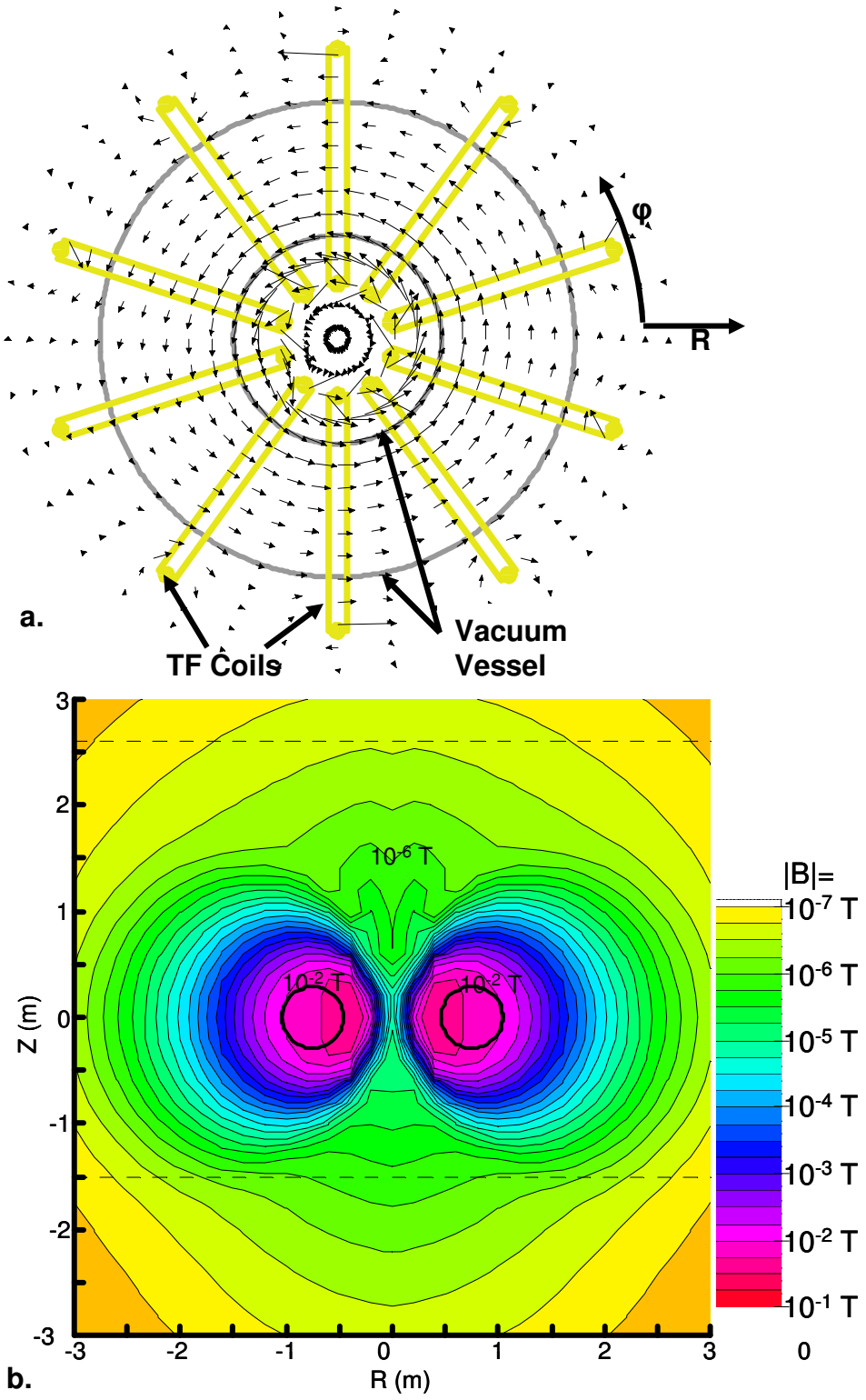

Fig. 3.17 TF field vectors and strengths

a) Top view of torus on the z=0 plane

b) Side view torus on the φ=0/180° plane, I_{TF} = 125 A

The rotational transform of the magnetic axis computed by IFT is plotted for different TF coil currents in Fig. 3.18. For the current ratio I_{TVF}/I_{HF} =.136 used in this simulation, an asymptotic rotational transform of ι≈.1 is reached with large negative TF currents. Furthermore, TF currents in excess of 125 A do not further increase the rotational transform. Producing flux surfaces with rotational transforms exceeding ι=1/2 has not been achieved in vacuum field mapping or through simulation.

It should be noted that increasing the current in the TF coils not only raises the rotational transform but also shifts the magnetic flux surfaces inward. The TVF field is used to reposition the radial location of the plasma

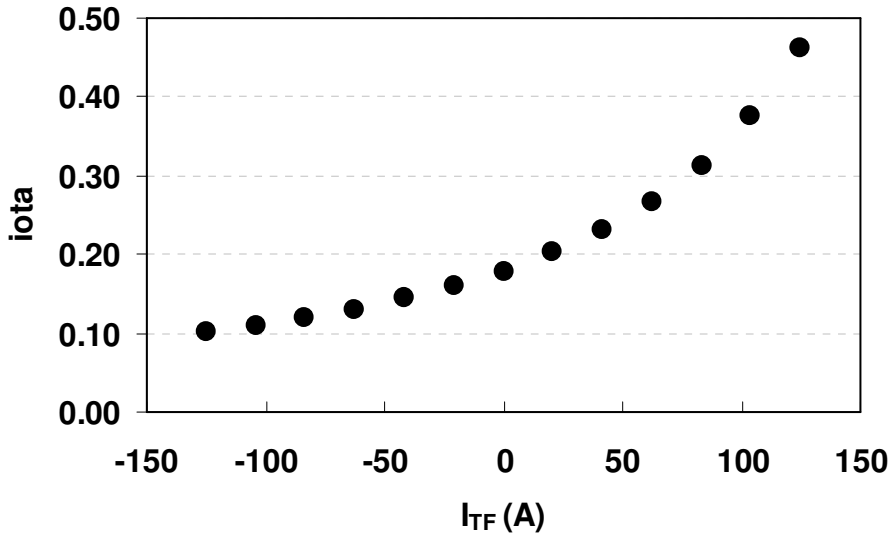

Fig. 3.18 Rotational transform of the magnetic axis vs. TF current
I_{HF}=300 A, I_{TVF}=-40.7 A
Positive TF currents produce fields in the positive toroidal direction.

3.5 OH FIELDS

The purpose of the OH coil system is to induce a toroidal electric field within the plasma to drive a toroidal plasma current. The OH coil set can be considered the primary winding of a transformer with the conducting plasma ring being the secondary. By steadily increasing the current through the OH solenoid, a toroidal current is induced in the plasma due to the changing magnetic flux enclosed by the toroidal loop of plasma. This induced changing flux Φ, produces an electric field $\vec{E}$ in the plasma due to Faraday's Law, Eq. 3.4, which in turn drives a plasma current.

$$\frac{\partial \Phi}{\partial t} = \oint \vec{E} \cdot \vec{dl} \tag{3.4}$$

The magnetic field produced by the OH coil system is shown in Fig. 3.19(a). To minimize the effect the changing magnetic field of the OH coil system has on the steady state magnetic configuration of CTH, the combined magnetic fields of the OH1, OH2, and OH3 coils are designed to produce minimal magnetic flux inside the vacuum vessel. We see that the purpose of the OH2 and OH3 coils is to pull the magnetic field outward around the vacuum vessel so it does not directly interact with the plasma. In this way the plasma does not experience the magnetic field produced by the OH coil system, only the induced electric field of Eq. 3.4.

During plasma experiments the maximum current in the OH coils is roughly 2.5 times that of the HF coil Therefore in keeping this ratio relative to I_{HF} = 300 A, the field strength produced by 750 A in the OH coils is shown in Fig. 3.17(b). The fields created by the OH coil system inside the vacuum vessel are over 3 orders of magnitude smaller than those found near the central axis.

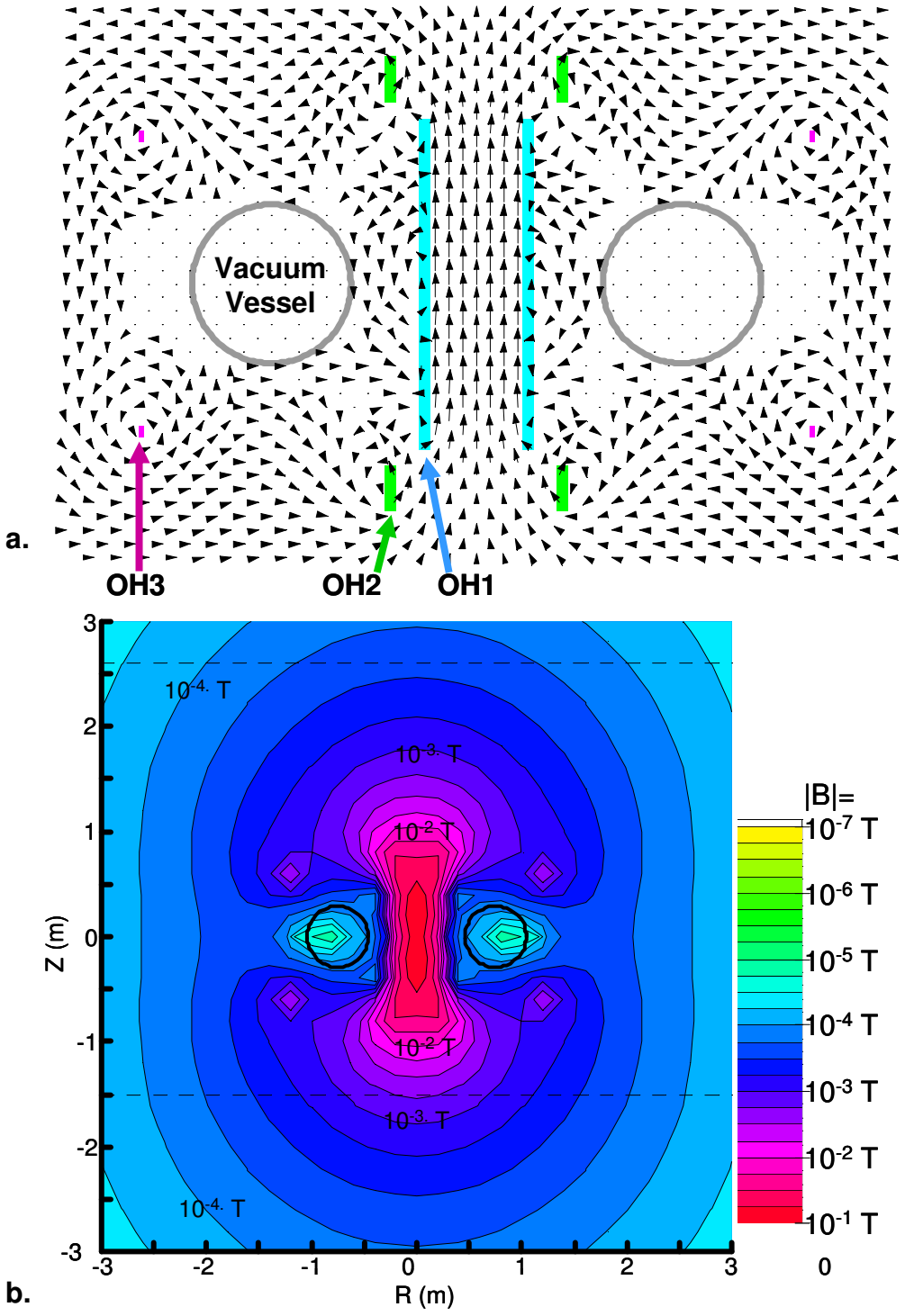

Fig. 3.19 OH field vectors and strengths
I_{OH} = 750 A

CHAPTER 4: FIELD MAPPING SETUP

4.1 FIELD MAPPING OVERVIEW

Magnetic field mapping[31] is an experimental technique used to measure the vacuum magnetic field configuration in stellarators. By experimentally determining the field line geometry, one can (1) ensure that closed nested flux surfaces are indeed produced by currents in the coils and (2) compare the measured field line trajectories with those computed by a vacuum field simulation to arrive at a more accurate model for the stellarator coils.

Field mapping experiments are performed by collecting electrons emitted from an electron gun placed inside the vacuum vessel, as shown in Fig. 4.1. Once they leave the gun, the guiding center of the electron orbits follow the magnetic field lines to a good approximation, and thus make a number of toroidal transits. The electron beam intersects a stainless steel wire mesh screen located two field periods away from the electron gun. The screen is coated with zinc-oxide, a compound which fluoresces in visible light when struck by electrons with sufficient energy, typically greater than 100 eV. As the electron beam intersects the plane of the screen, some of the electrons strike the screen, producing a point of light. The rest of the electrons pass through the screen and continue around the machine until they intersect the screen again on their second pass, and so on. Therefore the light pattern on the screen represents a puncture plot of the electron trajectories at the toroidal location of the screen. To the extent that the trajectories match the field lines

themselves, these experimental puncture plots directly correspond to the computed surface-of-section plots from the IFT field line following code. A photograph of the screen is taken with a digital camera. The size, shape, location, and rotational transform of low order rational surfaces with rotational transforms, such as, ι =1/3, 1/4, 2/5, etc. along with magnetic axis are obtained in this way.

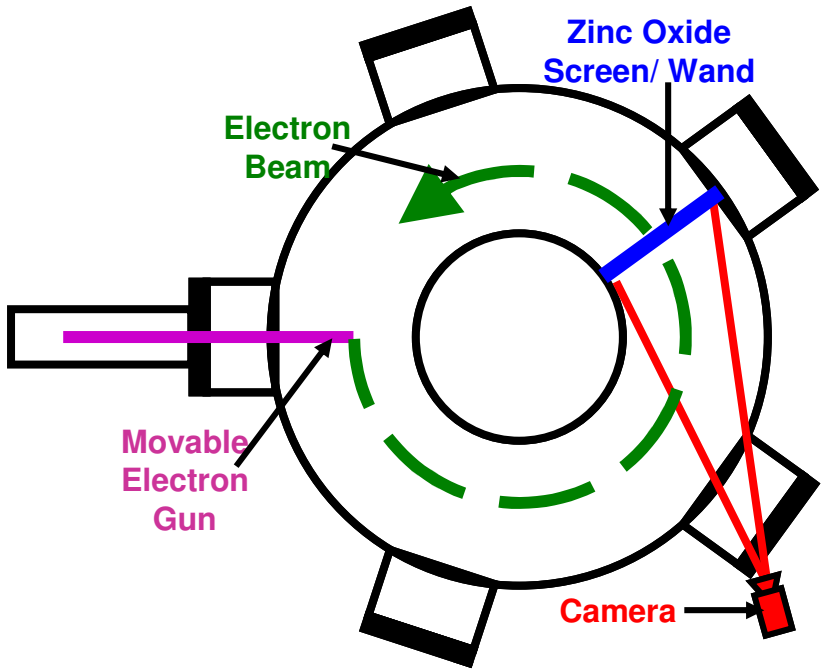

Fig. 4.1 Field mapping setup

A similar field mapping method makes use of a zinc oxide coated movable wand[32] instead of a screen. The wand is swept through the poloidal plane of the flux surface at a given toroidal location. In this method, electrons are only removed from the electron beam where they intersect the wand, typically at two locations for a given wand position. An image of the entire surface is obtained with an extended time exposure photograph, taken as the wand travels through the flux surface.

In both methods, points of interest in the puncture plot photograph, such as the magnetic axis, undergo a calibrated transformation from the photograph pixel point (x,y) to a point in real space (r,φ,z) with the use of LabView Vision Software®[33]. The locations of these experimental points are then compared to computed SOS plots to quantify discrepancies between our coil model used in the computer simulation and the actual coils of CTH as discussed in Ch. 6.

4.2 Electron Gun

The ideal electron gun would produce an intense, filament like, beam of electrons resulting in a bright signal from the zinc-oxide screen. In addition, this electron gun would produce a minimal amount of stray light such that the signal from the zinc-oxide is not masked by the unwanted light of the gun. Lastly, the ideal electron gun would be capable of being positioned anywhere inside the vacuum vessel without obstructing the electron beam as it makes successive toroidal transits. The electron gun used in field mapping studies on CTH was designed with these principles in mind. A diagram of the electron gun tip is shown in Fig. 4.2.

Electrons are thermionically emitted from a clean tungsten wire with diameter of 0.12 mm heated to incandescence located inside a thin stainless steel (SS) tube with a hole for the electrons to escape. For this diameter wire, filament currents in the range of 2 – 2.5 A produce the best field mapping results. Filament currents less than 2 A do not produce enough energetic electrons for a visible signal, while filament currents greater than 2.5 A generate an excessive amount of light within the vacuum vessel and produce larger spots on the screen. The filament is biased to -100 V relative to the vacuum vessel.

The electrons are accelerated away from the negatively biased filament and escape through a 1.0 mm diameter hole in the stainless steel tube which must be aligned with the local magnetic field direction. Once the electrons leave the gun, the trajectory of their guiding centers is determined by the magnetic field within the vessel.

Inside the electron gun, the tungsten filament wire is formed into a small three turn coil with a diameter of approximately 0.8 mm. Each filament lead makes a press-fit contact inside the two holes of a long ceramic tube with the tungsten electrical feeds, which are connected to a DC power supply used to heat the filament. The tungsten filament is positioned such that its axis is centered parallel to that of the hole in the stainless steel tube, as shown in Fig. 4.2. If the filament is not properly aligned, the emerging electron beam signal is weak and magnetic surfaces are not visible.

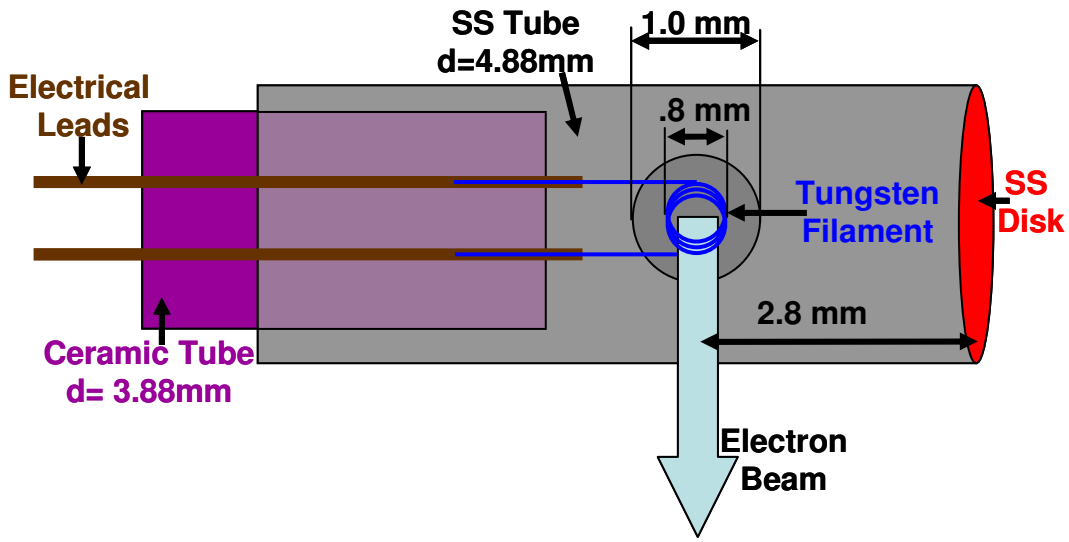

Fig. 4.2 Electron gun tip

Once the gun is assembled, the resistance of the filament is checked for continuity ($R<1\ \Omega$) and for electrical isolation from the SS housing ($R>100\ M\Omega$). Then a 0.14 mm thick stainless steel disk is spot-welded to the outer end of the SS tube. The SS disk

reduces the light contamination from the filament when magnetic surfaces are being observed.

The electron gun is mounted to a vacuum feed-through capable of multidimensional movement. The drive apparatus shown in Fig. 4.3 allows the gun tip to move 0.57 m radially and ±40° (±.302 m from the midplane) vertically. In addition, the gun tip is capable of swiveling around its axis by 375°. This range of motion allows the gun tip to be placed almost anywhere within a poloidal plane of the vacuum vessel at the toroidal location of the gun.

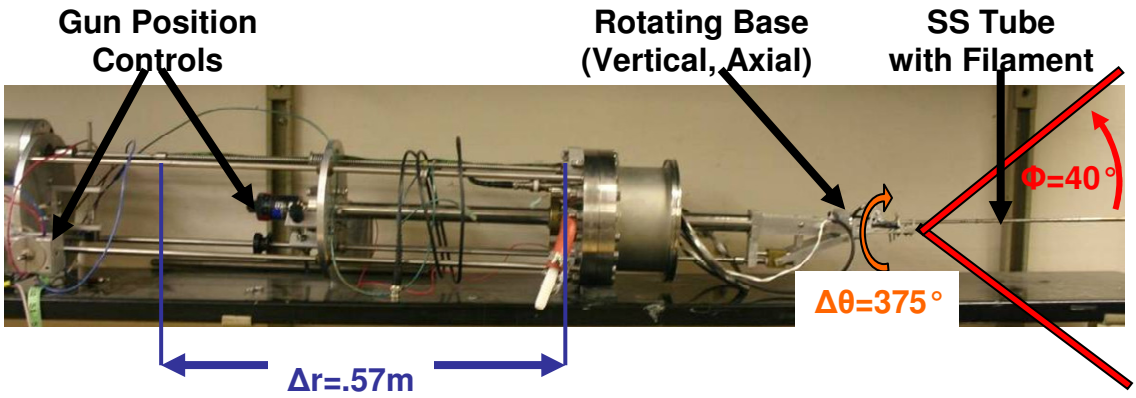

Fig. 4.3 Electron gun and positioning assembly

4.3 SCREEN

One method of detecting the electron beam makes use of a highly transparent stainless steel mesh screen placed two field periods away from the electron gun in the toroidal cross-section of the vacuum vessel. The screen is made of wires 0.12 mm in diameter. The screen mesh size is 2.25 mm wide by 3.9 mm high, for a computed transparency of 91.5 %.

The screen diameter of 0.584 m required to cover the entire poloidal plane of the vessel, is larger than the 0.406 m diameter of side port tube, and therefore the screen is

designed to be folded in half, put into the vacuum vessel, and then fully assembled once inside. To do this the screen is stretched between four semicircular aluminum support rim (SR) pieces, two on the top and two on the bottom with a gap between the top and bottom as shown in Fig. 4.4(b), labeled SR1. This gap allows the screen to be folded in half for insertion into the vessel. With the screen inside the vacuum vessel, two additional semicircular support rims, labeled SR2, connect the screen upper and lower sections making the screen into a rigid disk.

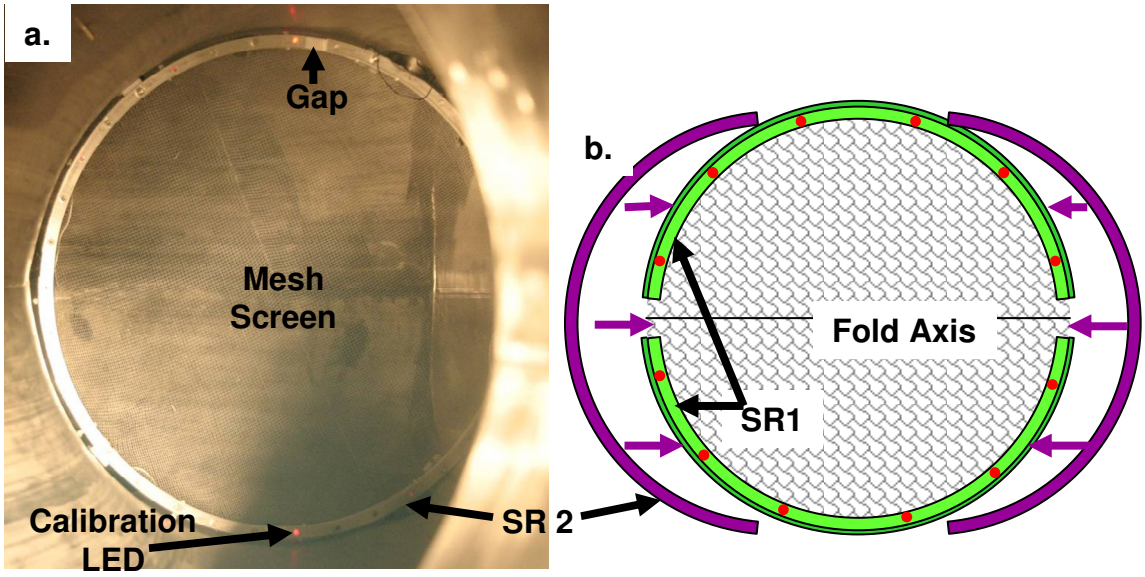

Fig. 4.4 Field mapping screen setup
a) Photo of the screen installed inside a vacuum vessel side port.
b) Exploded-view diagram of the screen

Before the screen is placed inside the vacuum vessel, a layer of zinc-oxide is applied to the screen. Three bottles, each with 8 grams of zinc-oxide are mixed with 18 ml of methanol. The zinc-oxide does not dissolve in the methanol but can be suspended in solution if the mixture is thoroughly stirred. The mixture is then airbrushed evenly onto the screen using a standard airbrush kit.

Mounted to the support rims are 12 light emitting diodes (LEDs) that aid in the transformation from the photographic image to the rectangular coordinates relative to the magnetic coils. The positions of the LEDs are measured with a coordinate measuring machine once the screen is secured to the vacuum vessel. Lastly the screen is grounded to the vacuum vessel to avoid charge build up during field mapping.

While field mapping, the amount of light produced by the zinc-oxide is determined by the intensity of the electron beam. After each intersection of the beam with the screen the density of electrons in the beam becomes smaller. Thus the visible dot resulting from the first pass of the beam is the brightest, the one from the second pass the second brightest and so on. Up to 30 toroidal transits have been observed, before the electron beam density becomes insufficient for resolution of the beam on the screen. Because only the first 30 transits of the beam are observed, the screen method of field mapping is ideal for identifying the rotational transform of a flux surface, discussed in Sec 4.9, but makes visualizing the complete surface difficult.

4.4 WAND

An alternate method of imaging magnetic flux surfaces uses a thin stainless steel wand coated in zinc oxide. The wand is swept vertically through the magnetic flux surface by means of a vacuum vessel feed-through similar to that of the electron gun, and is capable of 0.60 m of radial motion and ±44° of vertical rotation as shown in Fig. 4.5.

For calibration purposes, the support rims containing the calibration LEDs are placed inside the vacuum vessel with the screen removed. To avoid charge build-up on

the wand and the creation of an electrostatic field within the vessel, the wand is grounded to the vacuum vessel.

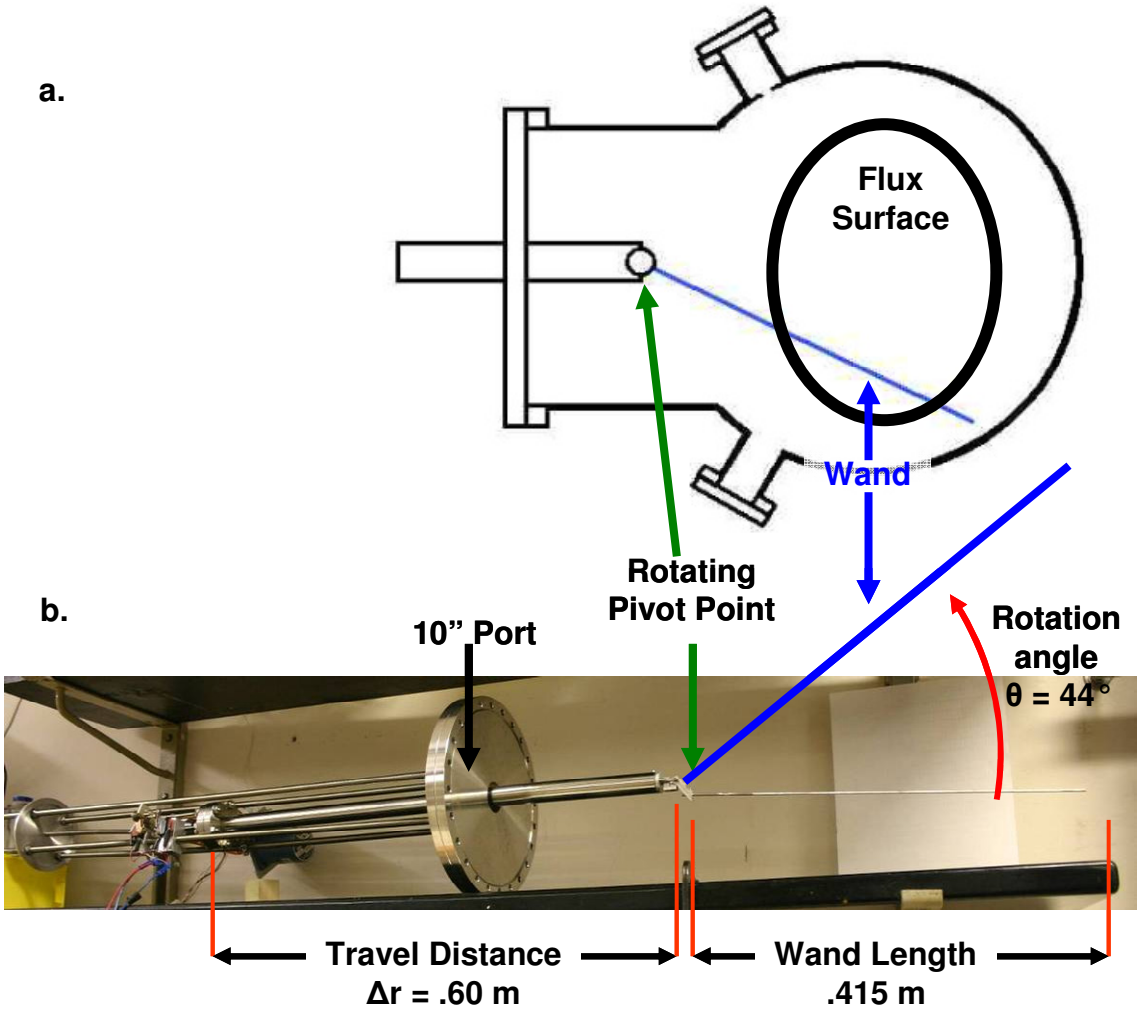

Fig. 4.5 Setup of field mapping with the wand
a) Diagram of the wand inside the vacuum vessel
b) Photograph of the wand apparatus.

To collect data with the wand, a long time exposure photograph (up to 30 seconds) is taken with a digital camera as the wand is in motion through the flux surface. The wand motion is controlled by a stepper motor. An example of a flux surface image collected with the wand is shown in Fig. 4.6. We see from the figure that the wand

method works well to visualize the entire surface including magnetic island surfaces as discussed in Ch. 7 but reveals only limited rotational transform information about the flux surface.

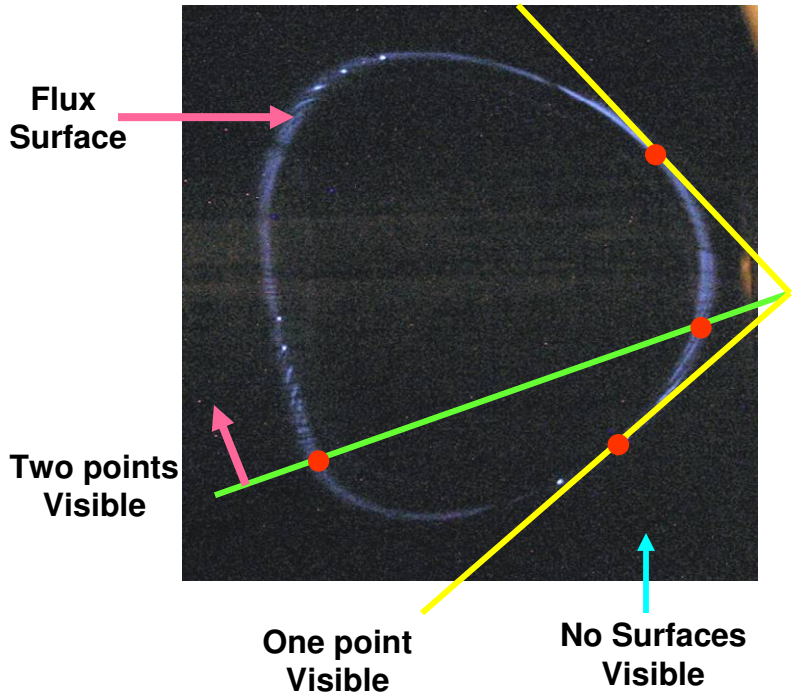

Fig. 4.6 Example wand flux surface
Photograph of the flux surface obtained by the wand method (blue D shape). The wand passes through different regions as it is rotated upward from below the surface. Before the wand reaches the surface nothing is visible. The yellow line is the wand as it intercepts the surface at one point (shown in red). The green line is the wand as it intersects the surface at two places (shown in red).

4.5 CAMERAS

A photograph of the flux surfaces visible on the screen or wand is taken with a digital camera positioned at a side port, one field period away. Several different camera models were tried, including; a Watec LCL-902K® low light sensitivity digital security video camera, a Kodak point and shoot style digital camera, a Cannon digital Rebel SLR camera®, and a Nikon D-40x digital SLR camera®.

The images gathered from the two SLR cameras were of much better quality than the other two cameras. The Cannon digital Rebel is a 6 mega pixel camera, with an ISO up to 1600, exposure times of up to 30 seconds, and aperture of 4.5. The Nikon D-40x is a 10 mega pixel camera, with an ISO up to 1600+, exposure times of up to 30 seconds, and aperture of 4.5. To further improve the aperture values, the addition of a faster lens could be added to these cameras. The capability of long exposure time photographs meant that the wand could be swept at slow enough speeds such that the image of the flux surface was easily visible during the wand studies. In dealing with color photographs produced by the SLR cameras, image processing allows the background light emitted from the electron gun to be removed while maintaining the image of the green/blue florescence of the zinc-oxide. Lastly the high pixel count resulted in excellent resolution in the photographs (of order ~0.5mm). By comparison, the screen mesh size is 2x3 mm and the width of the electron beam is typically ~5mm. The data presented in Chs. 6 and 7 was collected with either the Digital Rebel or Nikon D-40x cameras.

4.6 Creating a Calibration Template File

After the photographs of the various flux surfaces were taken, the positions the florescent dots in the photograph, including the magnetic axis position, were extracted using LabView Vision® software. The first step in this process is the creation of a calibration template file which converts a point in the photograph's pixel space, (x,y), to a point in the cylindrical coordinates of the laboratory, e.g., (r,φ,z). The positions of the LEDs embedded in the screen frame pieces are known in cylindrical coordinates, (r,φ,z) by measurements made during the installation of the screen or wand. The pixel locations

of the LEDs, (x,y) are obtained in a calibration photograph of the LEDs. These pixel space points (x,y) and real space points (r,z) are used as input to a LabView image transformation routine which creates a calibration template file.

The calibration template can then be used by a second LabView routine that converts points in the photograph pixel space to points in lab's real space. To test the calibration template, the LED locations are computed by the second LabView routine and compared to the known LED positions. The calibration procedure typically exhibits errors of up to 0.5 mm, some of which results from inexact LED measurements with the CMM, lens distortions inside the photograph, and difficulty in determining the center of the 5 mm diameter LED's in the photograph. If the calibration template results in errors larger than 1mm, the calibration template is recomputed. For the calibration template file to work properly, it is crucial that the camera remain stationary during this entire process.

4.7 Magnetic Axis Position

The location of fixed points such as the magnetic axis can be readily determined both experimentally and through simulation. With the ability to calculate the axis location both ways, a comparison can be made between the experimental results and those of the simulation model. When magnetic axis data is collected, the electron gun is not placed directly at the magnetic axis but instead on surfaces very near it, usually less than 0.01 m away to prevent blockage of the beam by the gun itself (only allowing one point to be visible). With only one point is visible on the screen from the first pass of the beam, there is no way of knowing how close its location is to the true magnetic axis location. To ensure that the true magnetic axis is found, the electron gun tip is moved away from the

axis slightly so that a complete surface surrounding the magnetic axis is visible, as shown in Fig. 4.7(a). The typical size of surfaces used to compute the axis location are between 0.005 - 0.02 m wide and 0.01 - 0.04 m high.

By the application of the calibration template file, the position of the magnetic axis in the photograph can be determined in the laboratory coordinates by one of three ways, depending on the quality of the data in photograph. In Fig. 4.7(b,c,d) the different methods used to calculate the magnetic axis are demonstrated using the same magnetic axis photograph.

Method 1 is illustrated in Fig. 4.7(b). The magnetic axis position (green point) is computed to be the average position of all the discrete visible points of the flux surface (red points). This method works well if the points are evenly distributed and clearly separated. In this example, the axis may be calculated to be higher than the true value, due to uneven vertical distribution of the points.

Method 2 is shown in Fig. 4.7(c). The magnetic axis position (green point) is computed to be the geometric center (center of mass) of the entire area enclosed by the flux surface points. This method utilizes the ability of the LabView Vision software to distinguish the bright and dark pixels of an image in relation to a threshold brightness value; forming a distinct boundary between the bright flux surface and the dark background. This method works well if the points are evenly distributed but not clearly separated.

Method 3 is shown in Fig. 4.7(d). The magnetic axis position (green point) is computed to be the radial average of the left and right edges of the flux surface (yellow points) and a vertical average of the top to bottom edges of the flux surface (red points).

This method works well if the points are not evenly distributed but the boundaries of the surface can be visually determined. This method requires the points of interest to be hand-picked.

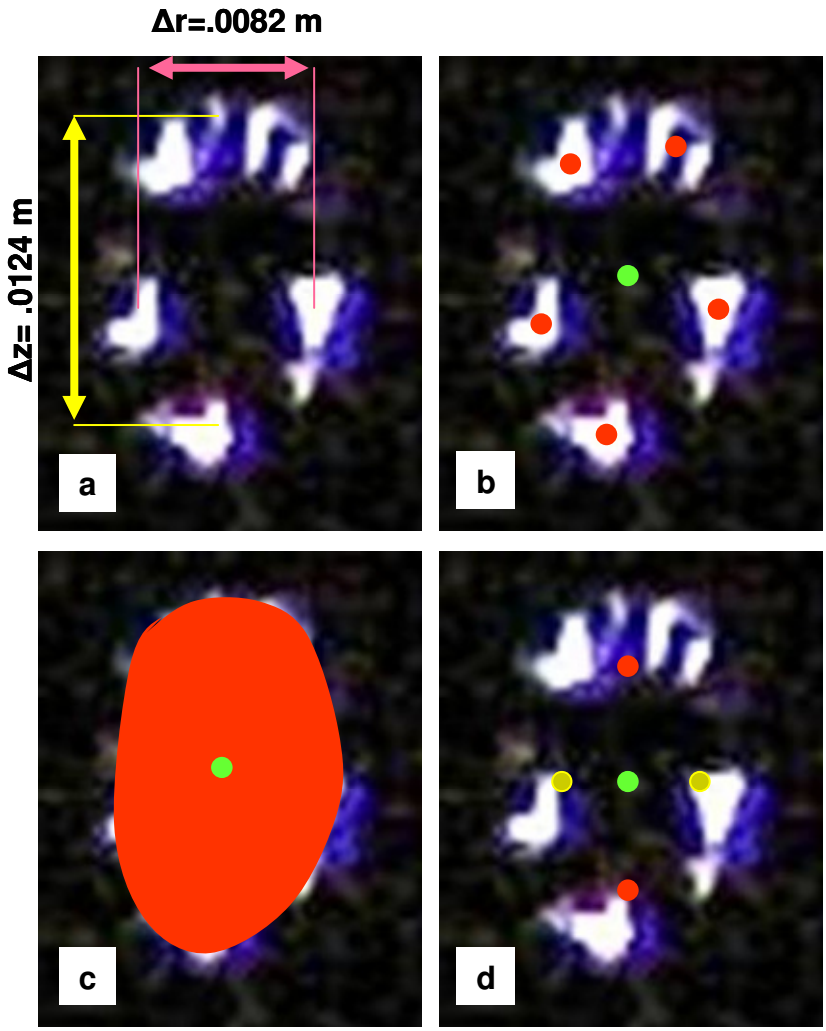

Fig. 4.7 Measurement methods of the magnetic axis position

The method used to calculate the magnetic axis position depends on the quality of the photo but the computed results of all three methods differ less than the error bar assigned to the size of the surface. Therefore the results of all three methods are considered to be of equal validity.

Because the measurement method of the magnetic axis involves measuring the center of a flux surface surrounding the magnetic axis and not the actual magnetic axis itself, the error bars associated with the magnetic axis position are a function of the size of the surrounding surface. The magnetic axis is inside this surface but not necessarily at the center. The error bars associated with the measured flux surface size are taken to be,

$$\sigma_{size} = 1/2(\Delta r, \Delta z), \tag{4.1}$$

where Δr corresponds to the radial width of the surface and Δz corresponds to the vertical height of the surface. For the example in Fig. 4.7(a), the error bars associated with the measured flux surface size are σ_{size} = (4.1,6.2) mm, half the surface size.

In addition, during field mapping experiments, multiple photographs are taken of the magnetic axis at each coil current setting. Each photograph is used to compute a magnetic axis position with a corresponding σ_{size} error bar. An example of this is shown in Fig. 4.8, with the individual data points and corresponding error bars also shown in green. The recorded magnetic axis position for each set of coil currents is the average of all the individual data points shown in Fig. 4.8 by the red point. The variation in the locations of the measured magnetic axis positions generates a 2nd error bar, σ_{spread}. The spread error bars are calculated as

$$\sigma_{spread} = ½ (\Delta r_{sp}, \Delta z_{sp}), \tag{4.2}$$

where Δr_{sp} is the radial spread in the data and Δz_{sp} is the vertical spread in the data.

Reasonable error bars for the final average magnetic axis position for each set of coils currents are taken to be

$$\sigma_{final} = ½ (\text{Minimum}(\sigma_{size}) + \sigma_{spread}), \tag{4.3}$$

which is the average of the error bar associated with the smallest individual flux surface, Minimum(σ_{size}), and the error bar associated with the spread in all the magnetic axis measurements, σ_{spread}. By its definition, small error bars for σ_{final}, can only be realized by having a small surface in amongst a tightly grouped collection of surfaces, such that both Minimum(σ_{size}), and σ_{spread}, are small. The error bar σ_{final} is shown in Fig. 4.8 by the black error bars encompassing all the individual data points. Typical values of σ_{final} range from 1-5 mm.

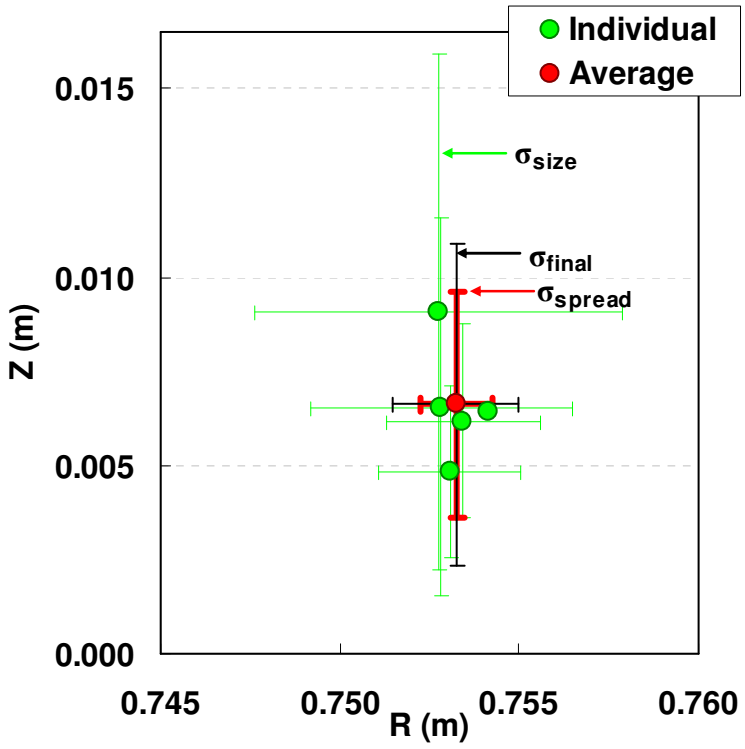

Fig. 4.8 Example of the magnetic axis error bars

4.8 Accounting For Drift

As mentioned in Ch.1, Eq. 1.7, the curvature and gradient of the magnetic field in toroidal magnetic confinement devices gives rise to drifts of charged particles across magnetic field lines. These drifts are present during field mapping experiments and must

be accounted for when comparing the experimental surfaces to those found computationally. The magnetic axis determined through field mapping experiments will be referred to as the "drift axis" whereas the actual magnetic axis will be referred to as the "field axis".

The optimization subroutine that will be used to analyze the data discussed in Sec. 5.2 is only capable of calculating the field axis. It cannot find the drift axis of a charged particle traveling along a magnetic field line. Therefore a separate simulation subroutine capable of calculating the magnetic axis position both with and without particle drifts is used to compare the drift axis acquired through field mapping to the field axis used in the optimization subroutine. The drift simulation code, is a particle following code, which computes the path of the guiding center of charged particles interacting with a magnetic field according to Eq. 1.7. The code takes into consideration the parallel and perpendicular velocities of the particles.

Shown in Fig 4.9 is an example of the field and drift magnetic axis locations computed by the subroutine. The field and drift magnetic axes are computed for coil currents of I_{HF} = 300 A and I_{TVF} = 36 A for several TF currents. The electrons are assumed to have energies of 100eV with equal parallel and perpendicular velocity components ($v_{\|} = v_{\perp}$). The computed field magnetic axis positions are shown as the black points. The computed drift magnetic axis positions are shown as the red points. The radial difference between the drift and field axes locations is 3-4 mm depending on the TF current. When field mapping experiments are performed under similar conditions, an appropriate correction factor (3-4 mm) is applied to the radial location of the drift magnetic axis, giving an estimate for the field magnetic axis. The difference between the

vertical locations of the drift and field axes is less than 0.1 mm. This is significantly smaller than the magnetic axis vertical error bars and thus the vertical drift is not corrected for. The field mapping data presented in Ch.6 has undergone similar drift correction calculation as the one shown in Fig 4.9.

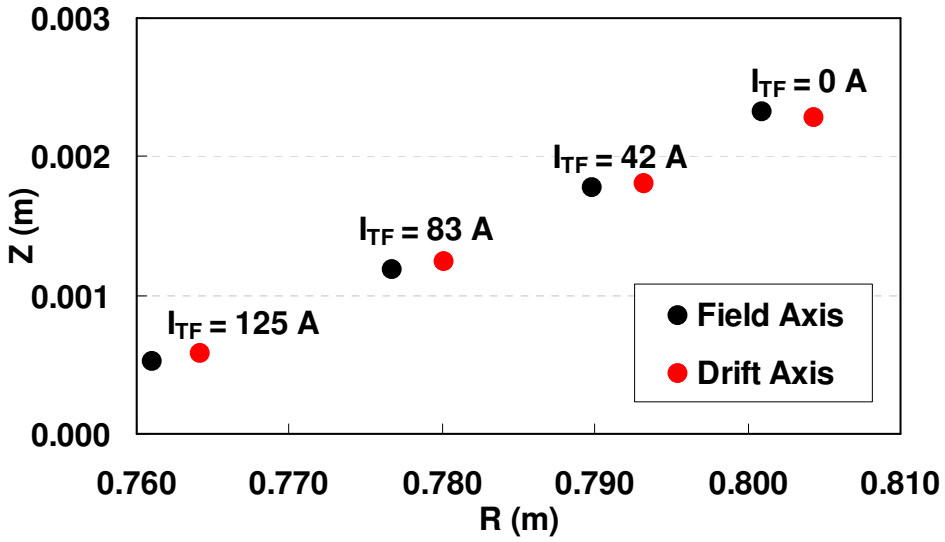

Fig 4.9 Comparison of field and drift magnetic axes

4.9 Rotational Transform of the Magnetic Axis

To experimentally determine the rotational transform of the magnetic axis, the rotational transform and area of several larger flux surfaces that enclose the magnetic axis are measured. A linear relationship between the rotational transform and area of a flux surface exists as shown in Fig. 3.6(b). By determining the linear relationship, one can extrapolate the fit to an area of zero, yielding the rotational transform of the magnetic axis. The following discussion will first address how to determine the rotational transform of a flux surface followed by an explanation of how the area enclosed by a flux surface is calculated.

The rotational transform of a rational flux surface is the ratio of the average number of poloidal circuits n, to the number of toroidal circuits m, a field line makes, $\iota = n/m$. Electrons traveling on field lines contained on a rational flux surface undergo an integer number of toroidal and poloidal transits before returning to the same poloidal location. The rotational transform of rational surfaces is determined from photographs taken of the screen.

The integer number of toroidal transits made by the electron beam contained on a rational surface is determined by counting the number of points visible on the screen. To determine the integer number of poloidal transits the brightness intensity pattern of the visible points on the screen is observed. Points successively getting dimmer with increasing poloidal angle are typical of an n=1 surface. Points alternating in intensity (bright, dim, bright, dim…) with increasing poloidal angle are typical of an n=2 surface. Points with an intensity pattern of (bright, dim, dimmer, bright, dim, dimmer…) are typical of an n=3 surface etc.

For example, a rational surface with a rotational transform of $\iota = 3/14$ is shown in Fig. 4.10. The numbers next to each point indicate which toroidal transit that point corresponds to. Counting the number of points, we get, m=14. The brightness intensity pattern of the points (bright, dim, dimmer, bright, dim, dimmer…), is indicative of a poloidal number n =3. Therefore the beam has gone around 14 times toroidally and 3 times poloidally such that the rotational transform is $\iota = 3/14$.

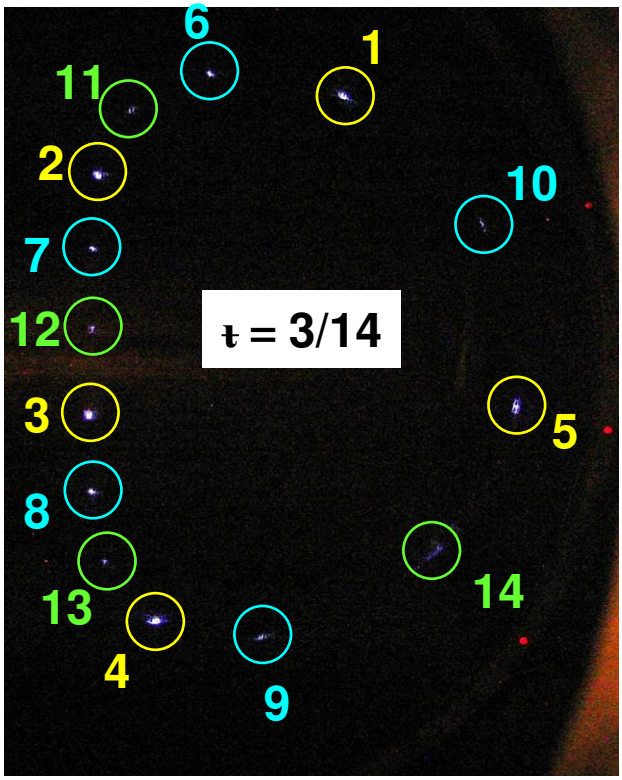

Fig. 4.10 Determining the rotational transform
The yellow circled points are the brightest points and represent the first 5 toroidal transits. The blue circled points are next 5 toroidal transits. The barely visible green circled points are the last 4 toroidal transits.

Once the rotational transform of one surface is unequivocally found, the rotational transform of nearby surfaces can easily be determined. For example, shown in Fig. 4.11 is a set of nested rational surfaces produced by a particular set of currents. The rotational transforms of all these surfaces should all have similar values. Using the $\iota = 3/14 = 0.214$ surface of Fig. 4.10 as a reference, a larger surface having 9 points must have a transform of $\iota = 2/9 = 0.222$. This surface cannot have a transform of $\iota = 1/9 = 0.111$, because this differs drastically from $\iota = 0.214$ of the neighboring surface. A smaller surface with 5 points is the $\iota = 1/5 = 0.200$ surface. The 16-point surface inside that is the $\iota = 3/16 = 0.188$ surface, and the 11-point surface inside that is the $\iota = 2/11 = 0.182$ surface. Notice that the rotational transform is decreasing as the size of the surface decreases.

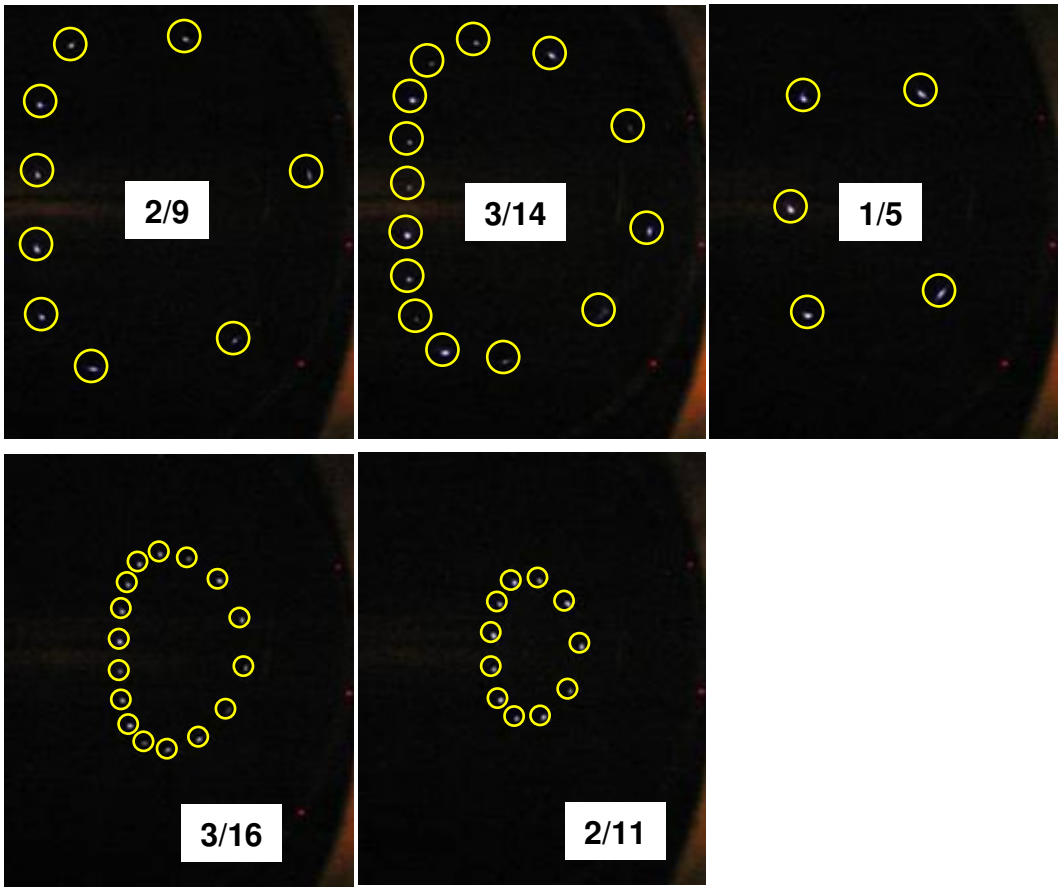

Fig. 4.11 Determining additional rotational transforms

The area enclosed within the flux surface at the toroidal location of the screen is approximated to be the area enclosed by an m-sided polygon; where m is the number of toroidal transits made by the electron beam and each of the vertices of the polygon is a measured point visible on the screen. This is illustrated in Fig. 4.12 with two different flux surfaces with different n values. The areas of the two surfaces are calculated to be the areas inside the yellow polygons. The gray shaded area was drawn in by hand and represents another approximation of the area of the flux surface if the entire flux surface were visible. The polygon describing the flux surface with rotational transform of $\iota = 1/5$ excludes large portions of the true area, whereas the polygon describing the $\iota = 3/14$ flux surface includes most of the true area. The polygon method although an approximation,

gives efficient estimates of the area, accurate enough for the purpose of this study. It should be mentioned that efforts to fit the points of the flux surface to a smooth spline fit curve were unsuccessful and inefficient.

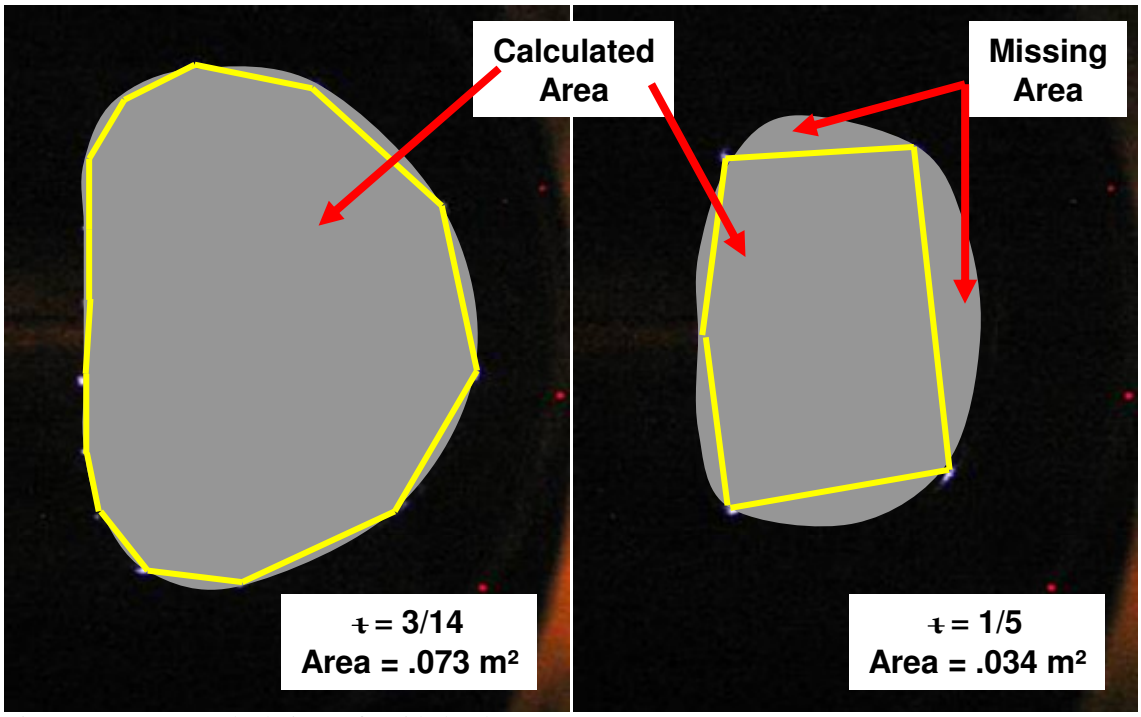

Fig. 4.12 Area calculations of n-sided polygons
n-sided polygons used to describe the $\iota = 3/14$ and $\iota = 1/5$ flux surfaces shown in Fig. 4.11.

The rotational transform of the magnetic axis is calculated using information gathered from the rotational transform and area of the larger surfaces. In Fig. 4.13 the rotational transform is plotted vs. the area for the various surfaces shown in Fig. 4.11. A linear relationship between the rotational transform and the area can be obtained by fitting the data to a straight line. In Fig. 4.13, there is good agreement between the fitted line and the data everywhere except for the 5-sided $\iota = 0.2$ surface. The calculated area of this surface is excluding large portions of the true area, and therefore its calculated polygonal area is smaller than the linear fit. Areas calculated from surfaces with fewer than ~8 sides generally exhibit this behavior and are excluded from the linear fit

whenever possible. With a relationship between the rotational transform and the area in hand, the fitted line can be extrapolated to an area of zero revealing the rotational transform of the magnetic axis, which is $\iota = 0.1738$ in this case.

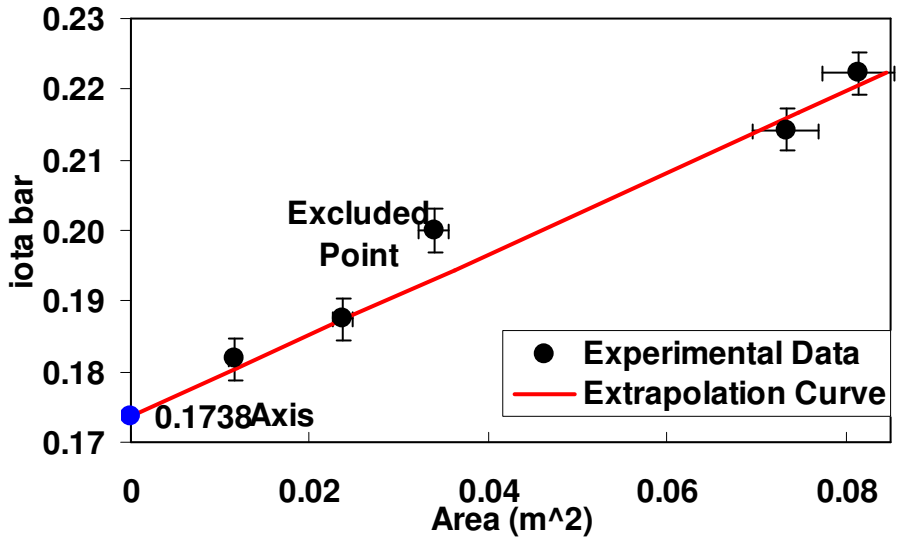

Fig. 4.13 Area vs. ι

Through the course of this chapter we have seen how field mapping is capable of determining both the position and rotational transform of the magnetic axis. In Ch.6. these experimental field mapping results will be compared to computer simulation results to quantify the discrepancies between the as-built CTH coil sets and the model coil sets used in the simulation.

CHAPTER 5: COIL OPTIMIZATION TECHNIQUES

5.1 MOTIVATION FOR AN OPTIMIZATION ROUTINE

Multiple field mapping experiments were performed with currents in the HF, OVF, and TVF coils to confirm the as-built HF coil winding law and the position of the OVF/TVF coils. The results of one such experiment are presented below in an effort to suggest to the reader the need for a sophisticated quantitative analysis method of the field mapping data (the optimization routine). Complete field mapping experimental results are presented in Ch.6.

In this example, field mapping experiments were performed with the screen located at the toroidal angle φ=252°. The HF current was maintained at I_{HF}= 300 A, while the TVF current was varied from 30 -54 A. The locations of the magnetic axis determined experimentally are shown in Fig. 5.1. As expected, the magnetic axis is shifted radially inward by 0.15 m as the TVF current is increased. The vertical position of the axis is near the midplane at low TVF currents, but rises to 0.022 m above the midplane as the TVF current is increased, indicating that something is breaking the up-down symmetry. The error bars σ_{final} on the experimental data points are computed according to Eq. 4.3.

Throughout all of Ch. 6 the experimental field mapping results will be compared to the simulated results computed using various models of the coils. Doing the same thing here, the magnetic axis positions are first computed using the design winding laws of the HF coil, (Eqs. 2.3 and 2.4) and then computed using the as-built winding laws of the HF

coil, (Eqs. 2.5 and 2.4). Like the experimental data, the radial position of the axis is shifted inward as I_{TVF} is increased in both simulations. However, the magnetic axis in both simulations is shifted radially outward 0.02 - 0.03 m from their corresponding experimental data points.

With regard to the vertical position of the magnetic axis, the absence of up-down symmetry breaking terms in the design winding law causes the axis to remain near the midplane regardless of the TVF current. This is not in agreement with the experimental results. The as-built winding law, on the other hand, includes sine(θ) terms in the radial winding law, breaking the up-down symmetry of the HF coil. As with the experimental results, the computed axis rises above the midplane as the TVF current is increased using the as-built model of the coils. Agreement between the vertical position of the experimental field mapping results and those of the as-built HF coil winding law are still poor at 0.003 - 0.006 m. Clearly both simulation models produce magnetic axis position data that does not accurately describe the results found experimentally.

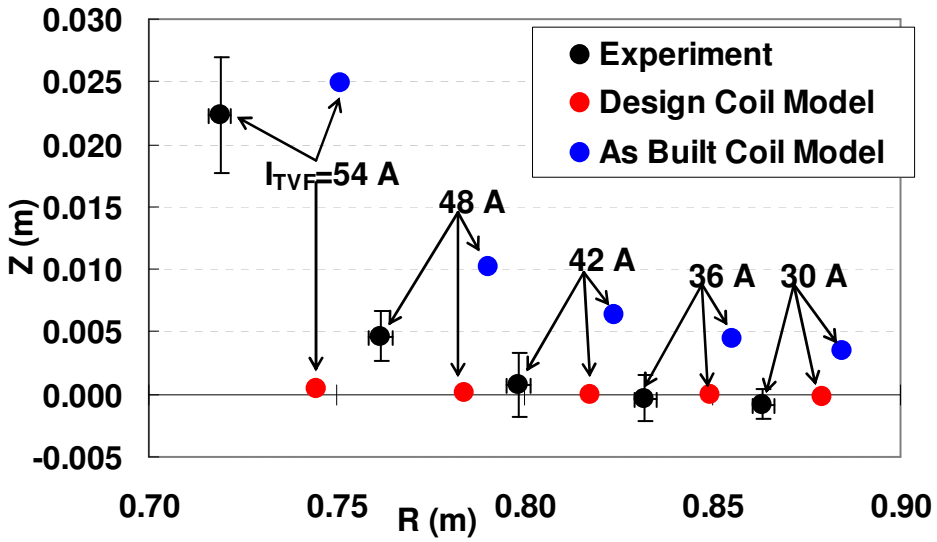

Fig. 5.1 Magnetic axis position (example)

The modifications made to the as -built radial winding law of the HF coil results in computed magnetic axis positions that are significantly different from the design coil model results. Recall from Ch. 2 the as -built radial winding law was fit from coil depth measurements with error bars of ~0.002 m, giving the coefficients of the as-built winding law a significant level of uncertainty. This prompts a few questions. Could further changes be made to the radial winding law coefficients within the 0.002 m uncertainty, to improve the agreement between the experimental field mapping results and those found through simulation? But how should one decide which parameters to change and by how much and which to keep fixed? Furthermore, if we allow terms in the radial winding law to vary by up to 2 mm, shouldn't we also allow the terms in the toroidal winding law to also vary by their uncertainty values? Or for that matter, why not allow modifications to be made to the OVF/TVF coils? On top of that, experimental evidence will be presented in Sec.5.4 that shows that the background magnetic field near the vacuum vessel is not constant, and therefore should also be allowed to vary. The problem is further complicated when information about the rotational transform of the magnetic axis is taken into account. Lastly multiple sets of data taken at various field periods over a range of field strengths make determining a set of coil parameters by trial-and-error nearly impossible.

We are now in the position to see the complexity of the problem. Given experimental field mapping data, how does one change the simulation coils such that the simulation data accurately models the experimental data while not allowing unreasonable coil modifications to be made. A new subroutine in the IFT code does exactly this!

5.2 How the Optimization Routine Works

A new optimization subroutine in IFT minimizes the differences between the experimental field mapping data and that computed through simulation. Utilizing a singular value decomposition (SVD)[34] minimization process, small modifications are made to parameters in the simulation coil model, such as the HF winding law, OVF coil positions, and the background magnetic field of the laboratory with the intention of reducing the differences between experimental field mapping data and the simulated data.

An outline of the optimization subroutine is shown in Fig. 5.2. The subroutine is initially given two types of information, signals and parameters. The signals are values which IFT is trying to match. These include the multiple radial positions, vertical positions, and rotational transforms of the experimental magnetic axis data denoted as $EXP_i=(r_i, z_i , \text{ŧ}_i)$. Each experimental signal has its own corresponding error bar, $\sigma_i = (\sigma r_i, \sigma z_i, \sigma \text{ŧ}_i)$. In addition there is a set of simulated signals computed by IFT denoted as $IFT_i = (R_i, Z_i , \text{ŧ}_i)$.

The parameters (P_j) are used to compute the simulated signals and include things such as; the coil currents, the coefficients of the HF winding law, the circular coils' sizes and positions, and the background field in the laboratory. The subroutine is allowed to vary the values of the parameters in order to better match the experimental and simulated signals. To do so, each parameter is given an initial starting value $P0_j$, a goal value the parameter is expected to remain near Pg_j, and a parameter measurement uncertainty σp_j. The parameter starting value does not necessarily need to be its goal value. The optimization subroutine is given the experimental signal and parameter values and returns modified parameter values $P1_j$, and the corresponding IFT signal values they produce

$IFT1_i$. Throughout this discussion the subscripts i and j will denote the number of signals and parameters respectively.

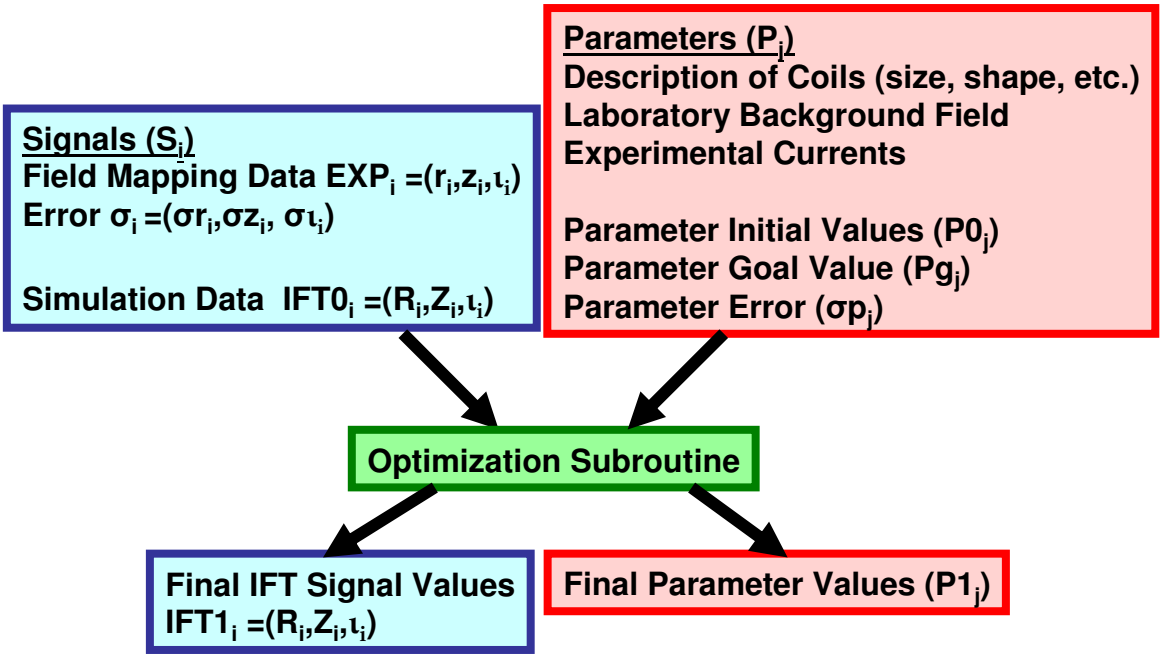

Fig. 5.2 Optimization subroutine overview

The optimization subroutine is schematically depicted in Fig 5.4. First, the experimental signal value is compared to the IFT computed signal to give a difference in signals, ΔS_k. The vector ΔS_k is composed of the differences in all signal data points (Δr_i, Δz_i, $\Delta \iota_i$), but also includes the difference in the initial parameters values to the parameter goals values ΔP_j, and is defined as,

$$\Delta S_{k=i+j} = (EXP_i - IFT_i, Pg_j - P0_j). \tag{5.1}$$

By including the parameters in with the signals, the parameters are forced to remain near their corresponding goals. These differences are then normalized using the uncertainties for each signal, (σ_i, σp_j),

$$\Delta Sn_k = \left(\frac{\Delta S_i}{\sigma_i}, \frac{\Delta S_j}{\sigma p_j}\right). \tag{5.2}$$

This is done to ensure that signals that are accurately known are weighted more heavily than the signals that are not as well specified. The normalization of the signals makes them dimensionless. Next, a normalized Jacobian matrix A_{ij}, is calculated. The Jacobian matrix quantifies the relationship of each parameter to each signal, and is defined by the equation,

$$A_{ij} = \frac{\partial S_i}{\partial P_j}. \tag{5.3}$$

As shown in Fig 5.3, the Jacobian matrix, A_{ij} maps points from the normalized parameter space, ΔPn_j to the normalized signal space. ΔSn_i such that

$$A_{ij} \cdot \Delta Pn_j = \Delta Sn_i. \tag{5.4}$$

In other words, given the Jacobian matrix and a known change in a parameter value, the corresponding change in the signal values can be determined.

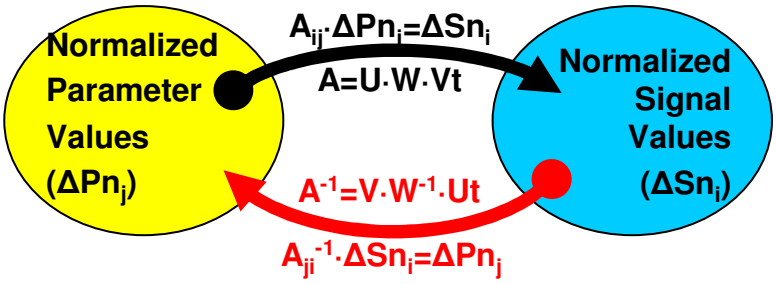

Fig 5.3 Parameter space mapped to/from signal space

The inverse problem that we are trying to solve is to determine the optimal changes in parameters to create the observed changes in the signals. In order to do this, the inverse Jacobian matrix A_{ji}^{-1}, is computed using a singular value decomposition (SVD) technique. For a detailed description of the SVD procedure see Numerical Recipes[26]. During the SVD process the Jacobian is broken up into 3 matrixes such that,

$$A_{ij} = U_{ii} \cdot W_{ij} \cdot Vt_{jj} . \tag{5.5}$$

These matrixes have the following properties; $U_t=U^{-1}$, $V_t=V^{-1}$, where the subscript t, denotes the transpose of the matrix. The singular value matrix W is diagonal. It follows that inverse Jacobian is given by

$$A_{ji}^{-1} = V_{jj} \cdot W_{ji}^{-1} \cdot Ut_{ii} . \tag{5.6}$$

The inverse Jacobian is the derivative of each parameter with respect to each signal

$$A_{ji}^{-1} = \frac{\partial P_j}{\partial S_i}, \tag{5.7}$$

and maps points from the normalized signal space to the normalized parameter space. The normalized changes to each parameter are computed from the inverse Jacobian and the normalized difference in signals such that, [35,36]

$$\Delta Pn_j = \sum_i A_{ji}^{-1} \cdot \Delta Sn_i . \tag{5.8}$$

From Eq. 5.8, the change produced in each parameter is determined by the change needed in each signal. The parameters are not strictly restricted to stay within the parameter uncertainty value of the goal value but the optimization imposes larger penalties the farther the parameter deviates from the goal value.

These changes in the normalized parameters are then unnormalized and added to the original parameter values giving the new parameter values $P1_j$, shown in the yellow box of Fig 5.4. The new magnetic axis position and rotational transform IFT1, are computed with the new parameter values, and compared to the experimental data.

As one would expect some coil parameters have large effects on the magnetic axis and others do not. Coil parameters that have very little effect on the magnetic axis are generally not included in the optimization.

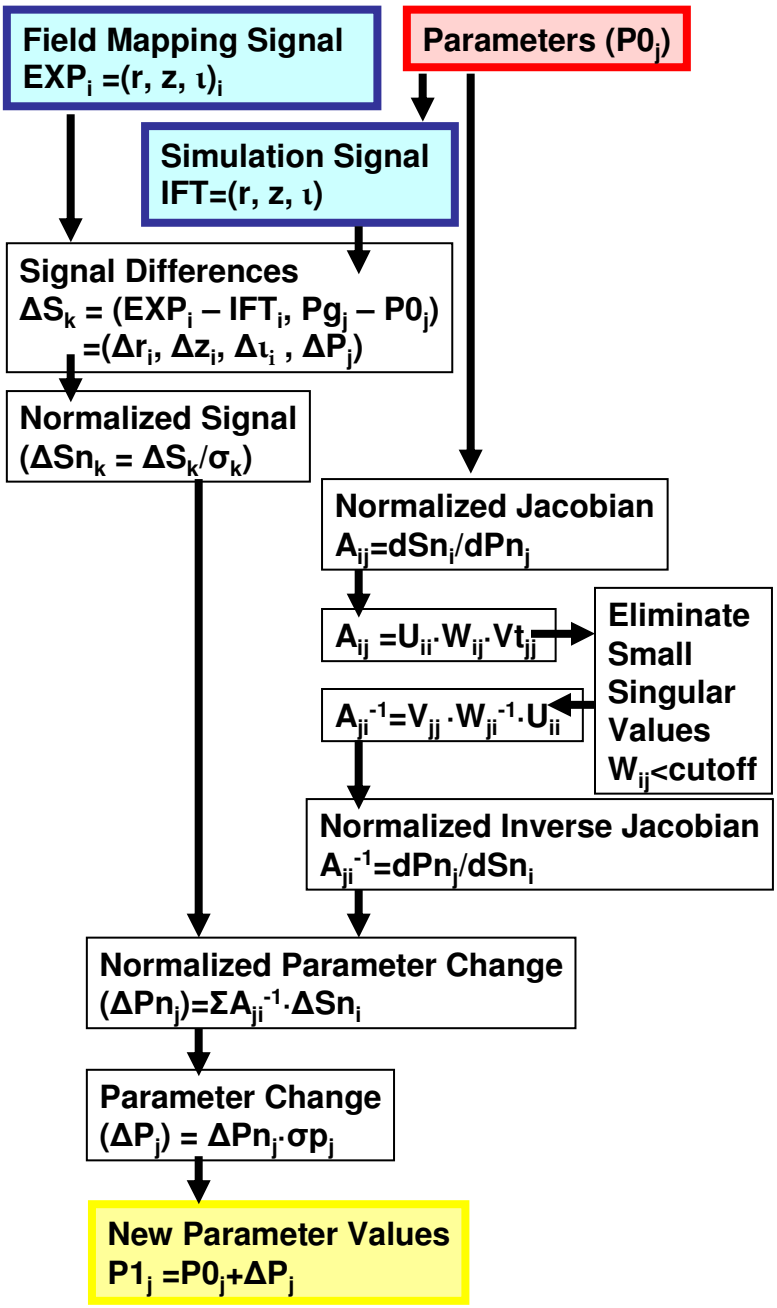

Fig 5.4 Optimization schematic

A quantitative measure of the accuracy of the fit for both the signals and parameters is χ^2, defined as,

$$\chi^2 = \sum_{i}^{\#signals} \frac{(EXP_i - IFT_i)^2}{\sigma_i^2} + \sum_{j}^{\#parameters} \frac{(Pg_j - P1_j)^2}{\sigma_j^2} \tag{5.9}$$

The χ^2 value is minimized in the optimization procedure.[37] We see that if the difference between an experimental and simulation data point is greater than the uncertainty for that data point, then $\chi^2>1$. A small χ^2 value means the simulation results match the experimental data relatively well within the given measurement uncertainty. A large χ^2 value means the simulation results do not match the experimental data within the given uncertainty. Typically if χ^2 is smaller than the number of signals the fit is considered good. For example in Fig. 5.1 there are 10 signals (5 radial positions and 5 vertical positions) one would consider the fit good if $\chi^2 < 10$.

5.3 THE MAGNETIZATION PROBLEM

In order to effectively use the optimization routine, the background field, which is influenced by the magnetization of ferromagnetic material near CTH, must be included in the calculation. In this section, the effects of magnetization will be shown to be a problem significantly influencing the flux surfaces during field mapping studies. While in the following section a discussion of how to overcome these difficulties using the optimization code will be addressed.

When ferromagnetic materials are in the presence of an external magnetic field, the atomic dipole moments of the material align themselves with the externally applied

field. In this way the material is said to become magnetized and the overall field strength within the material is increased according to Eq. 5.10. [38, 39]

$$\vec{B} = \mu_0(\vec{H} + \vec{M}) \tag{5.10}$$

Here $\vec{B}$ is the magnetic field, $\vec{H}$ is the magnetic field due to free currents and $\vec{M}$ is the magnetic dipole moment per unit volume due to the magnetization of the ferromagnetic material. In addition to this magnetization, ferromagnetic materials also retain some of their magnetization once the external field is removed. Ferromagnetic materials are said to have a remnant magnetic field which follows a magnetic hysteresis curve specific for the material type and past history. The strength of the magnetization field for both effects is dependent on the strength of the externally applied field, volume of the ferromagnetic material and permeability μ of the material. In a complicated magnetic field geometry such as CTH, the magnetization vector $\vec{M}$ produced by ferromagnetic materials is extremely difficult to calculate without accurate knowledge of the location, mass, permeability, and hysteresis curve of the ferromagnetic materials involved.

Known ferromagnetic materials which experience significant magnetic fields produced by the CTH coils include reinforced steel bars ("rebar") cast into the concrete floor and ceiling, a large iron pipe located near the ceiling above the machine, several vacuum vessel bellows ($\mu>1.2$), stepper motors ($\mu>1.2$), a vacuum vessel leak valve ($\mu>2$), and several port covers ($\mu>1.05$). Although the port covers do not have a large permeability, their large size and close proximity to the plasma may significantly influence the magnetic flux surfaces.

Unequivocal evidence that field mapping experiments on CTH were influenced by magnetization of local materials was obtained during a field mapping experiment

involving the TF coil set. During this experiment, the TF currents were first increased in 20 A increments from 0 to 140 A. The black curve in Fig 5.5 shows the position of the magnetic axis for this initial upward scan in TF currents. This was followed by a TF scan in which the TF currents were decreased in 20 A increments from 130 to 10 A. The red curve in Fig 5.5 shows the magnetic axis position of this second scan of TF currents. The paths traced out by these two curves are not the same. The non-repeatability of the axis position is explained by a changing background field caused by the magnetization of ferromagnetic materials in the vicinity of CTH. Simulations performed with IFT indicate that a 0.2 G radial field and a 4.3 G vertical field difference is needed to lower the magnetic axis by the 4 mm seen experimentally between the I_{TF} = 0 A data point and the I_{TF} = 10 A data point.

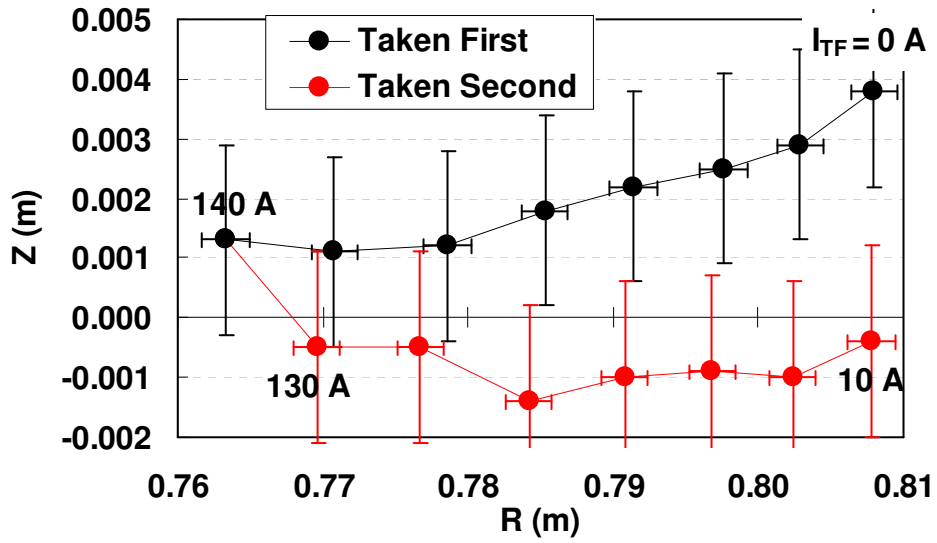

Fig 5.5 TF magnetization evidence

This finding motivated a series of tests investigating the fields created by the magnetization of ferromagnetic material around CTH. The apparent magnetization caused by energizing the HF/OVF/TVF coils was studied first. In this study the magnetic

axis was first repeatedly measured at an HF current of I_{HF} = 100 A and a TVF current of I_{TVF} = 12 A, shown in Fig. 5.6 by the black cluster of points. Then the currents in the HF and TVF coils were increased to I_{HF} = 300 A and I_{TVF} = 36 A for approximately 10 minutes. Following this the currents in the HF and TVF coils were decreased to their original values of I_{HF} = 100 A and I_{TVF} = 12 A and the magnetic axis was measured again, shown by the red cluster of points in Fig. 5.6. The two clusters are separated by a radial distance of .012 m and a vertical distance of.018 m. To move the magnetic axis by this amount IFT simulation estimates require the background field (radial and vertical) to vary by only 0.1 G and 3.3 G respectively.

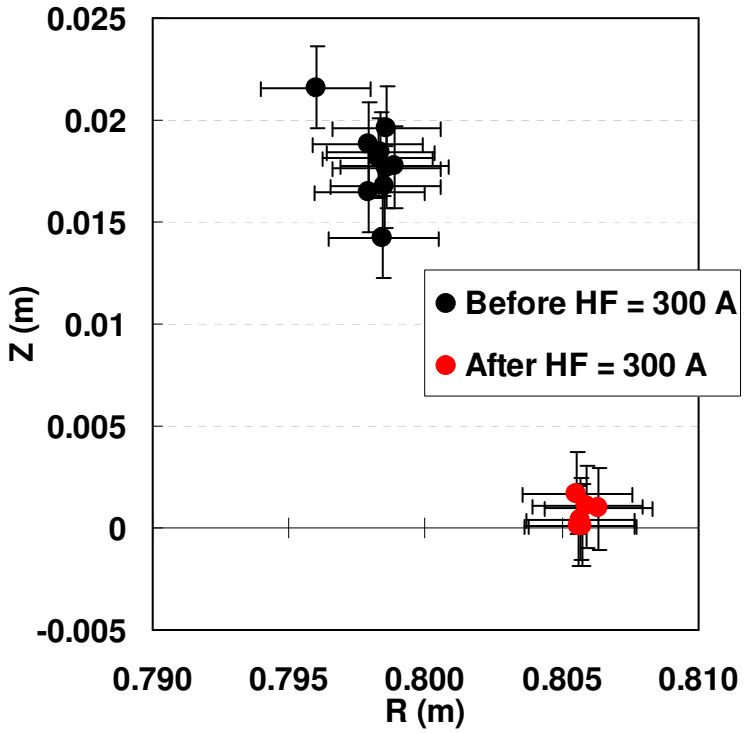

Fig. 5.6 HF magnetization test

The examples shown in Fig 5.5 and Fig. 5.6 showed how under supposedly identical conditions the position of the magnetic axis was significantly altered when the

magnetic field conditions between the measurements were changed. Simulations require small changes of less than 1 G in the radial field to produce these effects. Physical measurements of the remnant background magnetic field made with a hand held Gauss meter around the side ports, shown in Fig. 5.7 confirm that background field changes on this order are reasonable. The remnant field is significantly larger than the background field of the earth at Auburn, Al (B_{east}= 0G, B_{north}= .2 G, B_{up}= -.4 G) [40] Also, measurements made at different toroidal locations show significant differences in the background field, revealing that the background field is non-uniform in space.

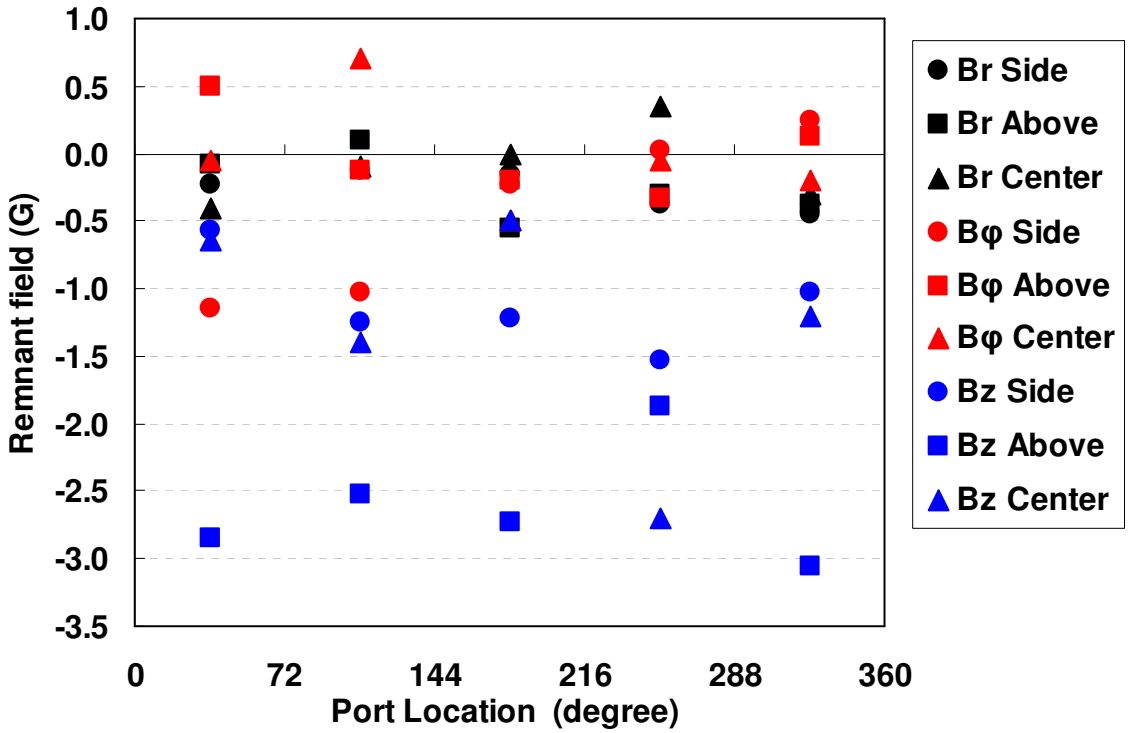

Fig. 5.7 Remnant background field measurements
Field measurements were made at five locations around the five side ports, to the left and right, above and below, and in the center of each port cover.

Whereas measuring the remnant field is relatively straightforward, measuring the relatively small modifications in the magnetic field due to magnetization during field

mapping is more difficult. This is because the magnetic field produced by the CTH coils is much larger than the magnetization field. In fact, field mapping is a good way to measure magnetic field errors produced by magnetization because of its sensitivity to relatively small fields. However, unambiguously distinguishing small discrepancies in the coil architecture through field mapping (a main goal of this study) becomes increasingly difficult.

In any case, the magnetization problem, being so pronounced in field mapping studies, needs to be addressed in the context of the optimization code. Special steps were taken while using the optimization code in order to obtain information about the CTH coils. These steps are the topic of discussion in the next section.

5.4 Overcoming the Magnetization Problem

In the initial discussion of the optimization routine, parameters were things that the optimization routine was allowed to modify to better simulate the experimental results. With the realization that magnetization plays a role in the field mapping results, a further distinction is made between three different types of parameters:

1. parameters that are known (The optimization is not allowed to vary parameters of this type.)
2. parameters that are unknown (yet nearly constant) over the course of all experiments
3. parameters that are unknown but assumed to be changing over the course of the experiment.

For example suppose one wanted to use the experimental results in Fig. 5.1 to determine the HF coil parameters. Type 1 parameters would include things such as the number of turns (assuming there is not an electrical short circuit). Type 2 parameters would include things such as the HF coil winding law coefficients defined by Eq. 2.1 and Eq.2.2 and the OVF/TVF coils radius and position. Type 3 parameters would include things such as the changing background field and the currents applied to the coils.

With evidence that magnetization problems were significantly influencing the position of the magnetic axis, a two step iterative technique was developed for using the optimization routine shown schematically in Fig 5.8. The first step modifies the type 3 parameters. The second step modifies the type 2 parameters.

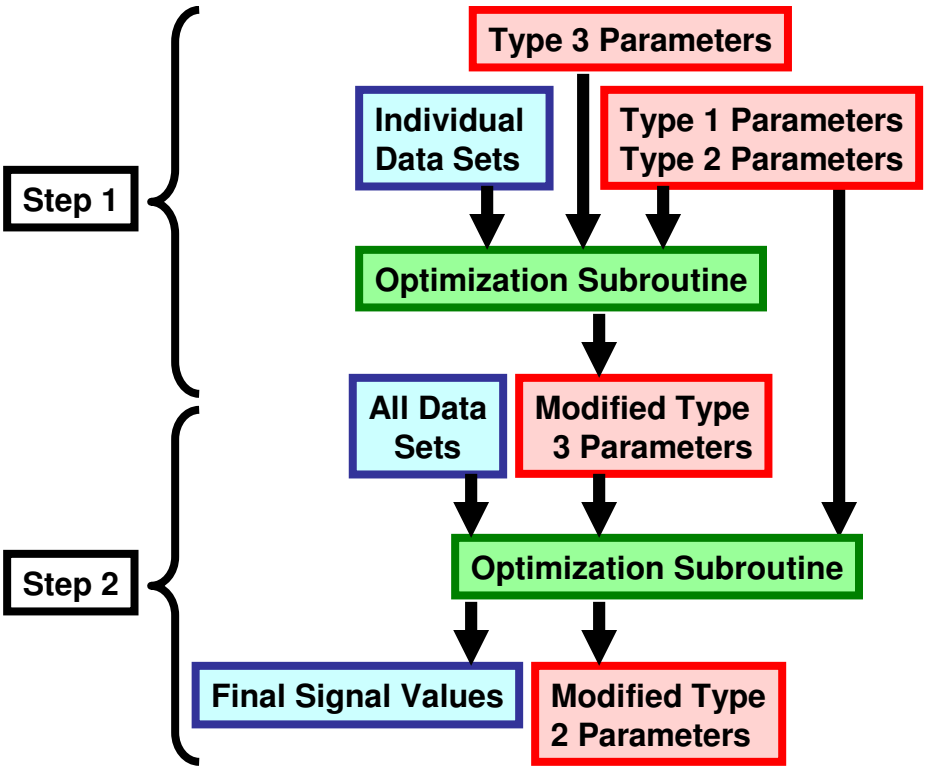

Fig 5.8 Optimization steps to account for magnetization

The two step process is illustrated in the following example. Suppose one wanted to use the results of multiple field mapping experiments (multiple data sets) to determine the HF coil parameters and corresponding background field values. This is essentially what we will be doing in Sec. 6.1.

Step 1 Initially, the optimization routine is given the experimental field mapping results for the individual data sets along with the measured values of the HF coil parameters and an estimated background field. With this information the optimization routine is used to calculate the background field values for the each data set. During this step the HF coil parameter values are not varied by the optimization routine.

Step 2 The optimization routine is then given the experimental field mapping results for all data sets and the background field values just determined. With this information the optimization routine is allowed to vary the HF coil parameter values taking into consideration all the data points. During this step the background field values are not varied by the optimization routine.

To ensure that the initial background field calculations of step 1 do not overcompensating for deficiencies in the initial guess of the type 2 coil parameters, the data sets are again given to the optimization separately and the background field is recalculated now with the modified coil parameters. This is followed by another recalculation of the coil parameters given the latest values of the background field.

Thus we see that in this two step iterative process, first the background field values needed for each data set were calculated then the coil parameter values were

calculated using all the data. After several iterations, the coil parameter values and background field parameters make negligible changes resulting in a set of parameter values and background fields that best fit the data and minimize χ^2. The data sets found in Ch.6 were all analyzed using this iterative method of the optimization routine.

CHAPTER 6: FIELD MAPPING RESULTS

In this chapter, field mapping results are used to develop an accurate model of the CTH coil sets. The experimental results of 4 field mapping experiments are presented. The first and most important is the study of the fields produced by the HF, OVF, and TVF coils. This is followed by subsequent field mapping studies performed with additional SVF, TF, and OH coils sets. The experimental results of each study are first compared with the simulation results of the IFT code using a coil model based on mechanical measurements made of the coils. Then utilizing the optimization process discussed in Ch.5 small changes are made to the coil model parameters and background fields followed by a recalculation of the magnetic axis.

Several assumptions about the background field should be mentioned. The background field is assumed to be a uniform horizontal and vertical field across the volume of the vacuum vessel, constant for data taken on the same day, but changing from day to day. The background field is assumed to be given in terms of the horizontal and vertical directions, Bx (east), By (north), and Bz (up). The validity of these assumptions will be discussed following the results. Lastly, it should also be mentioned that data collected on the same day is often referred to as a data set.

6.1 Field Mapping with the HF, OVF, TVF Coils

In its simplest configuration, CTH requires currents only in the HF, OVF, and TVF coils to produce closed magnetic flux surfaces. Therefore to limit the number of free parameters, field mapping experiments were first performed with currents in just the HF, OVF, and TVF coil sets. The HF coil, being helical, has the most complex geometry of all coils on CTH, hence it was thought that errors in this coil's geometry would be the most likely to occur. The HF coil is also the coil closest to the plasma, and thus has the greatest effect on the observed magnetic configuration.

The first of these experiments was performed upon the completion of the HF coil and after the OVF/TVF coil packs were mounted for three purposes:

1. To prove CTH produces closed flux surfaces,
2. To test the HF/OVF/TVF coils for any pronounced errors,
3. To test the field mapping experimental setup.

The results of this preliminary study are shown in Fig. 6.1. The experimental magnetic axis was found to be shifted above the midplane by 0.1 m. Whereas the magnetic axis position computed through simulation using the design model of the coils (16 turns in each of the OVF coils) is located on the midplane. The large radial field required to produce the vertical shift in the axis was believed to be produced by a short circuit in one of the coil sets. For example, an unbalanced OVF coil set would produce a radial field shifting the axis vertically, similar to the results seen experimentally. A computational study showed that when the number of turns in the upper OVF coil was reduced to 9 the simulation results mimic the experimental results, as shown in Fig. 6.1.

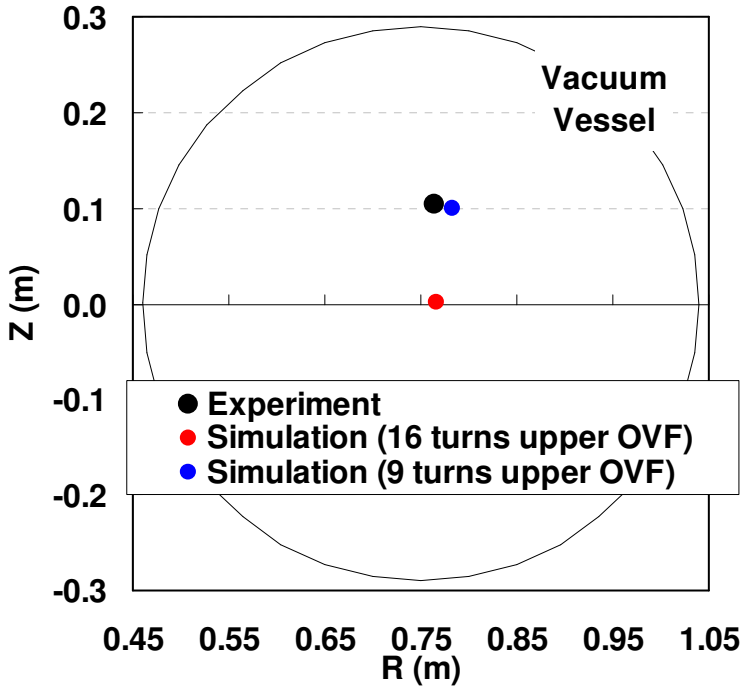

Fig. 6.1 Magnetic axis position with OVF short
I_{HF} = 500 A, I_{TVF} = 70 A

Electrical resistance tests comparing the upper and lower OVF coils suggested about 1/2 the turns in the upper OVF coil were not carrying current. Fortunately, the short circuit was located near the edge of the coil pack and could be visually identified and repaired. In this initial study the error within the coil and its corresponding effect on the flux surfaces were major, illustrating one reason why field mapping is important.

After the short in the OVF coil was fixed further field mapping experiments were conducted again with currents in the HF/OVF/TVF coils. Five sets of data were taken each with a constant HF current of I_{HF}=300 A. In each data set the TVF current was varied from 9% to 16% of the HF current. During the course of these experiments the number of turns in the TVF coil was reduced from 108 turns to 90 turns by electrically removing two layers (18 Turns) from both the upper and lower TVF coils. The reason for

the different TVF coil configurations is discussed in Appendix-A. Due to the decreased number of turns in the 90 Turn configuration, I_{TVF} during these tests is slightly larger than during the 108 Turn configuration. In all field mapping experiments the currents were measured to within ±0.1 A. The magnetic axis position (R, Z), and rotational transform ŧ, were measured at two toroidal locations, φ=36° and φ=252°. Ideally differences between data sets taken at different toroidal locations should reveal information about field period symmetry breaking errors, such as a tilted poloidal field coil. Unfortunately the changing background field due to magnetization makes determining symmetry breaking errors within the coil sets more difficult. The experimental parameters and type of data collected are shown for the various data sets in Table 6.1.

Data Set	Wand/ Screen	Location φ	I_{HF} (A)	I_{TVF} (A)	TVF Turns	Information Gathered
HF-A	Wand	36º	300	28-42	108	R, Z
HF-B	Screen	36º	300	28-42	108	R, Z, ŧ
HF-C	Screen	252º	300	28-40	108	R, Z, ŧ
HF-D	Screen	252º	300	30-56	90	R, Z, ŧ
HF-E	Wand	36º	300	30-54	90	R, Z

Table 6.1 HF/OVF/TVF field mapping setup

The data was analyzed according to the procedure outlined in Ch. 4. The measured magnetic axis positions are shown in relation to the vacuum vessel in Fig. 6.2(a). In Fig. 6.2(b) the same magnetic axis positions are shown in greater detail revealing the vertical behavior of the axis. As expected, the magnetic axis moves radially inward as the TVF current is increased. The vertical position of the axis is near the midplane at low TVF currents, but unexpectedly rises above the midplane as the TVF current is increased. This vertical rise of the axis indicates that the up-down symmetry of the magnetic field is being broken at large TVF currents.

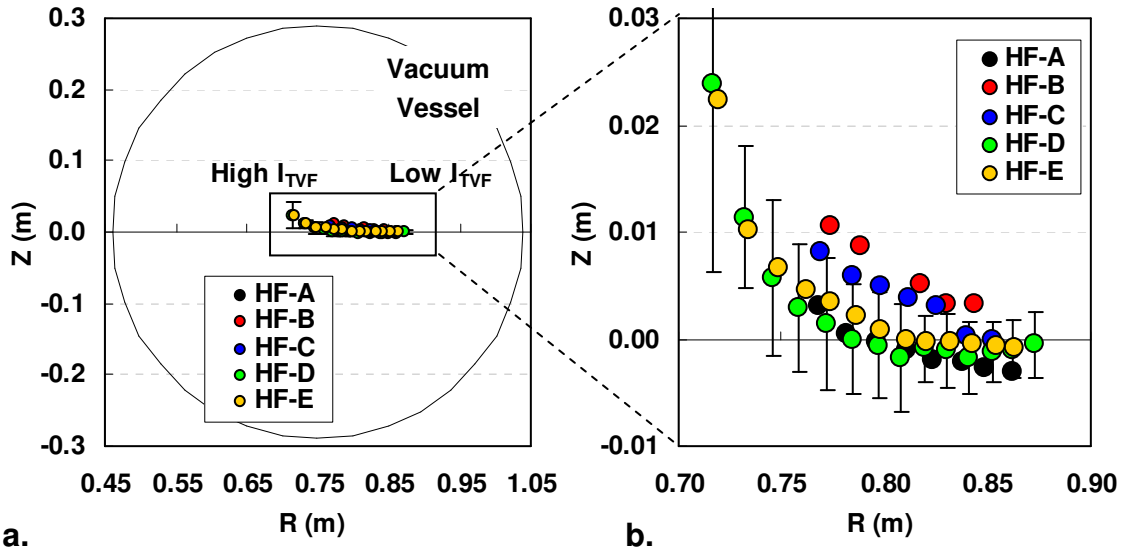

Fig. 6.2 Magnetic axis position (HF/OVF/TVF study)

The radial position of the magnetic axis vs. the ratio I_{TVF}/I_{HF} is shown in Fig. 6.3(a). Here both the TVF and HF currents are expressed in A-Turns to account for the different TVF coil configurations used. A spread in radial position of 0.02 m can be seen between the different data sets. The error bars on the radial position are typically 1-3 mm, too small to be visible within the plot.

In a similar plot, the vertical position of the magnetic axis vs. the ratio I_{TVF}/I_{HF} is shown in Fig. 6.3(b). Ideally, without symmetry breaking errors, the magnetic axis should remain near the midplane regardless of I_{TVF}. This is shown not to be the case. The spread in the vertical position of the magnetic axis is observed to be up to 0.02 m between the different data sets. The error bars on the vertical position have been omitted on all but one data set, but are of similar magnitude for the others.

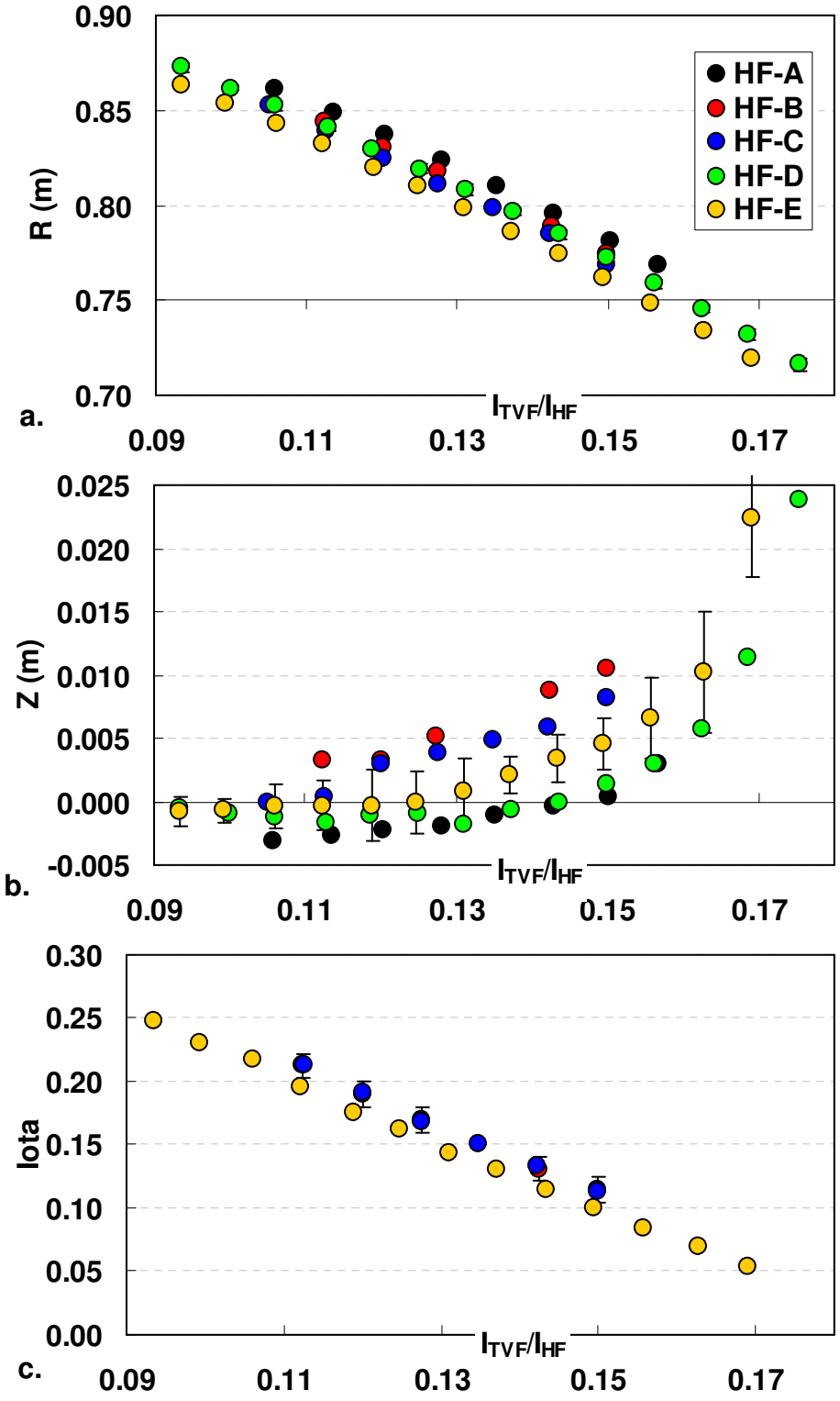

Fig. 6.3 Field mapping results (HF/OVF/TVF study)
Magnetic axis (a) radial position, (b) vertical position, (c) rotational transform.

Lastly the rotational transform of the magnetic axis vs. I_{TVF}/I_{HF} is shown in Fig. 6.3(c). As expected, the rotational transform decreases with increasing TVF current. Differences in rotational transform of up to 0.02 are observed between the different data sets. Rotational transform information was not collected for data set HF-A or D because of the wand data collection method. The error bars on the rotational transform are too small to be visible, typically 0.005.

In addition to checking for closed flux surfaces, a primary goal of field mapping is to modify the design model of the CTH coils so that the field line following code IFT, better simulates the experimental results of field mapping. The first modification to the design model was to use information from measurements made during construction and assembly process. The coil model prior to using the coil optimization routine is referred to as $IFT_{HF\text{-}pre}$. This coil model includes the "as built" winding law of the HF coil's minor radius discussed in Ch. 2. The measured HF coil pack was found to have a smaller radius than the design value. The "as built" winding law is also not up-down symmetric having non-zero sine(θ) coefficients within the radial winding law. The coil model $IFT_{HF\text{-}pre}$ also includes the measured positions of the OVF coils. Because the TVF and OVF coils are part of the same coil pack and physically locked together, the TVF coils are defined relative to the OVF coil within the coil model. This way changes made to an OVF coil are also made to the TVF coils within the same coil pack. Also included in the coil model is the expected ambient magnetic field of Auburn, Alabama, found from the National Geophysical Data Center[31] website. Table 6.2 gives the coil parameter design values and measured values, the background magnetic field, and uncertainty estimates for each parameter used in the coil optimization routine.

Parameter	Description	Design Values	Measured Values ($IFT_{HF\text{-}pre}$)	Uncertainty σ
a_{r0} (m)	Cos(0θ)	0.385	0.3836	0.002
a_{r1} (m)	Cos(1θ)	0	0.0000	0.002
a_{r2} (m)	Cos(2θ)	0	0.0005	0.002
a_{r3} (m)	Cos(3θ)	0	0.0001	0.002
b_{r1} (m)	Sin(1θ)	0	-0.0007	0.002
b_{r2} (m)	Sin(2θ)	0	0.0002	0.002
b_{r3} (m)	Sin(3θ)	0	-0.0001	0.002
a_{f0} (radians)	Cos(0θ)	0	0.0000	0.002
a_{f1} (radians)	Cos(1θ)	0	0.0000	0.002
a_{f2} (radians)	Cos(2θ)	0	0.0000	0.002
a_{f3} (radians)	Cos(3θ)	0	0.0000	0.002
b_{f1} (radians)	Sin(1θ)	-0.252	-0.2520	0.002
b_{f2} (radians)	Sin(2θ)	0.052	0.0520	0.002
b_{f3} (radians)	Sin(3θ)	-0.024	-0.0240	0.002
OVF-U-Rad (m)	OVF Upper radius	1.266	1.2660	0.001
OVF-L-Rad (m)	OVF Lower radius	1.266	1.2660	0.001
OVF-U-Z (m)	OVF Upper height	0.523	0.5230	0.001
OVF-L-Z (m)	OVF Lower height	-0.523	-0.5230	0.001
Bx (G)	East	-0.01		1.0
By (G)	North	0.23		1.0
Bz (G)	Up	-0.44		1.0

Table 6.2 Coil parameters for the coil model $IFT_{HF\text{-}pre}$

The uncertainty estimates of the four cosine(θ) terms in the radial winding law were calculated to be 1/3 the 0.006 m spread in the measured coil depth data of Fig. 2.7 at the θ = 180° location. Similar uncertainties were assumed for the sine(θ) terms of the radial winding law. The uncertainty estimates used for the toroidal winding law terms were calculated by estimating a ±0.0015 m error in the coils toroidal winding law. Converting this error to radians at the major radius of the HF coil produces an error of approximately 0.002 radians. The estimated uncertainty in the circular coil measurements is assumed to be 0.001 m based on measurement error. Although the magnetization results shown in Ch. 5 reveal that the background field significantly changes, at the time of this analysis the background field was expected to remain within 1 G of the earth's

magnetic field in Auburn, Al. The consequences of this assumption will be discussed later.

Using the coil model $IFT_{HF\text{-}pre}$, the position and rotational transform of the simulation magnetic axis is computed and compared to the experimental data. The differences between the experimental results and the simulation results (Experiment – Simulation) vs. the I_{TVF}/I_{HF} current ratio are shown in Fig. 6.4(a,b,c). For simplicity, error bars have been included on only one data set for each case with error bars on the other data sets having similar magnitudes. Ideally, if the existing simulation coil model was accurate, the differences between the experimental data and the simulation data would be evenly scattered near zero in the difference plot. Clearly the simulation coil model $IFT_{HF\text{-}pre}$ does not accurately model the experimental data.

The χ^2 values associated with the differences in radial, vertical, and rotational transform values computed from the coil model $IFT_{HF\text{-}pre}$ are listed in Table 6.3. Remember that χ^2 is a measure of the accuracy of the fit between the experimental results and the simulation results. If χ^2 is less than the number of signals (the number of data points) the fit is considered good. In this case χ^2 is well above the number of signals for each of the three types of data revealing a poor fit.

	Number of signals	χ^2 ($IFT_{HF\text{-}pre}$)	χ^2 ($IFT_{HF\text{-}post}$)
R	47	8695	2
Z	47	310	29
ι	24	386	3
Coil Parameters	18	0	2
Total	118	9391	36

Table 6.3 χ^2 values of the HF coil optimization
Note: the total number of signals does not include the 18 coil parameters whereas the total χ^2 does.

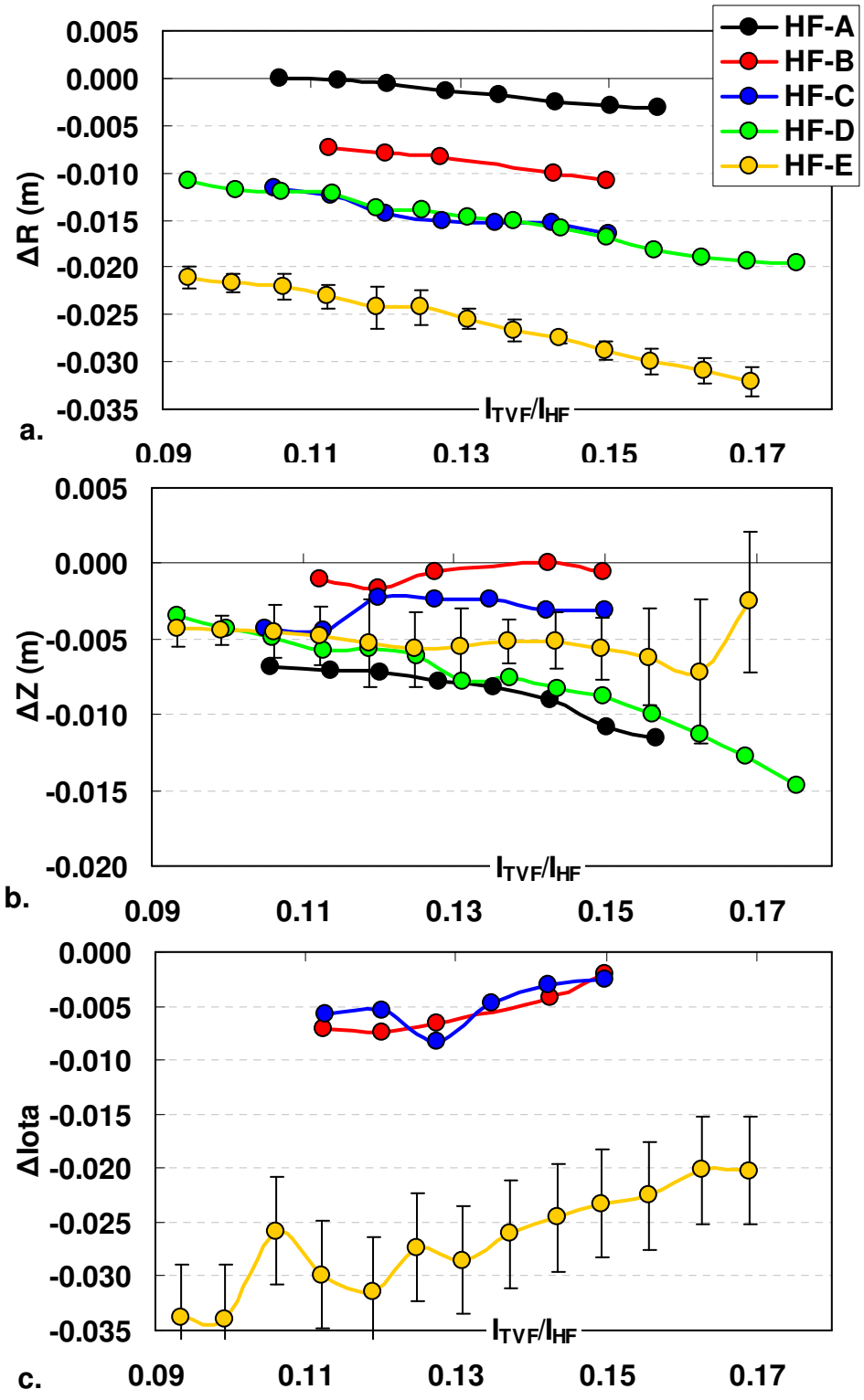

Fig. 6.4 Magnetic axis comparison before optimization (HF study)
Magnetic axis (a) radial difference (b) vertical difference (c) rotational transform difference
Δ= Experiment - Simulation

To investigate the possible causes of the poor results presented in Fig. 6.4, let's observe the effects the various parameters listed in Table 6.2 have on the position and rotational transform of the magnetic axis. This will give some intuition on how the various parameters affect the magnetic axis and we will be able to speculate as to the outcome of the optimization routine.

To do this, the position and rotational transform of the magnetic axis are first computed using the coil model $IFT_{HF\text{-}pre}$ and currents I_{HF} =300 A and I_{TVF} = 42 A. Then each parameter is individually modified by its corresponding uncertainty value and the new magnetic axis is calculated. The uncertainty estimate for each parameter is an indication of the expected changes which could occur for each parameter after using the optimization routine. Essentially this is how the optimization routine calculates the Jacobian matrix A, given by Eq. 5.3 in Ch. 5 The changes in the magnetic axis produced by the variations in the parameters are shown in Fig. 6.5.

For example, altering the radial winding law coefficient a_{r0} by 0.002 m; results in a 0.002 m radial shift, virtually no vertical shift, and a 0.003 rotational transform shift of the axis. Therefore, modifications made to the a_{r0} term are not going to influence the vertical position of the axis but it will affect the radial position and rotational transform.

The three most dominate terms in determining the radial position of the magnetic axis are, the winding law coefficients a_{r1} and b_{f1}, and the background vertical field Bz. Thus, these parameters will be heavily utilized by the optimization routine in order to best fit the radial experimental data. Other terms in the winding law and OVF coil parameters have less effect on the radial position of the magnetic axis. The radial measurements are not a good guide in determining these other coil parameters leaving the

extent to which they are know less certain. It is now evident how inaccurate modeling of the vertical background field can produce significant differences between the various data sets in Fig. 6.4(a). It should be noted that the horizontal field components also have significant effects on the radial position of the magnetic axis though not as large as the vertical field.

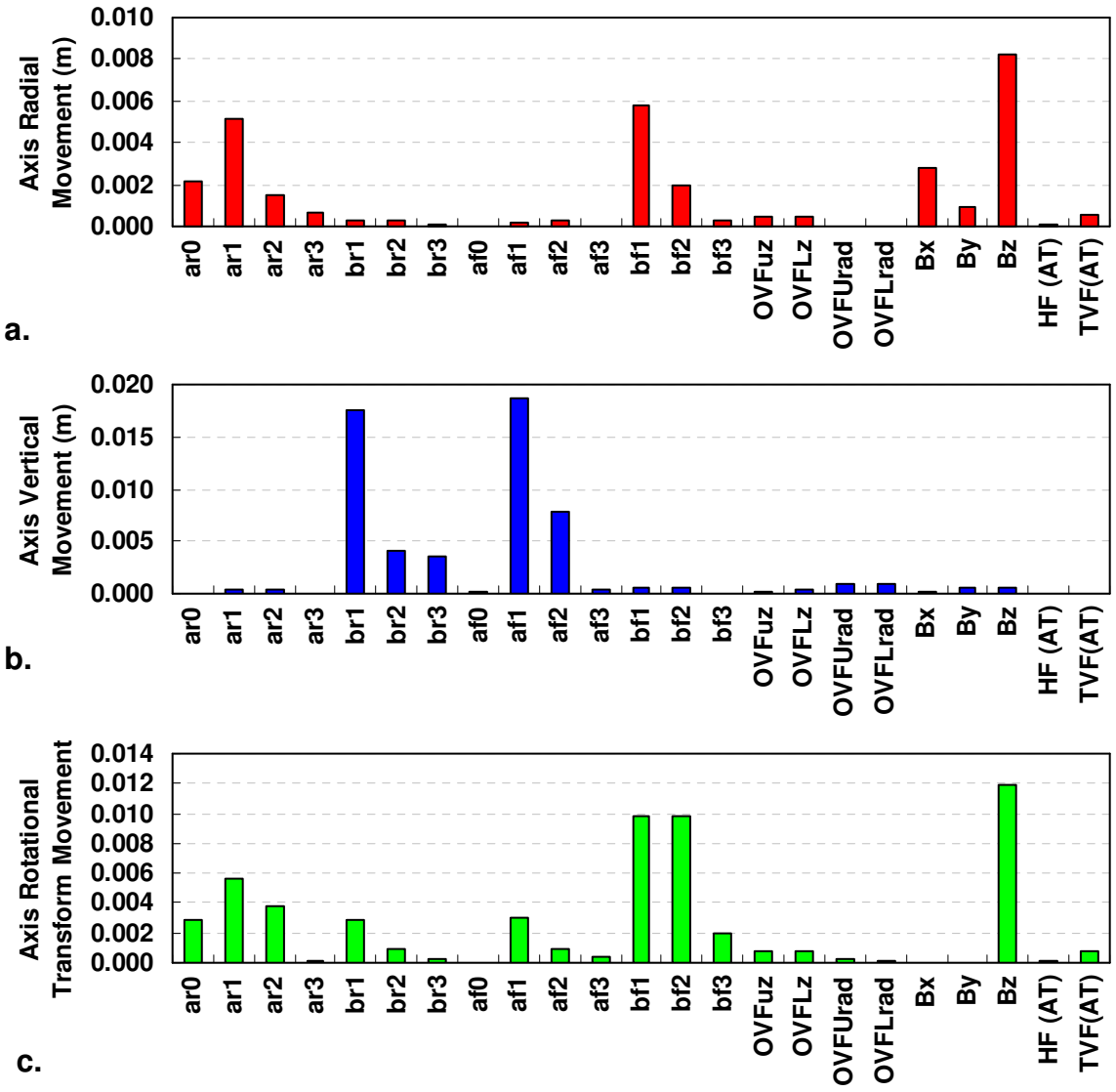

Fig. 6.5 HF/OVF Jacobian
The HF radial winding law coefficients were modified by 0.002 m. The HF toroidal winding law coefficients were modified by 0.002 radians. The OVF terms were modified by .001 m. The background field terms (Bx, By, Bz) were modified by 1 G.

The vertical position of the magnetic axis is largely determined by the up-down symmetry breaking parameters in the winding law; mainly the terms b_{r1}, a_{f1}, and a_{f2}. The horizontal and vertical background field is not as effective at altering the vertical position of the magnetic axis. Therefore in order to explain the differences in vertical position between the various data sets in Fig. 6.4(b) significant horizontal fields will be needed to compensate for the relatively minor effect they have on the vertical position. The application of a radial field (currently not implemented in IFT) would be a more effective method to alter the vertical position of the magnetic axis.

The rotational transform of the magnetic axis is largely determined by the winding law parameters b_{f1} and b_{f2} and along with the vertical background field Bz. As with the radial position data, the differences in rotational transform between the various data sets most likely can be attributed to a changing vertical background field.

Accurate knowledge of several winding law terms and the background field is crucial to accurately modeling the experimental field mapping results. The OVF coil parameters have relatively little effect on the magnetic axis and therefore exact knowledge of the placement of the OVF/TVF/RF coil pack is not crucial to accurately predicting the magnetic axis.

Starting from the coil model $IFT_{HF\text{-}pre}$, a coil optimization analysis was performed using the techniques discussed in Ch.5 resulting in a new coil model referred to as $IFT_{HF\text{-}post}$. To minimize the differences between the experimental and computed data the optimization routine was allowed to vary only those parameters listed in Table 6.2. It should be noted that the HF coil winding law was assumed to be field period symmetric.

Also the currents used in both the HF and TVF coils are assumed to be measured accurately and are not allowed to be varied by the optimization.

The coil parameters for the two models $IFT_{HF\text{-}pre}$ and $IFT_{HF\text{-}post}$ are shown in Table 6.4. All terms of the winding law are within the estimated 0.002 uncertainty level. The optimization left the OVF coil parameters nearly unchanged. Modifications made to the 18 HF/OVF coil parameters result in a χ^2 =2. Overall the HF/OVF coil model needed no unreasonable modifications to successfully simulate the experimental results, this indicated that the coils were constructed accurately.

parameter	$IFT_{HF\text{-}pre}$	$IFT_{HF\text{-}post}$	Uncertainty σ	Post-Pre
a_{r0} (m)	0.3836	0.3826	±0.002	0.0010
a_{r1} (m)	0.0000	0.0012	±0.002	-0.0012
a_{r2} (m)	0.0005	-0.0011	±0.002	0.0016
a_{r3} (m)	0.0001	0.0009	±0.002	-0.0008
b_{r1} (m)	-0.0007	-0.0009	±0.002	0.0002
b_{r2} (m)	0.0002	0.0002	±0.002	0.0000
b_{r3} (m)	-0.0001	0.0004	±0.002	-0.0005
a_{f0} (radians)	0.0000	0.0002	±0.002	-0.0002
a_{f1} (radians)	0.0000	0.0005	±0.002	-0.0005
a_{f2} (radians)	0.0000	0.0002	±0.002	-0.0002
a_{f3} (radians)	0.0000	0.0013	±0.002	-0.0013
b_{f1} (radians)	-0.2520	-0.2521	±0.002	0.0001
b_{f2} (radians)	0.0520	0.0530	±0.002	-0.0010
b_{f3} (radians)	-0.0240	-0.0243	±0.002	0.0003
OVF-U-Rad (m)	1.2660	1.2661	±0.001	-0.0001
OVF-L-Rad (m)	1.2660	1.2659	±0.001	0.0001
OVF-U-Z (m)	0.5230	0.5230	±0.001	0.0000
OVF-L-Z (m)	-0.5230	-0.5230	±0.001	0.0000

Table 6.4 Coil parameters for the coil model $IFT_{HF\text{-}post}$

The HF coil radial winding law incorporating the new coefficients of the coil model $IFT_{HF\text{-}post}$ is shown vs. the poloidal angle in Fig. 6.6. The figure also includes the coil depth measurements and winding law of $IFT_{HF\text{-}pre}$ shown previously in Fig. 2.7.

Good agreement exists between the two winding laws everywhere except on the inner midplane, where mechanical measurements of the coil were difficult.

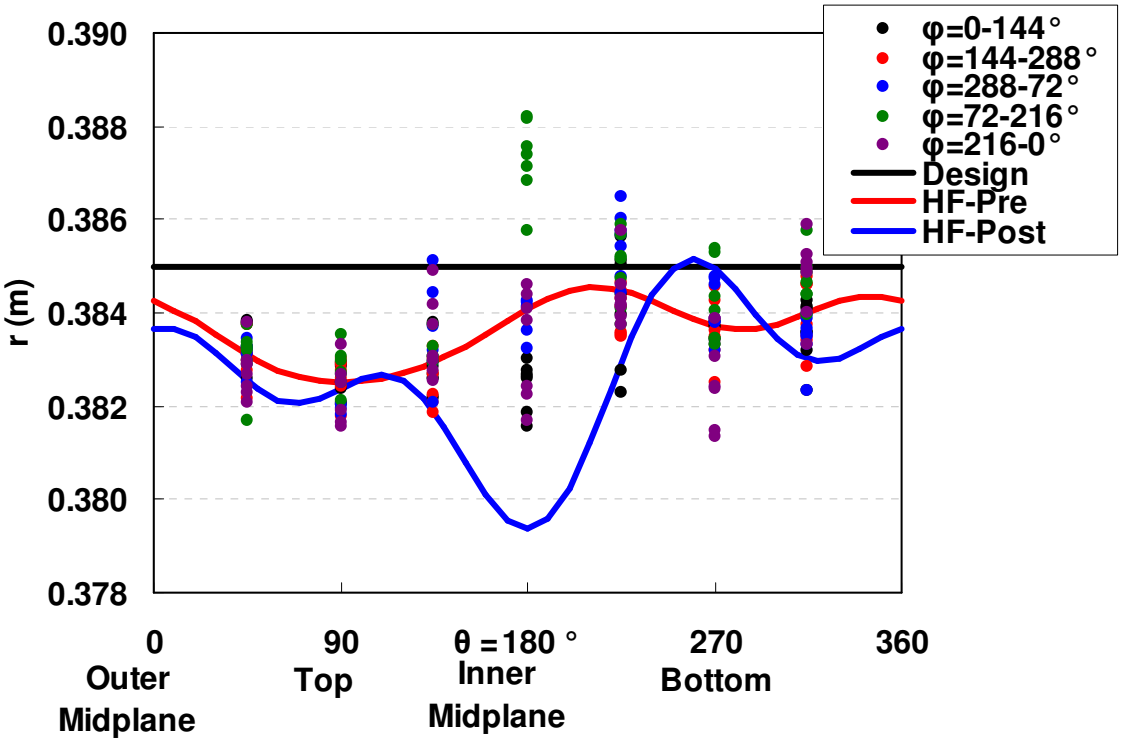

Fig. 6.6 HF minor radius vs. poloidal angle

In addition to computing the HF coil winding law, the minimization procedure is also used to determine the background field in the laboratory, assumed to be a uniform horizontal and vertical field across the volume of the vacuum vessel. Due to the effects of magnetization, the background field of the various data sets is not expected to be the same. The optimization assumes that during the course of the each data set the background field remains constant. The validity and the consequences of these assumptions will be seen shortly.

The background fields in the laboratory predicted by the optimization procedure for the different data sets are shown in Table 6.5. Also listed is the Earth's field predicted

for Auburn, Alabama by the National Geophysical Data Center. The optimization procedure finds that the fields due to magnetization effects are significant, with several data sets needing 2 G fields to accurately model the experimental data. The remnant magnetic field measurements shown in Fig. 5.7 confirm that fields of this magnitude are reasonable.

Interestingly, the vertical background field continually decreases as one proceeds through the data sets, with data set HF-A taken first in August and data set HF-E taken last in January. Although this may only be coincidence it could also be evidence that the effects due to of magnetization are growing more pronounced with prolonged exposure to the magnetic fields produced by CTH. Perhaps the ferromagnetic material in the floor and ceiling is becoming more magnetized with each subsequent field mapping experiment. No such trend exists for the horizontal components of the background field.

	Bx East (G)	By North (G)	Bz Up (G)
B_{Earth} Auburn	0.0	0.2	-0.4
HF-A	-1.6	-1.1	0.7
HF-B	1.2	1.7	-0.4
HF-C	-0.5	-0.8	-0.7
HF-D	-0.4	-0.4	-0.9
HF-E	0.1	0.7	-2.1

Table 6.5 Post optimization background fields

During the discussion of the background field, there were three assumptions made regarding the background field which were suspected of being incorrect from the start. The first is that the background field is a uniform horizontal and vertical background field constant throughout the volume of the vacuum vessel. The second is that the background field is assumed to remain constant throughout the entire data set. The third is that the background field should remain within 1 G of the earth's field. Although we suspect all

three of these assumptions to be invalid, the optimization was still able to predict background field values with these restrictions for the different data sets that sufficiently model the experimental results.

To better model the experimental data, the background field and its calculation could be modified in the following ways:

1) The background field could be computed for each data point individually.
2) The uncertainty on the background field could be increased to more reasonable values determined from external measurements, for example 3 G as measured in Fig. 5.7.
3) Lastly and perhaps most importantly the ineffective (and more than likely inaccurate horizontal background field) could be supplemented with a horizontal radial field and a toroidal field. The radial field should affect the vertical position of the axis efficiently, just as the vertical background field targeted the radial position.

With the new coil model and background field values, the positions and rotational transforms of the simulation magnetic axis were again computed and compared with the experimental results. The differences between the experimental data and the simulation results from the new coil model $IFT_{HF\text{-}post}$ vs. the current ratio I_{TVF}/I_{HF} are shown in Fig. 6.7. Comparing the results of Fig. 6.4 and Fig. 6.7 we see that the new coil model drastically improves both the position and rotational transform calculations of the magnetic axis for all data sets.

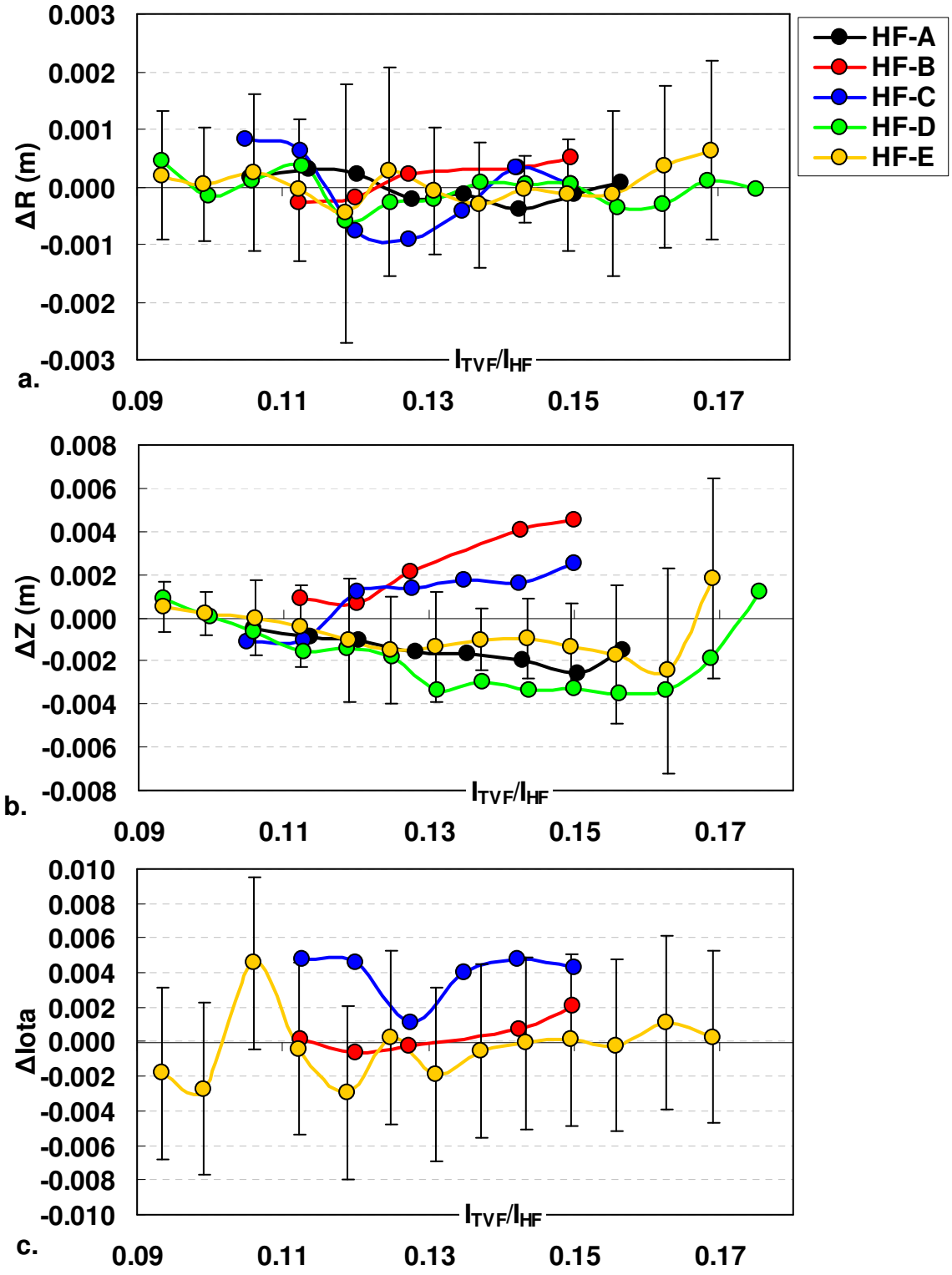

Fig. 6.7 Magnetic axis comparison after optimization (HF study)
(a) radial difference (b) vertical difference (c) rotational transform difference
Δ= Experiment - Simulation

The differences in radial position obtained from the old coil model $IFT_{HF\text{-}pre}$ were up to 0.02 m. With the new coil model $IFT_{HF\text{-}post}$ the differences are now reduced to less than 0.001 m. The large radial differences initially present in data set HF-E, were corrected for with a 2 G vertical field by the optimization. The differences in vertical position are improved from 0.015 m using $IFT_{HF\text{-}pre}$ to less than 0.005 m using $IFT_{HF\text{-}post}$. The differences in the rotational transform obtained from the model $IFT_{HF\text{-}pre}$ were up to 0.035 and are now less than 0.005 from $IFT_{HF\text{-}post}$. The χ^2 values associated with the differences in radial, vertical, and rotational transform values are listed in Table 6.3.

The results discussed so far have only dealt with the position and rotational transform of the magnetic axis. One may wonder how well the model $IFT_{HF\text{-}post}$ predicts the geometry of the surfaces outside the magnetic axis compared to $IFT_{HF\text{-}pre}$. In Fig. 6.8(a), a surface of sections plot shows several experimental nested flux surfaces (solid points) for one current setting (I_{HF} = 300 A, I_{TVF} = 34 A). The surfaces produced by the coil model $IFT_{HF\text{-}pre}$ are shown as the solid lines. The computed surfaces appear jagged due to magnetic islands on low order rational flux surfaces. The experimental surfaces are shifted radially inward from those predicted by computation.

A comparison between the experimental surfaces and those computed by the coil model $IFT_{HF\text{-}post}$ is shown in Fig. 6.8(b). Despite the fact that the optimization was only performed with information about the magnetic axis, the agreement between the experimental and computation results appears to be much better. In both these figures the simulation surfaces are computed with electron drift effects taken into account to make a true comparison with the electron beam field mapping measurements.

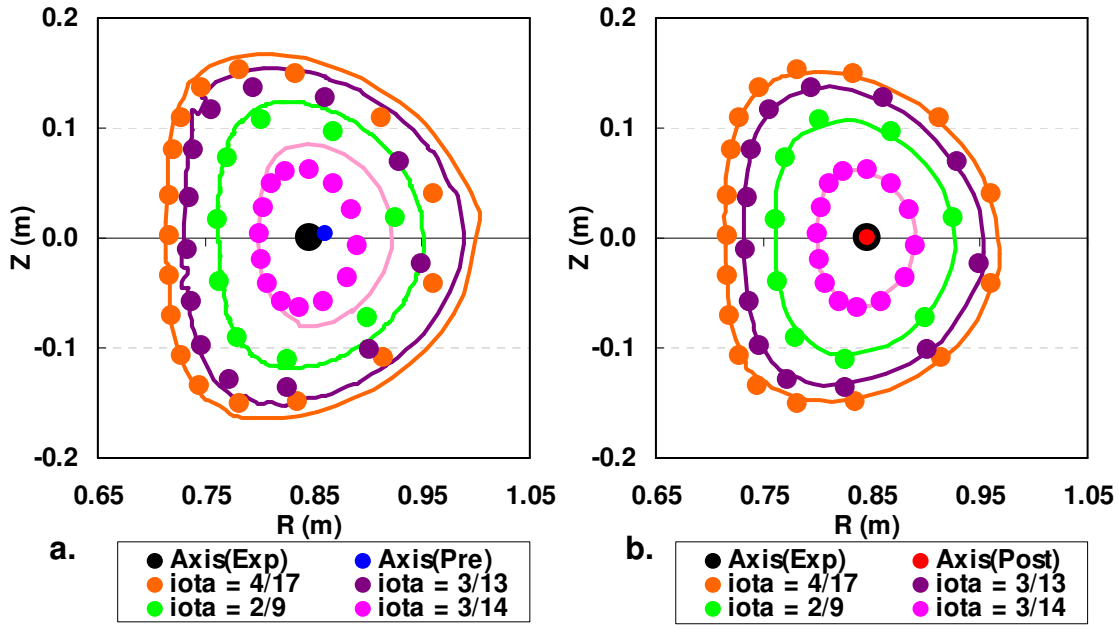

Fig. 6.8 SOS plot comparison (experiment vs. simulation)
a) Simulation surfaces computed with coil model $IFT_{HF\text{-}pre}$
b) Simulation surfaces computed with coil model $IFT_{HF\text{-}post}$

In conclusion, through field mapping measurements, the HF coil winding law was found to have no major discrepancies from its original design but does exhibit slight deviations from its design that break the up-down symmetry. The broken symmetry causes the magnetic axis to rise above the midplane at large TVF coil currents. The optimization process was able to account for this vertical rise of the magnetic axis resulting in a HF coil winding law that more accurately describes the experimental results of field mapping. In addition, the coil optimization also produced a set of background fields needed to correctly model the differences between the various data sets. The modifications made to the winding law affect the flux surfaces by roughly the same amount as the modifications to the background field do. The increasingly evident importance of the background fields has made determining the subtleties of the coils increasingly difficult. To gain further information about the HF/OVF/TVF coils field

mapping experiments should be performed under conditions where the background field is constant or at least known more accurately.

6.2 FIELD MAPPING WITH THE SVF COILS

Using the HF coil winding law obtained in Sec. 6.1, further field mapping and modeling studies were performed similar to those presented in the previous HF/OVF/TVF study, with an additional magnetic field produced by current applied to the SVF coils. Field mapping experiments were performed by varying the current in the SVF coil set while maintaining constant currents in the HF and TVF coils. As in earlier experiments, measurements of the magnetic axis were made at two field period locations, φ=36° and φ=252°. In Table 6.6, the experimental parameters are summarized for the various SVF data sets. It should be noted that the current ratio I_{TVF}/I_{HF} (expressed in A-turns) of data set SVF-C is 4% lower than that of data sets SVF-A and SVF-B, resulting in a radial outward shift of the flux surfaces.

Data Set	Wand/ Screen	Location φ =	I_{HF} (A)	I_{TVF} (A)	TVF Turns	I_{SVF} (A)	Information Gathered
SVF-A	Wand	36º	300	36	108	-45 – +45	R, Z
SVF-B	Screen	252º	300	36	108	-45 – +45	R, Z, ι
SVF-C	Screen	252º	300	41.5	90	-50 – +50	R, Z, ι

Table 6.6 SVF field mapping setup

The data was analyzed according to the procedure described in Ch. 4 resulting in magnetic axis information at two different field period locations. The position of the magnetic axis for the various SVF current settings is shown in Fig. 6.9. The magnetic axis is moved radially outward by 0.15 m as the current in the SVF coil is increased from -50 A to +50 A, and remains near the midplane for all but large positive values of I_{SVF}.

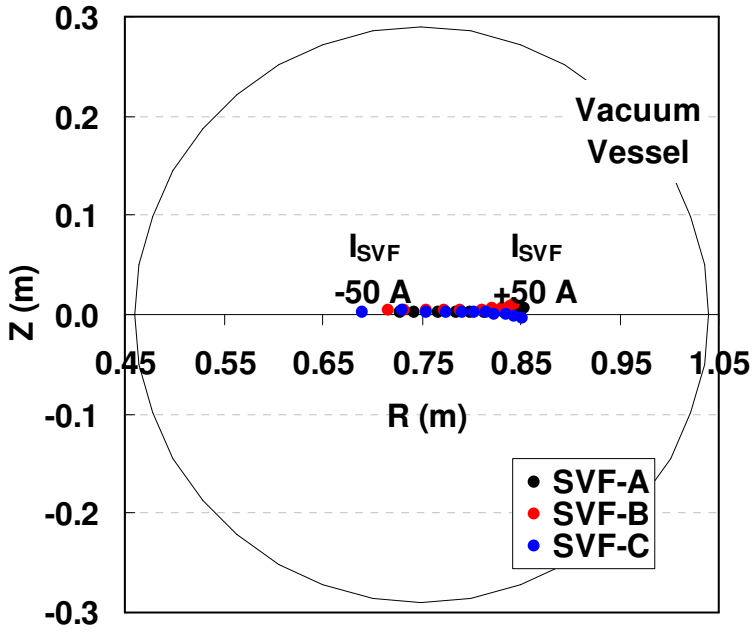

Fig. 6.9 Magnetic axis position (SVF study)

The magnetic axis information is shown in greater detail in Fig. 6.10 with the radial position, vertical position, and rotational transform of the magnetic axis plotted vs. I_{SVF}. Similar to the experimental results of the HF/OVF/TVF study, significant differences between the different data sets exist in all three types of data, supposedly from a changing background field. Interestingly, in Fig. 6.10(b), when I_{SVF} is increased to positive values the vertical position of the magnetic axis rises above the midplane for two data sets but falls below the midplane for one data set. Also, in addition to the rotational transform of the magnetic axis shown in Fig. 6.10(c) by the solid points, the rotational transform of the largest visible flux surface for data set SVF-C is shown by the hollow blue points. Similar to the simulation results shown in Fig. 3.16 as I_{SVF} increases the rotational transform shear, given by Eq. 3.3, also increases.

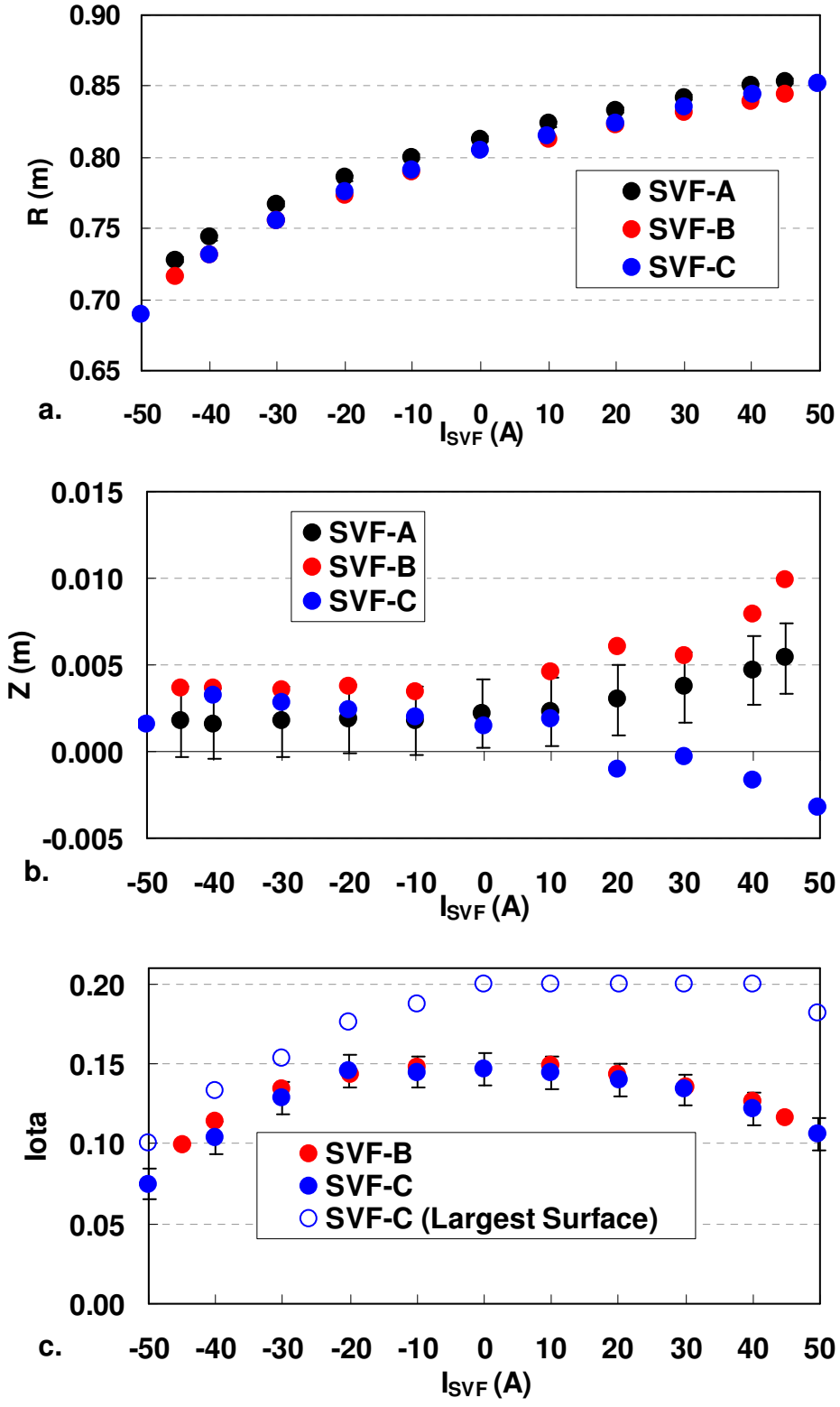

Fig. 6.10 Field mapping results (SVF study)
Magnetic axis (a) radial position, (b) vertical position, (c) rotational transform

The model of the HF/OVF/TVF coils developed in Sec. 6.1 included modified HF winding law terms and OVF coil positions, resulting in good agreement between the simulation and experimental data when appropriate background fields are applied. This newly developed coil model referred to as $IFT_{SVF\text{-}pre}$ in this study, will now be used to analyze the SVF data in a similar fashion as was done for the HF study.

The SVF coil parameters in the coil model $IFT_{SVF\text{-}pre}$ are defined by their measured values which differ slightly from their designed values. In Table 6.7, the coil parameter design values, measured values, and estimated uncertainties for each parameter are shown. The SVF coil uncertainties are based on mechanical measurement errors. The background fields used in the coil model $IFT_{SVF\text{-}pre}$ are again estimated to remain within 1 G of the ambient magnetic field of Auburn, AL. As mentioned during the HF study the inclusion of a radial field would further improve background field model.

SVF Parameter	Description	Design	Measured $IFT_{SVF\text{-}pre}$	Uncertainty σ
SVF-U-X (m)	Position East (Upper)	0	0.000	±0.001
SVF-L-X (m)	Position East (Lower)	0	0.000	±0.001
SVF-U-Y (m)	Position North (Upper)	0	0.000	±0.001
SVF-L-Y (m)	Position North (Lower)	0	0.001	±0.001
SVF-U-Z (m)	Position Vertical (Upper)	0.605	0.609	±0.001
SVF-L-Z (m)	Position Vertical (Lower)	-0.605	-0.609	±0.001
SVF-U-Xhat (radians)	Direction East (Upper)	0	.001	±0.002
SVF-L-Xhat (radians)	Direction East (Lower)	0	.001	±0.002
SVF-U-Yhat (radians)	Direction North (Upper)	0	-.001	±0.002
SVF-L-Yhat (radians)	Direction North (Lower)	0	0.000	±0.002
SVF-U-rad (m)	Upper Radius	.525	.523	±0.001
SVF-L-rad (m)	Lower Radius	.525	.525	±0.001
Bx (G)	East Field	-.01		±1
By (G)	North Field	.23		±1
Bz (G)	Up Field	-.44		±1

Table 6.7 SVF coil parameters before optimization

Using the coil model $IFT_{SVF\text{-}pre}$, the simulation magnetic axis position and rotational transform are computed and compared to the experimental data. The differences between the experimental results and the computed results vs. I_{SVF} are shown in Fig. 6.12. As with the HF coil model before the optimization, the simulation coil model $IFT_{SVF\text{-}pre}$ does not accurately model the experimental data with large differences existing in each of the three types of data. We should expect that inaccurate background fields are responsible for a large portion of this error. The χ^2 values associated with the differences in radial, vertical, and rotational transform values computed from the coil model $IFT_{SVF\text{-}pre}$ are listed in Table 6.10. The χ^2 value is well above the number of signals for each of the three types of data, revealing a poor fit.

During the coil optimization performed on the SVF coils, only SVF coil parameters will be modified. The HF and OVF coil parameters determined in Sec. 6.1 will remain constant. Therefore, in examining how each individual parameter used in the SVF optimization affects the magnetic axis, we consider only the SVF coil parameters.

The change produced in the magnetic axis after each upper SVF coil parameter was modified by its uncertainty is shown in Fig. 6.11 with the changes produced by modifications to the lower coil being similar. The position and radius of the SVF coil were modified by 0.001 m, the direction vectors of the SVF coil were modified by 0.002 radians and the background fields Bx, By, and Bz, were modified by 1 G.

The radial position and rotational transform of the magnetic axis are almost entirely determined by the background field, Bx, By, Bz, with the SVF coil parameters having significantly smaller effect. Thus we can expect that any radial and rotational transform discrepancies between the experimental data and the simulation data will most

likely be accounted for by variations made to the horizontal and vertical background fields. The only noticeable SVF coil parameters to appreciably affect the axis are the SVF coil radius and vertical position, each influencing the vertical position of the magnetic axis as much as the background field. Changes made to the horizontal position and direction of the SVF coil do very little to the magnetic axis.

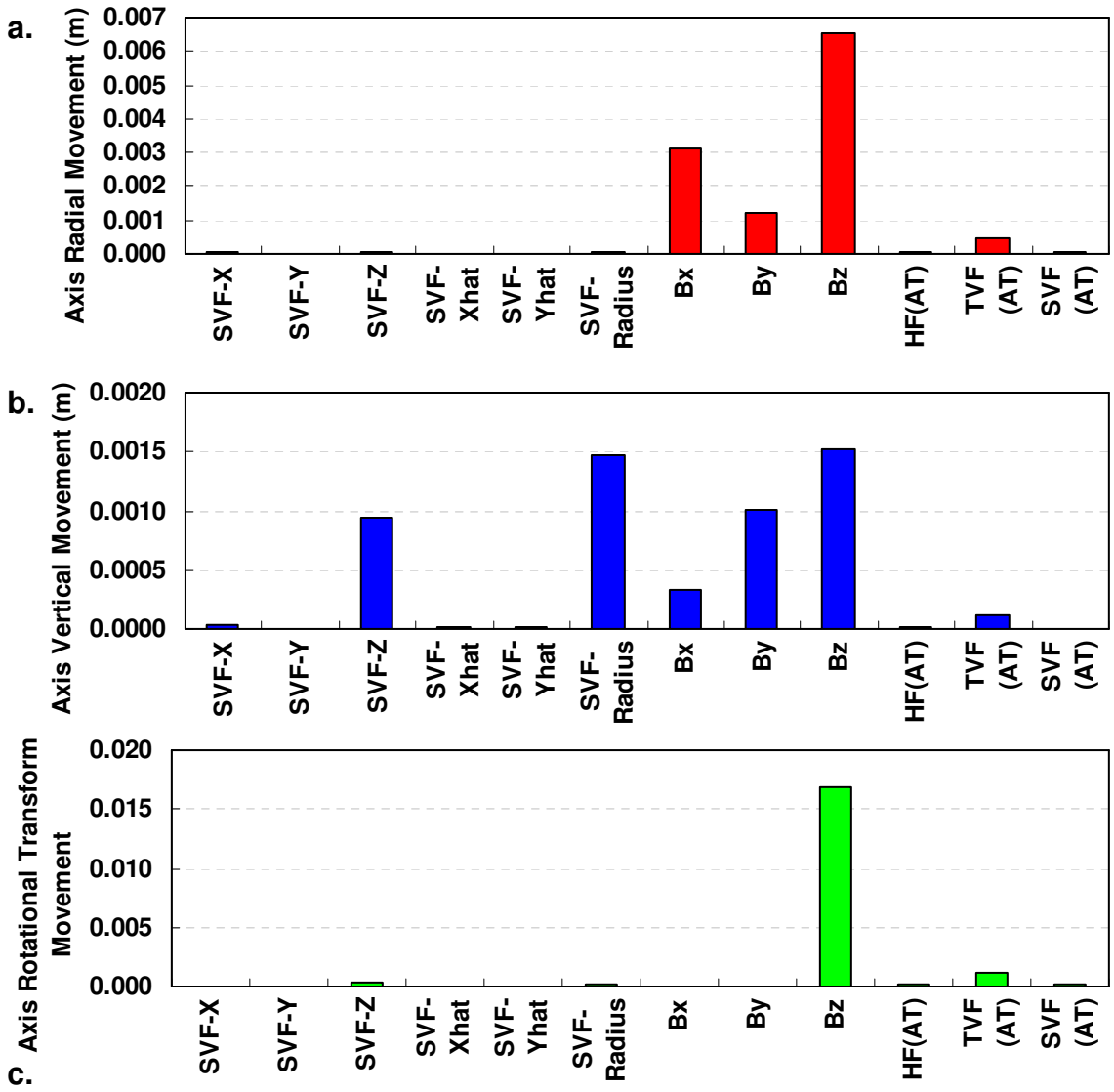

Fig. 6.11 SVF Jacobian
I_{HF} = 300 A, I_{TVF} = 42 A, and I_{SVF} = 40 A

Using the experimental SVF data shown in Fig. 6.12, the SVF coil parameters listed in Table 6.7 were modified using the coil optimization routine discussed in Ch. 5. The resulting coil model is referred to as $IFT_{SVF\text{-}post}$.

In Table 6.8 the parameter values for the coil models $IFT_{SVF\text{-}pre}$ and $IFT_{SVF\text{-}post}$ are listed. All parameters within the model except the SVF lower radius have undergone small modifications of less than 1mm. Due to its importance on the magnetic axis vertical position, modifications to the SVF radius are slightly larger. Field mapping experiments and use of the optimization routine have shown that the SVF coil is operating as designed without major errors.

parameter	$IFT_{SVF\text{-}pre}$	$IFT_{SVF\text{-}post}$	Post-Pre	Uncertainty σ
SVF-U-X	0.0000	-0.0001	-0.0001	±0.001
SVF-L-X	0.0000	-0.0001	-0.0001	±0.001
SVF-U-Y	0.0000	0.0000	0.0000	±0.001
SVF-L-Y	0.0010	0.0011	+0.0001	±0.001
SVF-U-Z	0.6090	0.6082	-0.0008	±0.001
SVF-L-Z	-0.6090	-0.6096	-0.0006	±0.001
SVF-U-Xhat	0.0010	0.0011	+0.0001	±0.002
SVF-L-Xhat	0.0010	0.0010	0.0000	±0.002
SVF-U-Yhat	-0.0010	-0.0012	-0.0002	±0.002
SVF-L-Yhat	0.0000	0.0000	0.0000	±0.002
SVF-U-Radius	0.5230	0.5239	+0.0009	±0.001
SVF-L-Radius	0.5250	0.5232	-0.0018	±0.001

Table 6.8 $IFT_{SVF\text{-}pre}$ and $IFT_{SVF\text{-}post}$ parameters

As with the HF coil study, the horizontal and vertical background fields were constant throughout each data set during the optimization. The background field values computed by the optimization for the different data sets are shown in Table 6.9. The simulation requires that several data sets need significant fields (2 G) to accurately model the experimental data.

	Bx (East-G)	By (North-G)	Bz (Up-G)
Predicted Field	0.0	0.2	-.4
SVF-A	0.2	1.2	0.2
SVF-B	-1.8	-2.2	-0.3
SVF-C	1.2	1.4	-2.2

Table 6.9 SVF background field results

The differences between the experimental results and the computed results calculated using the new coil model $IFT_{SVF\text{-}post}$ are shown in Fig. 6.13. A comparison of Fig. 6.12 and Fig. 6.13 shows that improvements have been made in all three types of data. The χ^2 values due to the radial, vertical and rotational transform differences are given in Table 6.10.

	Number of Signals	χ^2 ($IFT_{SVF\text{-}pre}$)	χ^2 ($IFT_{SVF\text{-}post}$)
R	32	930	13
Z	32	119	18
~~t~~	21	318	10
SVF Coil Parameters	12	0	5
Total	85	1367	46

Table 6.10 χ^2 values of the SVF coil optimization

Therefore in conclusion, the SVF coil set was shown to influence the magnetic flux surfaces as designed and was found to have no major errors. To accurately simulate field mapping results collected with the SVF coil small but reasonable modifications were made to the SVF coil model. Compared to the background field, the modifications made to the SVF coil have relatively little effect on the magnetic axis. As discussed in Sec. 6.1, further improvements could be made to the model by including radial components to the background field.

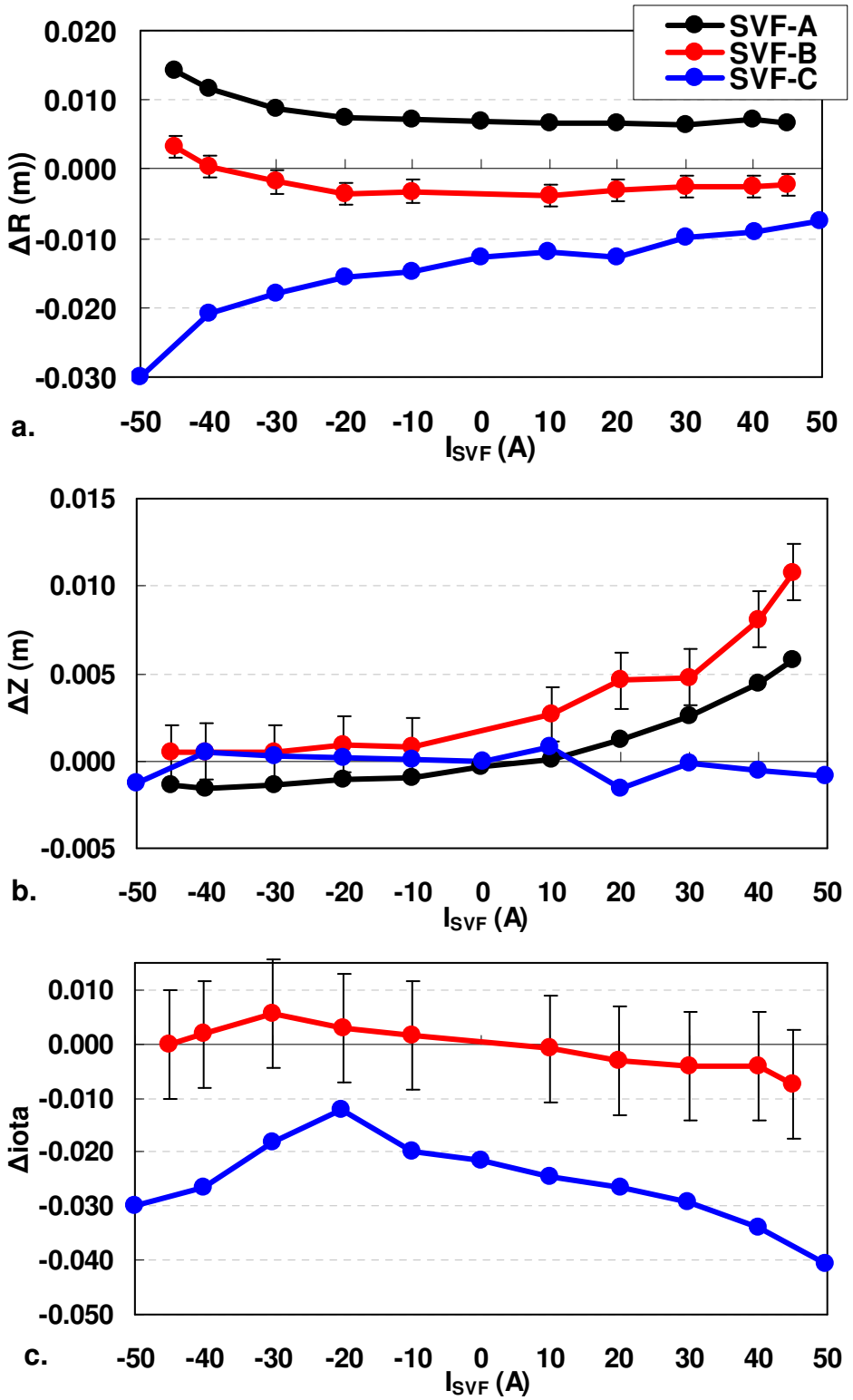

Fig. 6.12 Magnetic axis comparison before optimization (SVF study)
(a) radial difference (b) vertical difference (c) rotational transform difference
Δ= Experiment - Simulation

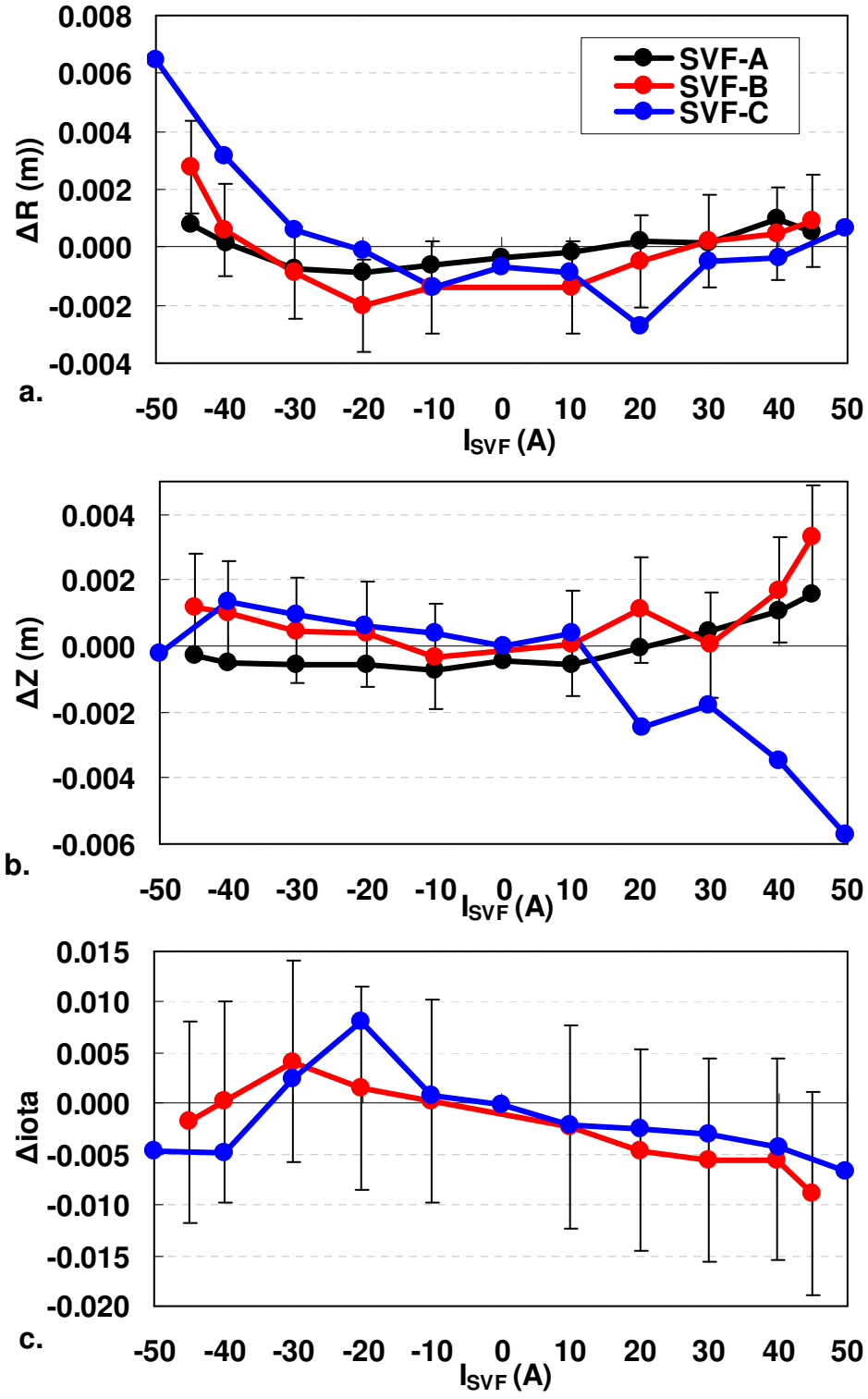

Fig. 6.13 Magnetic axis comparison after optimization (SVF study)
(a) radial difference (b) vertical difference (c) rotational transform difference
Δ= Experiment - Simulation

6.3 FIELD MAPPING WITH THE TF COILS

Using the HF winding law and the SVF coil positions determined in the previous sections, field mapping studies were performed using the TF coils. Field mapping with the TF coils was performed under two different scenarios. The first was done in the absence of any SVF current; while the TF current was varied from 0 to 140 A. The second was done at four separate TF current values over a range of SVF current values. In the second scenario the TF current values raised the rotational transform of the outer most flux surfaces to approximately ι = 1/5, 1/4, 1/3, and 1/2 (when I_{SVF} = 0 A). The experimental parameters for the various TF tests are listed in Table 6.11. It should be mentioned that the data set SVF-C presented in Sec. 5.2 is the data set TF-D presented here.

Data set	Wand/ Screen	φ=	I_{HF} (A)	I_{TVF} (A)	TVF Turns	I_{SVF} (A)	I_{TF} (A)	Info Gathered
TF-A	Wand	36º	300	36	108	0	0 – 140	R, Z
TF-B	Screen	36º	300	36	108	0	0 – 140	R, Z , ι
TF-C	Screen	252º	300	36	108	0	0 – 140	R, Z , ι
TF-D	Screen	252º	300	41.7	90	-50 – +50	0	R, Z , ι
TF-E	Screen	252º	300	41.7	90	-50 – +50	44	R, Z , ι
TF-F	Screen	252º	300	41.7	90	-50 – +50	78	R, Z , ι
TF-G	Screen	252º	300	41.7	90	-50 – +50	107	R, Z , ι

Table 6.11 TF experimental parameters

The radial position, vertical position and rotational transform of the magnetic axis are shown in Fig. 6.14, Fig. 6.15, and Fig. 6.16 respectively. In each of these plots, figure (a) shows the dependence of the magnetic axis on I_{TF} for data sets TF-(A,B,C), whereas figure (b) shows the dependence of the magnetic axis on I_{SVF} for data sets TF-(D,E,F,G)

The radial dependence of the magnetic axis on the TF current shown Fig. 6.14(a) is also shown in Fig. 6.14 (b) with the axis moving inward as the I_{TF} is increased. Also

careful examination of the data set TF-A in Fig. 6.14(a) shows that the data points do not follow a smooth curve but exhibit a jagged saw-tooth pattern. Similar, more pronounced behavior is seen in the vertical position of the magnetic axis discussed next.

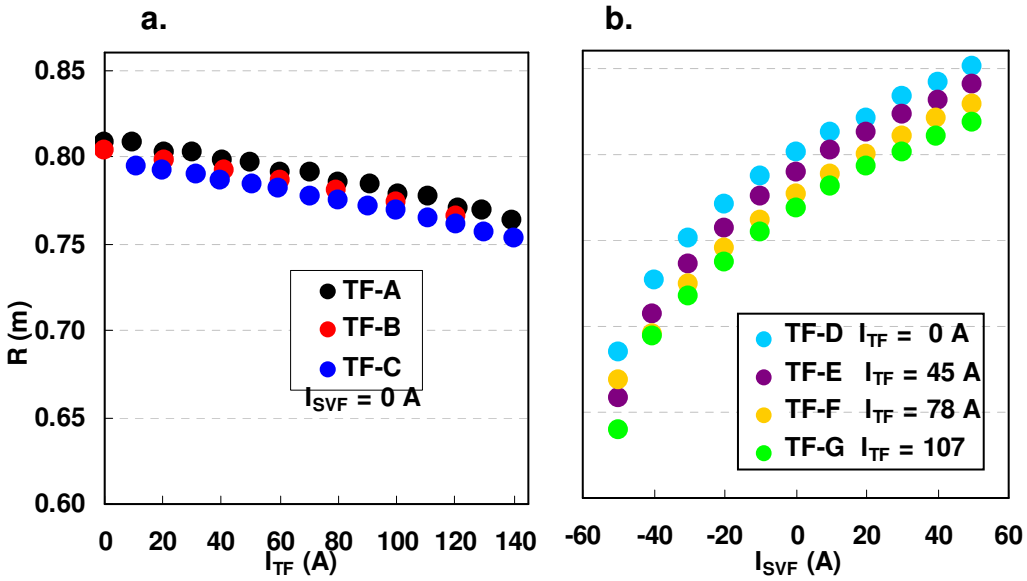

Fig. 6.14 Radial position of the magnetic axis (TF study)

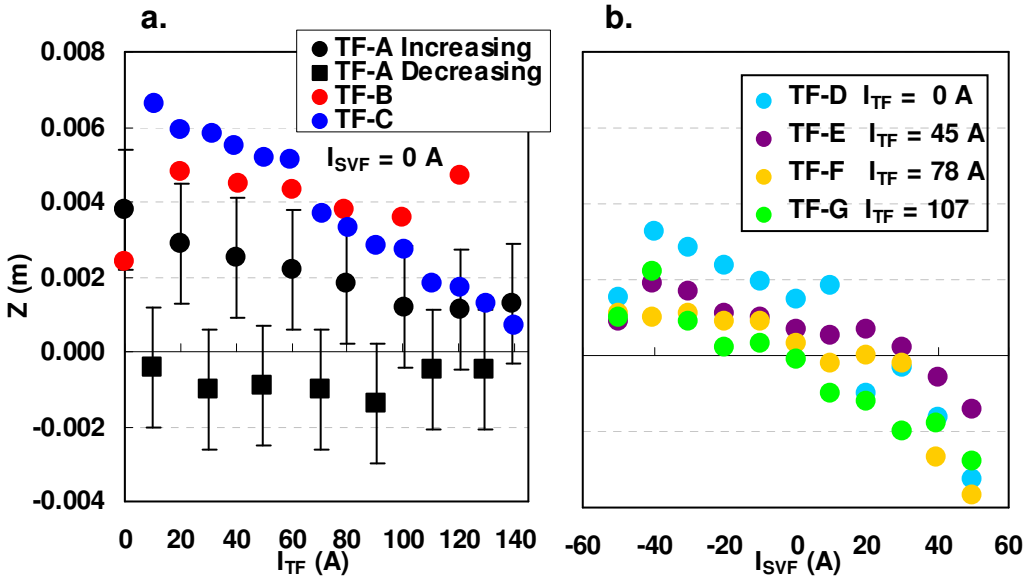

Fig. 6.15 Vertical position of the magnetic axis (TF study)

The most interesting feature among these plots is the peculiar path taken by the magnetic axis of data set TF-A visible in Fig. 6.15(a). Data set TF-A is the data set shown in Fig 5.5 where the effects of magnetization were first observed. If you recall, this data set was taken in two parts. During first part, the TF current was increased in 20 A intervals starting at 0 A and increasing up to 140 A, (0, 20, 40,… 140 A). This initial upward sweep in TF current is shown in Fig. 6.15(a) as the black circles. During the second part of the data set, the TF current was decreased in 20 A intervals starting at 130 A and decreasing to 10 A, (130, 110, 90,… 10 Amps), shown as the black squares. The vertical positions of the data points corresponding to I_{TF} = 0 A and I_{TF} = 10 A differ by 0.004 m, a significant amount. At the time the data was taken, the effects due to magnetization were not known or considered and in fact this data set started the entire magnetization investigation discussed in Sec.5.3. This evidence clearly shows that the background field within the vacuum vessel is changing during the course of an experiment, resulting in differences in the magnetic axis position. The other data sets were collected by increasing the TF current from 0 to 140 A incrementally such that the effects due to magnetization are not as visible. In spite of the peculiarity found in data set TF-A, the magnetic axis remains near the midplane regardless of I_{TF} or I_{SVF} suggesting that TF coils do not have any major defects.

The rotational transform of the magnetic axis is shown by the solid points in Fig. 6.16(a) and (b). As expected, the rotational transform of the magnetic axis increases as the TF current is increased. In addition, the rotational transform of the largest visible flux surface is shown by the solid lines in Fig. 6.16(b). The existence of low order rational surfaces (often in the form of magnetic islands) near the last closed flux surface often

dominate the flux surface measurement. This results in the jagged nature of the largest visible flux surface measurements. As expected the rotational transform shear, given by Eq. 3.3 increases as I_{SVF} increases. At low SVF currents the rotational transform shear is nearly flat. As the SVF current is increased the shear increases. By increasing both I_{TF} and I_{SVF} simultaneously, conditions are reached within the flux surfaces where two low order rational surfaces coexist. For example, with the application of I_{TF} =78 A and I_{SVF}= 50 A, the flux surfaces with rotational transform of ɬ = 1/4 and ɬ = 1/3 are both present. This is significant during field mapping studies involving islands which sometimes require two island chains to coexist simultaneously.

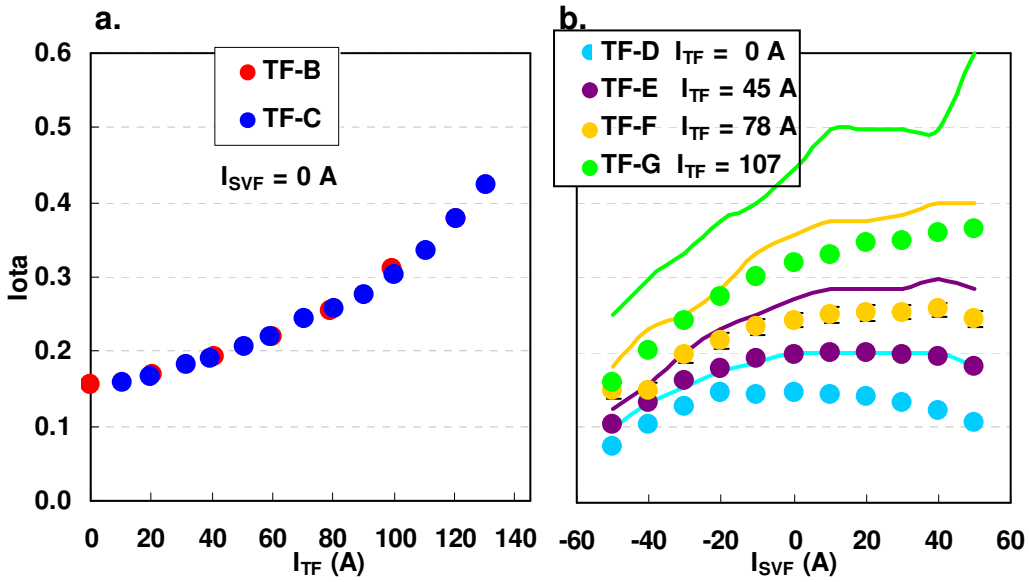

Fig. 6.16 Rotational transform of the magnetic axis (TF study)

The IFT coil model used in the forthcoming TF coil optimization builds upon improvements made to the model through the modifications made in Sec. 5.1 and Sec. 5.2. In this model the positions (X,Y,Z) and orientations (X_{hat}, Y_{hat}, Z_{hat}) of the TF coils are defined by their measured values which differ slightly from the designed values given

in Ch. 2. The position of each TF coil is estimated to be known within ±0.001 m. The orientation of each TF coil is estimated to be known within ±0.002 radians. These uncertainty estimates are partially due to mechanical measurement errors and partially due to inexact knowledge of the coil center within each TF coil pack.

Along with the usual constant horizontal and vertical fields pointing east, north, and up, a horizontal background toroidal field was also incorporated in the simulation model. The toroidal field was included in this TF study because conceivably the TF coils could create a remnant background toroidal field due to magnetization. Computationally the background toroidal field B_φ, is produced by toroidal field coils (not the same TF coils in place on the machine) according to

$$B_\varphi(R) = \frac{I}{2\,\mu_0\,R} \tag{6.1}$$

where R is the major radial distance, I is the current. In the previous field mapping studies B_φ was set to zero. During the TF coil optimization process the current I is the parameter that is varied.

Small changes to individual TF coil parameters have significantly less effect on the magnetic axis than the background field does. This is demonstrated in Fig. 6.17 where the parameters of an individual TF coil located at $\varphi = 198°$ were modified by the corresponding uncertainties. The resulting changes made to the magnetic axis at the toroidal location $\varphi = 252°$ are shown in Fig. 6.17 (this time plotted on a logarithmic scale). Compared to the effects that modifications to the background field have on the magnetic axis, modifications to the TF coils have little effect on the axis. Therefore we

can expect the coil optimization routine is going to do very little to the TF coil parameters and accomplish most of its fit through modifications made to the background field.

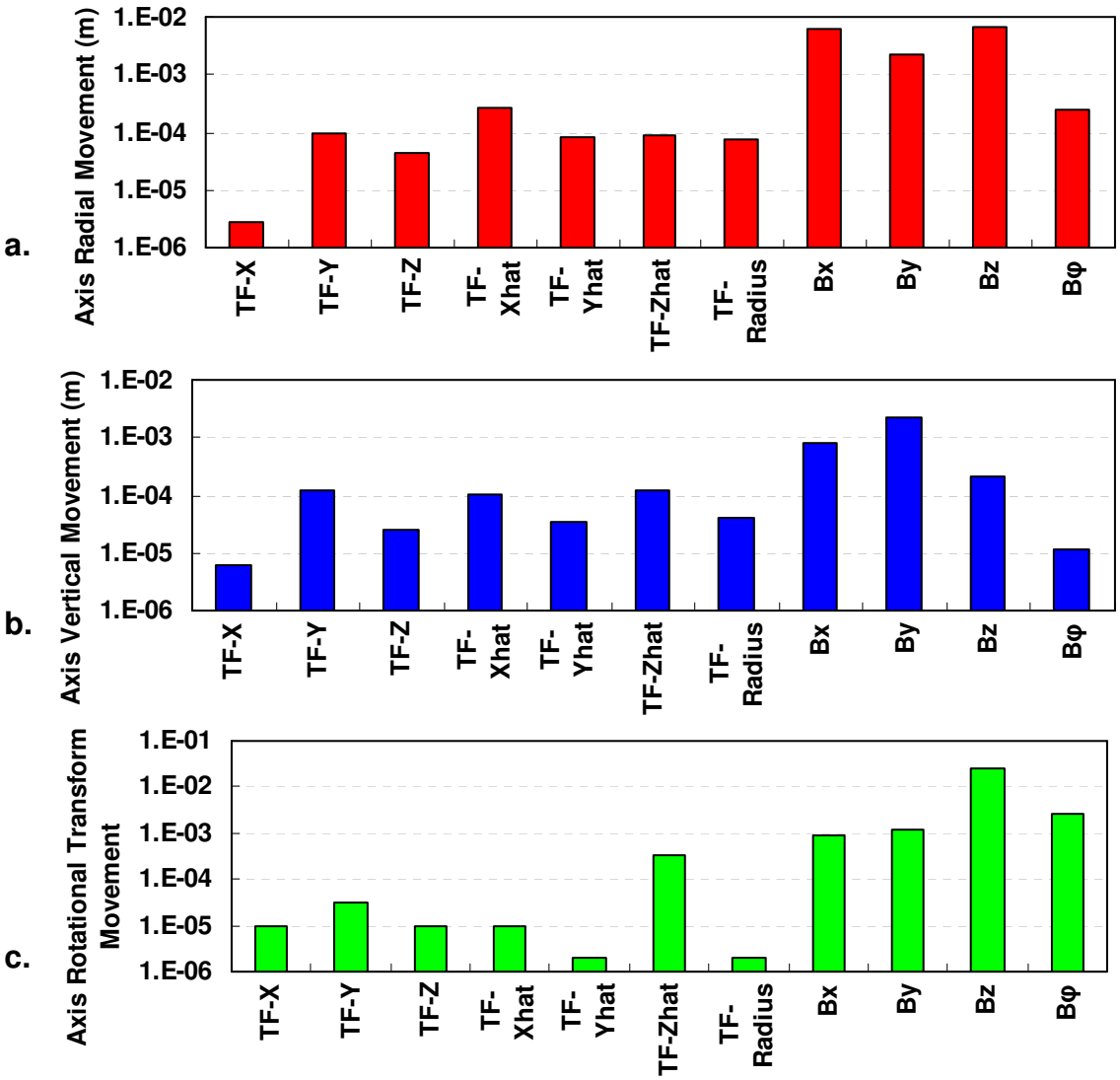

Fig. 6.17 TF Jacobian results

As we have seen with the other field mapping studies, due to an unknown background field the initial coil model does not accurately predict the position and rotational transform of the magnetic axis. The χ^2 values obtained from this preliminary model are given in Table 6.13 referred to as $IFT_{TF\text{-}pre}$.

Starting from the coil model $IFT_{TF\text{-}pre}$, a coil optimization was performed on the position (X,Y,Z), and direction (X_{hat}, Y_{hat}, Z_{hat}) of all 10 TF coils. The TF coil radius was not allowed to vary as a parameter. Also included in the optimization along with the usual horizontal and vertical background fields was the background toroidal field defined by Eq. 6.1. The background toroidal field was expected to remain near 0 G field at a radial distance of R= .75 m. The optimization analysis resulted in a new coil model referred to as $IFT_{TF\text{-}post}$.

The difference in TF coil parameters between the two coil models $IFT_{TF\text{-}post}$ and $IFT_{TF\text{-}pre}$ are shown in Fig. 6.18. Modifications to the TF coil positions are small, less than 0.0005 m. Modifications made to the direction vectors are also small less than 0.0015 radians (~ 0.0005 m). These modifications are well below the uncertainty values for all TF coils.

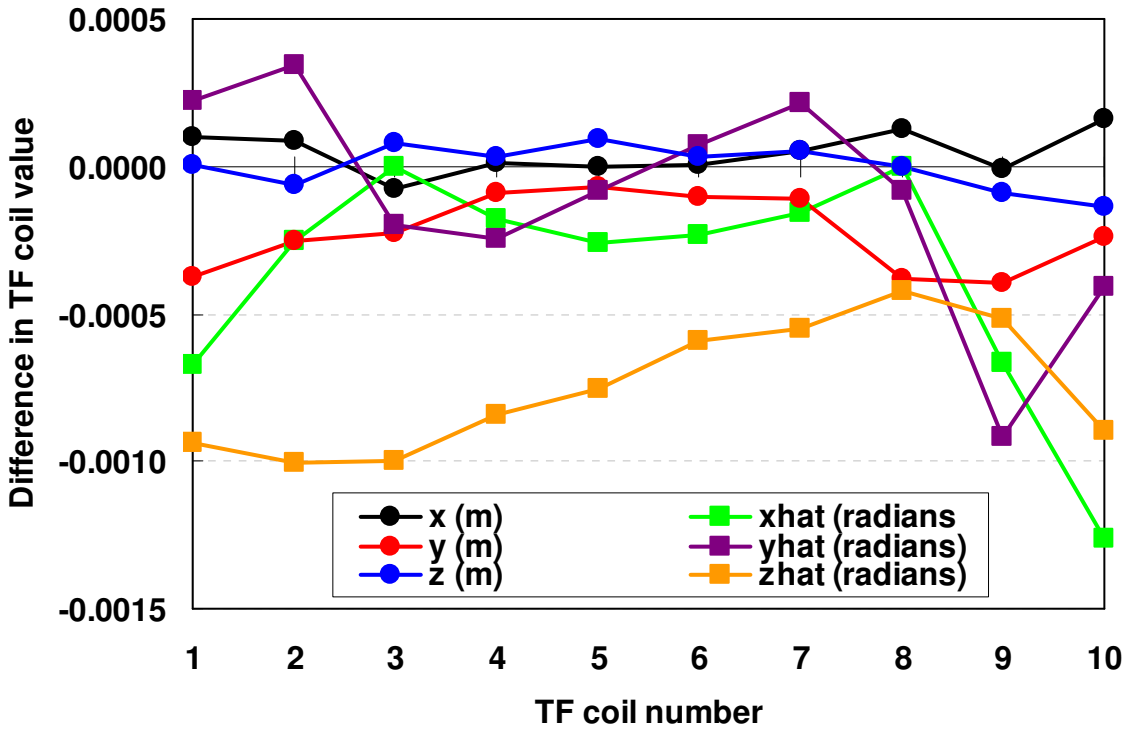

Fig. 6.18 TF coil parameter difference ($IFT_{TF\text{-}post}$ - $IFT_{TF\text{-}pre}$)

The background fields predicted by the coil optimization for the different TF data sets are listed in Table 6.12. Data sets TF-(E,F,G) were all taken the same day and therefore were assumed to have the same field. The background fields predicted are similar to those calculated during the previous field mapping studies.

	Bx East (G)	By North (G)	Bz Up (G)	Bφ (R=.75) (G)
Predicted Field	0.0	0.2	-0.4	0
TF-A	-0.4	-0.1	0.5	0.0
TF-B	1.0	0.7	-0.2	0.1
TF-C	-0.5	-0.5	-0.7	0.7
TF-E,F,G	0.6	1.1	-2.2	-0.3

Table 6.12 TF background field results

After the optimization, the coil positions and rotation transforms were again computed using the optimized coil model. The χ^2 values produced from the new model are listed in Table 6.13. Significant improvements are made in the radial position and rotational transform calculations largely due to corrections in the vertical background field. Improvements to the vertical position are more modest due to sensitivity in the vertical position of the axis to horizontal fields.

	Number of signals	χ^2 ($IFT_{TF\text{-}pre}$)	χ^2 ($IFT_{TF\text{-}post}$)
R	69	1576	22
Z	69	91	45
ι	53	1428	30
TF Coil Parameters	60	0	3
Total	191	3094	100

Table 6.13 χ^2 values of the TF coil optimization

The differences in data set TF-A between the field mapping results and those obtained through simulation using the optimized TF coil set are shown in Fig. 6.19. The jagged, saw-tooth like nature of the data points in both plots shows the effects that

magnetization is having on the radial and vertical position of the magnetic axis. During the optimization process it is assumed that the field for the entire data set is constant. With this assumption the obviously changing conditions seen in the data are neglected. The coil optimization was able to calculate a set of parameter values which split the difference between the two competing halves of data set TF-A, such that the differences are found equally spaced above and below the zero differences line.

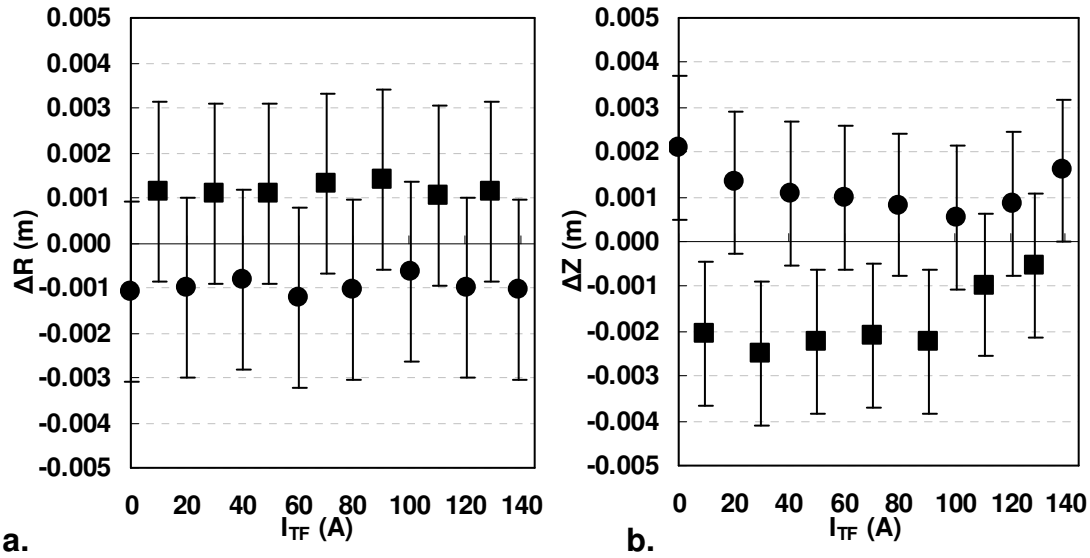

Fig. 6.19 Position differences after optimization (TF study)

It is believed that the fields produced by the TF coils caused the magnetization of ferromagnetic material which in turn resulted in the motion of the axis during the course of data set TF-A. Because the field of the TF coils is limited to the toroidal region of space immediately surrounding the vacuum vessel, as is shown in Fig. 3.17, the ferromagnetic material responsible for the axis motion must be located in this vicinity. Ferromagnetic material located near the floor and ceiling can not be blamed for these magnetization effects because the fields produced by the TF coils are minimal at those locations.

Further speculation as to the sources of the magnetic material can only be obtained by measuring the permeability of materials located near the vacuum vessel, where it was found that several of the 18" side port covers have a permeability in excess of $\mu>1.05$. Although this is a relative small permeability the large size of the port covers and their nonuniform distribution in space could lead to such magnetization effects as were seen during the TF field mapping experiment. In addition to the slightly magnetic port covers several bolts, motors, vacuum vessel diagnostics and values are found to have a $\mu>1.2$. Currently efforts are underway to reduce these sources of ferromagnetic material near the machine in the hopes of reducing the effects due to magnetization.

In conclusion, through field mapping experiments the TF coil set was shown to influence the magnetic flux surfaces as expected by raising the rotational transform profile. In order to more accurately model the experimental field mapping results small modifications were made to the TF coil model in addition to changes made to the background field. The small modifications made to the TF coils position and direction have negligible effects compared to those made by the changing background field.

6.4 Field Mapping with the OH Coils

Using the results of the previous sections, further field mapping studies were performed using the OH coils. Ideally as discussed in Ch. 3 the OH coils would not directly produce a magnetic field inside the plasma region and therefore should not affect the magnetic flux surfaces.

Initial field mapping studies performed at I_{HF} = 100 A and I_{OH} = 400 A, showed that this was not the case. The vertical position of the magnetic axis varied by 0.04 m

with the application of the OH currents. Typically vertical motion in the axis position is thought of as being caused by radial fields, in this case produced by one of the following: poor OH coil placement, poor OH coil radial construction, an electrical short present in the OH coil system, or magnetization effects which are dependent on the OH fields. Through the course of this section it will be shown that once again magnetization of ferromagnetic material is the most likely source of the radial field.

Following the initial OH field mapping investigation, a more intensive set of OH field mapping studies was performed in the hopes of determining the cause of the axis motion. During this second series of OH field mapping tests, the OH1, 2, 3 coil sets were electrically separated and field mapping experiments were performed with each set independently. During plasma operation, currents in the OH coil are typically 2.5 times larger than the currents in the HF coil. To maintain this large OH to HF current ratio during field mapping studies I_{OH} was swept from -800 to +800 A, while the HF current was maintained at I_{HF} =300 A. The experimental parameters for the various OH field mapping studies are listed in Table 6.14.

Data Set	Coils Used	I_{OH} (± 2 A)
-OH1	OH1	-800 – 0
+OH1	OH1	+500 – 0
-OH2	OH2	-800 – 0
+OH2	OH2	0 – +800
-OH3	OH3	-800 – 0
Screen Placement	φ=36º	
I_{HF} (A)	300 ± 1	
I_{TVF} (A)	42 ± .3	
TVF Turns	90	
Information Gathered	R, Z	

Table 6.14 Experimental setup of the OH1,2,3 separated study
The "+" and "-" sign in the data set label corresponds to the polarity of the OH current used during that data set. During normal plasma operation the polarity of the OH current is in the negative φ direction.

The position of the magnetic axis for the various OH data sets is shown in Fig. 6.20. When the OH coil system is used as designed, with all OH coils connected in series, the magnetic field produced inside the vacuum vessel is negligible, resulting in minimal motion of the axis. On the other hand, if the coils of the OH coil system are used independently a vertical field is produced inside the vacuum vessel, resulting in a radial shift of the axis positions. Therefore the radial motion of the magnetic axis shown in Fig. 6.20 is to be expected.

On the other hand, the vertical shift of the axis in each of the different data sets is unexpected, because if properly constructed, each OH coil set should be up/down symmetric and not produce a radial field. The OH1 coil produces a 0.015 m vertical shift, the OH2 coil produces a 0.006 m vertical shift, and the OH3 coil produces a 0.005 m vertical shift. It is conceivable that one or two of the OH coils was incorrectly aligned or poorly constructed leading to vertical motion in one or two of the data sets. But it seems highly unlikely that all three OH coil sets have errors large enough to produce the vertical shift seen of the magnetic axis in Fig. 6.20.

Before we move on it should be mentioned that there was an unexpected jump in axis position of the -OH1 data set, believed to be caused by magnetization effects still not fully understood. The jump occurred when the machine had been recently switched from running positive OH currents to running negative OH currents. Field mapping experiments witnessed this unexpected jump in axis location multiple times, produced under similar conditions. At I_{OH} = -200 A the magnetic axis rises by ~.01 m over the course of ~3 minutes.

Ruling out the other possible sources of error, we are again left with placing the blame on the complex nature of ferromagnetism. We typically think of the magnetic field produced by ferromagnetic materials as only dependent on the external field currently being applied to the material and the past magnetic history of the material. From the limited amount of data taken when the jump occurred, it appears as if the background magnetic field in this case is also dependent on the extent of time the material is subjected to the field. Further field mapping studies are needed to fully understand the mechanism which is causing this unexpected jump in magnetic axis position.

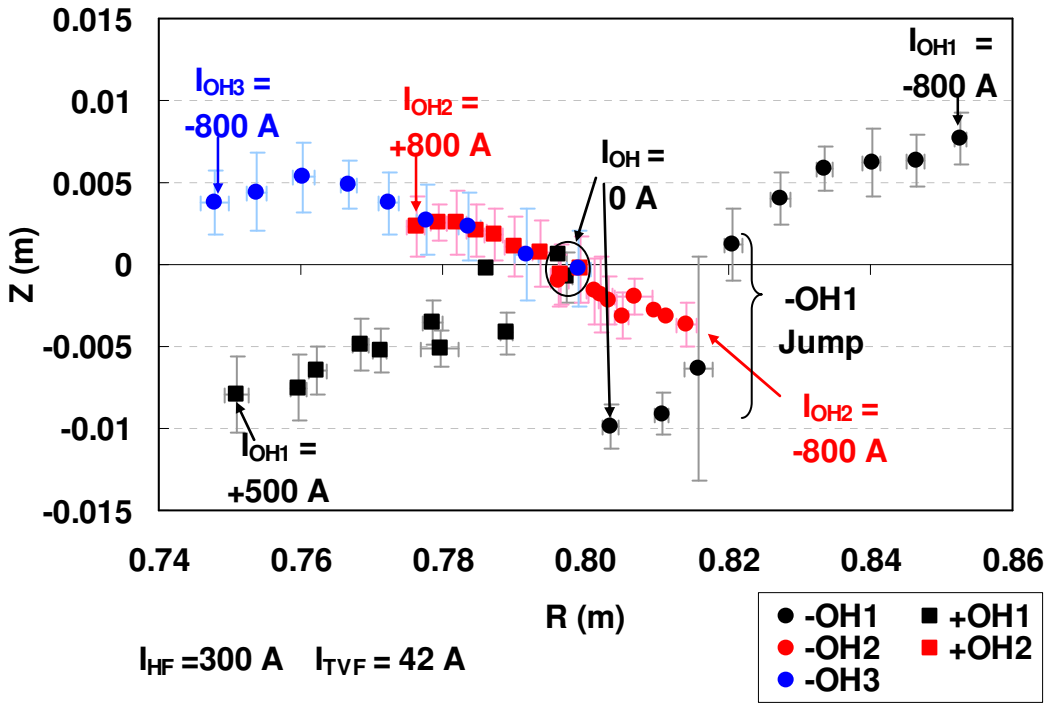

Fig. 6.20 Magnetic axis position for OH coils separated

A closer look at the locations of the magnetic axis when $I_{OH} = 0$ A is shown in Fig. 6.21 for the different data sets. The radial position of the magnetic axis varies by 0.008 m and the vertical position varies by 0.010 m, well beyond the experimental error bars and not accounted for by variations in the HF/TVF currents. The OH coil can not be

blamed for variations in the data, because these data points were taken when the OH coil was not even in use. The variations in axis position must be due to a changing background field. This is yet another example of the influence that magnetization effects are having on the magnetic axis position.

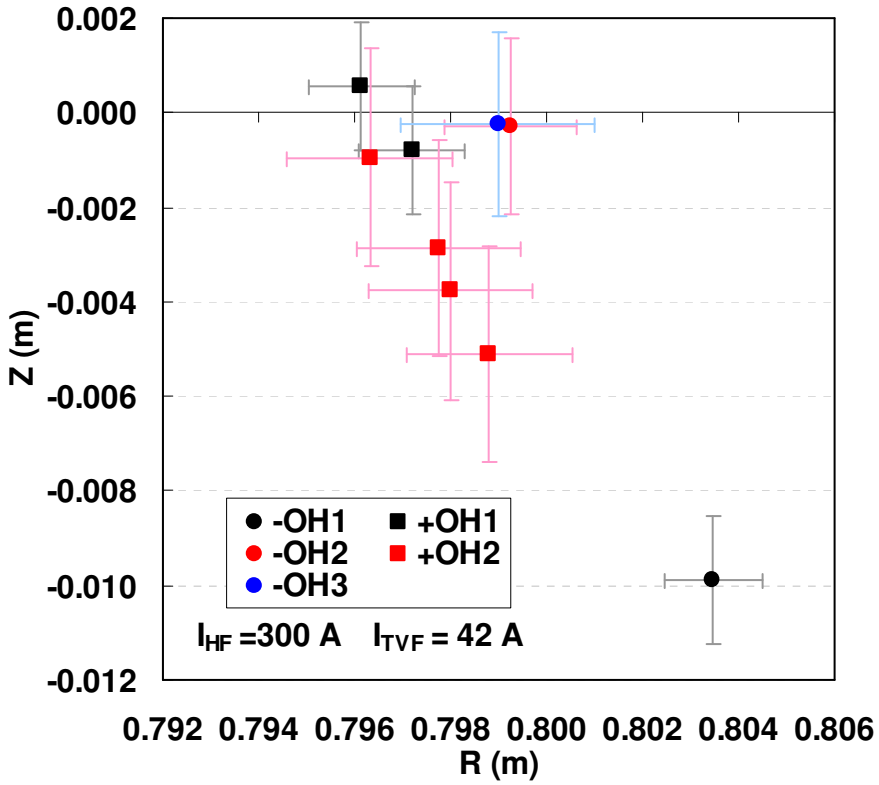

Fig. 6.21 Position of the magnetic axis while $I_{OH} = 0$ A

As mentioned earlier the vertical motion of the axis is most likely caused by an up/down asymmetry producing a radial field. A resistance test of the OH1 and OH2 coils determined that the asymmetry is not produced by an electrical short. The test was performed by measuring the decrease in voltage across the OH1 and OH2, upper and lower coils, as current was applied to OH coil system. From this, the average resistance of each coil was determined, listed in Table 6.15. Both the upper and lower coils show no

significant resistance differences. The upper OH1 coil is estimated to be missing .3 turns and the lower OH2 coil is estimated to be missing .1 turns. To comprehend a fraction of a turn, imagine only a portion of the total current passing through the electrical short with the rest passing through the regular OH coil. To reproduce the vertical shift of the magnetic axis shown in Fig. 6.20 simulation estimates require a 1.5 turn short needed in the upper OH1 coil and a .4 turn short needed in the upper OH2 coil. Therefore, although there is a slight discrepancy between the resistance measurements of the upper and lower coils, these discrepancies are not enough to explain the vertical motion of the axis. It is going to be assumed from this point forward that there is not an electrical short in any of the OH coils.

	OH1 Upper	OH1 Lower	OH2 Upper	OH2 Lower
Measured resistance (mΩ)	1.97	1.99	.83	.82
Measured missing turns	.3 ±.1			.1 ±.1
Missing turns needed	1.5		.4	

Table 6.15 OH1,2 resistance measurements

With the possibility of a short in the OH1 and OH2 coils eliminated, we next turn our attention to the position and size of the OH1 and OH2 coil sets as the possible source of the asymmetry. Using the coil optimization procedure on each coil set separately, the position (X,Y,Z), direction, (X_{hat}, Y_{hat}) and radius of the OH1 and OH2 coils were given to the optimization as parameters to vary along with the standard background field. The uncertainties on the coil position are estimated to be .002 m and the uncertainties in the coil radii are estimated to be .0005 m. In addition, in the –OH1 data set the low current data points found prior to the unexpected jump are excluded from the optimization analysis due to the suspected large variation in background field.

The coil optimization revealed that the only parameters which differed significantly from the measured values of the coils were the vertical positions of the OH(1,2) coils. The rest of the OH coil parameters remained virtually unchanged with sub-millimeter changes to their values. The designed and measured coil centers, along with the values computed by the optimization are listed in Table 6.16. We see that the optimization has lowered the position of the OH1 coil 1-3 mm from its measured values and raised the OH2 coil 3mm. Coil adjustments of this magnitude seem unlikely.

A list of the background fields calculated by the optimization for each data set are listed in Table 6.17. The optimization has predicted a large background field, 4.6 G. In order to match the experimental data the optimization had to significantly modify not only the OH coils but also the background field.

	Design value	Measure value	Post optimization	Uncertainty σ	Difference Measure - Post
OH1 Z upper	.301	.299	.298	±0.002	.0013
OH1 Z Lower	-.301	-.305	-.307	±0.002	.0025
OH2 Z upper	.748	.746	.749	±0.002	-.0032
OH2 Z Lower	-.748	-.755	-.752	±0.002	-.0032

Table 6.16 OH1,2 coil vertical positions

Background Fields	Bx East (G)	By North (G)	Bz Up (G)
Design	0	.2	-.4
+ OH1	-.5	-4.6	-1.5
- OH1	2.5	-.3	-2.5
+ OH2	-2.3	-4.6	-1.9
-OH2	-.4	-1.9	-2.0

Table 6.17 OH1,2 background fields

In Fig. 6.22(a) and (b) the magnetic axis position of the OH1 and OH2 studies are shown. The experimentally measured axis positions are plotted as the black and red

points. The green points labeled “OH coil parameters” show the computed axis position using the optimized coil parameters given in Table 6.16 and Table 6.17. The optimization had difficulty accounting for the vertical displacement of the axis in both field mapping studies. Because of the poor agreement between the experimental and simulation results, combined with the unlikely 3mm motion in the OH1 and OH2 coils, we were forced to consider another mechanism for the vertical motion of the axis. Perhaps the vertical shift in axis position is not due to the fields of the OH coils themselves but instead due to the OH coils magnetizing material which in turn creates a radial field.

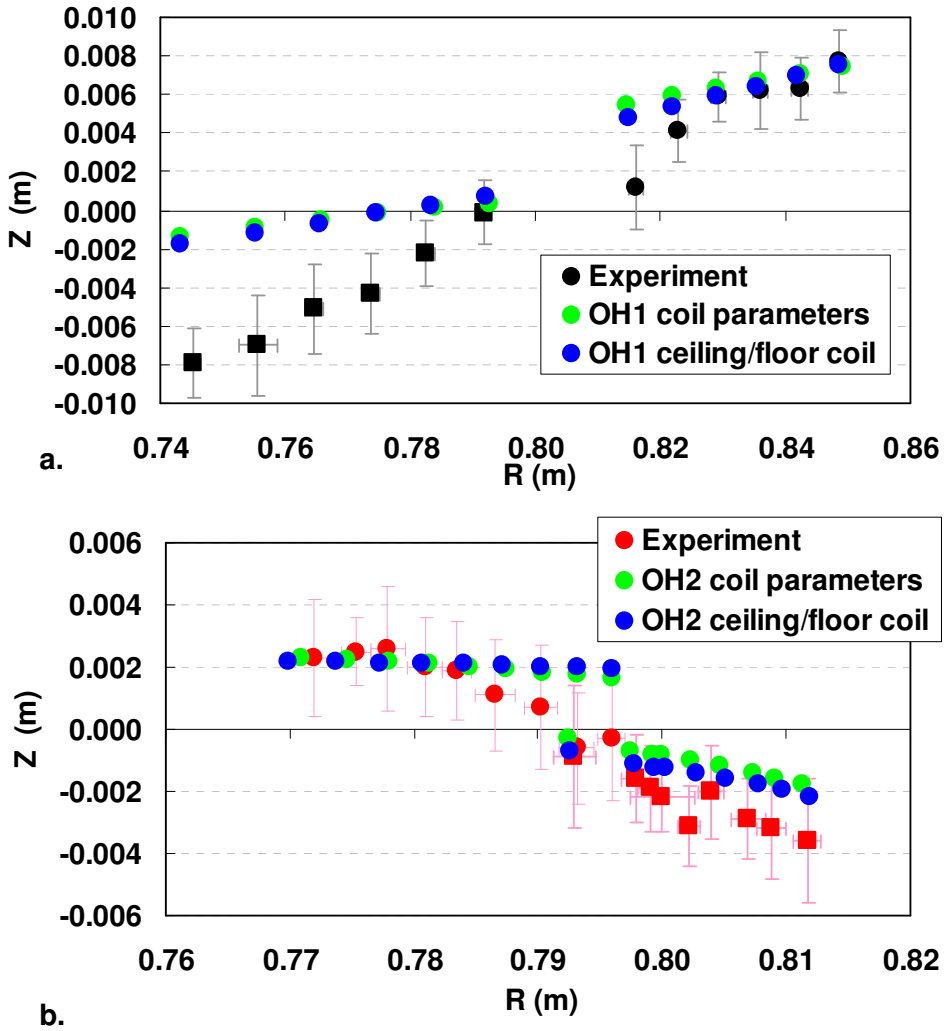

Fig. 6.22 OH results after optimization (separated OH coils)

We suspect that ferromagnetic material, in the form of structural rebar located in the floor and ceiling, is becoming magnetized by the field of the OH coils. As illustrated in Fig. 3.19 we know that the OH coil system produces significant magnetic fields that are concentrated along the central axis of the torus, with the strength of the field decreasing with increased distance from the midplane. Because the vacuum vessel is located closer to the floor than to the ceiling, 1) the floor becomes more magnetized than the ceiling, and 2) the magnetic field produced by the floor inside the vacuum vessel is more influential on the flux surfaces. Typically we think of up-down asymmetrical effects such as these producing radial fields.

In an effort to model the magnetization dependence of the floor and ceiling on the OH1 or OH2 coils, a fictitious ceiling and floor coil set was added to the simulation model. Note, these are fictitious coils used to mimic the magnetization effects and do not exist in real life. The ceiling coil was located 2.5 m above the midplane and the floor coil was located 1.6 m below the midplane (the locations of the ceiling and floor). Both coils were given a constant radius of .75 m.

The current in the ceiling coil was defined in terms of the current in the OH coil

$$I_{ceiling} = a \cdot I_{OH} . \tag{6.2}$$

Here "a" is a multiplication locking factor used in the simulation and I_{OH} is given in terms of A-Turns. Because we expect that the field produced by the ceiling coil to remain under 1 G at the midplane we require $a < 0.05$.

The field produced by the OH coils is in the same direction both above and below the machine. Therefore the magnetization of both the ceiling and floor should be in the

same direction. To ensure this, the current in the floor coil was defined in terms of the ceiling coil as,

$$I_{floor} = b \cdot I_{ceiling} . \tag{6.3}$$

Here "b" is another locking factor, with the restriction that b remain near 1, b = 1 ± 0.1.

Using the field mapping data presented in Fig. 6.20 a coil optimization was performed with the OH(1,2) data sets. The optimization was allowed to vary the ceiling and floor coils vertical position Z, radius R, and locking factors (a,b) for the fictitious coil current. The background fields were also allowed to vary for each data set just as they were previously.

The modifications made to the ceiling and floor coil parameters by the optimization are listed in Table 6.18 along with the radial and vertical fields of the ceiling/floor coils calculated on the midplane at a radial distance of R = .75 m given $I_{OH(1,2)}$ = 800 A. The ceiling and floor coils have produced fields which seem reasonable.

The computed magnetic axis positions using the modified ceiling/floor coils are shown in Fig. 6.22 by the blue points. The results of the ceiling/floor coil optimization are just as good if not better than the previous results (although neither appear to be a very good fit). Therefore since we already know that magnetization has a strong effect on the magnetic axis and we were suspicious of the optimization results performed on the OH coils vertical position, we come to the conclusion that the OH coils are constructed correctly and the vertical motion of the axis is caused by magnetization effects.

	Before optimization	After optimization (OH1 Study)	After optimization (OH2 study)
Vertical position ceiling (m)	2.5	2.511	2.579
Vertical position floor (m)	-1.6	-1.140	-1.287
Radius ceiling (m)	.75	.707	.535
Radius floor (m)	.75	.631	.783
Locking factor ceiling	0	.0126	.0136
Locking factor floor	1	1.0043	1.0035
Br (G)		.2	.1
Bz (G)		.3	.1

Table 6.18 Separated OH1,2 ceiling/floor parameters

Following the individual testing of each OH coil set separately, the OH coils were reconstructed in series to their design configuration and field mapping tests were performed on the OH coil system as a whole. The current in the HF coil was maintained at I_{HF} = 300 A, while the OH current was varied from 0 to -800 A.

The magnetic axis position for the various OH current settings is shown in Fig. 6.23. The axis is seen to travel 0.004 m radially and 0.009 m vertically. The radial shift in axis position is to be expected because even when the entire OH coil system is constructed properly, simulation shows there is still a slight downward field inside the vacuum vessel.

Using the same method to model the magnetization of the ceiling and floor as was done in the separated OH study, a coil optimization was performed on this set of field mapping data. The code was allowed to vary the background field, and the fictitious ceiling/floor coil's, radius, vertical position, and locking factor. The OH1,2,3 coil parameters were kept fixed at their measured locations. The optimized magnetic axis positions are shown in Fig. 6.23 as the solid line. Considering the complicated nature of magnetization and the simplified way in which it is being modeled the optimization did

an excellent job matching the experimental data. The ceiling and floor coil parameters determined by the optimization are listed in Table 6.19.

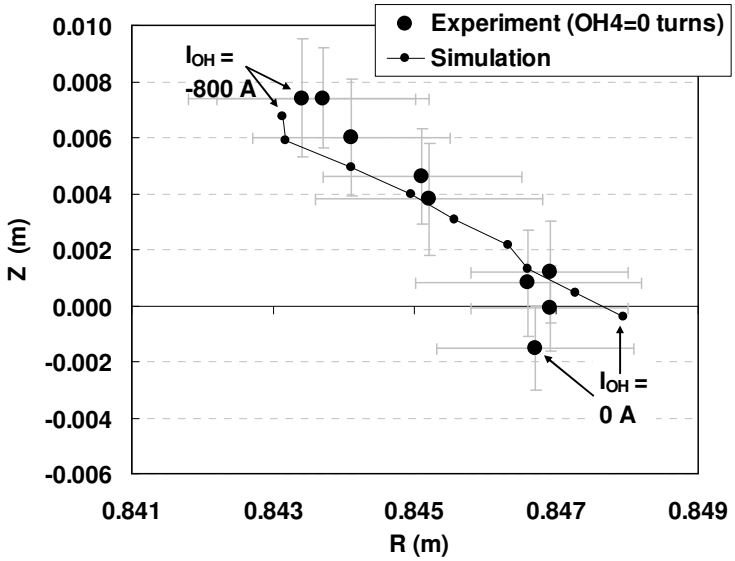

Fig. 6.23 Magnetic axis position for OH coils in series
I_{HF} = 300 A, I_{TVF} 33 A

	Before Optimization	After Optimization
Vertical position ceiling (m)	2.5	2.544
Vertical position Floor (m)	-1.6	-1.385
Radius ceiling (m)	.75	.617
Radius Floor (m)	.75	.758
Locking Factor Ceiling	0	.0252
Locking Factor Floor	1	1.0098
Br (G)		.3
Bz (G)		.6

Table 6.19 OH system ceiling/floor parameters (OH coils in series)

Lastly, in an effort to correct for the up/down asymmetry present in the OH coil system regardless of the source, an OH4 correction coil was installed inside the bottom of the upper OH2 coil. Note, as opposed to the fictitious ceiling and floor coils only used in the simulation, the OH4 coil was physically installed on CTH and connected in series to

the rest of the OH coil system. Two field mapping tests were performed with the OH4 coil. In one the OH4 coil was equipped with one turn, in the other the OH4 coil had two turns. In both tests I_{OH} was varied from 0 to -800 A.

The results of these field mapping studies are presented in Fig. 6.24. The application of the OH4 coil correction field significantly reduced the vertical motion of the axis. When the OH4 coil is equipped with 1 turn the vertical position of the magnetic axis increases by only 0.004 m as I_{OH} was increased to -800 A, whereas when the OH4 coil was equipped with 2 turns the vertical position of the magnetic axis actually decreases by -0.001 m as I_{OH} was increased to -800 A. A two turn OH4 correction coil permanently installed on CTH with a radius ~.3 m located .75 m above the midplane should be adequate to minimize the vertical motion of the axis. Final adjustments to the vertical position of the OH4 coil can be determined through further field mapping tests.

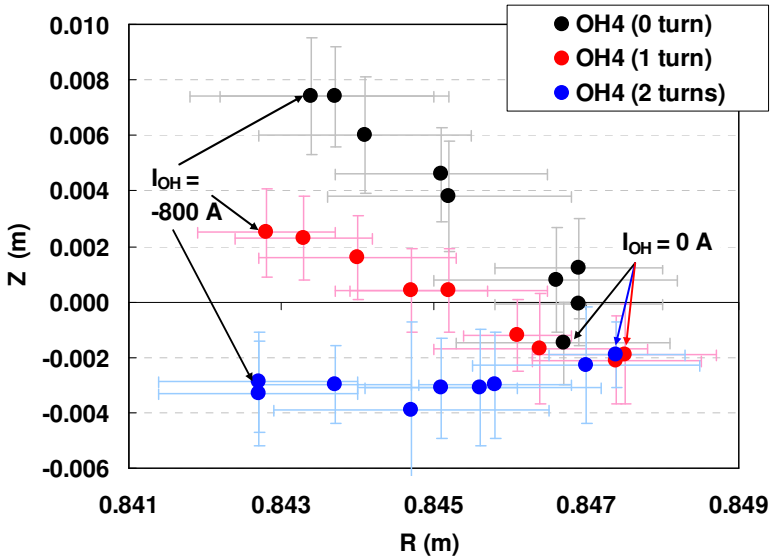

Fig. 6.24 OH4 coil field mapping results

Concluding this section, field mapping experiments were performed with the OH1, OH2 and OH3 coils independently. The results of these studies showed that a radial

field was produced by all the OH coils. Resistance measurements determined that the coils did not have an electrical short large enough to account for the vertical shift seen in the magnetic axis position. A coil optimization performed on the OH1 and OH2 coils' position and size revealed that the coils' vertical position must be altered 1- 3mm from their measured position. This significant change in coil position seemed unlikely and a better explanation was desired with magnetization of material in the ceiling and floor considered to be the cause of the magnetic axis vertical motion. A coil optimization analysis performed on the OH1 and OH2 data revealed that fictitious ceiling and floor coils representing the magnetization of the ceiling and floor can produce radial fields similar to those seen field mapping.

Another field mapping study performed on the OH coil system as a whole revealed similar vertical motion of the axis. The vertical motion was again attributed to magnetization of the ceiling and floor and was modeled in IFT with similar ceiling and floor coils. To correct for the vertical motion of the axis, an OH4 coil was installed equipped with 1 or 2 turns. Field mapping tests performed with the entire OH coil set including the new OH4 coil revealed that the vertical shift in the axis location can be controlled and mitigated by the addition of the OH4 coil.

6.5 Concluding Remarks

First and most importantly, field mapping experiments performed on CTH have verified the existence of closed magnetic flux surfaces contained within the vacuum vessel necessary for good plasma confinement.

Second, the positions and rotational transforms of the experimentally measured magnetic axis can be adequately simulated using a coil model based on the physically measured coils. Modifications made to the coil model through the use of the coil optimization routine improve the agreement between the simulation and experimental data. Because only slight modifications to the coil model were needed to simulate the experimental data, the CTH coils are believed to be constructed and operating within the coils' designed tolerance specifications without any major defects. With that said, it should be mentioned, that in order to accurately simulate the rise of the magnetic axis above the midplane at large TVF currents, modifications were made to the up-down symmetry breaking terms in the HF coil winding law. These HF coil winding law coefficients have significantly more influence on the magnetic axis than the other circular coils parameters.

Third, throughout the chapter we have seen evidence that the magnetic axis is sensitive to the background field; which, due to the existence of ferromagnetic material in the vicinity of CTH, can change significantly. Therefore, in addition to the modifications made to the CTH coils themselves, further improvements are made to the coil model by allowing the optimization routine to calculate the background field for each field mapping experiment separately. These further improvements to the background field are often times more significant in determining the position of the axis than the modifications made to the CTH coils themselves.

The background field for each of the data sets (except the TF and OH) was assumed to be a uniform horizontal and vertical field, constant throughout the entire data set. By making this assumption the radial, poloidal and toroidal components of the

background field which one should also assume to exist are neglected. Also neglected are changes in the magnetic background field that occur within the data set. Lastly, this assumption neglects the fact that the background field is not uniform in space but is composed instead of many magnetic dipole fields created by ferromagnetic material and unwanted extraneous current loops (electrical feeds).

To overcome some of these issues I have several suggestions.

1. IFT should be given additional radial and poloidal background field coils to enhance the background field already in place.
2. To ensure that changes in the background field that may have occurred during the course of the data set are accounted for, the background field should be calculated for each field mapping data point separately instead of for the whole data set.
3. To more accurately model the background field dependence on the current in the CTH coils, the current in fictitious magnetization coils could be linked to the CTH coil currents. This method was demonstrated in the OH study, where a radial field dependent on the OH current was needed to accurately describe the OH field mapping data.
4. Lastly, in the simulation model, dipole current loops could be placed at suspected locations of ferromagnetic material, but without accurate knowledge about the ferromagnetic material involved in creating the background field (what it is, its past history etc.) incorporating accurate magnetic dipole current loops in the simulation is going to be difficult.

CHAPTER 7: MAGNETIC ISLANDS

7.1 INTRODUCTION

In Ch. 6, the model of CTH coil sets was developed which more accurately described the experimental field mapping results performed with the magnetic axis data. This coil model incorporated small modifications to the physical description of the CTH coil sets and suggested that the background field of the laboratory was significantly larger and more complicated than previously believed. The small deviations of the constructed coils from their designed specifications and the existence of background fields break the designed up-down and field period symmetry of the magnetic field. This broken symmetry results in the creation of perturbation magnetic fields that in turn generate magnetic island on low order rational flux surfaces.[41, 42]

A photograph of the ι=1/3 flux surface in the presence of a perturbative magnetic field is shown in Fig. 7.1(a). This magnetic island flux surface differs from the unperturbed flux surface in Fig. 7.1(b), in that the island flux surfaces has several distinctive physical features not present in non-island flux surfaces. These features are the O-points, X-points, and the separatrix.[43] with their properties discussed in detail in Sec. 7.2.

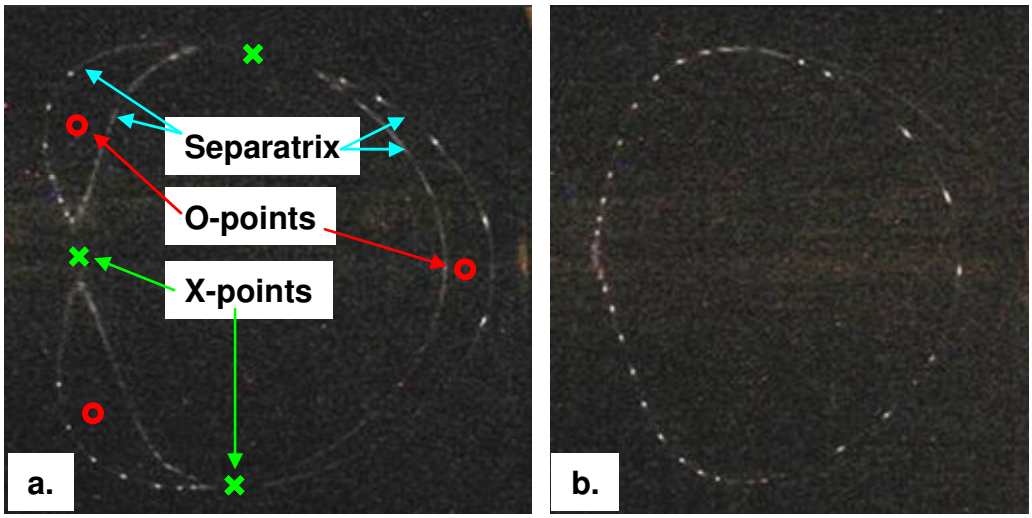

Fig. 7.1 1/3 magnetic island surface

The study of magnetic islands is important because the existence of magnetic islands nested within the set of closed flux surfaces can significantly increase or decrease the radial transport of particles and energy across flux surfaces depending on the plasma conditions. [44,45] Therefore, accurate knowledge and control of any islands within the plasma is essential for obtaining good plasma confinement.

The purpose of this chapter is to demonstrate how the magnetic islands observed in the vacuum field configurations of CTH were measured and manipulated. To do this, field mapping measurements are made on a particular set of magnetic islands in CTH. Through simulation, the perturbation fields that created the measured islands are predicted. Lastly, a correction field is applied opposite to that of the predicted perturbation field using a set of error correction coils.

7.2 Magnetic Island Properties

The components of the perturbation field that are perpendicular to the flux surface are responsible for the creation of the magnetic island. Assuming a flux surface with a

circular cross-section, the perturbation field perpendicular to the flux surface can be represented by its Fourier spectrum according to Eq. 7.1.

$$B_{pert} = \sum_{n=1}^{\infty}\left(\sum_{m=1}^{\infty} B_{m,n} \cdot \mathrm{Cos}(m\theta + n\varphi - \delta)\right) \tag{7.1}$$

Here m is referred to as the poloidal mode number, n is the toroidal mode number, δ is a phase angle shift, and the coefficients $B_{m,n}$ represent the strength of each Fourier component. Recall that on a rational flux surface, m is also the number of toroidal circuits made by a field line and n is the number of poloidal circuits such that the rotational transform is defined as ι=n/m.

Symmetry breaking perturbation fields can be caused by either internal perturbations from the coils themselves, or external errors caused by background magnetic fields. During the design process of CTH, the coils were optimized to not produce significant magnetic islands,[15] therefore any significant internal perturbation fields created by the coils are caused by imperfections in the constructed coils. These include the dipole fields created at the electrical feeds of the coils, the electrical input lines to the coils, or any winding defects in the coils themselves. External perturbations of the magnetic field include the magnetic field created by the ferromagnetic materials near the CTH vacuum vessel discussed in Sec. 5.3 and the earth's field. In general internal errors vary linearly with the applied coil current, while external errors do not as discussed in Sec. 7.6.

The creation of magnetic islands by a simple perturbation field is illustrated in the following simulation example. The simulated islands exhibit similar features as the islands observed on CTH. A uniform horizontal perturbation field with magnitude 1 G

and direction φ=0° is applied to the coil model developed in Ch. 6, producing a 1/3 island near the last closed flux surface, as seen in Fig. 7.2. The currents in the simulation coils are; I_{HF}=280 A, I_{TVF}=38 A, I_{SVF}=27 A, I_{TF}=93.8 A.

Shown in Fig. 7.2(a) are two toroidal cross-sections of the vacuum vessel, at φ=180° and φ=0°. The perturbation field is parallel to the cross-sectional plane of the vacuum vessel at these locations. Shown in Fig. 7.2(b) is a surface of section plot of the 1/3 island at these two toroidal locations. The graph on the left is at a toroidal location of φ=180°, a side port location where the surfaces are vertically compressed and shifted radially outward. The graph on the right is taken at φ=0°, a top/bottom port location, where the surfaces are vertically elongated and shifted radially inward. The horizontal axes of both graphs is a measure of radial distance with negative radial values for the φ=180° plot and positive radial values for the φ=0° plot. In this way, the error field is directed to the right in both graphs and the central axis of the machine is located between the two plots.

Magnetic island flux surfaces have three basic physical features; O-points, X-points and the separatrix. The O-points and X-points are fixed points[46] meaning they return to the same poloidal location after m toroidal transits, 3 in this case. The numbers next to each fixed point in Fig. 7.2(b) represent the number of toroidal circuits the field line has undergone at that point. In both plots, the fixed points rotate in the positive poloidal direction, which appears backwards in the φ=180° plot because we are viewing the poloidal plane from the back side.

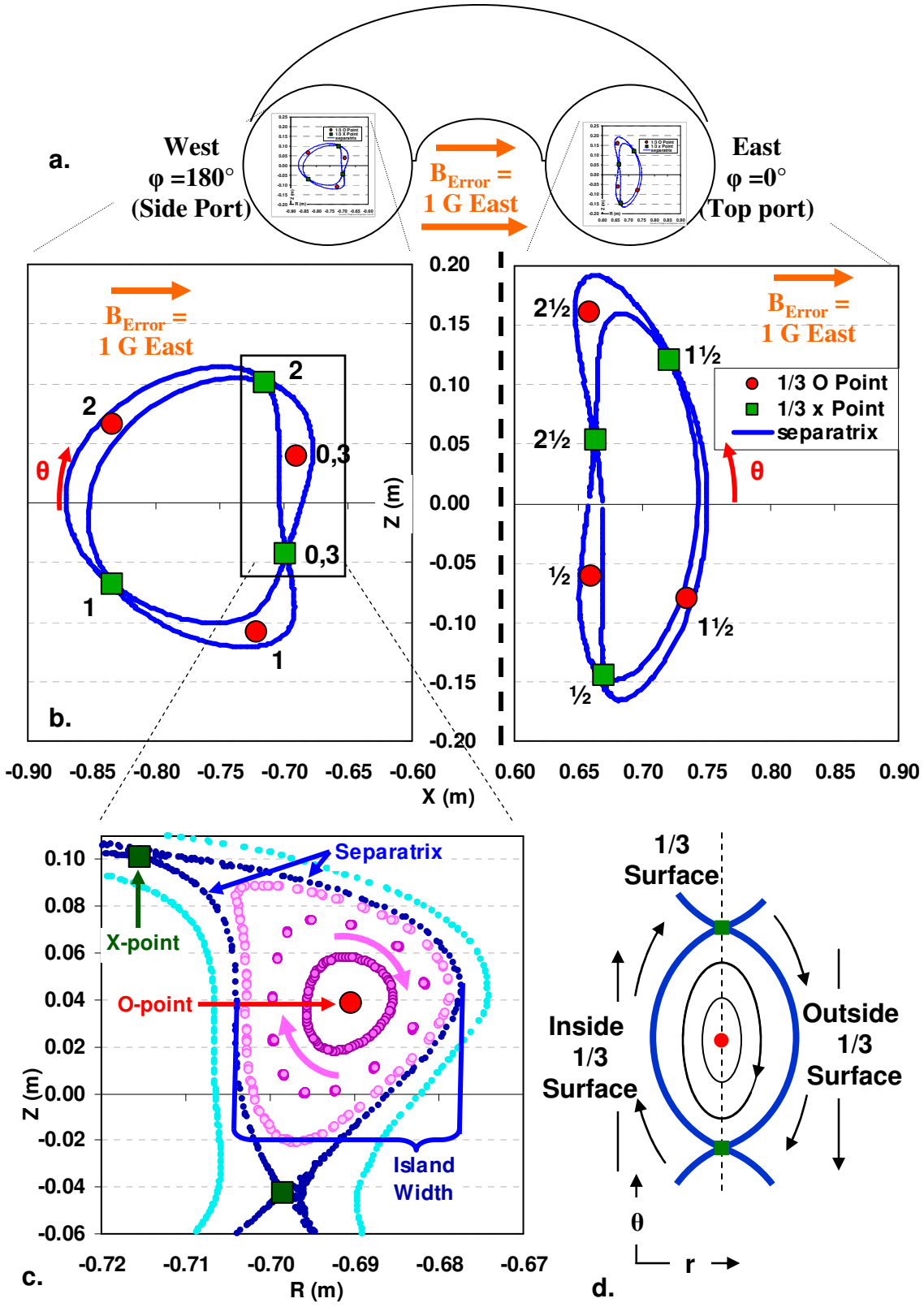

Fig. 7.2 1/3 magnetic island simulation

Shown in Fig. 7.2(c) is a detailed view of the island structure around the upper right O-point in the φ=180° chart. The O-point, shown in red, is at the center of the island. There are closed nested flux surfaces surrounding the O-point similar to the surfaces surrounding the magnetic axis. In this way, the O-point and the magnetic axis are very similar fixed points known as attractors. Field lines located near an O-point will remain near the O-point as the field line undergoes its toroidal rotation. The separatrix, shown in dark blue, is the last closed flux surface of the island that forms its boundary. The X-points, shown in green, are fixed points located where the inner separatrix surface meets the outer separatrix surface. Field lines inside the boundary of the two separatrix surfaces near an X-point (pink points) will migrate away from the X-point revolving around the O-point as the field line undergoes its toroidal rotation. Field lines outside the boundary of the two separatrix surfaces near an X-point (aqua points) will migrate away from the X-point circling the magnetic axis as the field line undergoes its toroidal rotation.

Lastly in Fig. 7.2(d) is a schematic diagram of an island structure showing the direction of the field lines relative to the 1/3 flux surface. In this diagram, the 1/3 surface is designated by the dashed line. Inside the 1/3 flux surface the rotational transform is less than 1/3 and the field lines rotate in the positive θ direction relative to the 1/3 flux surface. It should be mentioned that field lines inside the 1/3 flux surface still have a positive poloidal rotation and only relative to the 1/3 surface do we say their rotation is negative. Outside the 1/3 flux surface the rotational transform is greater than 1/3 and the field lines rotate in the negative θ direction relative to the 1/3 flux surface.

The simulated island shown in Fig. 7.2(b) was created with an error field in the φ=0° direction. Next let's observe the simulation island when the direction of the perturbation field is rotated in the toroidal direction, keeping the magnitude of the field strength fixed. In Fig. 7.3, a surface of section plot at the toroidal location φ=180° shows the 1/3 island O-point locations vs. the directions of the error field. The horizontal axis is now the usual radial measure with east to the left and west to the right, opposite that of the vacuum vessel diagram to the left and Fig. 7.2(b).

The original O-points we have seen previously were generated with a 1G error field directed east (φ=0°), represented by the large red points. As the toroidal direction of the error field is increased, the O-point undergoes negative poloidal rotation, until it returns to its original poloidal location. The X-points of the island move in a similar fashion. Changing the direction of the external error field does not significantly change the size of the island.

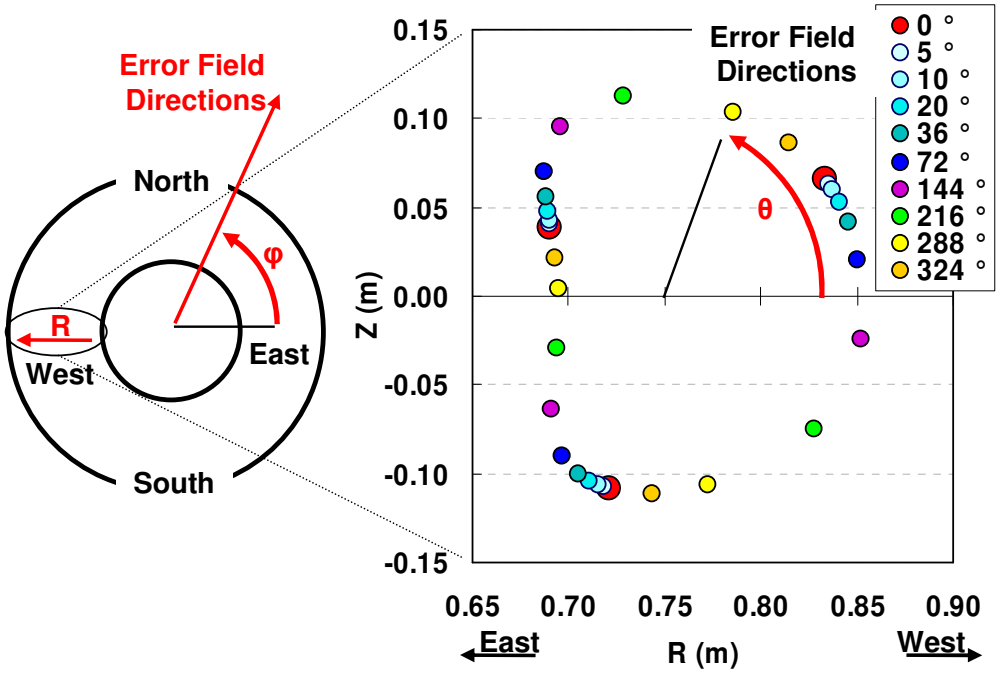

Fig. 7.3 1/3 O-point position vs. error field direction

Next let's observe the island when the perturbation field is kept fixed in the φ=0° direction but the magnitude of the field strength is varied. Shown in Fig. 7.4 are the locations of the 1/3 O-points at φ=180° for various external error field magnitudes from +2 to -2 G. A -2 G field in the φ=180° direction is identical to a +2 G field in the φ=0° direction. Once again the horizontal axis has been adjusted such that east is to the left in the plot. The existence of the 1/3 island structure is due in part to the externally applied field but also due to the slightly asymmetrical coil model (determined in Ch.6) used in this simulation.

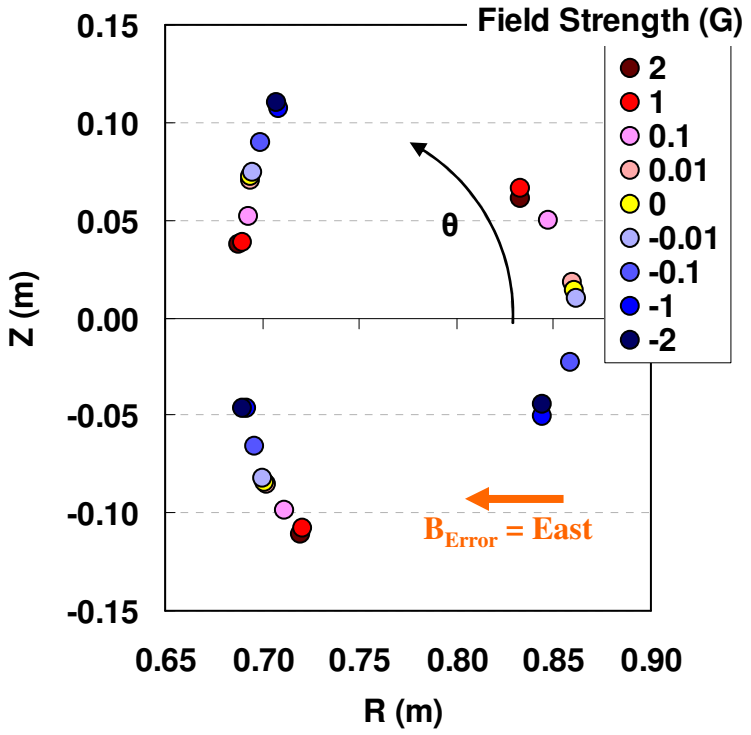

Fig. 7.4 1/3 O-point position dependence on field strength

When the magnitude of the error field is sufficiently large ($|B_{error}| > 1$), the O-point locations are determined predominately by the external field and their locations remain nearly constant. When there is no external error field the O-point locations are

determined exclusively by the asymmetries associated with the coil model. As the external field strength is decreased from positive to negative values, the locations of the O-points rotate in the negative poloidal direction. Also as one would expect, the locations of the O-points for the -1 G error field coincide with the locations of the X-points for the +1G field shown in Fig. 7.2(b).

Next, let's observe the island width as it depends on the strength the perturbation field. In Fig. 7.5(a,b,c) the separatrix surface is shown for various external field strengths. The rotation of the island shown in Fig. 7.4 can be seen when the field strength is varied in addition to a drastic change in island width. From plots such as these of the island separatrix surfaces, estimates are made of the island width across the widest portion of each island. The island width dependence vs. the error field strength is shown in Fig. 7.5(d). As the error field strength is decreased to zero the island width becomes small (~0.005m) but never zero due to the asymmetrical coil model used for the simulation. Increasing the external error field in either direction increases the island width.

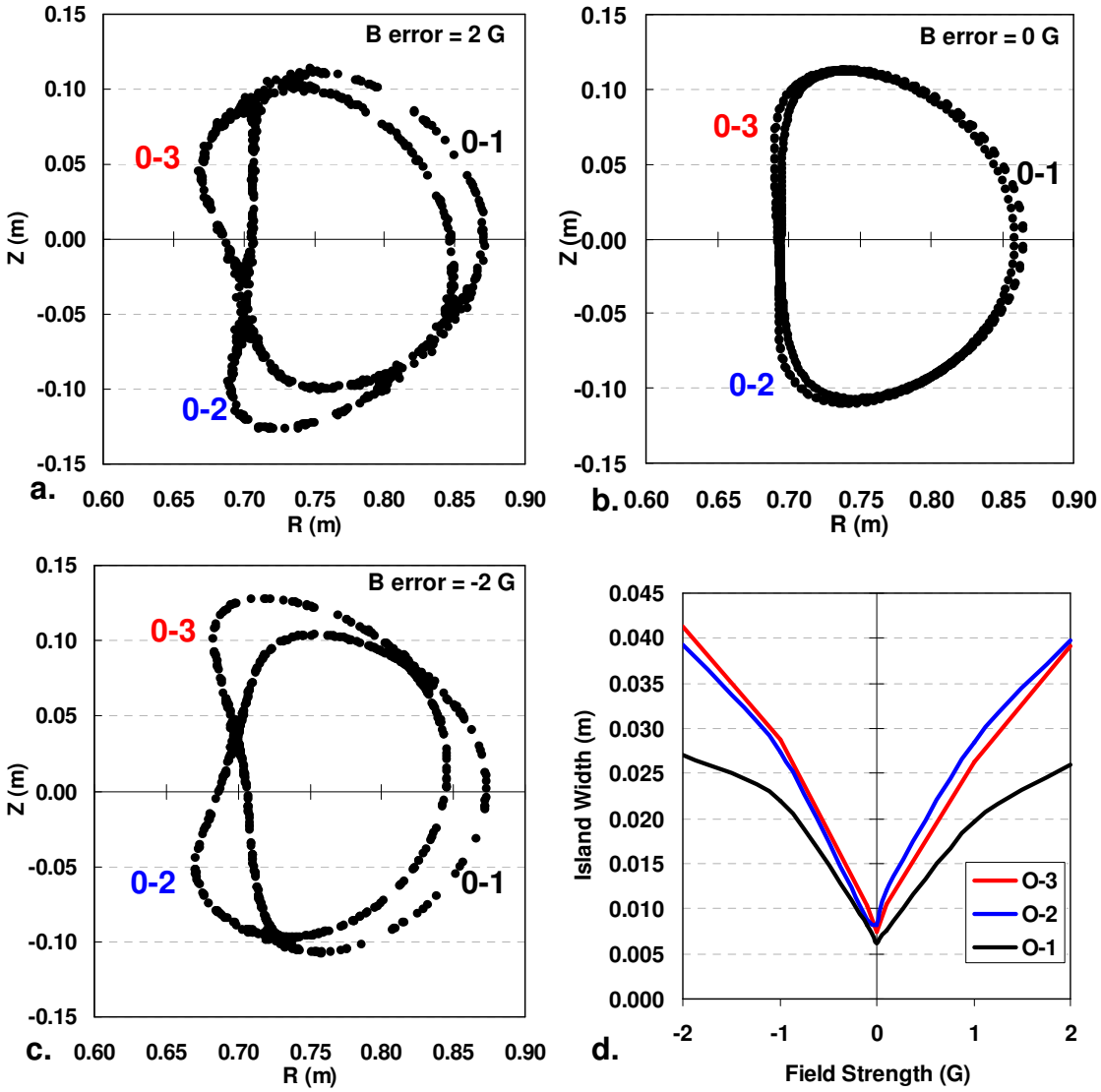

Fig. 7.5 Island width dependence on external error field

7.3 Initial Field Mapping Measurement of the 1/3 Magnetic Island

Field mapping experiments were performed with the wand at the φ = 180° toroidal location. These field mapping experiments were intended to measure the location of the O-points and X-points of the 1/3 magnetic island along with the width of the island separatrix. The island structure visible at the ι = 1/3 rational flux surface was chosen for analysis because of its relatively large size, and its ease of production with TF coil

current. The currents in the HF, TVF, and TF coils were I_{HF}=300 A, I_{TVF}=37.5 A and I_{TF}=90.7 A. The TVF coil was equipped with 108 turns during the experiments. The stochastic effects often apparent in the last closed flux surface were avoided by positioning the $\iota = 1/3$ surface inside at least one clearly defined flux surface but still near the outer edge of the flux surfaces.

A photograph of the 1/3 island with the electron gun located just inside the separatrix surface is shown in Fig. 7.6(a). Positioning the electron gun tip on the actual separatrix, such that both inner and outer portions of the entire island surface are illuminated simultaneously is extremely difficult and photographs such as the one shown in Fig. 7.6(a) are often used as a estimate for the separatrix surface. From this photograph the location of the island X-points along with the width of the island at its widest location are determined.

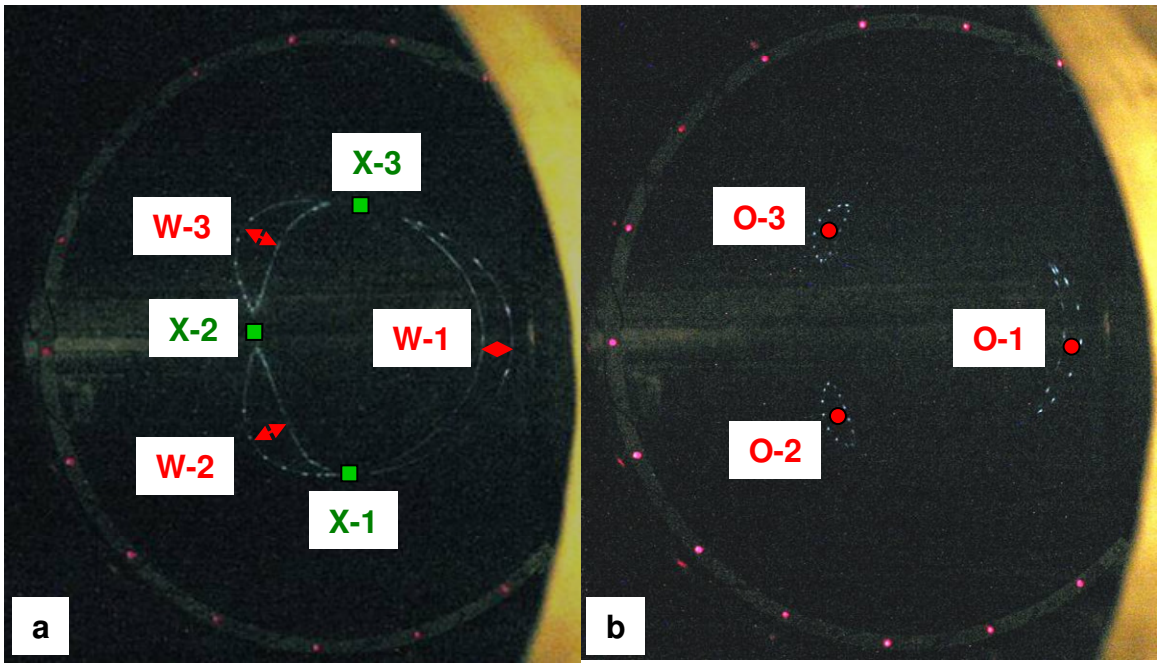

Fig. 7.6 1/3 island photographs

A photograph of a surface near the 1/3 island O-point is shown in Fig. 7.6(b). As with the data collection method for the magnetic axis, if the gun is inserted too far into the island the gun tip will block the electron beam on the second pass and only several points of light will be visible on the screen. Therefore photographs such as the one shown in Fig. 7.6(b) are used to obtain the island O-point locations.

The locations of the fixed points are extracted from the photographs in Fig. 7.6 with the same technique used to compute the magnetic axis locations discussed in Ch. 4. The locations of these fixed points are listed in Table 7.1 along with the width of the island separatrix. Error bars on the O-point and X-point locations are 0.01 m in the radial and vertical directions. Error bars on the island width are estimated to be 0.005 m.

	Radial Location (m)	Vertical Location (m)	Island Width (m)
O-1	.890	-.020	.030
O-2	.660	-.075	.037
O-3	.665	.086	.037
X-1	.746	-.122	
X-2	.660	.009	
X-3	.758	.120	

Table 7.1 1/3 island measurements

7.4 Determining the Error Field

The simulated islands shown in Sec. 7.2 were manipulated by varying the horizontal background field producing the island. Now, using the same island manipulation techniques we are going to match the fixed points locations of the simulation island to those found through field mapping by making modifications to the horizontal (n=1) error field. Although the actual error fields producing the island are composed of a spectrum of m and n values containing both horizontal and vertical fields,

the island can be simulated with a simple n=1 horizontal field. By determining the horizontal field creating the island, an appropriate correction field can then be applied through the side error correction coils in the opposite direction to reduce the island size.

The various modifications made to the vertical and horizontal background fields are shown in the sequence of charts in Fig. 7.7. In Fig. 7.7(a) the direction of the horizontal field is rotated through a range of toroidal angles. When the horizontal field is in the $\varphi = 112°$ direction the island is rotated to approximately the correct position such that the simulation O-points are aligned with the experimental O-points. Second, in Fig. 7.7(b) the vertical field of the lab is increased to +0.8 G upward, raising the rotational transform and moving the flux surfaces inward such that all three O-points are aligned with the experimental data. Lastly in Fig. 7.7(c) the horizontal field strength is decreased to 0.8 G such that the island width of the simulation island approximately matches the experimental island width. In Fig. 7.7(d) the simulated island separatrix is shown along with the experimental O and X-points with good agreement between the two sets of data. Therefore to produce an island with properties similar to those determined by field mapping, the simulation island requires a 0.8 G horizontal error field directed in the $\varphi = 112°$ toroidal direction along with a 0.8 G vertically upward field.

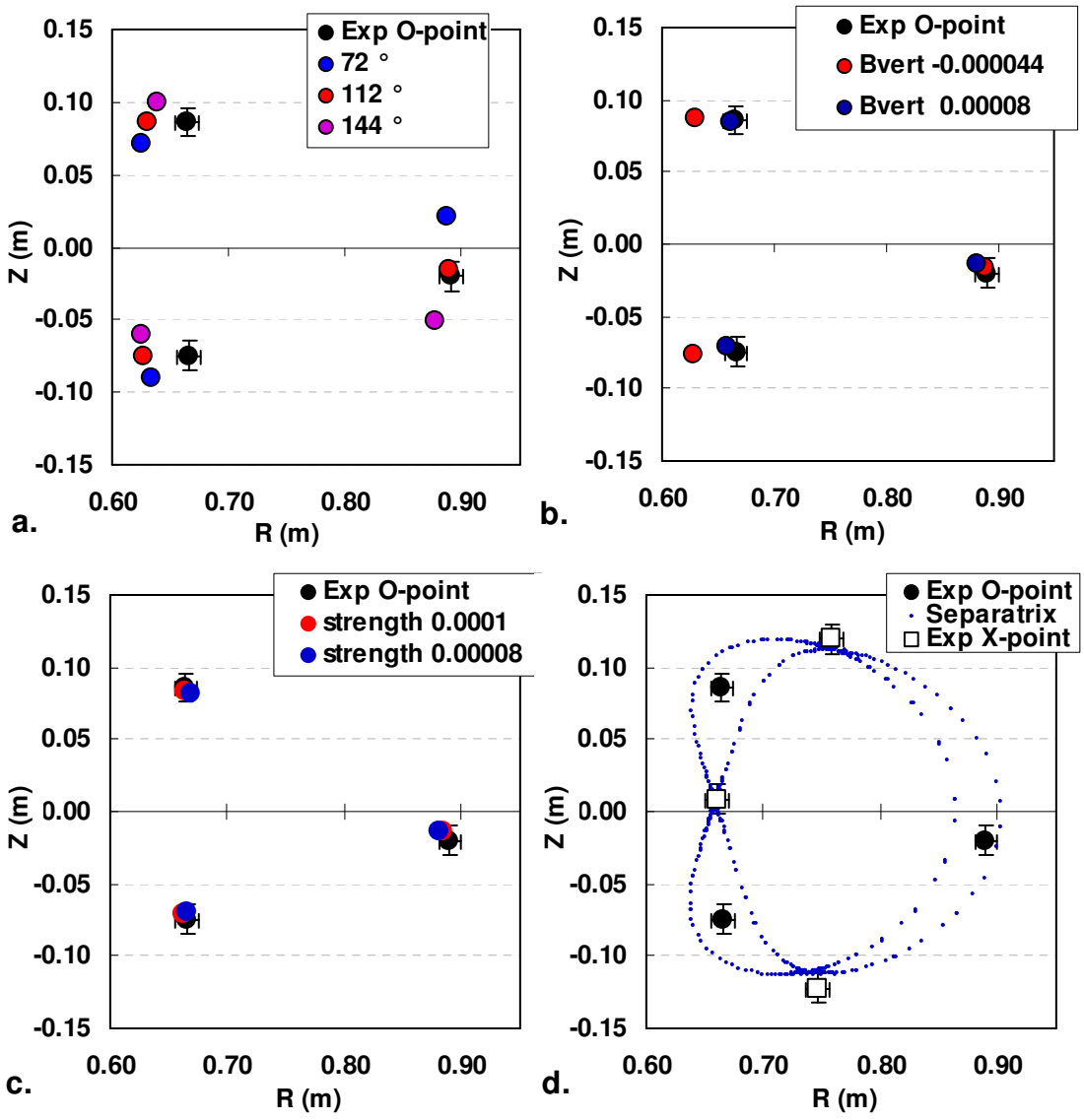

Fig. 7.7 Matching the simulated and experimental islands

The goal of island field mapping studies is not only measure the island but to minimize the island size with a set of error correction coils (ECCs). The ECCs are mounted on all side, top, and bottom ports of the vacuum vessel with the same circular diameter as the port tubes (0.40 m and 0.20 m). The various toroidal and poloidal locations of the ECCs allow both horizontal and vertical correction fields to be produced.

This allows the ECCs to produce perturbation fields targeting specific islands with various m and n values.

Through the analysis above, it was shown that the island can be adequately simulated with a horizontal error field. Therefore a counteractive n=1 error field equal in magnitude but opposite in direction to the one responsible for the island should reduce the island size. To produce a horizontal field of this nature, the five error correction coils mounted on the side ports of CTH were used with the appropriate current in each coil. The ratio of currents for the various side coils necessary to produce the error field was computed from Eq. 7.1, setting m=3, n=1, θ=0°, δ=112° and φ being the five toroidal locations of the side coils. The term $B_{m,n}$ will eventually be varied but for now we set $B_{m,n}$ =1. The relative currents values are listed in Table 7.2 labeled as "Primary ECC Ratio", normalized such that the current in the φ=108° coil is one.

ECC Location	Primary ECC Ratio ($\vec{P}$)	Secondary ECC Ratio ($\vec{S}$)
36°	.234	1.000
108°	1.000	0.081
180°	.384	-0.950
252°	-.763	-0.668
324°	-.855	0.537

Table 7.2 ECC current ratios

The primary current ratio listed in Table 7.2 was first obtained from a newly developed Fix Stellarator code (FS)[47],[48] for an earlier island experiment. In that experiment the current ratio successfully altered the 1/3 island. Subsequent efforts to use FS have been unsuccessful in producing a similar current ratio for the island information shown in Fig. 7.6. In the interest of machine run time and because we knew that the ratio

above successfully altered the island we adopted it for the island minimization presented below. Therefore the procedure previously discussed illustrates how one would obtain the current ratio but was done after the experiment was completed.

7.5 MINIMIZING THE ISLAND SIZE

Next, experiments were performed to minimize the island size with a set of error correction coils. Keeping the primary current ratio ($\vec{P}$) of the correction coils fixed, the multiplication factor (I_p) of the current ratio was varied from I_p = 45 to 182 A. Here I_p is acting as the term $B_{m,n}$ in Eq. 7.1. The current applied to each correction coil in the primary sweep is determined by Eq. 7.2.

$$\vec{I}_{applied} = I_p \cdot \vec{P} \tag{7.2}$$

In Fig. 7.8 the field predicted through simulation to be responsible for creating the island is shown at φ=112°. In the opposite direction are the correction fields produced by the ECCs in the primary sweep. The correction fields shown in Fig. 7.8 are an average of the ECC fields inside the volume of the vacuum vessel as obtained from computation. The prediction of the 0.8 G horizontal field from the simulation was never reached because the island was minimized well before that point.

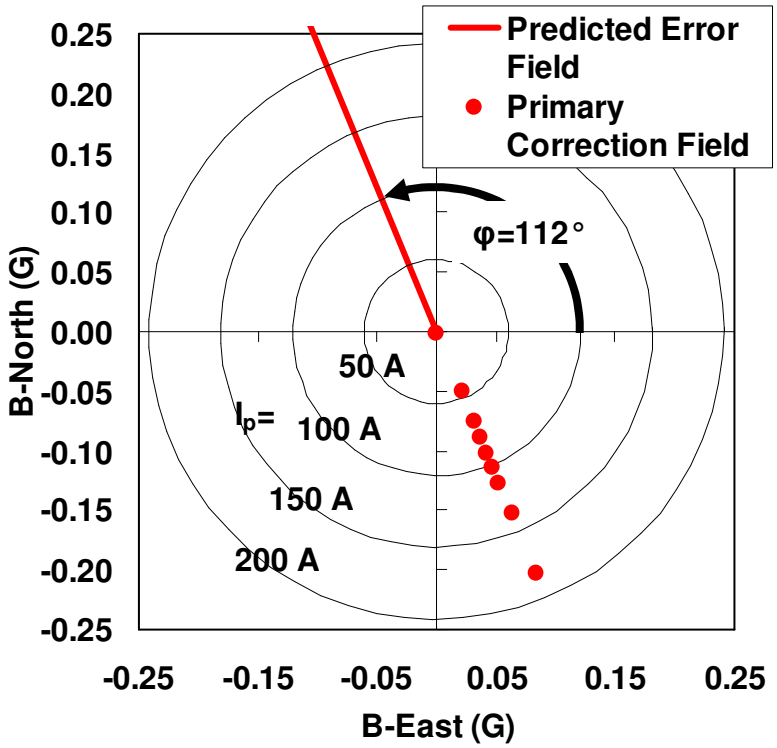

Fig. 7.8 Primary sweep current magnifications
The concentric circles represent the values of I_p used during the primary sweep. The horizontal and vertical axes correspond to the field strengths brought about by current values.

Photographs of select island separatrix surfaces are shown in Fig. 7.9 at various stages of correction. The original island is shown in Fig. 7.9(a). As I_p is increased in Fig. 7.9 (b) the fixed points' positions appear unchanged but the island size is decreased. Further increase in I_p (Fig. 7.9 (c)) results in a significantly smaller island, and in fact the island has become small enough that clearly distinguishing the island fixed points becomes difficult. The surface still appears to maintain a non-zero island width, suggesting that yet further improvements could be made with modifications to the correction field. Lastly, yet further increase in I_p (Fig. 7.9 (d)) yields an island structure comparable in magnitude to that seen originally although now the island fixed points are completely out of phase from the original island. The O-points of the original island are

now at the approximate locations of the X-points of the overcorrected island and visa-versa. At this point the field produced by the ECCs is overpowering the original error field and creating its own island structure.

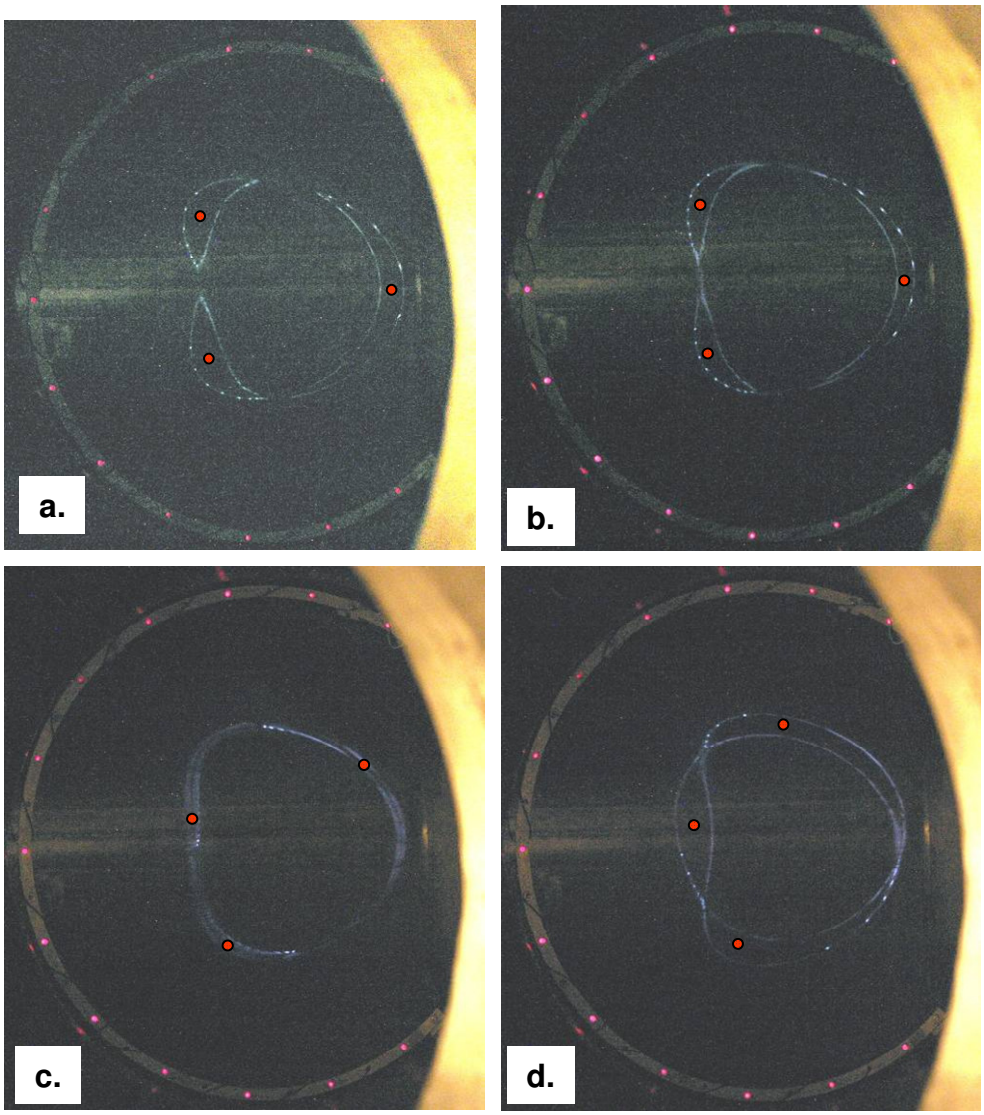

Fig. 7.9 Primary sweep results

a)	Original Island	I_p =0 A
b)	Primary Under Corrected	I_p =45.6 A
c)	Primary Corrected	I_p =79.8 A
d)	Primary Over Corrected	I_p =182 A

Through photographs such those shown in Fig. 7.9 the O and X-point locations were determined shown in Fig. 7.10(a, b). The initial island O and X-point locations are

shown as the dark red points labeled “0”. As the magnitude of the correction field is increased, the O and X-points undergo a poloidal rotation until the fixed points remain stationary at large correction field values, when the island has been overcorrected.

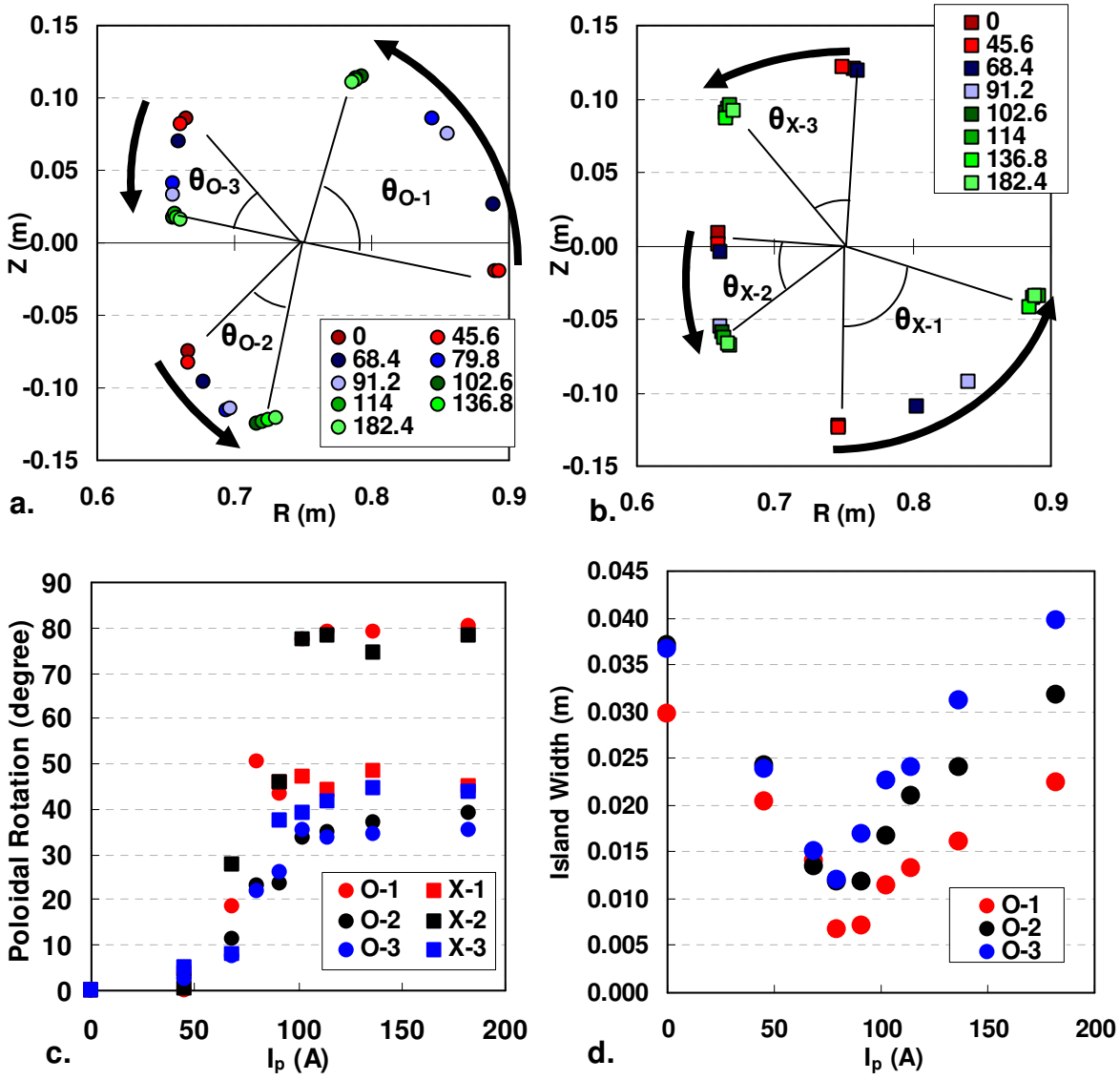

Fig. 7.10 Island primary sweep results
a) O-point locations
b) X-point locations
c) O,X-point poloidal rotation
d) 1/3 island width

The poloidal rotation of each fixed point vs. I_p is shown in Fig. 7.10(c). Here we have defined the amount of poloidal rotation θ, each fixed point has undergone from its starting location. Below I_p=50 A and above I_p=100 A, this angle is relatively constant. Within these current regimes the island is either undercorrected and dominated by the original error field or overcorrected and dominated by the error correction field. Initial island widths shown in Fig. 7.10(d), were measured to be between 0.03 - 0.04 m depending on the poloidal O-point location. When the island is overcorrected, the island width increases to nearly the original island width values. Further increase in I_p beyond I_p=180 A should yield still larger islands widths.

In contrast, when I_p=50-100 A there is significant rotation of the fixed points and the island width is significantly reduced by a factor of three to less than .01 m. This is similar to the simulation results shown in Fig. 7.4 and Fig. 7.5 when the island underwent a shift in position and minimized its size with only slight modifications to the horizontal field strength. Because the island undergoes a rapid poloidal rotation while at its minimum size, the primary correction field applied when I_p=79.8 A is nearly equal and opposite that of the error field causing the island. From the primary sweep of the correction currents we see that our initial guess of the island phase was quite accurate.

In an effort to further minimize the island size, a secondary sweep of currents was performed in which the correction field was swept perpendicular to the primary field as shown in Fig. 7.11. Because the initial current ratio guess $\vec{P}$ was effective in minimizing the island size, we do not expect significant improvements will result from the secondary sweep. The current ratios used to produce the secondary perpendicular field $\vec{S}$, are listed in Table 7.2, labeled “Secondary ECC Ratio”. This secondary set of currents was

calculated from Eq. 7.1, now setting δ=22° (perpendicular to 112°). The secondary current ratio is normalized so the φ=36° coil is one.

The current applied to each coil used in the secondary sweep is given by Eq. 7.3.

$$\vec{I}_{applied} = I_p \cdot \vec{P} + I_s \cdot \vec{S} \tag{7.3}$$

Where I_p =79.8 A is the multiplication factor applied to the primary current ratio $\vec{P}$ and I_s is the multiplication factor applied to the secondary current ratio $\vec{S}$. During the secondary sweep I_s was varied from I_s=-60 to +60 A.

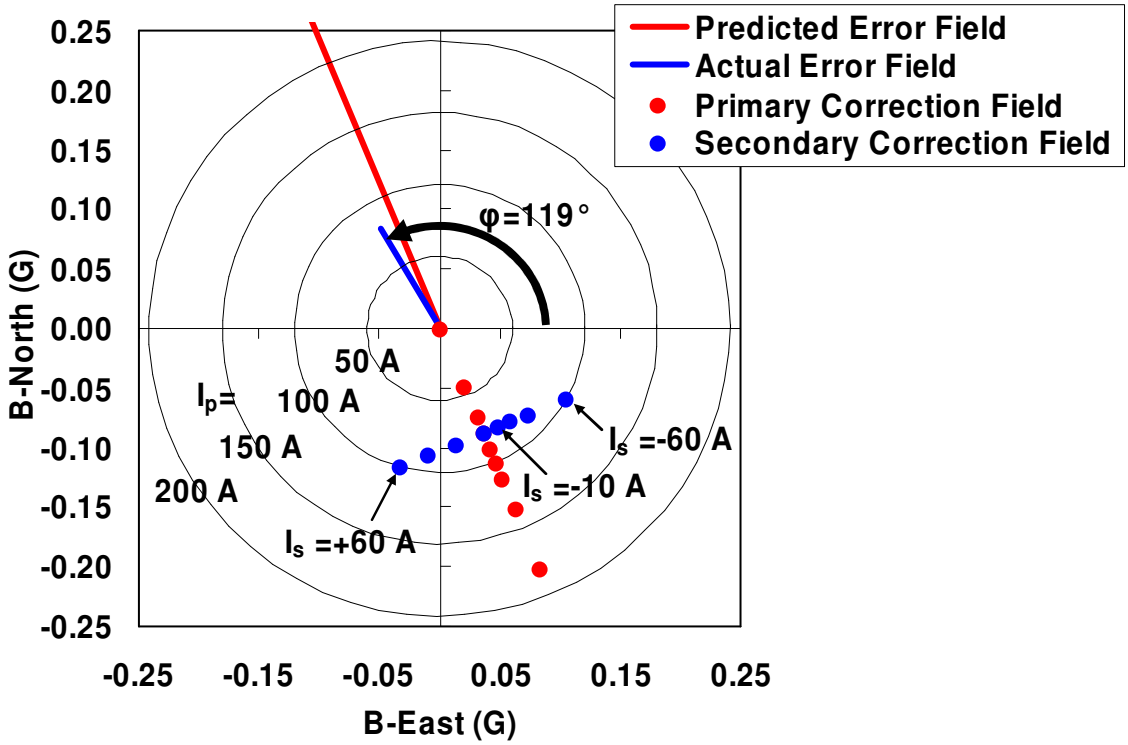

Fig. 7.11 Secondary sweep fields

Shown in Fig. 7.12 are several photographs of the separatrix surface during the secondary sweep. During the primary sweep when excessive correction field was applied the island was dominated by the correction field. Similar behavior occurred during the secondary sweep shown in Fig. 7.12(a,d) with significant out of phase islands being

formed at both I_s = +60 and -60 A. Comparison of the minimum island size of the primary sweep and that of the secondary sweep shown in Fig. 7.12(b) and (c) reveals that slight improvements have been made to the island size in the secondary sweep, confirming once again that the initial primary current ratio guess was quite accurate. The minimum island width obtained in the secondary sweep was less than 0.009 m for I_s=-10.

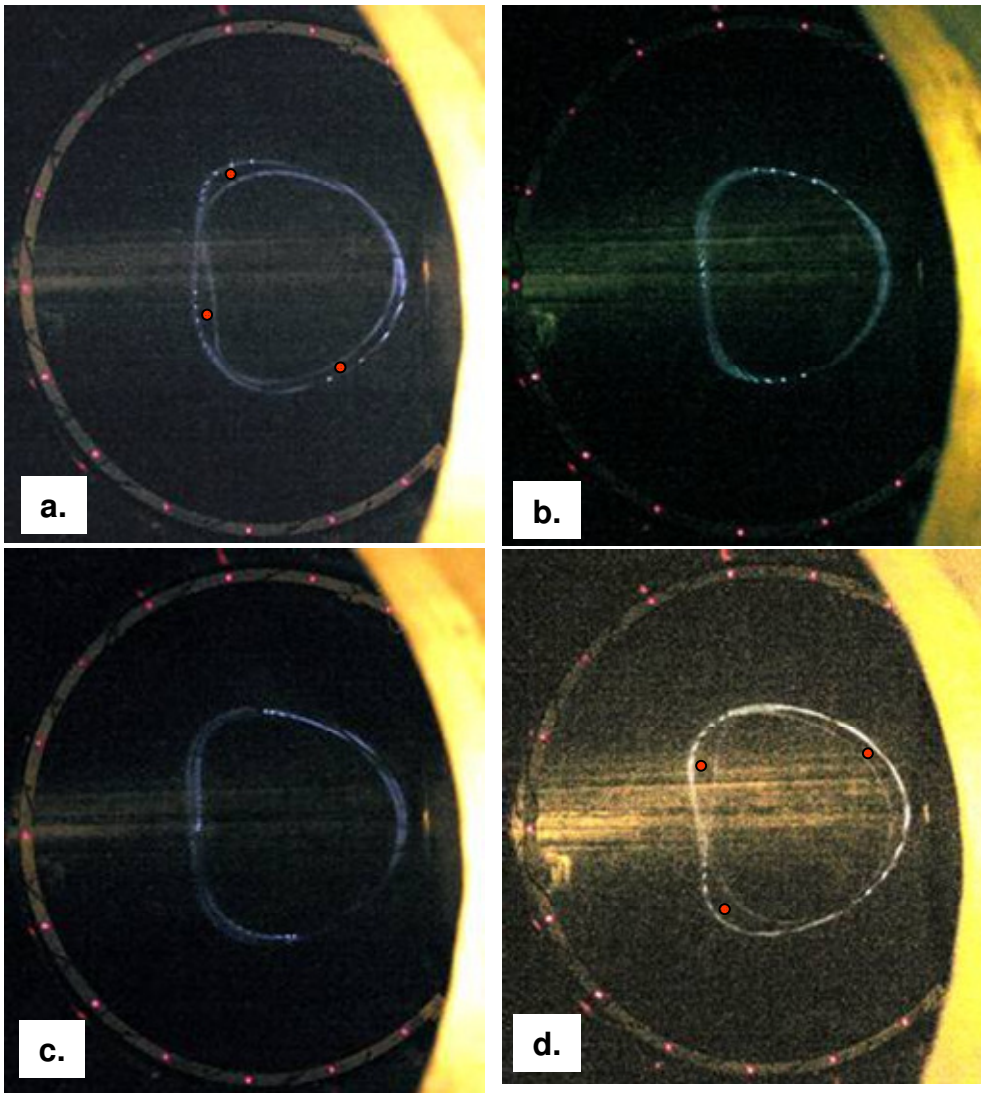

Fig. 7.12 Secondary sweep results
- a) Secondary Over Corrected (-) I_s =-60 A
- b) Secondary Corrected I_s =-10 A
- c) Primary Corrected I_s =0A
- d) Secondary Over Corrected (+) I_s =+60 A

In Fig. 7.12(b) where the secondary correction has minimized the island width, the island structure did not disappear altogether, but instead created a flux surface with non-zero width that appears “fuzzy”. This “fuzzy” flux surface may be caused by several factors. The actual perturbation field is probably a complex field consisting a full spectrum of m and n values. These m and n values include higher order harmonics of the 1/3 flux surface such as the 2/6, 3/9 etc. When the n=1 correction is applied and the 1/3 island is minimized the higher order harmonics now become visible because they are no longer masked by the 1/3 island. Also because the correction field is being applied through a limited number of correction coils the actual correction field is not uniform in space and is not a true n=1 perturbation. Therefore total cancellation of the n=1 perturbation field creating the 1/3 island is not realized. Lastly, the island size, measured to be less than 0.01 m is now approaching the thickness of the electron beam ~0.005 m, making accurate measurements of the island thicknesses increasingly difficult.

In conclusion, field mapping measurements of the magnetic island without an ECC field determined the 1/3 island fixed point locations and island widths. A horizontal error field was used to computationally recreate the island, giving an estimate to the error fields responsible for creating the island. A set of error correction coil currents was used to produce an opposing error field and the magnitude of the currents was swept while the island was observed. At the location in the primary sweep where the island size was minimized, a secondary sweep of currents was performed such that the correction field was perpendicular to the initial primary sweep. The currents in the 5 side ECCs used to make the final minimization of the 1/3 island are listed in Table 7.3. These current ratio

values can be calculated from Eq. 7.1 by setting m=3, n=1, θ=0°, δ=299.7°, B_{mn} =80.5 A, and φ being the five toroidal locations of the side coils.

ECC Location	ECC Current (minimized)
36°	8.7
108°	79.0
180°	40.1
252°	-54.2
324°	-73.6
δ	119.7
B_{mn}	80.5

Table 7.3 Final ECC current ratios

7.6 Island Dependence on Background Field Strength

In the measurement and minimization of the 1/3 island in the previous sections, the origins of the error fields responsible for producing the island were not considered. In an effort to distinguish between the internal field errors and the external field errors another island study was performed in which the overall field strength was varied.

Here the term “internal error” refers to fields dependent on the current in CTH coils at the time of the experiment. This includes field errors created by asymmetries in the coils themselves and also temporary magnetization effects that depend on the currents in the coils. The term “external error” refers to fields independent of the current in the CTH coils at the time of the experiment. This includes the earth’s field and also the remnant portion of the magnetization field that is expected to be nearly constant during the course of the experiment.

We know from the Fig. 7.4 and Fig. 7.5 that the 1/3 island is influenced by both internal errors and external errors and that these two different types of error fields will

scale differently with increasing CTH fields. When the overall strength of the CTH confinement field is decreased, the relative magnitude of the external errors become comparatively larger, whereas, when the overall strength of the CTH field increases the relative magnitude of the external errors will become comparatively smaller. Thus if the confinement field is sufficiently varied from low field values to high field values the island characteristics will first be dominated by the external errors followed by internal errors. By measuring the phase and width of the island at both low and high field values through field mapping it may be possible to determine the relative strengths of the external errors compared to the internal errors.

The O and X point locations of the island are shown Fig. 7.13(a) for the various HF current settings. The radial location of the fixed points varies up to 0.05 m but the poloidal location of the fixed points remains constant. The lack of poloidal rotation in the fixed points reveals that either the external field is in the same direction as the internal error field (which is unlikely) or that the magnitude of the HF field was not varied over a wide enough range. For example, in the field strength simulation (Fig. 7.4) the fixed points remained stationary in two different regimes, when the external error was significantly larger than the internal error of the coils ($|B_{ext}|=1G>>|B_{int}|$) or when the external error was significantly smaller than the internal error of the coils ($|B_{ext}|=0.01G<<|B_{int}|$). In the region when the internal and external errors were comparable ($|B_{ext}|\approx|B_{int}|$) significant poloidal rotation of the fixed points was visible. Thus if the external and internal error fields were similar in magnitude and in different directions, the fixed points should have rotated in the experiment.

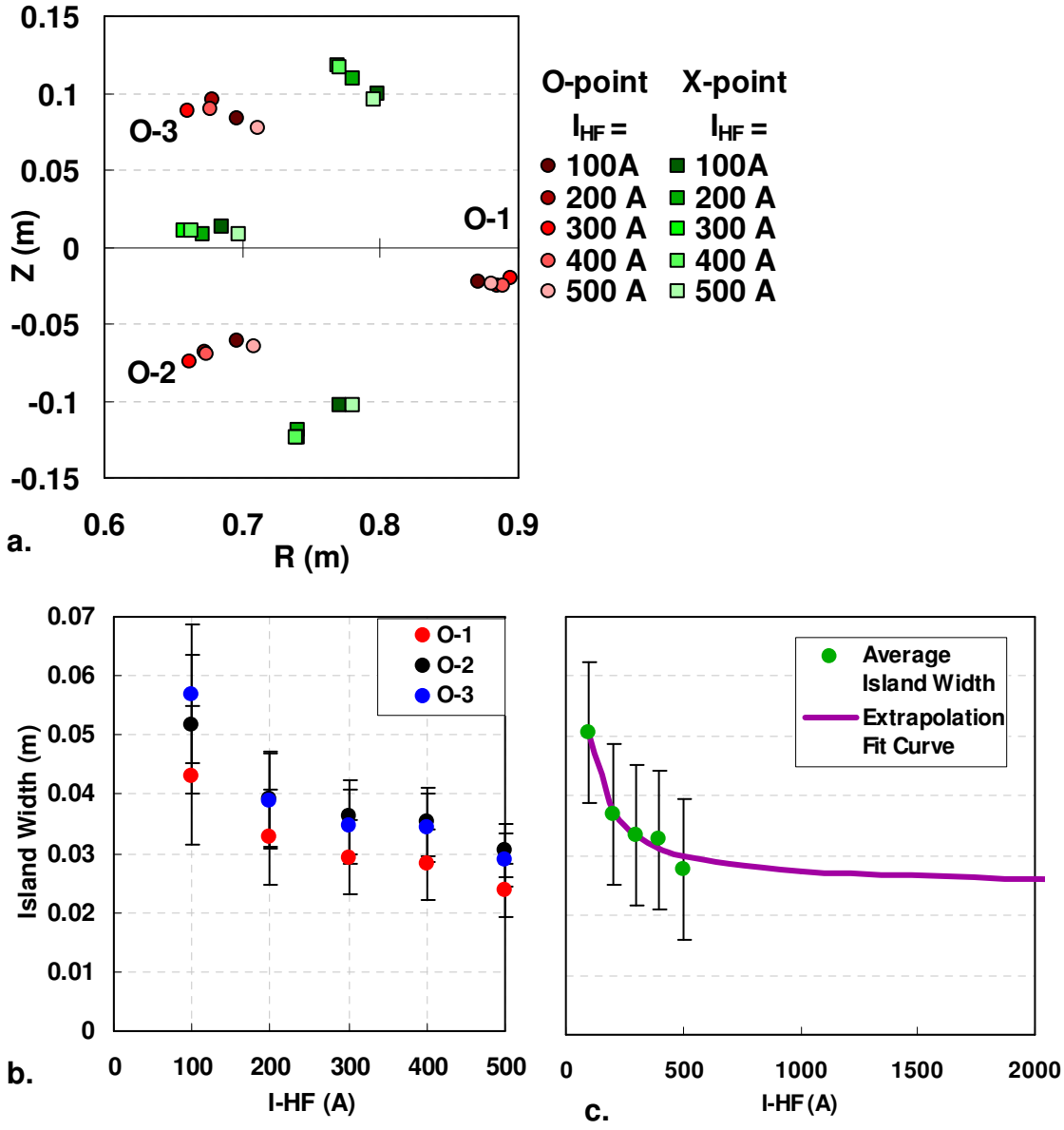

Fig. 7.13 1/3 island dependence on HF field strength
I_{HF} = 100 to 500 A, I_{TVF}/I_{HF} =0.125, I_{TF}/I_{HF}=0.3

At each of the HF current settings, measurements were made of each islands' width shown in Fig. 7.13(b). The island width of all three O-points significantly decreases as the HF current is increased, from .040-.055 m at I_{HF}=100 A, to .025-.030 m at I_{HF}=500 A. To extrapolate the island width vs. I_{HF} to the high field regime we define the island width as[49]

$$\delta = 4\sqrt{\frac{R_0 B_{mn}}{m B_T \iota'}} \tag{7.4}$$

where R_0 is the major radius of the machine, B_{mn} are the Fourier harmonics of the error field perpendicular to the flux surface, B_T is the toroidal component of the magnetic field which is dependent on the HF current, and ι' is the radial derivative of the rotational transform.

If B_{mn} is due to only external error fields, the only term dependent on the HF current is B_T and the island width can be expressed as,

$$\delta_{external} = 4\sqrt{\frac{R_0 B_{mn}^{external}}{m B_T \iota'}} = \sqrt{\frac{c_2}{I_{HF}}}\,. \tag{7.5}$$

On the other hand if the error field is only due to internal errors, then B_{mn} is a function of I_{HF} and to first order can be expressed as $B_{mn}=b_{mn}\, I_{HF}$, where now b_{mn} are Fourier harmonics independent of I_{HF}. Doing a similar substitution for B_T ($B_T = b_T\, I_{HF}$) the island width can be expressed as

$$\delta_{internal} = 4\sqrt{\frac{R_0 B_{mn}^{internal}}{m\iota' B_T}} = 4\sqrt{\frac{R_0 b_{mn}}{m\iota' b_T}} = c_1 \tag{7.6}$$

where now all terms inside the square root are constant with respect to the HF current. Combining the external and internal errors the total island width can be expressed as

$$\delta = \delta_{internal} + \delta_{external} = c_1 + \sqrt{\frac{c_2}{I_{HF}}} \tag{7.7}$$

Fitting the coefficients c_1 and c_2 to the island width data, the resulting curve can be extrapolated to large HF current values for an estimate of the island size. The average island width will be .015 m ±.01 m in plasma field conditions (I_{HF}=5000 A). Estimates to

correct an island of this size when the HF current is 5000 A give roughly 620 ±100 A-Turns in the φ=108° correction coil with the rest of the coil currents determined by the ratio of currents listed in Table 7.3.

APPENDIX

A. WHY A 90 TURN TVF COIL

The TVF coils were designed to have a total of 108 turns in both the upper and lower coil packs but approximately half way through field mapping experiments 18 turns were removed from both the upper and lower the TVF coil packs resulting in a TVF coil with only 90 turns. In following discussion the reasoning for reducing the number of turns in the TVF coil is discussed.

In conjunction with the I_{HF} = 300 A data sets presented in Sec. 6.1 additional data was taken at a lower HF current setting of I_{HF} = 100 A. The experimental setup and type of data collected are shown for the various data sets in Table A.1.

Data Set	Wand/ Screen	Location φ =	I_{HF} (A)	I_{TVF} (A)	TVF Turns	Information Gathered
HF-A (100)	Wand	36º	100	9-15	108	R, Z
HF-A (300)	Wand	36º	300	28-42	108	R, Z
HF-B (100)	Screen	36º	100	9-15	108	R, Z, t
HF-B (300)	Screen	36º	300	28-42	108	R, Z, t
HF-C (100)	Screen	252º	100	9-15	108	R, Z, t
HF-C (300)	Screen	252º	300	28-40	108	R, Z, t

Table A.1 Parameters for initial field mapping experiments

The measured vertical position of the magnetic axis vs. I_{TVF}/I_{HF} for these field mapping tests are shown in Fig. A.1. Similar to the results presented in Sec.6.1, as I_{TVF} is increased, the magnetic axis rises above the midplane with the effect being more

pronounced for the lower HF current. In addition data sets HF-B and HF-C are found above the midplane even at low I_{TVF}.

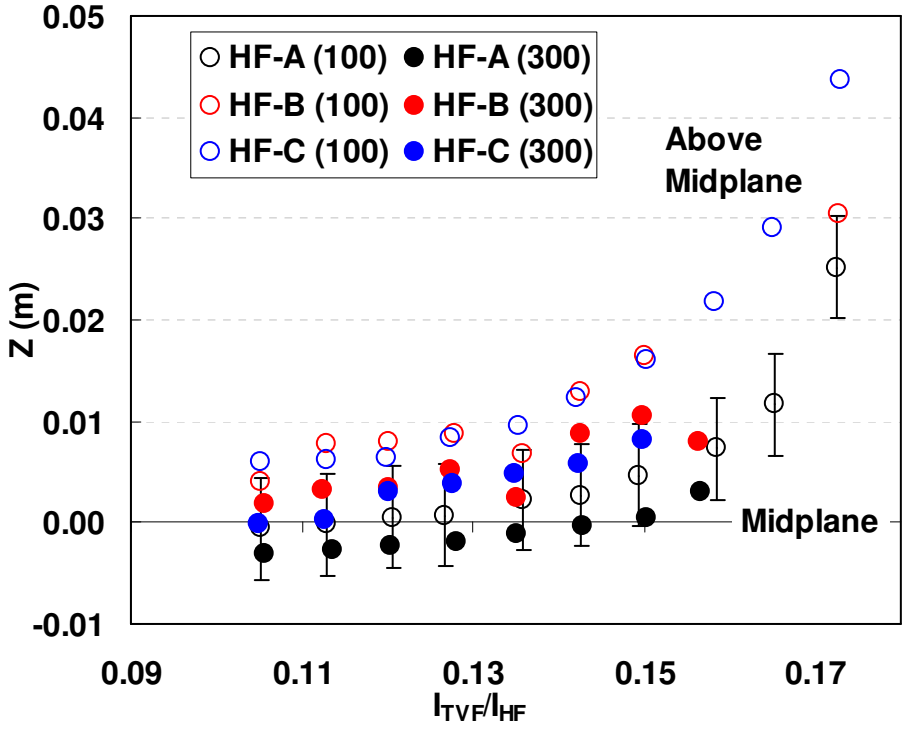

Fig. A.1 Magnetic axis vertical position for HF-(A,B,C)
Here I_{TVF}/I_{HF} is the ratio of A-Turn current in the TVF coil to the A-Turn current in the HF coil.

The experimental field mapping data (R, Z, ŧ) was analyzed using the coil optimization routine described in Ch.5. At the time, the optimization code had recently just been developed and was later found to have several bugs. The optimization procedure led us to suspect that the upper TVF coil had fewer turns than the lower coil. This was confirmed with measurements made using Rogowski coils, suggesting that ~2 turns were missing from the upper TVF coil. Further measurements of the voltage drop between turns in the upper TVF coil showed that ~1 turn was missing in the middle layers of the lower TVF coil in the upper coil stack as shown in Fig. A.2. The TVF coil feeds are constructed such that each of the 18-turn double pancakes could be electrically

disconnected. The suspect coil and its corresponding mate in the lower TVF coil pack, were provisionally removed from the TVF coil circuit before more field mapping measurements were made.

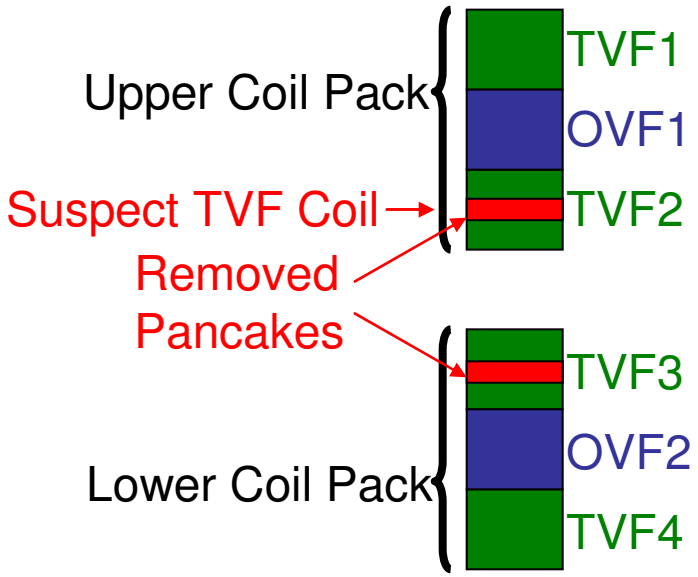

Fig. A.2 Removed pancakes of the TVF coil

Further HF/OVF/TVF field mapping experiments were conducted with the reduced 90 turn TVF coil. Four sets of data were obtained at two HF currents, I_{HF} = 100 and 300 A. The experimental setup and type of data collected for each data set are shown in Table A.2 below.

Data Set	Wand/ Screen	Location φ =	I_{HF} (Amps)	I_{TVF} (Amps)	TVF Turns	Information Gathered
HF-D-100	Screen	252°	100	10-17	90	R, Z , t
HF-D-300	Screen	252°	300	30-56	90	R, Z , t
HF-E-100	Wand	36°	100	10-17	90	R, Z
HF-E-300	Wand	36°	300	30-54	90	R, Z

Table A.2 HF-(D,E) setup (90 TVF Turns)

During this latter field mapping campaign, the effects of magnetization and the influence that it has on the magnetic axis were realized in a separate field mapping

experiment involving the TF coils. Measurements made with a Hall probe found that the remnant magnetic field near the vacuum vessel could be up to 3 G. This is roughly 3% of the field during field mapping experiments run at I_{HF} =100 A, but only 1% of the field during field mapping experiments run at I_{HF} =300 A. Because of the pronounced effect magnetization has on the I_{HF} = 100 A data, these data sets were no longer considered valid in determining the HF coil winding law and were omitted.

With only the I_{HF} = 300 A data in consideration, a comparison in the vertical position of the two TVF coil configurations is shown in Fig. A.3. There is not a clear distinction between the data of the two different TVF coil configurations. For every missing turn in the TVF coil during the collection of data for HF-(A,B,C), one would expect that the magnetic axis would be 1-6 mm higher than that of HF-(D,E) which is not shown in the data. The differences in the magnetic axis position can be attributed to variation in the background field of the laboratory due to magnetization of ferromagnetic material and are not necessarily a result of TVF coil short.

With this new evidence, data sets HF-(A,B,C) are equally valid and are included in the HF coil optimization, Sec. 6.1. The analysis presented in Sec. 6.1 makes no assumption of a short in the TVF coil. Further experimental tests are needed on the TVF coil to say with certainty whether there is a TVF short. Currently during plasma operation the TVF coil is in a 90 turn configuration because it is found to improve control of the radial position of the plasma when toroidal ohmic currents are induced in the plasma.

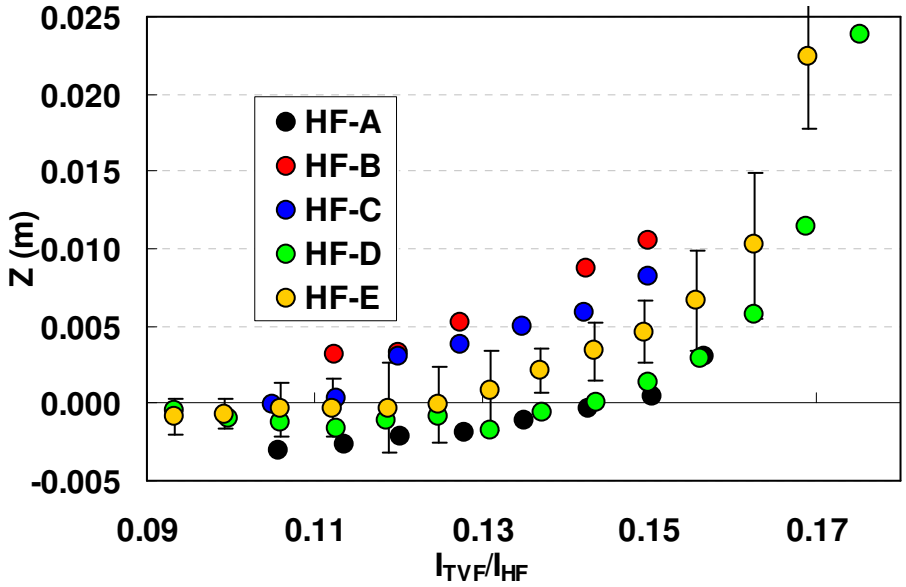

Fig. A.3 Vertical position of the magnetic axis vs. TVF current.

1 S. Atzeni and J. Meyer-ter-Vehn. *The Physics of Inertial Fusion*, Oxford University Press, New York p. 5 (2004)
2 S. Atzeni and J. Meyer-ter-Vehn, IBID p. 12
3 S. Atzeni and J. Meyer-ter-Vehn, IBID p. 4
4 F. Chen, *Introduction to Plasma Physics and Controlled Fusion*, Plenum Press, New York (1984) p. 20
5 C.M. Braams and P.E. Scott, *Nuclear Fusion, Half a Century of Magnetic Confinement Fusion Research*, Institute of Physics Publishing, Philadelphia p. 37 (2002)
6 J. Wesson, *Tokamaks (The International Series of Monographs on Physics, 118)*, Oxford University Press, New York (2004)
7 B.A. Carreras et al. Nucl. Fusion Vol. 28 No. 9 p. 1613 (1988)
8 A. Boozer, Physics of Plasmas Vol. 5 No. 5 p. 1647 (1998)
9 T.C. Hender et. al. Nucl. Fusion Vol. 47, No. 6 p. s128 (2007)
10 F. Chen, IBID p. 29
11 R.K. Wangsness, *Electromagnetic Fields 2nd ed.*, John Wiley and Sons, New York, p. 246 (1986)
12 J.R. Cary and J.D. Hanson, Phys. Fluids Vol. 29 No.8 p. 2464 (1986)
13 K. Miyamoto, *Plasma Physics for Nuclear Fusion*, The MIT Press, Cambridge MA, p.16 (1976)
14 M. Wakatani, *Stellarator and Heliotron Devices*, Oxford University Press, New York, p.10 (1998)
15 J.D. Hanson and J.R. Cary, Phys. Fluids Vol. 29 No. 4 p. 767 (1984)
16 J.R. Cary and J.D. Hanson, IBID
17 K. Miyamoto, IBID p. 35
18 S.H. Strogatz, *Nonlinear Dynamics and Chaos*, Westview Press, Cambridge Ma, p. 17 (1994)
19 S.P. Hirshman and J.C. Whitson, Phys Fluids, Vol. 26 No. 12 p. 3553 (1983)
20 R. Takahashi et al., *Proceedings of the International stellarator/Heliotron workshop*, IAEA Tech. Comm. Meeting, Vol. 2, p. 220 (1986)
21 G.J. Hartwell, R. Gandy, M. Henderson et al., Rev. Sci. Instrum Vol. 59 No. 3 p.460 (1988)
22 G.J. Hartwell, R. Gandy, M. Henderson et al., IBID
23 T.S. Pedersen, *Stellarator News*, Is. 97 p. 1 (2005)
24 G.J. Hartwell et al. Design and Construction of the Compact Toroidal Hybrid, (to be published)
25 New England Wire Technologies, 130 North Main Street, Lisbon, NH 03585
26 Princeton Plasma Physics, Laboratory, James Forrestal Campus, P.O. Box 451
27 J.P Pattern, 5038 N 125th St., Butler, WI 53007
28 M.A. Henderson et al. Rev. Sci. Instrum Vol. 63 No. 12 p. 5678 (1992)
29 M. Wakatani, IBID p. 20
30 K. Miyamoto IBID p. 37
31 G.J. Hartwell, R. Gandy, M. Henderson et al., Rev. Sci. Instrum Vol. 59 No. 3 p.460 (1988)
32 R. Jaenicke, E. Ascasibar, P. Grigull et. al., Nucl. Fusion, Vol. 33 No5 p. 687 (1993)
33LabView 8.0 for Machine Vision © 2008 National Instruments Corporation, 11500 N. Mopac Expwy, Austin, TX 78759
34 W.H. Press, B.P. Flannery, S.A. Teukolsky, W. T. Vetterling, *Numerical Recipes in Fortran 77: The art of scientific computing, 2nd ed*, Cambridge University Press, New York, p. 51 (1996)
35 Private Communication J.D. Hanson (V3FIT Minimization) Auburn University
36 W.H. Press, B.P. Flannery, S.A. Teukolsky, W. T. Vetterling, IBID p. 651
37 Private Communication J.D. Hanson (V3FIT Minimization) Auburn University
38 R.K. Wangsness, IBID p. 338
39 J.D. Jackson, *Classical Electrodynamics 3rd ed.*, John Wiley and Sons, New York, p. 200 (1999)
40 http://www.ngdc.noaa.gov/seg/geomag/magfield.shtml
41 A.J. Lichtenberg and M.A. Lieberman, *Regular and Chaotic Dynamics 2nd ed*., Springer-Verlag, New York, p.77 (1983)
42 R.F. Gandy, G.J. Hartwell, J.D. Hanson, S.F. Knowlton, and H. Lin, Phys. Fluids B Vol. 5 No. 12 p. 4384 (1993)
[43] S.H. Strogatz, *Nonlinear Dynamics and Chaos* Westview Press, Cambridge Ma, p. 17 (1994)

44 A. Komori, R. Sakamoto, T. Morisaki, et al., 28th EPS Conference on Contr. Fusion and Plasma Phys., Funchal June 18-22 (2001) p. 1505
45 R. Jaenicke, et al., Plasma Physics and Controlled Fusion Vol. 44 p. B193 (2002)
46A.J. Lichtenberg and M.A. Lieberman, IBID p.49
47 J.D. Hanson, Nucl. Fusion, Vol. 34 No. 3 p. 441 (1994)
48 J.D. Hanson, IEEE Trans Plas Sci, Vol 27 No. 6 p. 1588 (1999)
49 M.A. Henderson, PHD Dissertation, Auburn University p. 161 (1991)